



저작자표시-비영리-변경금지 2.0 대한민국

이용자는 아래의 조건을 따르는 경우에 한하여 자유롭게

- 이 저작물을 복제, 배포, 전송, 전시, 공연 및 방송할 수 있습니다.

다음과 같은 조건을 따라야 합니다:



저작자표시. 귀하는 원저작자를 표시하여야 합니다.



비영리. 귀하는 이 저작물을 영리 목적으로 이용할 수 없습니다.



변경금지. 귀하는 이 저작물을 개작, 변형 또는 가공할 수 없습니다.

- 귀하는, 이 저작물의 재이용이나 배포의 경우, 이 저작물에 적용된 이용허락조건을 명확하게 나타내어야 합니다.
- 저작권자로부터 별도의 허가를 받으면 이러한 조건들은 적용되지 않습니다.

저작권법에 따른 이용자의 권리는 위의 내용에 의하여 영향을 받지 않습니다.

이것은 [이용허락규약\(Legal Code\)](#)을 이해하기 쉽게 요약한 것입니다.

[Disclaimer](#)

A THESIS
FOR THE DEGREE OF DOCTOR OF PHILOSOPHY

Hybrid Nanostructured Materials for Supercapacitors and Self-Powered Systems



ANANTHAKUMAR RAMADOSS

Faculty of Applied Energy System (Major: Mechanical Engineering)

GRADUATE SCHOOL
JEJU NATIONAL UNIVERSITY

2015. 02

Hybrid Nanostructured Materials for Supercapacitors and Self-Powered Systems

Ananthakumar Ramadoss

(Supervised by Professor Sang-Jae Kim & Professor Gui-Shik Kim)

A thesis submitted in partial fulfillment of the requirement for the degree of
Doctor of Philosophy

2014. 12.

This thesis has been examined and approved.

Thesis Director, Prof. Young Sun Mok	 Professor, Department of Chemical & Biological Engineering, Jeju National University
Thesis Committee Member, Prof. Gui-Shik Kim	 Professor, Department of Mechanical Engineering, Jeju National University
Thesis Committee Member, Prof. Sang-Jae Kim	Professor, Department of Mechatronics Engineering, Jeju National University
Thesis Committee Member, Prof. Hyeon Suk Shin	Associate Professor, Department of Chemistry, Ulsan National Institute of Science and Technology
Thesis Committee Member, Prof. Sang Min Lee	Assistant Professor, School of Mechanical Engineering, Chung-Ang University

December , 2014.

Faculty of Applied Energy System (Major: Mechanical Engineering)

GRADUATE SCHOOL

JEJU NATIONAL UNIVERSITY

REPUBLIC OF KOREA

I would like to dedicate this thesis to

My Beloved Father, Mother, Brother and Sisters



제주대학교 중앙도서관
JEJU NATIONAL UNIVERSITY LIBRARY

For their endless love, support and encouragement

Acknowledgement

First of all I thank the ‘**GOD ALMIGHTY**’ for showering me his abundant blessings, strength and wisdom to achieve this task successfully.

It gives me pride and pleasure to express my deep sense of gratitude to my beloved supervisor **Prof. Sang Jae Kim**, for his supervision, advice and guidance as well as giving me extraordinary experience throughout the work. He has been supportive since the day I began working on this project. I always remember his saying “whatever experience you are gaining, that will all help you at some moment of your life time” and “Try to achieve your goal with the available resources around you”. I could not simply acknowledge by expressing mere thanks for such a responsive supervisor.

My earnest gratefulness to my co-research supervisor, **Prof. Gui-Shik Kim**, for his constant supervision and scholarly advice throughout the course of this research work. I specially thank him for his immense patience for all the activities carried out by me throughout my research period.

I express my sincere thanks to **Dr. M. Jayachandran** and **Dr. B. Subramanian**, Scientists, Electrochemical Materials Science Division, Central Electrochemical Research Institute, Karaikudi, who initiated my research carrier and actively directed me in the research with their constant support, encouragement and enthusiastic advice.

I have been still finding a suitable word to express my ineffable sense of gratitude to *my friend*, **Mr. Balasingam Suresh Kannan** for his constant help, guidance, advice, carrying and encouragement to complete this work successfully.

I sincerely thank **Dr. Subrata Kundu, Dr. R. Thangamuthu, and Mr. M. Murugesan**, Central Electrochemical Research Institute, Karaikudi for their constant support and encouragement. I extend my gratefulness to **Dr. K. Selvaraju, and Dr. G. Selvan**, Thanthai Hans Roever College, Perambalur for their immense moral support.

I would like to thank **Dr. K. Karthikeyan, Mr. B. Saravanakumar, and Mr. K. Thiayagarajan**, for their timely help in experiments, support, valuable opinions and continuous encouragement to my life even at outside lab during my Ph.D. carrier.

It gives me an immense pleasure to gratitude my acknowledgment and thanks to current and former member of our research team **Dr. Rajneesh Mohan, Dr. Shrikant Saini, Dr. V. Gunasekaran, Dr. S. Radhakrishnan, Mr. Eui-Youg Hong, Ms. Shin So Yoon, Mr. Taehyun Kim, Mr. V. Ganesh Kumar, Mr. Nagamelleshwara Rao, Mr. Arunkumar, Ms. Sophia, Mr. Ko, Ms. Minhee and Mr. Seong Mingeon**, for their continuous support, helps rendered in the laboratory and valuable discussion in the weekly meetings to complete this research work successfully.

Staying away from home is always challenging and tough. However, I am glad to have friends in Jeju who always made be believe they are there when it matters and has been part of my happiness and hard ships. **Dr. Anil, Dr. Dharaneetharan, Mr. Sebastian Ananth, Dr. Saranya, Dr. Sridharan, Dr. Navaneethan, Dr. Purushothaman, Dr. Ganesh, Dr. Umasuthan, Dr. Gandhi, Dr. Karuppia, Mr. Sudhagar, and Ms. Mothi Seran**. I would like thank all of them for giving me so many wonderful memories to cherish during my stay in Jeju.

I wish to express my heartfelt and profound thanks to **Dr. S. N. Karthi, Dr. Vidhya, Dr. Raja, Mr. Siva, Mr. Gopi, Ms. Mathi, Ms. Bavya, Mr. Praba, Mr.**

Murali, Mr. Angu, Mr. Sathish and Mr. Arun, for their kind help and motivation made this work as a pleasure and great one. I would also like to thank, **Dr. Manivasakan, Dr. Suthan Kissinger, Dr. Yuvakkumar, Dr. Rajkumar, Ms. Kowsalya, and Mr. Balaji** for their kind help and motivation.

I would like to thank the following Jeju friends, who made homely environment during my stay in Korea “**Dr. Kalpa, Dr. Nauman, Mr. Kamran Ali, Mr. Zhahid, Dr. Zubair, Dr. Adanan Ali, Dr. Naeem, Dr. Murtaza, Mr. Safdar, Mr. Farrukh, Mr. Razhid, Mr. Sohail, Mr. Junaid, Mr. Mamoon, Mr. Lakmal, Mr. Anushka, and Mr. Suresh**”. I also thank all the JISO members who has been very co-operative and supporting during my stay in Jeju.

I am very much thankful to Research Instrument Center at JNU for providing the instrumental facilities during my study and I also thank **Mr. J. E. Koh** for his cheerful assistance in FE-SEM measurements. I also thank Brain Korea 21 plus and graduate school of Jeju National University for provided the funds for my Ph.D. work.

I bow before **my parents (Mr. T. Ramadoss & Ms. R. Sudamani)** who have sacrificed their today for the betterment my tomorrow with love and gratitude. I am very much grateful to them. Words can hardly substitute the indebted that I owe to my inspiring, **brother (Mr. R. Ashokkumar), sisters (Ms. R. Ananthi & Ms. R. Arivuchudar) and friends** who stood behind in all possible ways to complete this work successfully. Without the above I might not complete this research work as great full one.

Finally, my thanks are due to all those who have helped me directly and indirectly for the successful completion of my research work.

R. ANANTHAKUMAR

Table of Contents

Acknowledgement	i
Table of Contents	iv
Nomenclature	xiv
List of Tables	xvii
List of Schemes	xviii
List of Figures	xix
Abstract-Hangul	xxxii
Abstract	xxxvi
 CHAPTER I- Introduction	
1.1. Global energy issues and the importance of energy storage devices...	1
1.2. Principle and mechanism of supercapacitors	5
1.2.1. Electrochemical double layer capacitors.....	5
1.2.2. Pseudocapacitors	6
1.2.3. Hybrid supercapacitor	8
1.3. Electrode materials	9
1.3.1. Carbon materials	10
1.3.2. Metal oxides	11
1.3.3. Conducting polymers	13
1.3.4. Transition metal dichalcogenides	14
1.3.5. Graphene and graphene based composite materials	15
1.4. Energy harvesting: Nanogenerator	19
1.4.1. Mechanism of piezoelectric nanogenerator	20
1.4.2. Piezo-materials	21

1.5. Objectives and scope of thesis	22
1.6. Structure of this thesis	24
1.7. References	26

CHAPTER II- Materials Characterization and Electrochemical Techniques

2.1. Reagents and apparatus	43
2.2. Materials synthesis	45
2.2.1. Hydrothermal synthesis	45
2.2.2. Microwave synthesis	46
2.2.3. Electrodeposition	46
2.2.4. Graphene oxide synthesis by modified Hummer's method	47
2.3. Materials characterization	48
2.3.1. X-ray diffraction (XRD)	48
2.3.2. Raman spectroscopy	48
2.3.3. Fourier transform infrared (FT-IR) spectrometer	49
2.3.4. Field-emission scanning electron microscopy	49
2.3.5. High-resolution transmission electron microscopy	49
2.3.6. Energy dispersive X-ray spectroscopy analysis (EDS)	49
2.3.7. X-ray photoelectron spectroscopy (XPS)	50
2.3.8. UV-Vis spectrophotometer (UV-Vis)	50
2.3.9. Brunauer, Emmett and Teller (BET) surface area analysis	50
2.4. Electrode fabrication and cell assembly	51
2.4.1. Electrode fabrication	51
2.4.2. Cell assembly	52
2.5. Electrochemical Testing	53

2.5.1. Cyclic voltammetry	54
2.5.2. Galvanostatic charge/discharge	54
2.5.3. Electrochemical impedance spectroscopy	55
2.6. Calculation of electrochemical parameters	55
2.7. References	57

CHAPTER III- Transition Metal Oxide/Hydroxides Based Hierarchical Nanostructure for Electrochemical Supercapacitors

3.1. Synthesis and Electrochemical Performance of Vertically Aligned TiO₂ Nanorods

3.1.1. Introduction	62
3.1.2. Experimental methods	63
3.1.2.1. Preparation of TiO ₂ NR arrays by hydrothermal method ...	63
3.1.2.2. Electrochemical characterization of TiO ₂ NR arrays	64
3.1.3. Results and discussion	65
3.1.3.1. Growth mechanism of TiO ₂ NR arrays	65
3.1.3.2. Structural properties of TiO ₂ NR arrays	66
3.1.3.3. Morphological properties of TiO ₂ NR arrays	67
3.1.3.4. Electrochemical characterization	68
3.1.4. Conclusion	72
3.1.5. References	73

3.2. Synthesis and Electrochemical Performance of TiO₂@MnO₂ Core-Shell Nanostructure

3.2.1. Introduction	79
3.2.2. Experimental methods	80
3.2.2.1. Preparation of TiO ₂ @MnO ₂ core-shell nanostructures	80

3.2.2.2. Electrochemical measurements	81
3.2.3. Results and discussion	82
3.2.3.1. Structure, morphology and composition analysis	83
3.2.3.2. Electrochemical characterization	90
3.2.4. Conclusion	97
3.2.5. References	98
3.3. Synthesis and Electrochemical Performance of TiO₂@CoO₃ Core-Shell Nanostructure	
3.3.1. Introduction	105
3.3.2. Experimental details	106
3.3.2.1. Preparation of TiO ₂ /Co ₃ O ₄ core-shell nanostructure	106
3.3.2.2. Electrochemical characterization	107
3.3.3. Results and discussion	107
3.3.3.1. Structure, morphology and compositional analysis	108
3.3.3.2. Electrochemical characterizations	110
3.3.4. Conclusion	115
3.3.5. References	116
3.4. Synthesis and Electrochemical Performance of TiO₂@Co(OH)₂ Core-Shell Nanostructure	
3.4.1. Introduction	119
3.4.2. Experimental methods	120
3.4.2.1. Preparation of TiO ₂ /Co(OH) ₂ hierarchical nanostructure ...	120
3.4.2.2. Electrochemical characterization	121
3.4.3. Results and discussion	121
3.4.3.1. Synthesis and characterisation	121

3.4.3.2. Electrochemical analysis	125
3.4.4. Conclusion	131
3.4.5. References	132
 CHAPTER IV- Two Dimensional Nanomaterials for Electrochemical Supercapacitors	
4.1. Synthesis and Electrochemical Performance of MoS₂ Nanostructure	140
4.1.1. Introduction	140
4.1.2. Experimental methods	141
4.1.2.1. Synthesis and characterization of mesoporous MoS ₂ nanostructure	141
4.1.2.2. Electrochemical measurements	142
4.1.3. Results and discussion	143
4.1.3.1. Structure, morphology and compositional analysis	143
4.1.3.2. Electrochemical characterization of mesoporous MoS ₂ nanostructure electrode	147
4.1.4. Conclusion	152
4.1.5. References	153
4.2. Synthesis and Electrochemical Performance of Graphene Coated Fabrics	
4.2.1. Introduction	160
4.2.2. Experimental Section	161
4.2.2.1. Synthesis of graphene oxide (GO)	161
4.2.2.2. Fabrication of the graphene-coated fabric	162
4.2.2.3. Electrochemical measurements of graphene-coated fabric electrode	162
4.2.2.4. Fabrication of a flexible solid-state SSC	163

4.2.3. Results and discussion	163
4.2.3.1.Characterisation of the graphene-coated fabric	164
4.2.3.2.Electrochemical performance of the graphene-coated fabric electrode	167
4.2.3.3.Electrochemical performance of the flexible solid-state SSC	170
4.2.4. Conclusion	173
4.2.5. References	174

CHAPTER V- Graphene-Based Composites for Electrochemical Supercapacitors

5.1. Synthesis and Electrochemical Performance of Graphene-ZnO Nanocomposites

5.1.1. Introduction	181
5.1.2. Experimental methods	182
5.1.2.1.Synthesis of graphene oxide	182
5.1.2.2.Synthesis of GO-Zn(OH) ₂ composite	183
5.1.2.3.Synthesis of graphene-ZnO nanocomposite	183
5.1.2.4.Preparation of electrodes and electrochemical characterization	184
5.1.3. Results and discussion	185
5.1.3.1.Structural analysis	185
5.1.3.2.Morphology and compositional analysis	187
5.1.3.3. Electrochemical analysis	189
5.1.4. Conclusion	193
5.1.5. References	194

5.2. Synthesis and Electrochemical Performance of TiO₂/rGO/TiO₂ Hybrid Nanostructure	
5.2.1. Introduction	202
5.2.2. Experimental methods	203
5.2.2.1. Preparation and characterization of rGO / TiO ₂ NR / rGO electrode	203
5.2.2.2. Electrochemical characterization of rGO / TiO ₂ NR / rGO electrodes	205
5.2.3. Results and discussion	205
5.2.4. Conclusion	214
5.2.5. References	216
5.3. Synthesis and Electrochemical Performance of Graphene-TiO₂ Nanocomposites	
5.3.1. Introduction	220
5.3.2. Experimental methods	222
5.3.2.1. Synthesis of TiO ₂ nanoparticles	222
5.3.2.2. Synthesis of reduced graphene oxide	222
5.3.2.3. Synthesis of the graphene-TiO ₂ hybrid nanostructure	223
5.3.2.4. Preparation of electrodes and electrochemical characterization	224
5.3.2.5. Electrochemical measurements in two electrode system ...	225
5.3.3. Results and discussion	225
5.3.3.1. Material characterizations	225
5.3.3.2. Electrochemical studies	234
5.3.3.3. Electrochemical performance in two-electrode system	241
5.3.3.4. Performance of solid-state supercapacitor devices.....	245
5.3.4. Conclusion	246

5.3.5. References	247
5.4. Synthesis and Electrochemical Performance of Graphene-V₂O₅ Nanocomposites	
5.4.1. Introduction	252
5.4.2. Experiment details	253
5.4.2.1.Synthesis of reduced graphene oxide/vanadium pentoxide composites	253
5.4.2.2.Fabrication of working electrodes and their electrochemical characterization	255
5.4.2.3.Electrochemical measurements in two electrode system ...	256
5.4.2.4.Fabrication of solid-state supercapacitors	256
5.4.3. Results and discussion	256
5.4.3.1. Structural analysis of the as-prepared samples	257
5.4.3.2.Compositional analysis of the as-prepared samples	261
5.4.3.3.Morphology and microstructure analysis of the as-prepared samples	263
5.4.3.4.Electrochemical performance of the as-prepared samples ..	265
5.4.3.5.Electrochemical performance in two-electrode system	274
5.4.3.6.Performance of solid-state supercapacitor devices	278
5.4.4. Conclusion	279
5.4.5. References	280
CHAPTER VI- Self-Powered Systems	
6.1. Introduction	285
6.2. Fabrication of a flexible solid-state SSC	286
6.3. Piezoelectric output of the Lead zirconate titanate (PZT) film	286

6.4. Self-powered UV sensors	288
6.4.1. Graphene-based all-solid state flexible supercapacitor for self-powered systems	288
6.4.2. Graphene-TiO ₂ symmetric supercapacitor for self-powered systems	290
6.4.3. Graphene-V ₂ O ₅ symmetric supercapacitor for self-powered systems	291
6.5. Conclusion	293
6.6. References	294

CHAPTER VII- Self-Charging Supercapacitor Power Cell: Energy Conversion and Storage

7.1. Symmetric Supercapacitor Based on MnO₂ with PVDF-ZnO Separator

7.1.1. Introduction	298
7.1.2. Experiment details	298
7.1.2.1. Synthesis of MnO ₂ nanowires	298
7.1.2.2. Fabrication of a self-charging supercapacitor power cell (SCSPC)	299
7.1.3. Results and discussion	300
7.1.3.1. Characterization of piezoelectric materials (separator as well as power source)	301
7.1.3.2. Characterization of electrode materials	302
7.1.3.3. Electrochemical behavior of the self-charging supercapacitor power cell	305
7.1.3.4. Mechanism of self-charging supercapacitor power cell	306
7.1.3.5. Self-charging performance of as-fabricated SCSPC	310
7.1.4. Conclusion	315
7.1.5. References	317

7.2. Asymmetric Supercapacitor Based on Graphene and Graphene- V₂O₅ with PVDF-ZnO Separator	
7.2.1. Introduction	321
7.2.2. Experiment details	321
7.2.2.1. Fabrication of a self-charging supercapacitor power cell (SCSPC)	321
7.2.3. Results and discussion	322
7.2.3.1. Electrochemical behavior of the self-charging supercapacitor power cell	323
7.2.3.2. Mechanism of self-charging supercapacitor power cell	324
7.2.3.3. Self-charging performance of as-fabricated SCSPC	327
7.2.4. Conclusion	331
7.2.5. References	333
CHAPTER VIII- Conclusions and Future Work	
8.1. Conclusions	335
8.2. Suggestions for the Future Work	339
Appendix A List of Publications	340
Appendix A List of Conferences	343

Nomenclature

0-9

1D One dimensional

2D Two dimensional

3D Three dimensional

A

AC Alternating current

B

BET Brunauer-Emmett-Teller

BJH Barrett-Joyner-Halenda

C

CV Cyclic voltammetry

D

DI De-ionized

DMF Dimethylformamide

E

ECs Electrochemical capacitors

EDLCs Electrochemical double layer capacitors

EDS Energy dispersive X-ray spectroscopy analysis

EIS Electrochemical impedance spectroscopy

ESR Equivalent series resistance

F

FE-SEM Field-emission scanning electron microscope

FT-IR Fourier transform infrared

FTO	Fluorine-doped tin oxide
G	
GCD	Galvanostatic charge/discharge
GO	Graphene oxide
GV	Reduced graphene oxide/Vanadium pentoxide
H	
HR-TEM	High-resolution transmission electron microscope
I	
ITO	Indium-doped tin oxide
J	
JCPDS	Joint committee on powder diffraction standards
L	
LED	Light emitting diode
N	
NMP	<i>N</i> -Methyl-2-pyrrolidinone
NPs	Nanoparticles
NR	Nanorod
P	
PTFE	Polytetrafluoroethylene
PVDF	Poly(vinylidene difluoride)
PVA	Polyvinyl alcohol
R	
rGO	Reduced graphene oxide
S	



SAED	Selected area electron diffraction
SCE	Saturated calomel electrode
SCSPC	Self-charging supercapacitor power cell
SEM	Scanning electron microscope
SSC	Solid state supercapacitors
T	
TEM	Transmission electron microscope
TM	TiO ₂ @MnO ₂
TMDs	Transition metal dichalcogenides
X	
XRD	X-ray diffraction
XPS	X-ray photoelectron spectroscopy



List of Tables

Table 1.1	The basic characteristics of electrostatic capacitors, supercapacitors and batteries	3
Table 2.1	Materials and chemicals used in the research project	43
Table 2.2	Apparatus used in the research project	45



List of Schemes

Scheme 3.1.1	Schematic illustration of formation process of the vertically aligned TiO ₂ nanorod arrays on the FTO substrate.	65
Scheme 3.2.1	Schematic diagram illustrating the synthesis procedure of a TiO ₂ @MnO ₂ core-shell array electrode on a fluorine-doped tin oxide (FTO) substrate.	81
Scheme 3.3.1	Schematic diagram illustrating the synthesis procedure of a TiO ₂ @Co ₃ O ₄ core-shell array electrode on a fluorine-doped tin oxide (FTO) substrate.	107
Scheme 3.4.1	Schematic diagram showing the TiO ₂ /Co(OH) ₂ hierarchical nanostructure growth process.	122
Scheme 4.2.1	Schematic representation of the formation of the graphene nanosheets.	164
Scheme 5.1.1	Schematic representation of the growth process of the graphene-ZnO nanocomposite.	183
Scheme 5.2.1	Schematic diagram of an rGO / TiO ₂ NR / rGO electrode.	204
Scheme 5.3.1	Schematic representation of the formation process of the graphene-TiO ₂ hybrid nanostructure. The inset shows photographs of graphene oxide (GO), graphene, TiO ₂ , and graphene-TiO ₂ hybrid nanostructure.	224
Scheme 5.4.1	Schematic representation of reduced graphene oxide/vanadium pentoxide composites growth process.	254
Scheme 6.1.1	Electric circuit diagram for the self-powered photosensor.	288
Scheme 7.1.1	(a) Schematic diagram of the fabricated SCSPC. (b) The digital images of SCSPC based on aluminum foil and conductive fabric.	300
Scheme 7.2.1	Schematic representation of the self-charging supercapacitor power cell (SCSPC) structure. The rGO on aluminum foil are used as the positive electrode and G-V ₂ O ₅ composite on aluminum foil are used as the negative electrode; PVDF-ZnO as a separator. Inset shows the photograph of the SCSPC devices based on aluminum foil and conductive fabric.	322

List of Figures

Figure 1.1.1	Power density versus energy density for the various energy storage systems.	2
Figure 1.1.2	Schematic diagram of a supercapacitor device.	5
Figure 1.1.3	Electrochemical double layer capacitors	6
Figure 1.1.4	Different types of faradaic process (a) underpotential deposition, (b) redox pseudocapacitance, and (c) intercalation pseudocapacitance.	7
Figure 1.1.5	The capacitive performance for carbon based EDLC electrodes and pseudocapacitor electrodes.	11
Figure 1.1.6	Mechanism of the piezoelectric nanogenerator. (a) In the device, no signal is observed in the absence of external force. b) When compressive force is applied to the device, the piezoelectric potential is created inside the piezo-materials, which aligns the electric dipoles in a single direction (stress-induced poling), resulting in a flow of electrons. c) As the external force is removed, the piezoelectric potential disappeared, and the accumulated electrons flow back via the external circuit.	20
Figure 2.1.1	Fabricated binder and binder free electrodes on various current collectors	51
Figure 2.1.2	Electrochemical workstation.	54
Figure 3.1.1	(a) XRD pattern of TiO ₂ NR arrays synthesized by hydrothermal method (Peaks from the FTO substrate are indicated with asterisks symbol). (b) FT-IR spectrum of TiO ₂ NR arrays.	66
Figure 3.1.2	FE-SEM images of TiO ₂ NR arrays with different magnification. (a-b) top view, (c) cross-sectional view and (d) EDS spectrum of TiO ₂ NR arrays.	67
Figure 3.1.3	(a) Cyclic voltammogram curve of TiO ₂ NR films at scan rate of 125 mVs ⁻¹ in 1M Na ₂ SO ₄ electrolyte solution. (b)Cyclic voltammogram curves of TiO ₂ NR films at different scan rate from 5 to 125 mVs ⁻¹ in 1M Na ₂ SO ₄ electrolyte solution.	69

Figure 3.1.4	(a) Galvanostatic charge/discharge curve of TiO ₂ NR films at 0.5 $\mu\text{A cm}^{-2}$ and (b) Galvanostatic charge/discharge curve of TiO ₂ NR arrays at different current densities.	70
Figure 3.1.5	(a) Variation of the specific capacitance of TiO ₂ NRs electrode as a function of cycle number measured at 150 mV s^{-1} in 1 M Na ₂ SO ₄ aqueous solution, and (b) Nyquist plot of TiO ₂ NR films in 1M Na ₂ SO ₄ electrolyte solution.	71
Figure 3.2.1	(a) X-ray diffraction (XRD) patterns of FTO, TiO ₂ nanorod (NR) arrays, and TM-1, TM-2 and TM-3 core-shell nanostructures. TM-1, TM-2, and TM-3 correspond to the as-prepared 6-, 8-, and 10-h core-shell nanostructure samples. (b) Raman spectra of TiO ₂ NR arrays, and TM-1, TM-2, and TM-3 core-shell nanostructures.	84
Figure 3.2.2	FE-SEM images of (a, b) TiO ₂ NR arrays, and (c, d) TM-1, (e, f) TM-2 and (g-h) TM-3 core-shell nanostructures.	85
Figure 3.2.3	TEM images of (a-c) TiO ₂ NR arrays, and (d-f) TM-1, (g-i) TM-2 and (j-l) TM-3 core-shell nanostructure at different magnifications.	86
Figure 3.2.4	EDS spectra of (a) TM-1, (b) TM-2, and (c) TM-3 core-shell nanostructures and (d) TiO ₂ NR arrays. The inset shows EDS mappings of Ti, Mn, O and C elements in the TiO ₂ @MnO ₂ (a-c) core-shell arrays and (d) Ti and O elements in the TiO ₂ NRs.	87
Figure 3.2.5	XPS spectra of TiO ₂ NRs, and TM-1, TM-2, and TM-3 core-shell arrays for (a) the survey, (b) Ti 2p, (c) O 1s, and (d) Mn 2p.	89
Figure 3.2.6	(a) Cyclic Voltammetry (CV) curves of TiO ₂ NRs, and TM-1, TM-2, and TM-3 core-shell nanostructure electrodes at a scan rate of 5 mV s^{-1} in a 1-M Na ₂ SO ₄ electrolyte solution. CV curves of (b) TM-1, (c) TM-2, and (d) TM-3 electrodes at different scan rates.	91
Figure 3.2.7	Areal capacitance of TiO ₂ NRs, and TM-1, TM-2 and TM-3 electrodes as a function of scan rate.	92

Figure 3.2.8	(a) Galvanostatic charge/discharge (GCD) curves of TiO ₂ NRs, and TM-1, TM-2, and TM-3 core-shell nanostructure electrodes at a current density of 0.025 mA cm ⁻² in a 1-M Na ₂ SO ₄ aqueous solution. GCD curves of (b) TM-1, (c) TM-2, and (d) TM-3 electrodes as a function of current density.	93
Figure 3.2.9	Areal capacitance of TM-1, TM-2, and TM-3 electrodes as a function of current density.	94
Figure 3.2.10	(a) Nyquist plots of TM-1, TM-2, and TM-3 core-shell electrodes; the inset shows the TiO ₂ NR electrode. (b) Cycling performance of TM-3 core-shell electrode at a current density of 0.25 mA cm ⁻² for 4000 cycles.	96
Figure 3.3.1	XRD pattern of TiO ₂ @Co ₃ O ₄ core-shell nanostructure.	108
Figure 3.3.2	FE-SEM images (a) TiO ₂ NR arrays, (b-d) TiO ₂ @Co ₃ O ₄ core-shell nanostructure at different magnifications	109
Figure 3.3.3	XPS spectra of TiO ₂ @Co ₃ O ₄ core-shell nanostructure (a) survey, (b) Ti 2p, (c) Co 2p and (d) O 1s.	110
Figure 3.3.4	(a) CV curves of TiO ₂ NR arrays and TiO ₂ @Co ₃ O ₄ core-shell nanostructure electrodes. (b) CVs of TiO ₂ @Co ₃ O ₄ core-shell nanostructure at different scan rates.	111
Figure 3.3.5	(a) Specific capacitance of TiO ₂ @Co ₃ O ₄ core-shell nanostructure electrode at different scan rates. (b) GCD curves of TiO ₂ @Co ₃ O ₄ core-shell nanostructure electrode at different discharge current densities.	112
Figure 3.3.6	(a) Cycling stability of TiO ₂ @Co ₃ O ₄ core-shell nanostructure electrode for 3000 cycles. (b) Nyquist plots of TiO ₂ @Co ₃ O ₄ core-shell nanostructure electrode; the inset shows the TiO ₂ NR arrays.	113
Figure 3.4.1	XRD pattern of the TiO ₂ /Co(OH) ₂ hierarchical nanostructure, showing the tetragonal rutile phase of TiO ₂ NRs (JCPDS no:21-1276) and the α-phase of the Co(OH) ₂ nanowalls (JCPDS no:02-0925).	122
Figure 3.4.2	(a) Cross-sectional and (b) plan view FE-SEM images of the TiO ₂ NR arrays; (c) and (d) show plan view FE-SEM images of the TiO ₂ /Co(OH) ₂ hierarchical nanostructure; and (e) and (f) show cross-sectional FE-SEM images of the TiO ₂ /Co(OH) ₂ hierarchical	123

	nanostructure.	
Figure 3.4.3	XPS spectra of the TiO ₂ /Co(OH) ₂ hierarchical nanostructure. (a) Survey, (b) Co 2p, and (c) O 1s.	124
Figure 3.4.4	(a) CV curves of the TiO ₂ NRs and TiO ₂ /Co(OH) ₂ hierarchical nanostructured electrodes.	125
Figure 3.4.5	(a) CV curves of the TiO ₂ /Co(OH) ₂ hierarchical nanostructured electrode at different scan rates. (b) The areal capacitance and specific capacitance of the TiO ₂ NRs and TiO ₂ /Co(OH) ₂ hierarchical nanostructured electrodes as a function of scan rate.	127
Figure 3.4.6	Discharge curves of the TiO ₂ /Co(OH) ₂ hierarchical nanostructured electrodes at different discharge current densities.	128
Figure 3.4.7	Cycling performance of TiO ₂ /Co(OH) ₂ hierarchical nanostructured electrode at a current density of 2 mA cm ⁻² for 4000 cycles in 2-M KOH solution.	129
Figure 3.4.8	(a) FE-SEM image of the hierarchical nanostructure, after 4000 cycles. (b) Schematic representation of the direct electron transport path.	131
Figure 4.1.1	(a) XRD pattern and (b) EDS of the MoS ₂ nanostructure.	144
Figure 4.1.2	FE-SEM (a, b), TEM (c), HR-TEM images (d, e) and SAED pattern (f) of the MoS ₂ nanostructure.	145
Figure 4.1.3	Nitrogen adsorption–desorption isotherm (a) and BJH pore-size distribution plot (b) of the MoS ₂ nanostructure.	146
Figure 4.1.4	XPS spectra of MoS ₂ nanostructure (a) survey scan, (b) Mo 3d, and (c) S 2p.	147
Figure 4.1.5	CV curves of MoS ₂ nanostructure electrode at different scan rate in 1M (a) Na ₂ SO ₄ , and (b) KCl electrolyte solution. (c) Specific capacitance of MoS ₂ nanostructure electrode at different scan rates from 1 to 100 mV s ⁻¹ .	149
Figure 4.1.6	Galvanostatic charge/discharge curve of MoS ₂ nanostructure electrode at different current densities in 1M (d) Na ₂ SO ₄ , and (e) KCl electrolyte solution. (f) Variation of the specific capacitance of MoS ₂ nanostructure electrode as a function of cycle number	150

measured at 150 mVs^{-1} in $1 \text{ M Na}_2\text{SO}_4$ and KCl aqueous solution.

- Figure 4.1.7** Nyquist plots for MoS_2 nanostructure electrode measured during the cycle life testing in 1 M (a) Na_2SO_4 and (b) KCl electrolyte solution. 152
- Figure 4.2.1** (a) Photographs of the conductive fabric substrate, and the GO- and graphene-coated fabrics. FE-SEM images of the (b) GO- and (c, d) graphene-coated fabrics. 164
- Figure 4.2.2** (a) Raman spectra of the GO- and graphene-coated fabrics. The inset is an optical image of the latter. (b) FT-IR spectra of the GO- and graphene-coated fabrics. 165
- Figure 4.2.3** The C 1s XPS spectra of the (c) GO- and (d) graphene-coated fabrics. 166
- Figure 4.2.4** (a) CV curves of the graphene-coated fabric electrode at various scan rates with a potential window of $0\text{--}1 \text{ V}$ in $1 \text{ M H}_3\text{PO}_4$ solution. (b) Specific capacitance of the graphene-coated fabric at different scan rates. 167
- Figure 4.2.5** (a) GCD curves of the graphene-coated fabric at different current densities. (b) Specific capacitance calculated from the charge/discharge curves as a function of current density. 168
- Figure 4.2.6** (a) Capacitance retention ratio as a function of cycle number. (b) Nyquist plots of the graphene-coated fabric electrode before and after 1000 cycles. 169
- Figure 4.2.7** (a) CV curves of the graphene-coated fabric SSC measured at different scan rates over $0\text{--}1 \text{ V}$ in $\text{PVA}/\text{H}_3\text{PO}_4$ gel electrolyte. (b) Specific capacitance of the graphene-coated fabric SSC at different scan rates. 170
- Figure 4.2.8** (a) GCD curves of the graphene-coated fabric SSC at various current densities. (b) Specific capacitance of the graphene-coated fabric SSC as a function of current density. 171
- Figure 4.2.9** (a) Comparison of CV curves at 10 mV s^{-1} for the flexible graphene-coated fabric SSC measured as normal and bent. Photographs of (b) green and (c) red LEDs powered by graphene-coated fabric SSC devices connected in series. The insets are magnified images of the green and red LED glows. 173

Figure 5.1.1	(a) X-ray diffraction pattern of graphene-ZnO nanocomposite. (b) FT-IR spectra of GO and graphene-ZnO nanocomposite.	185
Figure 5.1.2	(a) Laser Raman spectrum of graphene-ZnO nanocomposite. (b) UV-visible absorbance spectra of graphene-ZnO nanocomposite.	187
Figure 5.1.3	FE-SEM image of graphene-ZnO nanocomposite.	188
Figure 5.1.4	XPS spectra of graphene-ZnO nanocomposite (a) survey, (b) Zn 2p, (c) O 1s and (d) C 1s.	189
Figure 5.1.5	(a) CV curves of graphene and graphene-ZnO electrodes at scan rate of 10 mV s^{-1} in 1 M KCl electrolyte. (b) CV curves of graphene-ZnO composite at different scan rates of 5, 10, 25 and 50 mV s^{-1} .	190
Figure 5.1.6	(a) Specific capacitance at different scan rates of graphene-ZnO nanocomposite. (b) Cycling stability of the graphene-ZnO nanocomposite electrode measured at 150 mV s^{-1} in 1 M KCl electrolyte.	191
Figure 5.1.7	Nyquist plots of graphene and graphene-ZnO electrodes in 1 M KCl electrolyte.	192
Figure 5.2.1	XRD diffraction patterns of (a) pure rGO and (b) the rGO / TiO ₂ NR / rGO hybrid nanostructure.	206
Figure 5.2.2	Raman spectra of (a) pure rGO and (b) the rGO / TiO ₂ NR / rGO hybrid nanostructure.	207
Figure 5.2.3	(a-b) Top view FE-SEM images of the rGO / TiO ₂ NR / rGO porous hybrid structure. (c-d) Cross-sectional views of the hybrid structure.	208
Figure 5.2.4	XPS spectra of an rGO / TiO ₂ NR / rGO electrode (a) wide scan survey, (b) Ti 2p, (c) O 1s, and (d) C 1s.	209
Figure 5.2.5	(a) Cyclic voltammograms (CVs) curves of as-prepared TiO ₂ NRs, rGO and an rGO / TiO ₂ NR / rGO electrode at a scan rate of 25 mV s^{-1} in 1 M Na ₂ SO ₄ electrolyte solution. (b) CVs of an rGO / TiO ₂ NR / rGO electrode at scan rates from 5 to 125 mV s^{-1} .	210
Figure 5.2.6	(a) Specific capacitance, as calculate from the CVs in Fig.6, of TiO ₂ NRs, rGO and an rGO / TiO ₂ NR / rGO electrode at various scan rates. (b) Nyquist plots for rGO	211

and an rGO / TiO₂ NR / rGO electrode. The inset shows the Nyquist plot of a TiO₂ NR electrode.

- Figure 5.2.7** (a) Galvanostatic charge-discharge curve of an rGO / TiO₂ NR / rGO electrode at a constant current density of 0.075 mA cm⁻² in 1 M Na₂SO₄. (b) Galvanostatic charge-discharge curves of an rGO / TiO₂ NR / rGO electrode at different current densities. 213
- Figure 5.2.8** Variation of the specific capacitance of an rGO / TiO₂ NR / rGO electrode as a function of cycle number measured at 200 mV s⁻¹ in 1 M Na₂SO₄. 214
- Figure 5.3.1** Typical XRD pattern of (a) GO, (b) graphene, (c) TiO₂ and (d) the graphene-TiO₂ hybrid nanostructure. 225
- Figure 5.3.2** Raman spectra of (a) GO, (b) graphene, (c) TiO₂, and (d) the graphene-TiO₂ hybrid nanostructure. 227
- Figure 5.3.3** FT-IR spectra of (a) GO, (b) graphene, (c) TiO₂, and (d) the graphene-TiO₂ hybrid nanostructure. 229
- Figure 5.3.4** XPS spectra of GO, graphene, TiO₂, and the graphene-TiO₂ hybrid nanostructure for (a) the survey scan, (b) Ti 2p, (c) C 1s, and (d) O 1s. 231
- Figure 5.3.5** (a-d) Different magnification of FE-SEM images, (c-d) TEM images, (e) SAED pattern, and (f) EDS image of the graphene-TiO₂ hybrid nanostructure. 233
- Figure 5.3.6** (a) CV curves of the as-prepared TiO₂, graphene and the graphene-TiO₂ hybrid electrode at a scan rate of 25 mV s⁻¹ in 1 M Na₂SO₄ electrolyte solution. (b) CV curves of the graphene-TiO₂ hybrid electrode at different scan rates from 5 to 125 mV s⁻¹. 236
- Figure 5.3.7** (a) Specific capacitance of graphene and the graphene-TiO₂ hybrid electrode at different scan rates calculated from CV curves. (b) Nyquist plots for graphene and the graphene-TiO₂ hybrid electrode in 1 M Na₂SO₄ electrolyte solution; the inset shows the Nyquist plot for TiO₂. 237
- Figure 5.3.8** (a) Galvanostatic charge-discharge curve of the graphene-TiO₂ hybrid electrode at a constant current density of 2.5 mA cm⁻² in 1 M Na₂SO₄ electrolyte solution. (b) Galvanostatic charge-discharge curves of the graphene-TiO₂ hybrid electrode at different current 239

densities (2.5, 5, 7.5 and 10 mA cm⁻²).

- Figure 5.3.9** (a) Variation of the specific capacitance of the graphene–TiO₂ hybrid electrode as a function of cycle number measured at 100 mV s⁻¹ in a 1 M Na₂SO₄ aqueous solution. (b) Nyquist plots of the graphene–TiO₂ hybrid electrodes after the 1st and 5000th cycles. 240
- Figure 5.3.10** (a) CVs of symmetric G-TiO₂ supercapacitor with different potential windows. (b) CVs of symmetric G-TiO₂ supercapacitor between 0.0 to 1.6 V at various scan rates. (c) The cell and single electrode capacitance of symmetric supercapacitor as a function of scan rate. 241
- Figure 5.3.11** (a) Galvanostatic charge/discharge curves of symmetric G-TiO₂ supercapacitor with different potential windows. (b) GCD curves of symmetric G-TiO₂ supercapacitor between 0.0 to 1.6 V at various current densities. (c) The cell and single electrode capacitance of symmetric supercapacitor as a function of current density. 243
- Figure 5.3.12** (a) Ragone plot of symmetric supercapacitor at various current densities. (b) The cycle performance of the symmetric supercapacitor in the potential window between 0.0 to 1.6 V at 0.5 A g⁻¹ for 2000 cycles; the inset shows the GCD cycles. (c) Nyquist plots of symmetric supercapacitor before and after 2000 cycles. 244
- Figure 5.3.13** Green, red and blue LED driven by two solid state symmetric supercapacitors connected in series; inset shows the enlarged portion of LED glow. 246
- Figure 5.4.1** XRD spectra of GO, rGO, GV-1, GV-2, and GV-3. 257
- Figure 5.4.2** Raman spectra of GO, rGO, GV-1, GV-2, and GV-3. 258
- Figure 5.4.3** FT-IR spectra of GO, rGO, GV-1, GV-2, and GV-3. 260
- Figure 5.4.4** XPS spectra of GO, rGO, GV-1, GV-2 and GV-3 for (a) the survey scan, (b) V 2p, (c) O 1s, and (d) C 1s. 262
- Figure 5.4.5** Morphological studies of GV-3 sample: FE-SEM (a-b), TEM images (c-d), SAED pattern (e), and EDS spectrum (f) of reduced graphene oxide/vanadium pentoxide composites. The morphological studies showed the V₂O₅ nanoparticles are uniformly distributed on the graphene nanosheets. 264

Figure 5.4.6	EIS curves of V ₂ O ₅ , rGO, GV-1, GV-2, and GV-3 electrodes.	265
Figure 5.4.7	(a) CV curves of V ₂ O ₅ , rGO, GV-1, GV-2, and GV-3 electrodes. CV curves of (b) GV-1, (c) GV-2, and (d) GV-3 electrodes at different scan rates in 1 M Na ₂ SO ₄ solution.	267
Figure 5.4.8	Specific capacitance of V ₂ O ₅ , rGO, GV-1, GV-2 and GV-3 electrodes at different scan rates calculated from CV curves.	268
Figure 5.4.9	(a) GCD curve of the V ₂ O ₅ , rGO, GV-1, GV-2, and GV-3 electrodes at a constant current density of 0.1 A g ⁻¹ in 1 M Na ₂ SO ₄ electrolyte solution. GCD curves of (b) GV-1, (c) GV-2, and (d) GV-3 electrode at different current densities.	270
Figure 5.4.10	(a) Specific capacitance of GV-1, GV-2 and GV-3 electrodes at different current densities calculated from GCD curves.	272
Figure 5.4.11	Stability measurement of G-V ₂ O ₅ electrodes: (a) Variation of the specific capacitance of the GV-1, GV-2 and GV-3 electrodes as a function of a cycle number measured at 150 mV s ⁻¹ in a 1 M Na ₂ SO ₄ aqueous solution. Nyquist plots of the (b) GV-1, (c) GV-2 and (d) GV-3 electrodes, after the 1 st and 5000 th cycles.	273
Figure 5.4.12	(a) CVs of symmetric G-V ₂ O ₅ supercapacitor with different potential windows. (b) CVs of symmetric G-V ₂ O ₅ supercapacitor between 0.0 to 1.6 V at various scan rates. (c) The cell and single electrode capacitance of symmetric supercapacitor as a function of scan rate.	275
Figure 5.4.13	(a) Galvanostatic charge/discharge curves of symmetric G-V ₂ O ₅ supercapacitor with different potential windows. (b) GCD curves of symmetric G-V ₂ O ₅ supercapacitor between 0.0 to 1.6 V at various current densities. (c) The cell and single electrode capacitance of symmetric supercapacitor as a function of current density.	276
Figure 5.4.14	(a) Ragone plot of symmetric supercapacitor at various current densities. (b) The cycle performance of the symmetric supercapacitor in the potential window between 0.0 to 1.6 V at 0.5 A g ⁻¹ for 2000 cycles; the	277

inset shows the GCD cycles. (c) Nyquist plots of symmetric supercapacitor before and after 2000 cycles.

- Figure 5.4.15** (a) Red and green LED driven by two solid state symmetric supercapacitors connected in series; inset shows the enlarged portion of LED glow. (b) Seven segment display with character “nano” powered by two tandem devices. 279
- Figure 6.1.1** The measured electrical output performance of the commercial PZT film based nanogenerator under continues pressing and releasing through finger. Short circuit current under (a) forward and (b) reverse connection with measuring system. The insets show the enlarged portion of the current profile in single press and release under forward and reverse connection. 287
- Figure 6.1.2** The measured electrical output performance of the commercial PZT film based nanogenerator under continues pressing and releasing through finger. Open circuit voltage under (c) forward and (d) reverse connection with measuring system. The insets show the enlarged portion of the voltage profile in single press and release under forward and reverse connection. 287
- Figure 6.1.3** Demonstration of a self-powered photosensor using the supercapacitor as an energy storage device. (a) Charging of four serially connected graphene-coated fabric-based SSCs by the nanogenerator. (b) Time- dependent photoresponse for multiple ON/OFF cycles at a constant illumination intensity of 8 mW cm^{-2} at $\lambda = 365 \text{ nm}$. Inset shows the zoomed portion of one ON/OFF cycle. (c) Time-dependent photoresponse with different illumination intensities at $\lambda = 365 \text{ nm}$. (d) Photoresponse current as a function of illumination intensity. 289
- Figure 6.1.4** Demonstration of a self-powered photosensor using the supercapacitor as an energy storage device. (a) Charging of two serially connected graphene-TiO₂ SSCs by the nanogenerator. (b) Time- dependent photoresponse for multiple ON/OFF cycles at a constant illumination intensity of 8 mW cm^{-2} at $\lambda = 365 \text{ nm}$. Inset shows the zoomed portion of one ON/OFF cycle. (c) Time-dependent photoresponse with different illumination intensities at $\lambda = 365 \text{ nm}$. (d) Photoresponse current as a function of illumination intensity. 291

- Figure 6.1.5** Demonstration of a self-powered photosensor using the supercapacitor as an energy storage device. (a) Charging of graphene-V₂O₅ SSCs by the nanogenerator. (b) Time-dependent photoresponse for multiple ON/OFF cycles at a constant illumination intensity of 8 mW cm⁻² at $\lambda = 365$ nm. Inset shows the zoomed portion of one ON/OFF cycle. (c) Time-dependent photoresponse with different illumination intensities at $\lambda = 365$ nm. (d) Photoresponse current as a function of illumination intensity. 292
- Figure 7.1.1** (a) FT-IR spectrum and (b) FE-SEM image of PVDF-ZnO separator. The β phase of PVDF and ZnO stretching vibrations are indexed. Open circuit voltage (b), and short-circuit current (c) generated in PVDF-ZnO separator. The inset shows the digital image of fabricated PVDF-ZnO nanogenerator device. 301
- Figure 7.1.2** (a) FE-SEM image of MnO₂ nanostructure. (b) XRD spectrum of MnO₂ nanowires. 303
- Figure 7.1.3** Electrochemical performance of MnO₂ electrode in three electrode system: (a) Cyclic voltammetry curves of MnO₂ electrode at different scan rates. (b) Relationship between the specific capacitance and scan rates of cyclic voltammetry tests. (c) Galvanostatic charge/discharge curves of MnO₂ electrode at different current densities in 1 M Na₂SO₄ aqueous electrolyte solution. (d) Nyquist plot of MnO₂ electrode. 304
- Figure 7.1.4** Electrochemical performance of SCSPC device in PVA/H₃PO₄ gel electrolytes: (a) Cyclic voltammetry scans of SCSPC at different scan rates. (b) Galvanostatic charge/discharge curves of SCSPC at different current densities. 305
- Figure 7.1.5** Working mechanism of the Self-Charging Supercapacitor Power Cell (SCSPC) driven by mechanical deformation. (a) Schematic diagram of the fabricated SCSPC at discharge condition. The MnO₂ on aluminum foil are used as the positive and negative electrodes; PVDF-ZnO film as a separator. (b) The mechanical deformation is applied on the top of the device; it creates a piezoelectric field (potential) in the PVDF-ZnO separator film. (c) Under the piezoelectric field, the H⁺ ions will migrate through PVDF-ZnO separator in the electrolyte to the negative electrode, leading to the corresponding charging reactions at the 308

two electrodes. (d) When external deformation is released, there is no piezoelectric field at the separator which breaks the attained chemical equilibrium; it causes a reverse reaction on both sides of the electrode, and ions are relocated into original position. (e) Completed self-charging cycle

- Figure 7.1.6** Self-charging performance of SCSPC monitored using electrochemical work station under periodic compressive straining: (a) The self-charging process of the SCSPC by human palm impact. During vibration the voltage keeps raising, indicating that the charging process is occurred due to the migration of the ions. (b) The self-charging process of the fabric based SCSPC. 311
- Figure 7.1.7** Self-charging and discharge cycles of SCSPC under different forces (9.8, 12.2, 14.9, and 18.8 N). (b) At force applied to the bottom side of the SCSPC. When the compressive force applied to the opposite side (bottom side) of SCSPC, the stored voltage was decreased (discharge) due to generation of opposite potential in separator. 312
- Figure 7.1.8** (a) Cycling performance of the SCSPC under compressive force. (b) Self-charging and discharging cycles of the SCSPC via periodic deformation. The discharge current is 10 μ A. 313
- Figure 7.1.9** Self-charging performance of serially connected five SCSPC: (a) The self-charging process of the serially connected five SCSPC under periodic compressive straining given by human palm impact to the whole devices. Inset shows photograph of the serially connected SCSPC. (b) The self-charging process of the serially connected five SCSPC under periodic compressive straining given by human palm impact to the each device for 60s interval. Inset shows the circuit diagram of serial connection. 314
- Figure 7.1.10.** The operation of green LED using serially connected SCSPC as the power source. 315
- Figure 7.2.1** Electrochemical performance of SCSPC device in H_3PO_4/PVA gel electrolytes: (a) Cyclic voltammetry scans of SCSPC device at different scan rates. (b) Galvanostatic charge/discharge curves of SCSPC device at different current densities. 323

- Figure 7.2.2** Working mechanism of the Self-Charging Supercapacitor Power Cell (SCSPC) driven by mechanical deformation. (a) Schematic diagram of the fabricated SCSPC device at discharge condition. (b) The mechanical deformation is applied on the top of the device; it creates a piezoelectric field (potential) in the PVDF-ZnO separator film. (c) Under the piezoelectric field, the H^+ ions will migrate towards negative electrode and PO_4^{3-} ions migrate towards positive electrode, leading to the corresponding charging reactions at the two electrodes. (d) When external deformation is released, there is no piezoelectric field at the separator which breaks the attained chemical equilibrium; it causes a reverse reaction on both sides of the electrode, and ions are relocated into original position. (e) Completed self-charging cycle. 325
- Figure 7.2.3.** Self-charging performance of SCSPC device measured using electrochemical work station under periodic compressive straining: (a) The self-charging process of the SCSPC device by human palm impact. During vibration the voltage keeps raising, indicating that the charging process is occurred due to the migration of the ions. (b) The self-charging process of the polarity changed SCSPC device. 327
- Figure 7.2.4.** (a) The self-charging process of the fabric based SCSPC device. (b) The self-charging process of the SCSPC device measured using Keithley instruments. 329
- Figure 7.2.5.** Self-charging performance of series connected six SCSPC devices: (a) The self-charging process of the series connected six SCSPC devices under periodic compressive straining given by human palm impact to the whole devices. Inset shows photograph of the series connected SCSPC devices. (b) The self-charging process of the series connected six SCSPC devices under periodic compressive straining given by human palm impact to the each device for 60 s interval. Inset shows the circuit diagram of series connection. 330
- Figure 7.2.6.** The operation of green LED using series connected six SCSPC devices as the power source. 331

초록


에너지에 대한 수요는 높아지고, 화석연료의 양은 한정되어 있으며, 환경오염에 대한 우려가 높아지면서 친환경적인 에너지수확기술 및 에너지 저장과 관련한 연구 및 개발이 증가하고 있다. 또한, 급격한 기술의 발전과 나노기술의 도입으로 전자기기들은 소형화 되면서 적은 양의 전력이 필요하게 되었다. 이에 따라 자가발전 웨어러블/포터블 디바이스에 대한 개발도 활발해지고 있다.

에너지하베스팅 소자 중에, 나노발전소자는 낮은 주파수의 기계적에너지를 압전과 마찰-대전효과를 이용해 에너지를 효과적으로 수확하는 소자이다. 다른 한편으로는, 전기화학 커패시터는 고용량, 높은 주기 안정성, 빠른 충/방전 능력으로 기존의 배터리를 대체할 것으로 촉망받는 에너지저장 장치이다.

슈도커패시터의 낮은 전도율과 전기적 더블레이어로 인해 제한된 충전축적 (charge accumulation)은 실제 활용에 제한이 있다. 따라서, 최근에는 새로운 전극 물질의 개발을 통해 슈퍼커패시터의 성능을 향상시키는데 많은 노력을 쏟고 있다. 이 논문에는 전도성 기판 위에 binder-free 전극 또는 기타

전류를 수집하는 역할을 하는 두 가지의 물질 또는 구조를 통해 발전된 나노사이즈의 복합 구조를 구성하여 고성능의 슈퍼커패시터와 자가발전 시스템에 활용하는 것을 목표로 두었다.

1 장에서는, 수직으로 정렬된 TiO_2 나노로드 배열과 같이 1 차원의 계층 나노구조인 $\text{TiO}_2@ \text{MnO}_2$ 코어셸, $\text{TiO}_2@ \text{Co}_3\text{O}_4$ 코어셸과 $\text{TiO}_2/\text{Co}(\text{OH})_2$ 를 FTO 기판 위에 제작하여 첨가물이 없고 binder 가 적은 전극을 만들어내 고성능의 슈퍼 커패시터를 만들었다.

준비된 물질은 슈퍼커패시터 전극으로서의 특징을 잘 나타내고 있다.  $\text{TiO}_2/\text{Co}(\text{OH})_2$ 계층 나노구조 전극은 274.3 mF cm^{-2} 의 높은 면적당 비정전용량(areal specific capacitance)과 좋은 주기안정성을 통해 훌륭한 의사용량성(pseudocapacitive) 특성을 나타냈다.

전기화학적 성능이 향상된 $\text{TiO}_2/\text{Co}(\text{OH})_2$ 전극은 나노계층구조에 기인하며 이는 큰비중의 표면면적을 지니며 공동의 특성-물질과 짧은 이온과 전자 발산 과정을 달성하며, 빠른 속도와 좀 더 효율적인 전해질 이온의 접촉, 그리고 더 많은 전기활성물질을 제공하여 페러데이 에너지 저장, 높은 비정전용량의 결과를 가진다.

2 장에서는, 기계적 강도와 전극물질의 표면적을 향상시키고자 2 차원 나노물질인 MoS_2 와 그래핀 나노시트를 합성하여 슈퍼 커패시터의 전극으로서의 특성을 분석하였다. 유연 고체상태의 그래핀이 코팅된 SSC 직물은 27.7 kW kg^{-1} 의 출력밀도에서 5.8 W h kg^{-1} 의 에너지밀도를 가지면서 뛰어난 전기화학 성능을 보였다. binder-free 그래핀이 코팅된 직물전극을 사용하여 측정된 뛰어난 전기화학 성능을 통해 유연 슈퍼 커패시터에 적극 활용될 것으로 보인다.

3 장에서는, G-ZnO, rGO/TiO₂/rGO, G-TiO₂ 와 G-V₂O₅ 를 혼합하여 전극을 합성하였으며 그래핀과 메탈이 산화되는 것을 방지하고자 하였다. 전기화학 실험을 통해 G-V₂O₅ 전극이 35 F g^{-1} 의 높은 cell capacitance 와 12.5 W h kg^{-1} 의 에너지밀도, 0.3 kW kg^{-1} 의 출력밀도와 뛰어난 주기 안정성을 가지는 것을 확인하였다. 이에 더불어, 고체형 슈퍼 커패시터를 이용하여 LED 와 4-digit 7 세그먼트를 밝히는 실험을 통해 성능을 확인하였다.

4 장에서는, 나노발전소자를 이용하여 제작한 슈퍼 커패시터를 충전시켜 photosensor 를 동작시키는 자가발전 시스템을 제작하였다. 다양한

결과를 통해 고체형 슈퍼커패시터가 자가발전소자에 활용될 때 효율적인 에너지 저장 장치 역할을 하는 가능성을 확인하였다.

본 논문의 마지막 장에서는, PVDF-ZnO 을 사용하여 압전 특성과 더불어 양극과 음극에 각각 반응하는 전기화학 세퍼레이터(separator)의 역할을 하는 특성을 통해 처음으로 자가충전 성능을 가진 Self-Charging Supercapacitor Power Cell (SCSPC) 소자를 제작하였다. SCSPC 의 메커니즘은 산화/환원반응 (유도전류 반응) 에 반응하는 압전 포텐셜에 기초한다.

SCSPC 는 자가충전기능을 손바닥으로 충격을 주었을 때 나타났다. 여기에, SCSPC 을 구동원으로 하여 직렬로 연결된 녹색 LED 를 밝혔다. 결과 및 고찰을 통해, 우리는 SCSPC 의 개발로 새로우면서 유망한 슈퍼 커패시터의 연구방향을 제시하였으며, 유연한 포터블/웨어러블 전자기기에 지속적인 전원공급을 할 수 있는 가능성을 높였다.

Abstract

Increasing demand for energy, limitations in fossil fuel availability, and environmental concerns have promoted the study and development of new eco-friendly technologies for energy harvesting and storage. Likewise, the rapid growth of technology and the introduction of nanotechnology have enabled device miniaturisation and lowered their operating power requirements; this has encouraged the development of self-powered wearable and portable devices. Among the energy harvesting devices, nanogenerator is an effective device to harvest the low frequency mechanical energy through piezoelectric and tribo-electrification processes. On the other hand, the electrochemical capacitor is one of the most promising alternative energy storage devices to the conventional batteries because of its higher power capacity, longer cyclic stability, and fast charging/discharging capability. The limited charge accumulation in the electrical double layer and poor conductivity of pseudocapacitors limits the practical applications. Therefore, much research has been carried out in recent years to improve the performance of supercapacitors by developing new electrode materials. This thesis work was aimed to construct advanced complex nanoscale architectures with a combination of two types of materials and/or structures on a conducting substrate as binder-free electrodes or other current collectors for high-performance supercapacitors and self-powered systems.

First section, one dimensional hierarchical nano-architectures such as vertically aligned TiO_2 nanorod arrays, $\text{TiO}_2@ \text{MnO}_2$ core-shell, $\text{TiO}_2@ \text{Co}_3\text{O}_4$ core-shell and $\text{TiO}_2/\text{Co}(\text{OH})_2$ onto FTO substrate was prepared to obtain a conducting additive-free and binder-less electrode for high-performance supercapacitors. The

prepared materials were well-characterized and evaluated as supercapacitor electrodes. The $\text{TiO}_2/\text{Co}(\text{OH})_2$ hierarchical nanostructured electrode exhibited excellent pseudocapacitive behaviour with a high areal specific capacitance of 274.3 mF cm^{-2} and good cycle stability. The enhanced electrochemical performance of the $\text{TiO}_2/\text{Co}(\text{OH})_2$ electrode is attributed to the hierarchical nano-architectures, which possess a large specific surface area and could achieve synergetic properties of materials and short ionic and electronic diffusion paths, which could lead to faster kinetics, more efficient contacts with the electrolyte ions, and provide more electroactive sites for Faradaic energy storage, resulting to the high specific capacitance.

In the second section, to improve the mechanical strength and high surface area of electrode materials, a two dimensional nanomaterials such as MoS_2 and graphene nanosheets were synthesized, characterized and evaluated as a supercapacitor electrodes. A flexible solid-state graphene-coated fabric SSC exhibited excellent electrochemical performance with an energy density of 5.8 W h kg^{-1} at a power density of 27.7 kW kg^{-1} . The obtained electrochemical performance results from the binder-free graphene coated fabric electrode have shown promising results as the best candidates for flexible supercapacitors.

The third section, G-ZnO, rGO/ TiO_2 /rGO, G- TiO_2 , and G- V_2O_5 hybridized (nanocomposite) electrodes were prepared to mitigate the shortcomings of both graphene and transition metal oxides. The electrochemical studies clearly confirm the G- V_2O_5 electrode exhibiting a higher cell capacitance of 35 F g^{-1} , energy density of 12.5 W h kg^{-1} , power density of 0.3 kW kg^{-1} and excellent cycling stability. Further,

we have demonstrated the performance of the solid-state supercapacitor by lighting-up of LED and also showed the 4-digit seven segmented display.

Fourth section, a self-powered system was demonstrated by charging the fabricated supercapacitor using a nanogenerator to power a photosensors. The various results demonstrated the feasibility of using fabricated solid state supercapacitors as efficient energy storage components and their application in self-powered devices.

Self-charging supercapacitor power cell (SCSPC) was fabricated for the first time. The fabrication method, mechanism and it's self-charging performance of SCSPC were explained in the last section of the thesis. PVDF-ZnO was used as a piezoelectric as well as a separator and various electrochemical active materials were used as positive and negative electrodes, respectively. The working mechanism of the self-charging supercapacitor power cell (SCSPC) is based on piezoelectric-potential driven electrochemical oxidation and reduction reaction (faradaic reaction). The SCSPC exhibited the self-charging capability under palm impact. Further, the green LED was operated using serially connected SCSPC as the power source. From the above results and discussion, we concluded that the as-fabricated SCSPC provide a new promising direction in the supercapacitor research for the development of next generation self-powered sustainable power source for portable, wearable and flexible electronic devices.

CHAPTER-I

Introduction

1.1. Global energy issues and the importance of energy storage devices

At present, the rapid development worldwide economy has triggered serious global warming issues and lack of fossil fuels, which possess a significant threat to the survival and development of mankind [1-4]. Therefore, in order to address these issues, scientists and engineers have been conducting intense research on the design and fabrication of efficient energy conversion and storage technologies to exploit sustainable and clean energy [1]. In fact, there is a rapid increase in renewable energy generation from solar and wind, the most abundant and readily available resources. Given the intermittent nature of solar and wind energy, which are the efficient energy storage systems are critically needed to make the best of the electricity generated from these sources since they can promote the reliability and effective use of the entire power system (generation, transmission and distribution) by storing energy when in excess while releasing it when in high demand.

In many application areas, some of the most effective and practical technologies for electrochemical energy conversion and storage devices are batteries, fuel cells, conventional capacitors and electrochemical supercapacitors [5, 6]. The key parameters to evaluate the performance of energy storage systems and their potential for practical applications include specific capacitance ($F\ g^{-1}$), specific capacity ($mAh\ g^{-1}$), energy density ($Wh\ Kg^{-1}$), power density ($W\ kg^{-1}$), cycle life, cost and environmental safety [7-9]. **Figure 1.1.1** shows the Ragone plot of power density versus specific energy density for the energy storage systems (Reprinted with

permission from Elsevier). Fuel cells and batteries are often considered to be high-energy density systems (but low power densities due to their slow reaction kinetics), while supercapacitors or ultra-capacitors and conventional capacitors are considered to be high-power density systems. It should be noted that no single energy source can match all power and energy region.

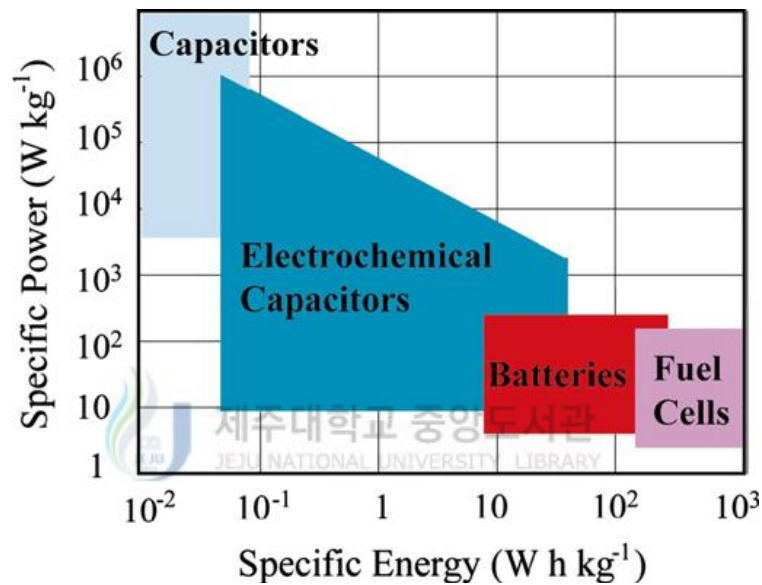


Figure 1.1.1 Power density versus energy density for the various energy storage systems.

Among those energy storage systems, currently, the dominating energy storage systems are batteries and supercapacitors that have found a broad range of applications. The basic differences between batteries and supercapacitor are charge storage mechanisms and their materials/structures. Further, **Table 1.1** summarizes the detailed comparison of the important parameters of electrostatic capacitors, supercapacitors and batteries (Reprinted with permission from RSC) [10]. Batteries store energy electrochemically (faradaic reactions), where chemical reactions release electrical carriers that can be extracted into a circuit. When a battery is charged, lithium ions move from anode to cathode through a separator when charging current

flows. While discharging, on the other hand, lithium ions move from cathode to anode and discharge current flows. Typically, batteries are key components for portable electronics, medical devices, industrial equipment and automobiles due their light weight, provide high energy density and recharge without memory effects. However, due to physical changes in materials/structures between the charged state and the discharges state, current battery technologies have performance limitations such as short cycle life, degrade the chemical compounds and calendar life and slow charge/ discharge rates (limited power capability).

Table 1.1 The basic characteristics of electrostatic capacitors, supercapacitors and batteries

Parameters	Electrostatic Capacitor	Supercapacitor	Battery
Charge Time	10^{-6} – 10^{-3} s	1–30 s	0.3–3 h
Discharge Time	10^{-6} – 10^{-3} s	1–30 s	1–5 h
Energy Density (Wh kg ⁻¹)	<0.1	1–10	20–100
Power Density (W kg ⁻¹)	>10 000	1000–2000	50–200
Cycle Life	>500 000	>100 000	500–2000
Charge/Discharge Efficiency	~1.0	0.90–0.95	0.7–0.85

On the other hand, the electrochemical supercapacitors (ECs) are considered to be one of the most important next-generation energy storage devices, mainly due to their higher power density, longer life cycle than batteries and higher-energy density than conventional dielectric capacitors [11-16]. The configuration of a typical supercapacitor consists of a pair of polarizable electrodes with current collectors, a separator, and an electrolyte, which are similar to that of a battery. In the ECs, energy is stored electrostatically on the surface of the material (based on electrochemical double-layer capacitance or redox pseudocapitance), and does not

involve chemical reactions. Given their fundamental mechanism, supercapacitors can be charged quickly, leading to a very high power density, and do not lose their storage capabilities over time. Supercapacitors can last for millions of charge / discharge cycles without losing energy storage capability. Such outstanding properties make them as a promising energy storage device in various applications such as hybrid-electric vehicle, memory backup system, mobile and military device [17-21]. Generally, carbon materials such as activated carbon, porous carbon, carbon nanotubes, and graphene etc., are used as electrode materials for EDLCs [22]. Metal oxides and conducting polymers are also used as the active materials for pseudocapacitors [23]. The electrolytes of supercapacitors can be either aqueous or organic. The aqueous electrolyte offers a low internal resistance but limits the operating potential window to be about 1.0 V determined by the thermodynamic electrochemical window of water (1.23 V). Organic electrolytes with a broader electrochemical window can significantly enhance the electrical charge (or energy) accumulated in supercapacitors than aqueous electrolytes. The main shortcoming of supercapacitors is their low energy density, which mean the amount of energy that can be stored in supercapacitors per unit weight is very small, particularly when compared to batteries. Additionally, the cost of supercapacitor materials often exceeds the cost of battery materials due to the increased difficulty in creating high-performance supercapacitor materials. However, an enormous amount of research still exists from the perspective of increasing the energy efficiency of supercapacitors, so that they may find their way into the market by replacing batteries. Advancement of supercapacitor technologies can benefit from the development of nanostructured electrode materials. Reasonably high surface area and optimum pore size of the

electrode materials for an appropriate electrolyte solution play an important role to ensure the excellent performance of a supercapacitor in terms of power density and energy storage capability.

1.2. Principle and mechanism of supercapacitors

The supercapacitor consists of two electrodes with a current collector immersed in electrolyte solution, separated by a dielectric porous separator. A dielectric separator between the two electrodes prevents charge propagation between the electrodes (**Figure 1.1.2** reprinted with permission from RSC). When the voltage is applied across the current collectors, the positive electrode attracts negative ions in the electrolyte, while the negative electrode attracts positive ions. The charge accumulated at both electrode surfaces generates energy when discharging. The charge storage mechanism of supercapacitor can be explained via two types, (i) electrochemical double layer capacitance (EDLC) and (ii) pseudocapacitance.

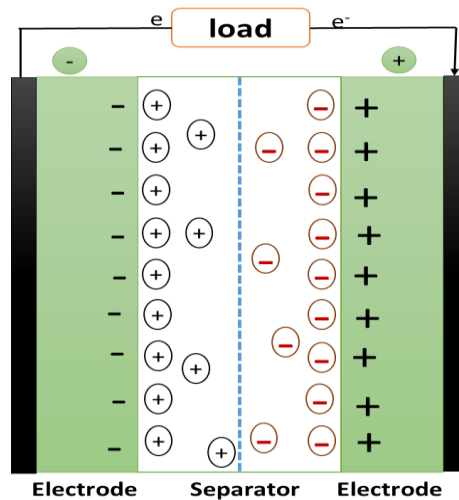


Figure 1.1.2 Schematic diagram of a supercapacitor device.

1.2.1. Electrochemical double layer capacitors

Electrochemical double layer capacitors (EDLCs), which store charges electrostatically via reversible ion absorption at the electrode/electrolyte interface

(**Figure 1.1.3** -reprinted with permission from RSC) [18, 24]. The charge transfer process in EDLCs is non-faradic, i.e. electron transfer across the electrodes does not occur and thus the accumulation of charge is purely electrostatic. The specific capacitance, C ($F g^{-1}$) of EDLC is measured using the following equation:

$$C = \left(\frac{\epsilon_0 \epsilon_r}{d} \right) A \dots\dots\dots (1.1)$$

where, ϵ_0 is the permittivity of vacuum, ϵ_r is the relative permittivity of the medium in the electrical double-layer, A is the specific surface area of the electrode/electrolyte interface accessible to ions, and d is the effective thickness of the electrical double-layer.

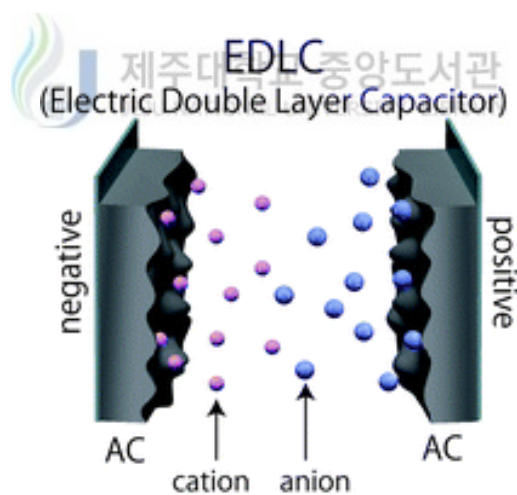


Figure 1.1.3 Electrochemical double layer capacitors.

1.2.2. Pseudocapacitors

Pseudocapacitor, where the energy is stored through fast reversible redox reactions between the electrolyte and the electroactive species on the electrode surface [7,25,26]. The accumulation of electrons at the electrode is a Faradaic process where the electrons generated by the redox reaction are transferred across the

electrolyte/electrode interface. Unlike redox process in battery, the Faradaic processes in a pseudo-capacitor are arises due to the thermodynamic change of potential (ΔV) during charge accumulation (ΔQ) and have better reversibility. The derivative $C = d(\Delta Q)/d(\Delta V)$ corresponds to the capacitance, which is referred to as pseudocapacitance. The theoretical pseudo-capacitance of metal oxide can be calculated using the following equation:

$$C = \frac{n \times F}{M \times V} \dots\dots\dots (1.2)$$

where n is the mean number of the electrons transferred in the redox reaction, F is the Faraday constant, M is the molar mass of the metal oxide and V is the operating potential window.

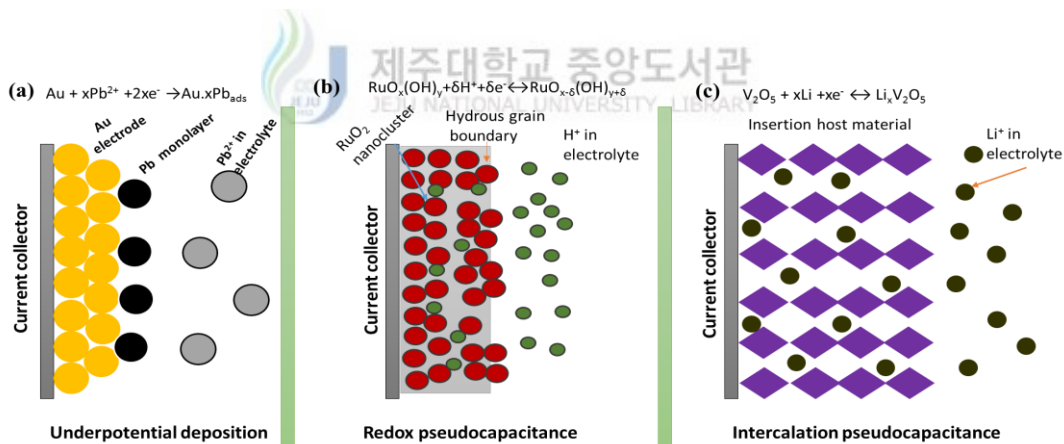


Figure 1.1.4 Different types of faradaic process (a) underpotential deposition, (b) redox pseudocapacitance, and (c) intercalation pseudocapacitance.

Further, Conway identified several types of faradaic mechanism (**Figure 1.1.4**) occur in the pseudocapacitive electrodes (Reprinted with permission from RSC) [7,26]: (1) Underpotential deposition occurs when metal ions form an adsorbed monolayer at a different metal's surface well above their redox potential. (2) Redox pseudocapacitance occurs when ions are electrochemically adsorbed onto the surface

or near surface of a material with simultaneous faradaic charge-transfer. (3) Intercalation pseudocapacitance occurs when ions intercalate into the tunnels or layers of a redox-active material accompanied by a faradaic charge-transfer with no crystallographic phase change.

1.2.3. Hybrid supercapacitor

In addition to EDLCs and pseudocapacitors, there is another special type of capacitor system, called ‘hybrid capacitors’, which usually combine the both EDLC and pseudo-capacitor in a single supercapacitor to form a hybrid supercapacitor. By utilizing both Faradaic and non-Faradaic processes to store charges, hybrid supercapacitors could achieve higher energy and power densities while keeping good cycling stability. Here, the redox reaction takes place on one of the electrodes and the non-Faradaic charge-discharge process occurs on another electrode in a single supercapacitor. Such a supercapacitor is so called an asymmetric hybrid supercapacitor. Other two types of hybrid supercapacitors are battery-like hybrids and composite hybrids. In practice, various types of supercapacitors have been developed to combine different electrode materials in order to improve the device performance. Typical EDLC materials are activated carbon, carbon nanotubes, and graphene-based active materials with high surface area [22, 27]. The second are pseudocapacitors, which are based on Faradic redox reactions of electroactive materials, including transition metal oxides such as RuO_2 , Fe_3O_4 , NiO , and MnO_2 , [23,25,28,29] and electronically conducting redox polymers such as polyanilines, polypyrroles, and polythiophenes [30]. More details about these two energy storage mechanisms and related materials are discussed in the following section.

The energy density (E) and power density (P) of supercapacitor can be calculated using the following equations:

$$E = \frac{1}{2}CV^2 \dots\dots\dots (1.3)$$

$$P = \frac{V^2}{4R_s} \dots\dots\dots (1.4)$$

where C is the specific capacitance, V is the cell voltage, and R_s is the equivalent series resistance (ESR). To achieve a supercapacitor with high performance, the indispensable requirements, such as large specific capacitance, high cell voltage and minimum ESR value should be achieved. The selection of electrode material and electrolyte solution is the most crucial criteria to optimize the overall performance of the supercapacitor. Here the value of the supercapacitor voltage (V) is depends on the materials used for the electrode and electrolyte. The operating voltage is determined by the stability window of the electrolyte. Capacitors in organic electrolytes, can operate in the range of 2–3 V, and the use of ionic liquids can extend this range to 3.5–4 V, whereas in aqueous electrolytes the electrochemical stability window is generally below 1 V.

1.3. Electrode materials

The capacitance and charge storage of supercapacitor mainly depend on the electrode materials used. Therefore, further developing new materials with high capacitance and improved performance relative to existing electrode materials is the most important method to overcome these challenges. In general, the electrode materials of supercapacitor can be classified into three types [7,31,32]: (1) carbon materials with high specific surface area, (2) conducting polymers, and (3) metal oxides, such as RuO_2 , IrO_2 , MnO_2 , NiO , Co_2O_3 , SnO_2 , V_2O_5 , and MoO .

1.3.1. Carbon materials

Carbon based materials are considered to be a prospective electrode materials for industrialization. Various forms of carbon nanomaterials have been investigated and used as active materials in EDLC electrodes. The advantages of carbon materials include abundance, lower cost, easy processing, non-toxicity, higher specific surface area, open porosity, good electronic conductivity, high chemical stability, corrosion resistant and wide operating temperature range [13,19]. Generally, carbon materials store charges in an electrochemical double-layer formed at the electrolyte and electrode interface. Therefore, the capacitance predominantly depends on the surface area accessible to the electrolyte ions. The important factors influencing their electrochemical performance are specific surface area, pore-size distribution, pore shape and structure, electrical conductivity, and surface functionality.

The most widely used active materials for EDLC applications are activated carbon, carbon aerogels, carbon nanotubes, templated porous carbons, carbon derived carbons, carbon nanofibres, onion-like carbons and graphene [33-40]. Considering many recent reviews that cover more extensively on carbon- based electrode materials for ECs. However, the performance of carbon materials (maximum capacitance) is restricted by the active electrode surface area and the pore size distribution. Therefore, the energy density of currently commercial available carbon –based EDLC supercapacitors is typically $3\text{--}5 \text{ W hKg}^{-1}$, which is much lower than that of an electrochemical battery ($30\text{--}40 \text{ Wh kg}^{-1}$ for a lead acid battery and $10\text{--}250 \text{ Wh kg}^{-1}$ for a lithium-ion battery) [41,42]. So it is difficult to further promote the performance of ECs based on pure carbon to fill the gap between batteries and ECs. The extensively studied and most representative electrode materials for ECs

including both carbon-based EDLC electrodes and pseudocapacitor electrodes [43] are given in **Figure 1.1.5** (Reprinted with permission from RSC).

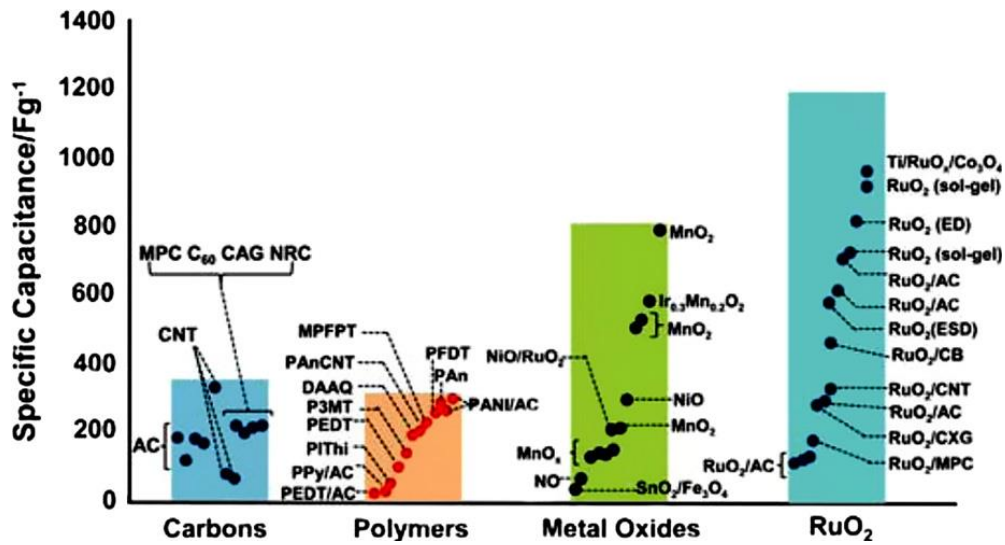


Figure 1.1.5 The capacitive performance for carbon based EDLC electrodes and pseudocapacitor electrodes.

1.3.2. Metal oxides



To improve the specific capacitance and the energy density, transition metal oxides are being investigated as the alternative materials for supercapacitor electrodes. In general, metal oxides can provide higher energy density than carbon materials and better electrochemical stability than polymer materials. The general requirements for metal oxides in supercapacitor applications [7] are: (1) the oxide should be electrically conductive, (2) the metal can exist in two or more oxidation states, and (3) the protons can freely intercalate into the oxide lattice on reduction (and out of the lattice on oxidation), allowing facile interconversion of $O^{2-} \leftrightarrow OH^-$. To date, the investigated metal oxides [7,19,26,28,29, 44-46] include ruthenium oxide (RuO_2), manganese oxide (MnO_2), cobalt oxide (Co_3O_4), nickel oxide (NiO), tin oxide (SnO_2), zinc oxide (ZnO), vanadium oxide (V_2O_5), titanium oxide (TiO_2), copper oxide (CuO), iron oxide (Fe_2O_3), tungsten oxide (WO_3), etc. The surface

functional groups, the defects and the grain boundaries can serve as the excellent redox centers for the charge storage reactions. The theoretical capacitance of typical metal oxides such as $\text{RuO}_2 \cdot x\text{H}_2\text{O}$, MnO_2 , Co_3O_4 , NiO and V_2O_5 are 1200-2200 (1.23 V), 1380 (0.9 V), 2584 (0.5 V), 3560 (0.45), and 2120 F g^{-1} (1 V), respectively [29, 47-50]. It could be observed that the metal oxide electrodes have one order higher specific capacitance than that of carbon electrodes.

Further, the most studied metal oxide in supercapacitors is ruthenium oxide because of its ultrahigh theoretical capacitance, wide potential window, metallic electrical conductivity (10^5 S cm^{-1}), highly reversible redox reactions, and three distinct oxidation states accessible within a 1.2 V voltage window, high proton conductivity, long cycle life, high rate capability, and good thermal and chemical stability [51-53]. Despite these very appealing electrochemical characteristics, commercial applicability of RuO_2 is so far hindered by the material cost. Therefore, considerable efforts have been devoted in recent years to develop more cost-effective transition metal oxide systems in which the metal cations occupy alternate layers or can support multiple valences have been investigated to replace RuO_2 for pseudocapacitive electrodes. Several reports have shown that other bare metal oxide electrodes can deliver large specific capacitance and high energy density at a slow scan rate or at a low current density. However, the specific capacitance and rate capability of these materials were still low at higher current densities. Therefore metal oxides may not be employed alone as the supercapacitor electrodes for practical purpose due to the following drawbacks [15]: (i) poor electrical conductivity, (ii) the strain developed in the metal oxide during the charge–discharge processes causes the cracking of the electrode, leading to poor long-term stability,

and (iii) the surface area, the pore distribution as well as the porosity are difficult to tailor in metal oxides. Therefore, significant efforts have been devoted to develop many metal oxides and mixed metal oxides electrode materials for high performance supercapacitor application. It is one of the most significant ongoing research in the field of energy storage systems in recent times.

1.3.3. Conducting polymers

Another type of pseudocapacitance material is conducting polymers, which possess many advantages including low cost, low environmental impact, high conductivity in a doped state, high voltage window, high storage capacity/porosity/reversibility, and adjustable redox activity through chemical modification make them as a suitable materials for supercapacitors [54-58]. Conducting polymers store the energy through redox process. When oxidation take place, ions from the electrolytes are transferred to the polymer backbone, and when reduction occurs, the ions are released from this backbone into the electrolyte. These redox reactions in the conducting polymer come about throughout its entire bulk, not just on the surface. Because the charging and discharging reactions do not involve any structural alterations such as phase changes, the processes are highly reversible.

Conducting polymer-based supercapacitor systems have three configurations [7, 59-61]: (1) p/p-type polymer configuration in which both electrodes use the same p-dopable polymer. When fully charged, one electrode is in the full p-doped (positive) state and the other in the uncharged state; (2) P/P'-type configuration in which the two different p-dopable polymers with a different range of oxidation and reduction electro-activities are used; and (3) n/p-type polymer configuration, electrodes use the same conducting polymer which can be both p- and n-doped in the

same molecule (one negatively charged (n-doped) and one positively charged (p-doped) conducting polymer electrode). The voltage window of this configuration is up to 3.1 V in non-aqueous solutions. The n/p-type polymer configuration is considered a significant advance in conducting polymers -based supercapacitors in terms of materials design and the stored energy density.

Typical electronically conducting polymers for redox pseudocapacitance are polyaniline (PANI), polythiophene (PTh), polypyrrole (PPy), and other p-conjugated conducting polymers [30]. Usually, the conducting polymers can only work within a particular potential window. When exceeding the potential limit, the polymer may be degrade at higher positive potential and as the potential is too negative, the polymer may be switched to an insulating state (un-doped state). Hence, the selection of a suitable potential range for supercapacitor performance is crucial. In addition, mechanical stress on conducting polymers may occur during the reduction/oxidation process, which limits (degrade) the stability of the electrode materials during many charge-discharge cycles. Hence, this reduced cycling stability and limited potential window has hindered the development of conducting polymer-based pseudocapacitors.

1.3.4. Transition metal dichalcogenides

Recently, two-dimensional (2D) inorganic nanomaterials, particularly layered transition metal dichalcogenides (TMDs), are emerging as a class of key materials in chemistry and electronics due to their intriguing chemical and electronic properties and therefore hold great promise for a variety of applications including electrocatalysts, electronics devices and energy storage [62-70]. Metal sulfides are also known to be electrochemically active materials for supercapacitor applications,

but to date very few metal sulfides such as CoS, NiS, WS₂, MoS₂, SnS and ZnS, have been employed to fabricate supercapacitor electrodes due to their high conductivity and high surface area [71-75]. Among the TMDs layered compounds, MoS₂, MoSe₂, WS₂, and WSe₂ are semiconductors; VS₂ and VSe₂ are metallic. Therefore, developing a TMDs materials by a cost effective, simple method for energy storage and energy conversion devices is extremely urgent. However, TMDs also have major drawbacks such as (i) TMDs can be easily oxidized by O₂ dissolved in the aqueous electrolyte, and (ii) due to their easily oxidized characteristics, they would be unstable in a high rate charging– discharging process. Therefore, much more efforts must be made to apply layered TMDs to supercapacitors, especially in an aqueous electrolyte.

1.3.5. Graphene and graphene based composite materials

Tremendous efforts in supercapacitor research have been made at finding innovative electrode materials for increasing the energy density and lowering the cost. Recently, graphene, a one atom thick, 2-D honeycomb nanostructure, is emerging as a promising candidate for electrochemical energy storage device applications owing to its low mass density, excellent electronic conductivity, outstanding intrinsic strength, high mobility of charge carriers, suitable pore size distribution, good chemical stability, superior thermal conductivity, and high surface area [76-79]. Therefore, graphene has been explored as an electrode material in supercapacitor devices.

Herein, we have briefly summarized a few important achievements concerning the application of graphene materials in the field of supercapacitors. Two pioneer studies by Rao's and Ruoff's group demonstration that graphene-based

supercapacitors exhibit excellent performance with a specific capacitance of 75 Fg^{-1} together with an energy density of 31.9 Wh kg^{-1} in ionic liquid electrolytes [80], and a specific capacitance of 135 and 99 Fg^{-1} in aqueous and organic electrolytes [81]. Lv et al. proposed a novel exfoliation approach at a very low temperature ($200 \text{ }^\circ\text{C}$) under high vacuum, and demonstrated that the graphene produced has a specific capacitance as high as 260 Fg^{-1} at a scan rate of 10 mVs^{-1} in an aqueous system [82]. Wang et al. reported that reduced graphene oxide exhibited a maximum specific capacitance of 205 Fg^{-1} in an aqueous electrolyte with an energy density of 28.5 Wh kg^{-1} [83]. Liu et al. reported that a graphene-based supercapacitor exhibits an ultrahigh energy density of 85.6 Wh kg^{-1} at room temperature and 136 Wh kg^{-1} at $80 \text{ }^\circ\text{C}$ [84]. The above results confirm that graphene holds considerable promise as a new anode material in supercapacitor due to its unique physical and chemical properties. However, in practical applications, graphene nanosheets usually suffer from agglomeration or restacking due to the strong van der Waals interactions, which lead to the loss of surface area and electrochemical performance. In addition, the limited capacity of graphite, many efforts have been focused on finding substitutes with larger capacity.

Generally, graphene is considered to be an ideal building block in composite materials combined with a variety of inorganic compounds, such as metal oxides, metal sulfides and polymers, which exhibit exceptional performance in various applications such as supercapacitor, battery, sensor, photovoltaic [85-87]. Therefore, significant synergistic effects are expected between graphene and inorganic components when combined at the molecular scale and these may create novel properties different from those of each individual component. The advantages of

graphene/metal oxide composites can be briefly summarized: (1) graphene nanosheets support for uniformly anchoring or dispersing metal oxides with well-defined size, shape and crystallinity; (2) metal oxides can effectively suppressing the agglomeration and re-stacking of graphene nanosheets; (3) graphene acting as a conductive agent for improving the poor electrical properties and charge transfer pathways of pure oxides; (4) graphene suppress the volume change and agglomeration of metal oxides; (5) oxygen-containing groups on graphene ensures good bonding, interfacial interactions and electrical contacts between graphene and metal oxides. Due to these synergistic effects, integration of metal oxides and graphene in a composite fully uses each active component and consequently achieves excellent electrochemical performance in supercapacitors through materials design and fabrication. With this numerous advantages, several structural models based on graphene/metal oxide composites are already proposed for supercapacitor applications [85-87] such as graphene decorated with SnO₂ [88], Co₃O₄ [89,90], RuO₂ [91,92], TiO₂ [92], MnO₂ [93-95], Mn₃O₄ [96], ZnO [97,98], Fe₃O₄ [92] etc).

However, several important challenges still urgently need to be overcome: (1) the controllability of the interface between graphene and metal oxides. (2) Rational design and control of the morphology and phase composition of metal oxides on graphene can ensure reproducibility and better understanding of the structure–property relationships. (3) To develop small, thin, light weight and even flexible energy storage devices for advanced thin and wearable electronics. (4) New approaches to fabricate graphene-based composites have to involve a combined focus on new chemistry, controlled synthesis and device-performance of novel composite materials with optimized properties and functionalities, which is essential

to improve the electrochemical performance of metal oxide/graphene composite materials for supercapacitors. (5) The large-scale, low-cost and simple production of graphene is among one of the most important challenges. Therefore, future efforts should be focused on the control of the size, morphology, quantity and distribution of functional components and improving the interfacial interactions between graphene and functional building blocks. With continuous exploitation, it is believed that graphene/metal oxide composite materials for supercapacitors will realize many practical applications such as in portable tools, personal electronics, electric vehicles, hybrid electric vehicles, and plug-in hybrid electric vehicles, etc.



1.4. Energy harvesting: Nanogenerator

In recent years, searching and developing for sustainable, renewable and green energy has been one of the most important tasks for the researchers to address the rapidly increasing global warming and energy crisis in the world [99-101]. As for energy harvesting from ambient environment such as solar, wind, thermal, chemical and mechanical energy has attracted huge attention in the researcher due to the independent and sustainable operating of such systems without the use of a battery [102-105]. Among them, harvesting mechanical energy from our living environment (include sound, friction, motion, wind, and noise) is widely considered to be one of the promising approaches to provide a clean and green energy source for self-powered devices, such as wireless sensor networks, implanted medical devices, nanorobotics, security applications and portable/wearable personal electronics [106-110]. The mechanical energy directly convert into electrical energy using piezoelectric, triboelectric, electromagnetic, and electrostatic principles [111-117].

Among the conversion methods, nanogenerator (NG) has been developed for converting low frequency mechanical energy into electricity though piezoelectric and tribo-electrification processes and they have been demonstrated to power small electronic devices [118-124]. The vibration energy is enormous and available everywhere at any time. The harvesting energy is small but it has the potential to operate wearable and portable devices with the asset of power source without external power. Basically, piezoelectric nanogenerator (PNG) depends on the piezoelectric potential which created by an externally applied force in the piezoelectric material for driving the flow of electrons to the external load. Since,

PNG have been developed to efficiently convert small scale mechanical energy into electricity and used as power source for diverse applications.

1.4.1. Mechanism of piezoelectric nanogenerator

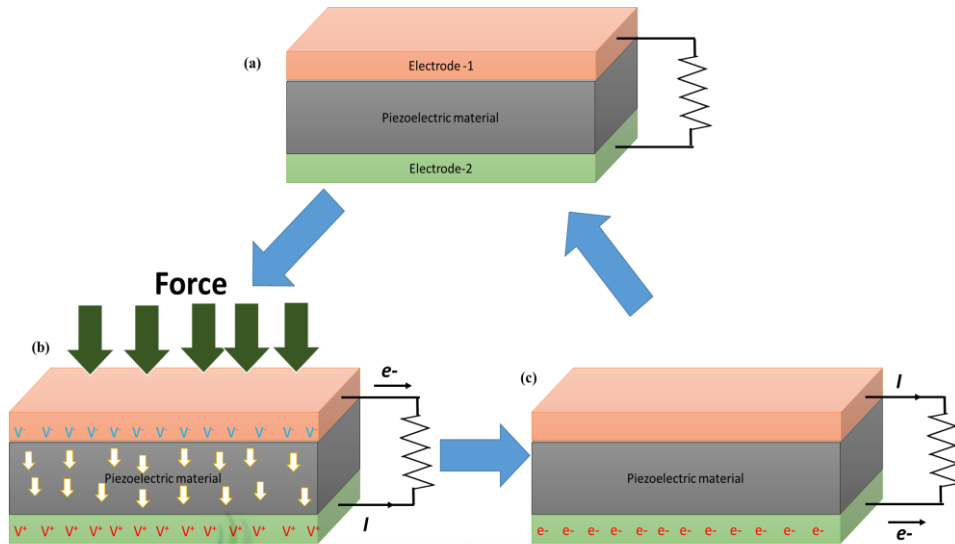


Figure 1.1.6 Mechanism of the piezoelectric nanogenerator. (a) In the device, no signal is observed in the absence of external force. b) When compressive force is applied to the device, the piezoelectric potential is created inside the piezo-materials, which aligns the electric dipoles in a single direction (stress-induced poling), resulting in a flow of electrons. c) As the external force is removed, the piezoelectric potential disappeared, and the accumulated electrons flow back via the external circuit.

The mechanism of the nanogenerator was explained through the piezoelectric effect [105]. At the initial state, there is no piezoelectric potential generation in device, as shown in **Figure 1.1.6a**. When a compressive force is applied to the device, the piezoelectric potential is generated inside the piezo-materials abruptly and the electric dipoles align strongly in a single direction due to stress-induced poling effect, which creates a significant potential across the electrodes, as shown **Figure 1.1.6b**. In order to screen the piezoelectric potential, positive and negative charges are accumulated at the top and bottom electrodes, respectively, resulting in voltage and current output signals from the device. Further, when the compressive

force is removed, the piezoelectric potential is diminished, and the accumulated charges move back to the opposite direction (**Figure 1.1.6c**). Therefore, continuous application and releasing of the compressive force results in AC-type voltage and current output signals from the nanogenerator.

1.4.2. Piezo-materials

Many research groups have attempted to fabricate high performance nanogenerators using different materials and architectural forms. A variety of nanostructured piezoelectric materials such as zinc oxide [125,126], lead zirconium titanate (PZT) [127], cadmium sulfide [128], barium titanate [129,130] gallium nitride, AlGaN nanocones [131] poly (vinylidene fluoride) [132] and polytetrafluoroethylene [133] and piezoelectric polymers in the form of nanorods, wires, fibers, micro belts and thin films were utilized for self-driven power source applications. Among the various piezoelectric materials studied for nanogenerator, many of the researches have focused on the materials with wurtzite structure such as ZnO, CdS and GaN. The greatest advantage of these material arises from the facile and cost-effective fabrication techniques.

1.5. Objectives and scope of thesis

To develop high-performance supercapacitors, the key shortcoming of supercapacitors, such as low energy density, and cost of electrode materials must be addressed. The inadequate charge accumulation in the electrical double layer limits the specific capacitance and energy density of EDLCs (carbon electrodes). In contrast, pseudocapacitors (metal oxide or conducting polymer electrodes) generally have higher specific capacitance and energy density which gradually decrease due to the poor electrical conductivity. Therefore metal oxides and carbon materials may not be employed alone as the supercapacitor electrodes for practical purpose. There is an urgent demand to improve the electrochemical performance of supercapacitor electrode materials. Thus, to exploit advanced electrode materials is the key to develop high-performance supercapacitors. Therefore, significant efforts have been devoted to develop various metal oxides, mixed metal oxides and carbon based-metal oxides electrode materials for high performance supercapacitor application. It is one of the most significant ongoing research in the field of energy storage systems in recent times.

With these considerations, this thesis aimed to design and prepare novel electrode materials that simultaneously possess high power density, high energy density as well as good rate capability, cyclic stability, low cost and environmentally free. The specific research activities in this thesis aim to:

- Construct complex nanoscale architectures with a combination of two types of metal oxide materials and/or structures on a conducting substrate as binder-free electrodes for high-performance supercapacitors.

- Investigate the mechanical properties including bending/folding strength as well as excellent flexibility of 2D nanomaterials by preparing MoS₂ and graphene nanosheets on flexible substrates as supercapacitor electrodes.
- Design novel nanostructured composite materials consisting of graphene and transition metal oxides for high-performance supercapacitor applications.
- Identify the proficiency and efficiency of the fabricated all-solid-state supercapacitors, to construct an energy module by integrating supercapacitor with nanogenerator, and photodetector for self-powered devices operation.
- Lastly, the thesis aimed to develop new self-charging supercapacitor power cell for directly converting mechanical energy into electrochemical energy. Such a device hybridizes a piezoelectric nanogenerator, a supercapacitor, and a power-management system, and can be directly used as a power source.

The results presented in this thesis may provide simple and effective approaches to preparing one dimensional, two dimensional and graphene-transition metal oxide based nanomaterials as supercapacitor electrodes. In addition, the development of SCSPC provide a new promising direction in the field supercapacitor research for the development of next generation self-powered sustainable power source for wearable and flexible electronic devices.

1.6. Structure of this thesis

This thesis is organized into eight chapters.

Chapter I gives a brief introduction about supercapacitor and nanogenerator devices and continued with comprehensive literature review on the working principle and the electrode materials for supercapacitors as well nanogenerator.

Chapter II provides details of the chemicals and reagents, experimental setups and methods used in the thesis. Also deals with the different characterization engaged in the analysis of materials properties like structural, optical, composition, morphological and electrochemical properties. The details about the cell and working electrodes preparation, gel-electrolyte preparation, electrochemical measurement techniques and equations used are presented.

Chapter III describes the preparation, characterization and electrochemical properties of TiO_2 NRs, $\text{TiO}_2@MnO_2$ core-shell, $\text{TiO}_2@Co_3O_4$ core-shell and $\text{TiO}_2/Co(OH)_2$ hierarchical nanostructured electrodes with an emphasis on the relationship between structure and electrochemical performance.

Chapter IV presents the electrochemical performance of fabricated two dimensional nanomaterials such as MoS_2 and graphene nanosheets electrodes. The synthesis and characterization of MoS_2 and graphene nanosheets electrodes are outlined in detail. The obtained results confirm that graphene-coated fabrics (solid state supercapacitor) could be effectively used in developing flexible supercapacitors.

Chapter V presents the experimental data of graphene decorated transition-metal-oxide nanoparticles (G-ZnO, G- TiO_2 and G- V_2O_5), mainly focusing on how graphene nanosheets structure benefit the ion transport as well as the influence of the transition metal oxide on the capacitive performance of the composite electrode. The

effect of the graphene nanosheets and the effective utilization of the pseudo-active materials are discussed in detail.

Chapter VI describes the proficiency and efficiency of the fabricated all solid state supercapacitors (SSC) in a self-powered system by integrating with nanogenerator, and photodetector. The various results demonstrated the feasibility of using fabricated solid state supercapacitor as efficient energy storage device and their application in self-powered system.

Chapter VII describes the fabrication and self-charging performance of Self-Charging Supercapacitor Power Cell (SCSPC) using PVDF-ZnO as a piezoelectric as well as a separator and electrochemically active materials as positive and negative electrodes, respectively for the first time. The fabrication and working mechanism of a SCSPC was discussed in detail. The SCSPC provide a new promising direction in the supercapacitor research for the development of next generation self-powered sustainable power source for wearable and flexible electronic devices.

Finally, **Chapter VIII** summarizes the salient features of the present study and outlined some suggestions for future work.

1.7. References

- [1] P. Yu, B. Lu, and Z. Xu, Super long-life supercapacitors based on the construction of nanohoneycomb-like strongly coupled CoMoO₄-3D graphene hybrid electrodes. *Adv. Mater.* 26(7) (2014) 1044-1051.
- [2] H. Wang, and H. Dai, Strongly coupled inorganic–nano-carbon hybrid materials for energy storage. *Chem. Soc. Rev.* 42 (2013) 3088-3113.
- [3] E. A. Rosa, and T. Dietz, Human drivers of national greenhouse-gas emissions. *Nature Clim. Change* 2 (2012) 581-586.
- [4] S. Chu, and A. Majumdar, Opportunities and challenges for a sustainable energy future. *Nature*, 488 (2012) 294-303.
- [5] J. R. Miller and P. Simon, Electrochemical capacitors for energy management. *Science* 321 (2008) 651-652.
- [6] P. Poizot, S. Laruelle, S. Grugeon, L. Dupont and J. M. Tarascon, Nano-sized transition-metal oxides as negative-electrode materials for lithium-ion batteries. *Nature* 407 (2000) 496-499.
- [7] B.E. Conway, *Electrochemical Supercapacitors: Scientific Fundamentals and Technological Applications*. Kluwer Academic/Plenum, New York, 1999.
- [8] A. Burke, Ultracapacitors: why, how, and where is the technology. *J. Power Sources* 91 (2000) 37.
- [9] D.R. Rolison, and L.F. Nazar, Electrochemical energy storage to power the 21st century. *MRS Bulletin* 36 (2011) 486-493.
- [10] Pandolfo, A. G. and A. F. Hollenkamp, Carbon properties and their role in supercapacitors. *J. Power Sources* 157(1) (2006) 11-27.

- [11] M. Jayalakshmi and K. Balasubramanian, Simple Capacitors to Supercapacitors - An Overview. *Int. J. Electrochem. Sci.* 3 (2008) 1196–1217.
- [12] A. Kuperman and I. Aharon, Battery-ultracapacitor hybrids for pulsed current loads: A review. *Renew. Sust. Energy Rev.* 15 (2011) 981–992.
- [13] Y. Zhang, H. Feng, X. B. Wu, L. Z. Wang, A. Q. Zhang, T. C. Xia, H. C. Dong, X. F. Li and L. S. Zhang, Progress of electrochemical capacitor electrode materials: A review. *Int. J. Hydrogen Energy* 34 (2009) 4889–4899.
- [14] X. Zhao, B. M. Sánchez, P. J. Dobson and P. S. Grant, The role of nanomaterials in redox-based supercapacitors for next generation energy storage devices. *Nanoscale* 3 (2011) 839–855.
- [15] M. Zhi, C. Xiang, J. Li, M. Li and N. Wu, Nanostructured carbon–metal oxide composite electrodes for supercapacitors: a review. *Nanoscale* 5 (2013) 72–88.
- [16] G. Yu, X. Xie, L. Pan, Z. Bao, and Y. Cui, Hybrid nanostructured materials for high-performance electrochemical capacitors. *Nano Energy* (2013) 2, 213–234
- [17] U. Eberle and R. von Helmolt, Sustainable transportation based on electric vehicle concepts: a brief overview. *Energy Environ. Sci.* 3 (2010) 689–699.
- [18] K. Naoi, S. Ishimoto, J. Miyamoto and W. Naoi, Second generation ‘nanohybrid supercapacitor’: Evolution of capacitive energy storage devices, *Energy Environ. Sci.* 5 (2012) 9363–9373.
- [19] G. P. Wang, L. Zhang and J. J. Zhang, A review of electrode materials for electrochemical supercapacitors. *Chem. Soc. Rev.* 41 (2012) 797–828.

- [20] P. Simon and Y. Gogotsi, Materials for electrochemical capacitors. *Nat. Mater.* 7 (2008) 845–854.
- [21] M. Winter and R. J. Brodd, What are batteries, fuel cells, and supercapacitors? *Chem. Rev.* 104 (2004) 4245–4269.
- [22] S. Bose, T. Kuila, A. K. Mishra, R. Rajasekar, N. H. Kim and J. H. Lee, Carbon-based nanostructured materials and their composites as supercapacitor electrodes. *J. Mater. Chem.* 22 (2012) 767-784.
- [23] Q. Lu, J. G. Chen and J. Q. Xiao, Nanostructured electrodes for high-performance pseudocapacitors. *Angew Chem. Int. Ed.* 52 (2013) 1882-1889.
- [24] L. L. Zhang and X. S. Zhao, Carbon-based materials as supercapacitor electrodes. *Chem. Soc. Rev.* 38 (2009) 2520–2531.
- [25] C. D. Lokhande, D. P. Dubal, and O. S. Joo, Metal oxide thin film based supercapacitors. *Curr. Appl. Phys.* 11 (2011) 255–270.
- [26] V. Augustyn, P. Simon and B. Dunn, Pseudocapacitive oxide materials for high-rate electrochemical energy storage. *Energy Environ. Sci.* 7 (2014) 1597-1614.
- [27] J. Huang, B. G. Sumpter, and V. Meunier, Theoretical model for nanoporous carbon supercapacitors. *Angew. Chem. Int. Ed.* 47 (2008) 520-524.
- [28] T. Cottineau, M. Toupin, T. Delahaye, T. Brousse, and D. Bélanger, Nanostructured transition metal oxides for aqueous hybrid electrochemical supercapacitors. *Applied Physics A* 82 (2006) 599-606.
- [29] D. Bélanger, T. Brousse, and J. W. Long, Manganese oxides: Battery materials make the leap to electrochemical capacitors. *Electrochem. Soc. Interfaces* 17 (2008) 49-52.

- [30] K. Naoi, and M. Morita, Advanced polymers as active materials and electrolytes for ECs and hybrid capacitor systems. *Electrochem. Soc. Interfaces* 17 (2008) 44-49.
- [31] H. Lee, M. S. Cho, I. H. Kim, J. D. Nam and Y. Lee, RuOx/polypyrrole nanocomposite electrode for electrochemical capacitors. *Synth. Met.* 160 (2010) 1055-1059.
- [32] D. Choi and P. N. Kumta, Nanocrystalline TiN derived by a two-step halide approach for electrochemical capacitors. *J. Electrochem. Soc.* 153 (2006) A2298-A2303.
- [33] D. Qu and H. Shi, Studies of activated carbons used in double-layer capacitors. *J. Power Sources*, 74 (1998) 99-107.
- [34] E. Raymundo-Pinero, K. Kierzek, J. Machnikowski and F. Beguin, Relationship between the nanoporous texture of activated carbons and their capacitance properties in different electrolytes. *Carbon* 44 (2006) 2498-2507.
- [35] O. Barbieri, M. Hahn, A. Herzog and R. Kotz, Capacitance limits of high surface area activated carbons for double layer capacitors. *Carbon*, 2005, 43, 1303-1310.
- [36] J. Biener, M. Stadermann, M. Suss, M.A. Worsley, M.M. Biener, K.A. Rose, and T.F. Baumann, Advanced carbon aerogels for energy applications. *Energy Environ. Sci.* 4 (2011) 656-667.
- [37] M. Kaempgen, C.K. Chan, J. Ma, Y. Cui, and G. Gruner, Printable thin film supercapacitors using single-walled carbon nanotubes. *Nano Lett.* 9 (2009) 1872-1876.

- [38] A. Izadi-Najafabadi, S. Yasuda, K. Kobashi, T. Yamada, D.N. Futaba, H. Hatori, M. Yumura, S. Iijima, and K. Hata, Extracting the full potential of single-walled carbon nanotubes as durable supercapacitor electrodes operable at 4 V with high power and energy density. *Adv. Mater.* 22 (2010) E235-E241.
- [39] J. Chmiola, C. Largeot, P.-L. Taberna, P. Simon, and Y. Gogotsi, Monolithic carbide-derived carbon films for micro-supercapacitors. *Science* 328 (2010) 480-483.
- [40] D. Pech, M. Brunet, H. Durou, P.H. Huang, V. Mochalin, Y. Gogotsi, P.L. Taberna, and P. Simon, Ultrahigh-power micrometre-sized supercapacitors based on onion-like carbon. *Nat. Nanotech.* 5 (2010) 651-654.
- [41] M. D. Stoller, C. W. Magnuson, Y. W. Zhu, S. Murali, J. W. Suk, R. Piner and R. S. Ruoff, Interfacial capacitance of single layer graphene. *Energy Environ. Sci.* 4 (2011) 4685-4689.
- [42] E. Frackowiak and F. Beguin, Carbon materials for the electrochemical storage of energy in capacitors. *Carbon* 39 (2001) 937-950.
- [43] K. Naoi, and P. Simon, New materials and new configurations for advanced electrochemical capacitors. *Electrochem. Soc. Interf.* 17 (2008) 34-37.
- [44] C.-C. Hu, K.-H. Chang, M.-C. Lin, and Y.-T. Wu, Design and tailoring of the nanotubular arrayed architecture of hydrous RuO₂ for next generation supercapacitors. *Nano Lett.* 6 (2006) 2690-2695.
- [45] V. Subramanian, S.C. Hall, P.H. Smith, and B. Rambabu, Mesoporous anhydrous RuO₂ as a supercapacitor electrode material. *Solid State Ionics* 175 (2004) 511-515.

- [46] D.-W. Wang, F. Li, and H.-M. Cheng, Hierarchical porous nickel oxide and carbon as electrode materials for asymmetric supercapacitor. *J. Power Sources* 185 (2008) 1563-1568.
- [47] S. Nandy, U. N. Maiti, C. K. Ghosh and K. K. Chattopadhyay, Enhanced p-type conductivity and band gap narrowing in heavily Al doped NiO thin films deposited by RF magnetron sputtering. *J. Phys.: Condens. Matter* 21 (2009) 115804.
- [48] M. Hamdani, R. N. Singh and P. Chartier, Co_3O_4 and Co- based spinel oxides bifunctional oxygen electrodes. *Int. J. Electrochem. Sci.* 5 (2010) 556–577.
- [49] W. Pan and J. H. Gong, Synthesis and electrochemical properties of V_2O_5 nanostructures. *Key Eng. Mater.* 2007, 336–338, 2134–2137.
- [50] A. Adeyemo, G. Hunterb and P. K. Dutta, Interaction of CO with hydrous ruthenium oxide and development of a chemoresistive ambient CO sensor. *Sens. Actuators B* 152 (2011) 307–315.
- [51] I. H. Kim and K. B. Kim, Electrochemical characterization of hydrous ruthenium oxide thin-film electrodes for electrochemical capacitor applications. *J. Electrochem. Soc.* 153 (2006) A383-A389.
- [52] Q. X. Jia, S. G. Song, X. D. Wu, J. H. Cho, S. R. Foltyn, A. T. Findikoglu and J. L. Smith, Ultra-fast intermetallic compound formation between eutectic SnPb and Pd where the intermetallic is not a diffusion barrier. *Appl. Phys. Lett.* 68 (1996) 1069-1071.
- [53] K. Sakiyama, S. Onishi, K. Ishihara, K. Orita, T. Kajiyama, N. Hosoda and T. Hara, Deposition and properties of reactively sputtered ruthenium dioxide films. *J. Electrochem. Soc.* 140 (1993) 829-834.

- [54] K. R. Prasad, K. Koga and N. Miura, Electrochemical deposition of nanostructured indium oxide: high-performance electrode material for redox supercapacitors. *Chem. Mater.* 16 (2004) 1845-1847.
- [55] M. Kalaji, P. J. Murphy and G. O. Williams, The study of conducting polymers for use as redox supercapacitors. *Synth. Met.* 102 (1999) 1360-1361.
- [56] Y. Zhou, B. He, W. Zhou, J. Huang, X. Li, B. Wu and H. Li, Electrochemical capacitance of well-coated single-walled carbon nanotube with polyaniline composites. *Electrochim. Acta* 49 (2004) 257-262.
- [57] V. Gupta and N. Miura, High performance electrochemical supercapacitor from electrochemically synthesized nanostructured polyaniline. *Mater. Lett.* 60 (2006) 1466-1469.
- [58] L. Fan and J. Maier, High-performance polypyrrole electrode materials for redox supercapacitors. *Electrochem. Commun.* 2006, 8, 937-940.
- [59] F. Fusalba, N. E. Mehdi, L. Breau and D. Belanger, Physicochemical and electrochemical characterization of polycyclopenta[2,1-b;3,4-b']dithiophen-4-one as an active electrode for electrochemical supercapacitors. *Chem. Mater.* 11 (1999) 2743-2753.
- [60] K. Naoi, S. Suematsu and A. Manago, Electrochemistry of poly(1,5-diaminoanthraquinone) and its application in electrochemical capacitor materials. *J. Electrochem. Soc.* 147 (2000) 420-426.
- [61] K. S. Ryu, K. M. Kim, Y. J. Park, N. G. Park, M. G. Kang and S. H. Chang, Redox supercapacitor using polyaniline doped with Li salt as electrode. *Solid State Ionics* 152 (2002) 861-866.

- [62] C. Tan and H. Zhang, Two-dimensional transition metal dichalcogenide nanosheet-based composites. *Chem. Soc. Rev.* (2015) DOI: 10.1039/C4CS00182F.
- [63] M. Chhowalla, H. S. Shin, G. Eda, L. J. Li, K. Loh and H. Zhang, The chemistry of two-dimensional layered transition metal dichalcogenide nanosheets. *Nat. Chem.* 5 (2013) 263–275.
- [64] X. Huang, Z. Y. Zeng and H. Zhang, Metal dichalcogenide nanosheets: preparation, properties and applications. *Chem. Soc. Rev.* 42 (2013) 1934–1946.
- [65] Q. H. Wang, K. Kalantar-Zadeh, A. Kis, J. N. Coleman and M. S. Strano, Electronics and optoelectronics of two-dimensional transition metal dichalcogenides. *Nat. Nanotechnol.* 11 (2012) 699–712.
- [66] M. S. Xu, T. Liang, M. M. Shi and H. Z. Chen, Graphene-like two-dimensional materials. *Chem. Rev.* 113 (2013) 3766–3798.
- [67] V. Nicolosi, M. Chhowalla, M. G. Kanatzidis, M. S. Strano and J. N. Coleman, Liquid exfoliation of layered materials. *Science*, 2013, 340, 1226419.
- [68] Y. F. Sun, S. Gao and Y. Xie, Atomically-thick two-dimensional crystals: electronic structure regulation and energy device construction. *Chem. Soc. Rev.* 43 (2014) 530–546.
- [69] H. Li, J. Wu, Z. Y. Yin and H. Zhang, Preparation and applications of mechanically exfoliated single-layer and multilayer MoS₂ and WSe₂ nanosheets. *Acc. Chem. Res.* 47 (2014) 1067–1075.

- [70] S. Ratha and C. S. Rout, Supercapacitor electrodes based on layered tungsten disulfide- Reduced graphene oxide hybrids synthesized by a facile hydrothermal method. *ACS Appl. Mater. Interfaces* 5 (2013) 11427–11433.
- [71] L. Zhang, H. B. Wu and X. W. Lou, Unusual CoS₂ ellipsoids with anisotropic tube-like cavities and their application in supercapacitors. *Chem. Commun.* 48 (2012) 6912-6914.
- [72] J. Yang, X. Duan, Q. Qin and W. Zheng, Solvothermal synthesis of hierarchical flower-like β -NiS with excellent electrochemical performance for supercapacitors. *J. Mater. Chem. A* 1 (2013) 7880-7884.
- [73] K. J. Huang, L. Wang, Y. J. Liu, Y. M. Liu, H. B. Wang, T. Gan and L. L. Wang, Layered MoS₂-graphene composites for supercapacitor applications with enhanced capacitive performance. *Int. J. Hydrogen Energy* 38 (2013) 14027-14034.
- [74] M. Jayalakshmi, M. M. Rao and B. M. Choudary, Identifying nano SnS as a new electrode material for electrochemical capacitors in aqueous solutions. *Electrochem. Commun.* 6 (2004) 1119-1122.
- [75] M. Jayalakshmi and M. M. Rao, Synthesis of zinc sulphide nanoparticles by thiourea hydrolysis and their characterization for electrochemical capacitor applications. *J. Power Sources* 157 (2006) 624-629.
- [76] A. K. Geim and K. S. Novoselov, The rise of graphene. *Nat. Mater.* 6 (2007) 183–191.
- [77] K. S. Novoselov, A. K. Geim, S. V. Morozov, D. Jiang, Y. Zhang, S. V. Dubonos, I. V Grigorieva and A. A. Firsov, Electric field effect in atomically thin carbon films. *Science* 306 (2004) 666–669.

- [78] S. Stankovich, D. A. Dikin, G. H. B. Dommett, K. M. Kohlhaas, E. J. Zimney, E. A. Stach, R. D. Piner, S. T. Nguyen and R. D. Ruoff, Graphene-based composite materials. *Nature* 442 (2006) 282–286.
- [79] M. Pumera, Graphene-based nanomaterials and their electrochemistry. *Chem. Soc. Rev.* 39 (2010) 4146-4157
- [80] S. R. C. Vivekchand, C. S. Rout, K. S. Subrahmanyam, A. Govindaraj, and C. N. R. Rao, Graphene-based electrochemical supercapacitors. *J. Chem. Sci.* 120 (2008) 9–13.
- [81] M. D. Stoller, S. J. Park, Y. W. Zhu, J. H. An, and R. S. Ruoff, Graphene-based ultracapacitors. *Nano Lett.* 8 (2008) 3498–3502.
- [82] W. Lv, D. M. Tang, Y. B. He, C. H. You, Z. Q. Shi, X. C. Chen, C. M. Chen, P. X. Hou, C. Liu, and Q. H. Yang, Low-temperature exfoliated graphenes: Vacuum-promoted exfoliation and electrochemical energy storage. *ACS Nano* 3 (2009) 3730–3736.
- [83] Y. Wang, Z. Q. Shi, Y. Huang, Y. F. Ma, C. Y. Wang, M. M. Chen, and Y. S. Chen, Supercapacitor devices based on graphene materials. *J. Phys. Chem. C* 113 (2009) 13103–13107.
- [84] C. G. Liu, Z. N. Yu, D. Neff, A. Zhamu, B. Z. Jang, Graphene-based supercapacitor with an ultrahigh energy density. *Nano Lett.* 10 (2010) 4863–4868.
- [85] L. L. Zhang, R. Zhou and X. S. Zhao, Graphene-based materials as supercapacitor electrodes. *J. Mater. Chem.* 20 (2010) 5983–5992.

- [86] Z. S. Wu, G. Zhou, L. C. Yin, W. Ren, F. Li, and H. M. Cheng, Graphene/metal oxide composite electrode materials for energy storage. *Nano Energy* (2012) 1, 107–131.
- [87] C. Xu, B. Xu, Y. Gu, Z. Xiong, J. Sun and X. S. Zhao, Graphene-based electrodes for electrochemical energy storage. *Energy Environ. Sci.* 6 (2013) 1388-1414.
- [88] J. Yao, X. P. Shen, B. Wang, H. K. Liu, and G. X. Wang, In situ chemical synthesis of SnO₂-graphene nanocomposite as anode materials for lithium-ion batteries. *Electrochem. Comm.* 11 (2009) 1849–1852.
- [89] W. Zhou, J. Liu, T. Chen, K. S. Tan, X. Jia, Z. Luo, C. Cong, H. Yang, C. M. Li, and T. Yu, Fabrication of Co₃O₄-reduced graphene oxide scrolls for high-performance supercapacitor electrodes. *Phys. Chem. Chem. Phys.* 13 (2011) 14462–14465.
- [90] J. Yan, T. Wei, W. M. Qiao, B. Shao, Q. K. Zhao, L. J. Zhang, and Z. J. Fan, Rapid microwave-assisted synthesis of graphene nanosheet/Co₃O₄ composite for supercapacitors. *Electrochim. Acta* 55 (2010) 6973–6978.
- [91] Z. S. Wu, D. W. Wang, W. Ren, J. Zhao, G. Zhou, F. Li, and H. M. Cheng, Anchoring hydrous RuO₂ on graphene sheets for high-performance electrochemical capacitors. *Adv. Funct. Mater.* 20 (2010) 3595–3602.
- [92] A.K. Mishra, and S. Ramaprabhu, Functionalized graphene-based nanocomposites for supercapacitor application. *J. Phys. Chem. C* 115 (2011) 14006–14013.

- [93] S. Chen, J. W. Zhu, X. D. Wu, Q. F. Han, and X. Wang, Graphene oxide–MnO₂ nanocomposites for supercapacitors. *ACS Nano* 4 (2010) 2822–2830.
- [94] Z. S. Wu, W. C. Ren, D. W. Wang, F. Li, B. L. Liu, and H. M. Cheng, High-energy MnO₂ nanowire/graphene and graphene asymmetric electrochemical capacitors. *ACS Nano* 4 (2010) 5835–5842.
- [95] J. Zhang, J. Jiang, and X. S. Zhao, Synthesis and capacitive properties of manganese oxide nanosheets dispersed on functionalized graphene sheets. *J. Phys. Chem. C* 115 (2011) 6448–6454.
- [96] B. Wang, J. Park, C. Y. Wang, H. Ahn, and G. X. Wang, Mn₃O₄ nanoparticles embedded into graphene nanosheets: Preparation, characterization, and electrochemical properties for supercapacitors. *Electrochim. Acta* 55 (2010) 6812–6817.
- [97] Y.P. Zhang, H.B. Li, L.K. Pan, T. Lu, and Z. Sun, Capacitive behavior of graphene–ZnO composite film for supercapacitors. *J. Electroanal. Chem.* 634 (2009) 68–71.
- [98] J. Wang, Z. Gao, Z. Li, B. Wang, Y. Yan, Q. Liu, T. Mann, M. Zhang, and Z. Jiang, Green synthesis of graphene nanosheets/ZnO composites and electrochemical properties. *J. Solid State Chem.* 184 (2011) 1421–1427.
- [99] Special Issue on Sustainability and Energy, *Science* 315 (2007) 721.
- [100] Special Issue on Harnessing Materials for Energy, *MRS Bulletin* 33 (2008) No. 4.
- [101] Z. L. Wang, Towards self-powered nanosystems: From nanogenerators to nanopiezotronics, *Adv. Funct. Mater.* 18 (2008) 3553–3567.

- [102] B. Tian, X. Zheng, T. J. Kempa, Y. Fang, N. Yu, G. Yu, J. Huang, and C. M. Lieber, Coaxial silicon nanowires as solar cells and nanoelectronic power sources, *Nature* 449 (2007) 885–889.
- [103] B. Poudel, Q. Hao, Y. Ma, Y. Lan, A. Minnich, B. Yu, X. Yan, D. Wang, A. Muto, D. Vashaee, X. Chen, J. Liu, M. S. Dresselhaus, G. Chen, and Z. Ren, High-thermoelectric performance of nanostructured bismuth antimony telluride bulk alloys, *Science* 320 (2008) 634–638.
- [104] Z. Shao, S. M. Haile, J. Ahn, P. D. Ronney, Z. Zhan, and S. A. Barnett, A thermally self-sustained micro solid-oxide fuel-cell stack with high power density, *Nature* 435 (2005) 795–798.
- [105] Z. L. Wang, and J. H. Song, Piezoelectric nanogenerators based on zinc oxide nanowire arrays, *Science* 312 (2006) 242–246.
- [106] Z. L. Wang, Self-powered nanosensors and nanosystems. *Adv. Mater.* 24 (2011) 280-285.
- [107] P. D. Mitcheson, E. M. Yeatman, G. K. Rao, A. S. Holmes, and T. C. Green, Energy harvesting from human and machine motion for wireless electronic devices, *Proc. IEEE* 96 (2008) 1457-1486.
- [108] J. A. Paradiso, and T. Starner, Energy scavenging for mobile and wireless electronics, *IEEE Pervas. Compu.* 4 (2005) 18-27.
- [109] J. A. Rogers, and Y. G. Huang, A curvy, stretchy future for electronics, *Proceedings of the National Academy of Sciences* 106 (2009) 10875-10876.
- [110] D.H. Kim, N. Lu, R. Ma, Y.S. Kim, R.H. Kim, S. Wang, J. Wu, S.M. Won, H. Tao, A. Islam, K. J. Yu, T. Kim, R. Chowdhury, M. Ying, L. Xu, M. Li, H. J. Chung, H. Keum, M. McCormick, P. Liu, Y. W. Zhang, F. G. Omenetto, Y.

- Huang, T. Coleman, and J. A. Rogers, Epidermal electronics, *Science* 333 (2011) 838-843.
- [111] Y. Qin, X. Wang, and Z. L. Wang, Microfibre–nanowire hybrid structure for energy scavenging, *Nature* 451 (2008) 809–813.
- [112] B. Saravanakumar, R. Mohan, K. Thiyagarajan, and S. J. Kim, Fabrication of a ZnO nanogenerator for eco-friendly biomechanical energy harvesting, *RSC Advances* 3(37), (2013) 16646-16656.
- [113] B. Saravanakumar, and S. J. Kim, Growth of 2D ZnO nanowall for energy harvesting application, *J. Phys. Chem. C* 118(17) (2014) 8831–8836.
- [114] S. P. Beeby, R. N. Torah, M. J. Tudor, P. Glynne-Jones, T. O'Donnell, C. R. Saha, and S. Roy, A micro electromagnetic generator for vibration energy harvesting, *J. Micromech. Microeng.* 17 (2007) 1257–1265.
- [115] P. D. Mitcheson, P. Miao, B. H. Stark, E.M. Yeatman, A.S. Holmes, and T.C. Green, MEMS electrostatic micropower generator for low frequency operation, *Sensor. Actuat. A-Phys.* 115 (2004) 523–529.
- [116] F. Fan, Z. Tian, and Z. L. Wang, Flexible triboelectric generator, *Nano Energy* 1 (2012) 328–334.
- [117] S. Wang, L. Lin, and Z. L. Wang, Nanoscale triboelectric-effect-enabled energy conversion for sustainably powering portable electronics, *Nano Lett.* 12 (2012) 6339–6346.
- [118] C. Y. Chen, T. H. Liu, Y. Zhou, Y. Zhang, Y. L. Chueh, Y. H. Chu, J. H. He, and Z. L. Wang, Electricity generation based on vertically aligned $\text{PbZr}_{0.2}\text{Ti}_{0.8}\text{O}_3$ nanowire arrays, *Nano Energy* 1 (2012) 424-428.

- [119] S.Y. Xu, G. Poirier, and N. Yao, Fabrication and piezoelectric property of PMN-PT nanofibers, *Nano Energy* 1 (2012) 602-607.
- [120] X. Chen, S.Y. Xu, N. Yao, and Y. Shi, 1.6 V Nanogenerator for mechanical energy harvesting using PZT nanofibers, *Nano Lett.* 10 (2012) 2133-2137.
- [121] F.R. Fan, L. Lin, G. Zhu, W. Wu, R. Zhang, and Z.L. Wang, Transparent triboelectric nanogenerators and self-powered pressure sensors based on micropatterned plastic films, *Nano Lett.* 12 (2012) 3109-3114.
- [122] G. Zhu, C.F. Pan, W.X. Guo, C.Y. Chen, Y.S. Zhou, R.M. Yu, and Z.L. Wang, Triboelectric-generator-driven pulse electrodeposition for micropatterning, *Nano Lett.* 12 (2012) 4960-4965.
- [123] Y.F. Hu, Y. Zhang, C. Xu, G. Zhu, and Z.L. Wang, High-output nanogenerator by rational unipolar assembly of conical nanowires and its application for driving a small liquid crystal display, *Nano Lett.* 10 (2010) 5025-5031.
- [124] J. W. Zhong, Q. Zhang, F. R. Fan, Y. Zhang, S. H. Wang, B. Hu, Z. L. Wang, and J. Zhou, Finger typing driven triboelectric nanogenerator and its use for instantaneously lighting up LEDs, *Nano Energy*, 2 (2012) 491-497.
- [125] M. P. Lu, J. Song, M. Y. Lu, M. T. Chen, Y. Gao, L. J. Chen and Z. L. Wang, Piezoelectric nanogenerator using p-Type ZnO nanowire arrays. *Nano Lett.* 9 (2009) 1223–1227.
- [126] R. Yang, Y. Qin, L. Dai and Z. L. Wang, Power generation with laterally packaged piezoelectric fine wires. *Nat. Nanotechnol.* 4 (2009) 34–39.

- [127] Y. Qi, J. Kim, T. D. Nguyen, B. Lisko, P. K. Purohit and M. C. McAlpine, Enhanced piezoelectricity and stretchability in energy harvesting devices fabricated from buckled PZT ribbons. *Nano Lett.* 11 (2011) 1331–1336.
- [128] Y. F. Lin, J. H. Song, Y. Ding, S. Y. Lu and Z. L. Wang, Piezoelectric nanogenerator using CdS nanowires. *Appl. Phys. Lett.* 92 (2008) 022105–022107.
- [129] K. I. Park, S. Xu, Y. Liu, G. T. Hwang, S. J. L. Kang, Z. L. Wang and K. J. Lee, Piezoelectric BaTiO₃ thin film nanogenerator on plastic substrates. *Nano Lett.* 10 (2010) 4939–4943.
- [130] K. I. Park, M. Lee, Y. Liu, S. Moon, G. T. Hwang, G. Zhu, J. E. Kim, S. O. Kim, D. K. Kim, Z. L. Wang and K. J. Lee, Flexible nanocomposite generator made of BaTiO₃ nanoparticles and graphitic carbons. *Adv. Mater.* 24 (2012) 2999–3004.
- [131] C. Pan, H. Wu, C. Wang, B. Wang, L. Zhang, Z. Cheng, P. Hu, W. Pan, Z. Zhou, X. Yang and J. Zhu, Nanowire-based high-performance “Micro Fuel Cells”: One nanowire, one fuel cell. *Adv. Mater.* 20 (2008) 1644–1648.
- [132] C. Sun, J. Shi, D. J. Bayerl and X. Wang, PVDF microbelts for harvesting energy from respiration. *Energy Environ. Sci.* 4 (2011) 4508–4512.
- [133] X. Wang, J. Song, F. Zhang, C. He, Z. Hu and Z. L. Wang, Electricity generation based on one-dimensional group-III nitride nanomaterials. *Adv. Mater.* 22 (2010) 2155–2158.

CHAPTER-II

Materials Characterization and Electrochemical Techniques

To fulfill the research objective, experimental work was done in the laboratory, followed by physicochemical characterization and evaluation of the electrochemical properties of the obtained materials. This chapter describes the experimental details including the materials, chemicals and apparatus used in the research project. The typical materials synthesis methods such as hydrothermal, microwave, electrodeposition and modified hummers method for graphene oxide synthesis; basic materials characterization techniques for structure, morphology, composition, surface area and optical properties confirmation; electrode fabrication, cell assembly, and electrochemical measurement is discussed in detail.



2.1. Reagents and apparatus

All reagents used in these thesis experiments were of analytical grade and were used directly without further purification. The list of materials and chemical used in this thesis are given in **Table 2.1**.

Table 2.1 Materials and chemicals used in the research project

Chemicals	Formula	Purity	Supplier
Titanium tetra-n-butoxide	$C_{16}H_{36}O_4Ti$	97%	Kanto Chemical Co., Inc. Japan
Hydrochloric acid	HCl	35%	Daejung Chemicals & Metals Co. Ltd, Korea
Sodium sulfate (anhydrous)	Na_2SO_4	99%	Daejung Chemicals & Metals Co. Ltd, Korea
Fluorine doped tin oxide (FTO) substrate	$SnO_2:F$		Sigma Aldrich
Glucose	$C_6H_{12}O_6$	98%	Daejung Chemicals & Metals Co. Ltd, Korea
Potassium permanganate	$KMnO_4$	99.3%	Daejung Chemicals & Metals Co. Ltd, Korea
Cobalt(II) nitrate hexahydrate	$Co(NO_3)_2$	97%	Daejung Chemicals & Metals Co. Ltd, Korea
Urea	$Co(NH_2)_2$	98%	Daejung Chemicals & Metals Co. Ltd, Korea
Ammonium fluoride	NH_4F	97%	Junsei, Chemical Co. Ltd. Japan
Potassium hydroxide	KOH	85%	Daejung Chemicals & Metals Co. Ltd, Korea
Sodium nitrate	$NaNO_3$	99%	Daejung Chemicals & Metals Co. Ltd, Korea
Sodium molybdate	Na_2MoO_4	98%	Sigma Aldrich
Thioacetamide	C_2H_5NS	98%	Wako Chemicals
Potassium chloride	KCl	99%	Daejung Chemicals & Metals Co. Ltd, Korea
Carbon black	C	99.9+%	Alfa Aesar
Polyvinylidene fluoride (PVDF)	$(CH_2CF_2)_n$	-	Sigma Aldrich
N-Methyl-2-pyrrolidinone	C_5H_9NO	99.7%	Daejung Chemicals &

(NMP)			Metals Co. Ltd, Korea
Ethanol	CH ₃ CH ₂ OH	99.9%	Fisher Scientific
Acetone	C ₃ H ₆ O	99.8%	Fisher Scientific
Phosphoric acid	H ₃ PO ₄	98%	Daejung Chemicals & Metals Co. Ltd, Korea
Polyvinyl alcohol (PVA)	(C ₂ H ₄ O) _x	99+%	Sigma Aldrich
Graphite	C	75%	Sigma Aldrich
Sulfuric acid	H ₂ SO ₄	98%	Daejung Chemicals & Metals Co. Ltd, Korea
Hydrogen peroxide	H ₂ O ₂	30%	Junsei Chemical Co. Ltd. Japan
Zinc nitrate	Zn(NO ₃) ₂	98%	Daejung Chemicals & Metals Co. Ltd, Korea
Sodium hydroxide	NaOH	98%	Daejung Chemicals & Metals Co. Ltd, Korea
Hydrazine hydrate	NH ₂ NH ₂ ·xH ₂ O	80%	Daejung Chemicals & Metals Co. Ltd, Korea
Methanol	CH ₄ O	99.8%	Daejung Chemicals & Metals Co. Ltd, Korea
Indium tin oxide	ITO	-	Sigma Aldrich
Dimethylformamide (DMF)	C ₃ H ₇ NO	99.8%	Daejung Chemicals & Metals Co. Ltd, Korea
Acetic acid	C ₂ H ₄ O ₂	99.5%	DC Chemical Co. Ltd,
Poly(tetrafluoroethylene) (PTFE)	(C ₂ F ₄) _n	-	Sigma Aldrich
Nickel foam	Ni	-	Heze Jiaotong Group Corporation, China
Stainless steel	316L SS	-	Nilaco, Japan
Vanadium pentoxide	V ₂ O ₅	99%	Daejung Chemicals & Metals Co. Ltd, Korea
Lithium chloride	LiCl	98%	Daejung Chemicals & Metals Co. Ltd, Korea
Ammonium persulfate	(NH ₄) ₂ S ₂ O ₈	98%	Kanto Chemical Co. Inc, Japan
Nitric acid	(HNO ₃)	60-62%	Junsei Chemical Co. Ltd. Japan
Aluminum	Al	-	Nilaco, Japan
Carbon fabric	C	-	DHLS, Korea

The general equipment's used for materials preparation and electrochemical measurements are given **Table 2.2**.

Table 2.2 Apparatus used in the research project

Apparatus	Model or Specification	Manufacturer
Hot plate & Magnetic stirrer	MS300HS	M TOPS
Autoclave	PTFE container	Latech
Oven	OF-02 GW	JEIO Tech
Microwave	MW-202BG	LG
Furnace	CRF-M15	Ceber
Tube furnace		
Centrifuge	GYROZEN -1580 MG	Gyrozen
Ultrasonicator	SONIC VCX 500 model (20 kHz, 500 W)	Sonics Materials, Inc.
Ultrasonic cleaner	ELMASONIC S15H	Elmasonic
Balance	AUW220D	Shimadzu
Electrochemical work station	AUTOLAB PGSTAT302N	Eco Chemie
Keithley nanovoltmeter & picoammeter	2182A & 6485	Keithley
Spin coater	SPIN-1200	Midas System

2.2. Materials synthesis

The synthesis of nanomaterials with controlled size and shape have attracted rapidly growing interest for many practical and technological applications. To fulfill the research tasks, the electroactive materials were mainly synthesized using following methods such as hydrothermal, microwave, electrodeposition, thermal treatment, etc.,

2.2.1. Hydrothermal synthesis

In recent years, hydrothermal method has become one of the most promising approach for preparing nanomaterials with different morphologies. Hydrothermal

synthesis is a process that utilizes single or heterogeneous phase reactions in aqueous media at temperature above 100 °C and pressure above 1 atm to crystallize nanomaterials directly from solution [1-2]. The growth process was performed in an autoclave (sealed steel pressure vessel), that can withstand high temperatures and pressures for a long time in which a nutrient is supplied along with water. A temperature gradient was maintained between the opposite ends of the growth chamber. At the hotter end, the nutrient solute dissolves, while at the cooler end, it is deposited on a seed crystal, growing the desired crystal.

The TiO₂ nanorod arrays, TiO₂@MnO₂ core-shell, TiO₂@Co₃O₄ core-shell nanostructure, MoS₂ nanosheets and MnO₂ nanowires were prepared through hydrothermal technique as presented in **Chapter-3.1, 3.2, 3.3, 4.2** and **Chapter-7.1**, respectively.

2.2.2. Microwave synthesis

Microwave irradiation techniques provides facile and fast routes to the synthesis of wide range nanomaterials with various compositions, sizes and shapes, without high temperature or pressure. Microwave synthesis based on two principle mechanisms: dipole rotation and ionic conduction [3-4]. Dipole rotation is an interaction in which polar molecules in a solvent try to align themselves with the quickly changing electric field of the microwave. Another, way to transfer energy is ionic conduction, which results if there are free ions or ionic species present in the substance being heated.

Herein, the graphene-ZnO, graphene-TiO₂ and graphene-V₂O₅ hybrid nanostructures were prepared for electrochemical supercapacitor through Microwave technique as presented in **Chapter-5.1, 5.3, and 5.4**.

2.2.3. Electrodeposition

The electrodeposition or e-coating, cathodic electrodeposition, or anodic electrodeposition, is a deposition process in which metal ions (colloidal particles) suspended in a solution are migrated by an electric field and deposit on the surface of the substrate [5]. The deposition process can be either cathodic or anodic reaction depending on the work piece to be coated (cathode or anode). The process is useful for applying materials to any electrically conductive surface.

In $\text{TiO}_2/\text{Co}(\text{OH})_2$ hybrid nanostructure, the $\text{Co}(\text{OH})_2$ nanowall was prepared by using electrodeposition method as presented in **Chapter 3.4**.

2.2.4. Graphene oxide synthesis by modified Hummer's method

Graphene oxide was successfully synthesized from expandable graphite powder by the modified Hummer's method [6-7]. Briefly, expandable graphite powder (2 g) was added into the concentrated H_2SO_4 (40 mL) solution with stirring for 2 h. KMnO_4 (6 g) was added slowly into the above solution with stirring while keeping the temperature of reaction less than 20 °C. The mixture was then stirred at 35-40 °C for 30 min, and then at 65-80 °C for 45 min. The resulting solution was diluted by adding 50 mL of water and the mixture was heated at 90 °C for 30 min, leads to the formation of dark brown solution. After additional stirring for 2 h, the dark brown solution was further diluted with distilled water (150 mL) and then H_2O_2 (10 mL) was added slowly and the color of the mixture was turned into brilliant yellow. The mixture was washed by repeated centrifugation and filtration, first with 5% HCl aqueous solution, and then with distilled water until the pH of the solution becomes neutral. Finally, 150 mL of water was added to the resulting precipitate and sonicated well in a probe type sonicator nearly 1 h to obtain a uniform suspension of

graphene oxide. After centrifuging and drying at 60 °C in hot air oven, the GO was obtained as a gray powder. The prepared GO was used for the synthesis of graphene, graphene-ZnO, graphene-TiO₂ and graphene-V₂O₅ nanomaterials as presented in **Chapter 4.1, and Chapter 5.**

2.3. Materials characterization

The synthesized nanomaterials were analyzed using several characterization techniques to identify the crystal phase, morphology, microstructure, size, composition and surface area. The detailed experimental conditions are given below.

2.3.1. X-ray diffraction (XRD)

X-ray diffractometer (XRD) is a non-destructive analytical characterization method to determine the crystal phase, purity, size and structure. The as-prepared samples were measured by using Rigaku X-ray diffractometer (XRD) operated at 40 KeV and 40 mA with CuK_α radiation in the range of 10-80° with a step of 0.02°.

2.3.2. Raman spectroscopy

The Raman studies are sensitive towards the crystallization, structural disorders and defects in nanostructures. Therefore, Raman-scattering studies have been performed for the as-synthesized resultant materials. Further, it is also used to study the bonding nature of various carbon materials such as graphene, graphene oxide and carbon nanotubes. Raman spectra of the samples were studied using a LabRam HR800 micro Raman spectroscope (Horiba Jobin-Yvon, France). The Raman system was operated at a laser power of 10 mW and an excitation wavelength of 514 nm with an Ar⁺ ion laser. The data were collected using a 10-s data point acquisition time in the spectral region of 100–3500 cm⁻¹.

2.3.3. Fourier transform infrared (FT-IR) spectrometer

FT-IR spectroscopy is an important technique for the direct monitoring of interaction between adsorbed molecules and the material. FT-IR spectra were measured at room temperature with an FT-IR spectrometer (Thermo Scientific Systems, Nicolet-6700) using the KBr pellet technique in the range of 4000 to 400 cm^{-1} .

2.3.4. Field-emission scanning electron microscopy

The surface morphology, and particle size of the prepared materials were studied by the field emission scanning electron microscope (FE-SEM, JSM-6700F, JEOL Ltd) with an acceleration voltage of 5 kV and filament current of 10 μA . Before measurement, the as-prepared samples were fixed onto a double-face conducted tape mounted on a metal stud and coated with platinum with a sputter coater (Cressington sputter coater -108 auto).

2.3.5. High-resolution transmission electron microscopy

The particle size, microstructure, and crystalline phase of the nanomaterials were studied by the high-resolution transmission electron microscopy (HR-TEM, JEOL-JEM 200CX) with an accelerating voltage of 200 kV. The samples used for TEM observations were prepared by dispersing the NPs in ethanol followed by ultrasonic vibration for 5 min, and then placing a drop of the dispersion onto a copper grid before loading in to the instrument.

2.3.6. Energy dispersive X-ray spectroscopy analysis (EDS)

The elemental composition of the prepared samples were measured using Energy Dispersive X-ray Spectroscopy (EDS). The EDS analysis was done with the

Field Emission Scanning Electron Microscopy (FE-SEM) instrument (Zeiss ultra FE-SEM instruments) with a separate EDS detector (INCA) connected to that instrument.

2.3.7. X-ray photoelectron spectroscopy (XPS)

The chemical composition and the state of elements present in the outermost part of samples was obtained by X-ray photoelectron spectroscopy (XPS) techniques using ESCA- 2000, VG Microtech Ltd and Theta Probe AR-XPS system (Thermo Fisher Scientific, U.K). Here a monochromatic X-ray beam source at 1486.6 eV (Aluminum anode) and 14 kV was used to scan upon the sample surface. A high flux X-ray source with Aluminum anode was used for X-ray generation, and a quartz crystal monochromator was used to focus and scan the X-ray beam on the sample.

2.3.8. UV-Vis spectrophotometer (UV-Vis)

The optical properties of the NPs were studied using UV-Vis spectroscopy (Hewlett Packard HP-8453) with a quartz cuvette path length of 1 cm. The data was collected in the range of wavelength 200 to 850 nm.

2.3.9. Brunauer, Emmett and Teller (BET) surface area analysis

Nitrogen (N₂) adsorption-desorption isotherm measurement was carried out to determine the surface area, pore-volume and pore-size distribution of the as-prepared samples. The Brunauer-Emmett-Teller (BET) analysis was performed with QuantachromeR ASiQwin™ c 1994-2012, Quantachrome Instruments v2.02 and nitrogen (N₂) gas was used as an adsorptive for the determination of the above parameters. The specific surface area of the samples were calculated by using the multiple-point BET model. The pore size distributions were obtained from the adsorption/ desorption branch of the isotherm by the Barrett-Joyner-Halenda (BJH)

method. The total pore volume was calculated from the volume of nitrogen adsorbed at a relative pressure of $P/P_0 = 0.95$.

2.4. Electrode fabrication and cell assembly

2.4.1. Electrode fabrication

The working electrodes were prepared by various methods depends on the nature of the electroactive materials. Briefly, the as-prepared samples, carbon black, and poly(tetrafluoroethylene) (PTFE) or polyvinylidene difluoride (PVDF) were mixed in a mass ratio of 75:20:5 or 80:10:10 and dispersed in the ethanol or N-methyl pyrrolidinone (NMP), solution, resulting in a homogeneous paste. The resulting solution mixture was coated onto a current collector substrate (Nickel foam, Aluminum foil, Stainless steel, and Carbon fabric) in $1\text{ cm} \times 1\text{ cm}$ with a spatula for the fabrication of the electrodes. The electrodes were then dried at $100\text{ }^\circ\text{C}$ for 12 h in a vacuum oven. The loading mass of the electrode active material was measured using balance before and after loading of mass on Ni foam. The fabricated binder and binder free electrodes are shown in **Figure 2.1.1**.



Figure 2.1.1 Fabricated binder and binder free electrodes on various current collectors.

2.4.2. Cell assembly

Two symmetric supercapacitors based on graphene-TiO₂ and graphene-V₂O₅ nanostructure were assembled. The as-prepared positive and negative electrode were pressed together and separated by a filter paper separator. The electrochemical measurements of the symmetric supercapacitors were carried out in 1M Na₂SO₄ aqueous electrolyte using the electrochemical working station in a two electrode cell at room temperature.

The solid-state supercapacitor devices were assembled by two pieces of prepared electrodes on current collector with a separator sandwiched in between and gel as a solid electrolyte. Prior to the assembling, all the electrodes and the separator were immersed into the gel electrolyte solution for 5 min and then assembled one by one and kept at 45°C for 12 h to vaporize the excess water in the electrolyte.

The LiCl/PVA electrolyte was prepared by mixing 4 g PVA and 8.5 g LiCl in 40 mL deionized water. Then the mixture was heated at 85 °C under vigorous stirring until the solution became clear.

The self-charging supercapacitor power cell (SCSPC) was assembled by a two piece of prepared electrodes (positive and negative) on aluminium foil as well as carbon fabric with PVA/H₃PO₄ gel electrolyte separator (PVDF-ZnO) in a middle. Prior to the assembling, all the electrodes and the separator were immersed into the gel electrolyte solution for 5 min. The assembled power cell was further dried at room temperature for 12 h. Here, PVDF-ZnO acts as a separator as well as a power source (piezoelectric effect). The PVDF-ZnO film separator was prepared by a solution-casting method in a ratio of 1:0.1 (PVDF:ZnO) in Dimethylformamide (DMF).

The PVA/H₃PO₄ gel electrolyte was prepared by mixing 3 g of polyvinyl alcohol (PVA) in 30 mL deionized water at 95 °C with stirring. After, the PVA was completely dissolved, 3 g of phosphoric acid (H₃PO₄) was added into the PVA solution under vigorous stirring until it formed a homogeneous sticky solution. Then the solution was cooled at room temperature and the solution became a clear and transparent gel.

2.5. Electrochemical Testing

To confirm the capacitive behavior and quantify the specific capacitance of the as-fabricated electrodes, Cyclic Voltammetry (CV), Galvanostatic Charge/Discharge (GCD) and Electrochemical Impedance Spectroscopy (EIS) tests were performed. All of the electrochemical experiments were investigated using an AUTOLAB PGSTAT302N electrochemical work station (**Figure 2.1.2**). A typical three-electrode experimental cell, equipped with a working electrode, platinum foil as a counter electrode, and an Ag/AgCl reference electrode, was used for measuring the electrochemical properties of the working electrodes. Three electrode configurations are common in fundamental research where it allows one electrode to be studied in isolation, without complications from the electrochemistry of the other electrodes. For measuring packaged supercapacitors (two electrode cell configuration), both reference and counter electrode leads are connected to the negative (-) terminal of the capacitor. The working electrode and working sense leads are connected to the positive (+) terminal. Various aqueous solution were used as the electrolytes, which include 1 M Na₂SO₄, 1 M KCl, 2 M KOH, and 1 M H₃PO₄ solution at room temperature. The PVA/H₃PO₄ and PVA/LiCl gel electrolytes were used for the solid state supercapacitors.



Figure 2.1.2 Electrochemical workstation.

2.5.1. Cyclic voltammetry

CV is generally considered to be an appropriate tool for estimating the difference between the non-Faradic and Faradic processes in an electrochemical reaction. In CV measurement, the voltage is swept between a lower limit to an upper limit at a fixed voltage. The voltage scan rate is calculated from the slope of the line. The current evolution was measured as a function of the voltage. The characteristics of the linear sweep voltammogram recorded depend on a rate of the electron transfer reaction, chemical reactivity of the active species and the voltage scan rate. The cyclic voltammetry (CV) data of the electrodes were obtained by changing the scan rates: 1, 5, 10, 25, 50, 75, 100, 125, and 150 mV s^{-1} .

2.5.2. Galvanostatic charge/discharge

The galvanostatic charge/discharge (GCD) studies are the most important and direct approach to evaluate the applicability of supercapacitors. A repetitive loop of charging and discharging is called a cycle. Most often, charge and discharge are conducted at constant current until a set potential is reached. The galvanostatic charge-discharge curves were obtained for various current densities.

2.5.3. Electrochemical impedance spectroscopy

Electrochemical Impedance Spectroscopy (EIS) is a powerful tool to understand the capacitive behavior and resistance associated with the as-prepared electrode surface. The advantage of EIS is that it is generally non-destructive to the investigated system. This enables the possibility for further electrochemical measurements and post mortem investigations. EIS is the most common method for measuring the equivalent series resistance (ESR) of supercapacitors. It also allows creating models to describe, underlying reaction mechanisms. With these models, capacitor non idealities can be investigated. Generally, a sinusoidal AC excitation signal is applied to the investigated system during an EIS experiment and the AC response is measured. Frequency sweeping in a wide range from high-to low-frequency enables the reaction steps with different rate constants, such as mass transport, charge transfer, and chemical reaction, to be separated.

In the present research, the EIS experiment for prepared samples were conducted at a frequency range of 0.1 Hz to 100 kHz. The EIS data were analyzed using Nyquist plots, which show the frequency response of the electrode/electrolyte system and are the plotted with the imaginary component ($-Z''$) of the impedance against the real component (Z').

2.6. Calculation of electrochemical parameters

The electrochemical parameters, such as the specific capacitance, Coulombic efficiency (η), energy (E), and power density (P) are important parameters for the investigation of the capacitive behavior of electrochemical cells [8-13].

The specific capacitance (C_s) of the electrodes can be calculated from the CV curves according to the following equation,

$$C_s = \frac{\int I(V)dv}{vm\Delta V} \dots\dots\dots (2.1)$$

where m indicates the mass of the electroactive material (g), v represents the potential scan rate (Vs^{-1}), ΔV is the voltage range of one sweep segment (V) and $\int I(V)dv$ is the integrated area under the CV curve loop (AV).

The specific capacitance of the electrodes can also be calculated from GCD curves according to the following formula,

$$C_s = \frac{I\Delta t}{m\Delta V} \dots\dots\dots (2.2)$$

where, C_s is the specific capacitance (F g^{-1}), I is the discharge current (A), Δt is the discharge time (s), m is the mass of the electroactive material (g), and ΔV is the potential range (V).

The specific capacitance of single electrode in the two electrode cell can be calculated using the following equation:

$$C_s = 4 \times C_m \dots\dots\dots (2.3)$$

C_s is the specific capacitance of the single electrode in the two-electrode cell (F g^{-1}) and C_m is the measured capacitance (F g^{-1})

The suitability of electrodes for supercapacitor applications was further evaluated by examining its Coulombic efficiency (η), energy (E) and power density (P). The Coulombic efficiency, energy density and power density values were calculated from galvanostatic charge/discharge curves by using the following equations:

$$\eta = \frac{t_D}{t_C} \times 100\% \dots\dots\dots (2.4)$$

$$E = \frac{C_m (\Delta V)^2}{7.2} \dots\dots\dots (2.5)$$

$$P = \frac{E \times 3600}{\Delta t} \dots\dots\dots (2.6)$$

where t_D is the time of discharging, t_C is the time of charging, E is the energy density (Wh Kg⁻¹), C is the specific capacitance (F g⁻¹), ΔV is the potential window (V), P is the power density (kW kg⁻¹) and t is the discharge time (s).

The areal capacitance of the electrodes, C_a (F cm⁻²), was calculated from the CV curves using the following equation:

$$C_a = \frac{\int IdV}{V\nu S} \dots\dots\dots (2.7)$$

where, $\int I dV$ is the area under the CV curve, ν is the scan rate (V s⁻¹), V is the sweep potential window (V), and S is the electrode active area (cm⁻²).

The areal capacitance of the electrode was calculated from the galvanostatic charge–discharge curves using the following expression:

$$C_a = \frac{I \times t}{V \times S}, \dots\dots\dots (2.8)$$

where C_a is the areal specific capacitance (F cm⁻²), I is the discharge current (A), t is time (s), V is the applied potential window (V), and S is the active surface area of the electrode (cm⁻²).

2.7. References

- [1] K. Byrappa and M. Yoshimura: Handbook of Hydrothermal Technology (Noyes Publications/William Andrew Publishing LLC, U.S.A. 2001).
- [2] S. Sōmiya, and R. Roy, Hydrothermal synthesis of fine oxide powders, Bull. Mater. Sci. 23(6) (2000) 453–460.
- [3] N. P. Herring, A. B. Panda, K. AbouZeid, S. H. Almahoudi, C. R. Olson, A. Patel, and M. S. El-Shall, Microwave synthesis of metal oxide nanoparticles. Metal Oxide Nanomaterials for Chemical Sensors. Integrated Analytical Systems, Springer New York (2013) 245-284.
- [4] B. Hayes, Microwave Synthesis: Chemistry at the Speed of Light. CEM Publishing, (2003).
- [5] I. Gurrappa and L. Binder, Electrodeposition of nanostructured coatings and their characterization - a review. Sci. Technol. Adv. Mater. 9 (2008) 043001-043012.
- [6] W. S. Hummers, and R. E. Offeman, Preparation of graphitic oxide. J. Am. Chem. Soc. 1958, 80, 1339.
- [7] Y. Zhu, S. Murali, W. Cai, X. Li, J. W. Suk , J. R. Potts , and R. S. Ruoff, Graphene and graphene oxide: Synthesis, properties, and applications, Adv. Mater. 22 (2010) 3906–3924.
- [8] C.G. Liu, Z.N. Yu, D. Neff, A. Zhamu, and B.Z. Jang, Graphene-based supercapacitor with an ultrahigh energy density. Nano. Lett. 10 (2010) 4863-4868.

- [9] J.W. Lang, X.B. Yan, X.Y. Yuan, J. Yang, and Q.J. Xue, Study on the electrochemical properties of cubic ordered mesoporous carbon for supercapacitors. *J. Power Sources* 196 (2011) 10472-10478.
- [10] D. Sun, X. Yan, J. Lang, and Q. Xue, High performance supercapacitor electrode based on graphene paper via flame-induced reduction of graphene oxide paper. *J. Power Sources* 222 (2013) 52-58.
- [11] A. Ramadoss, and S. J. Kim, Improved activity of a graphene-TiO₂ hybrid electrode in an electrochemical supercapacitor. *Carbon* 63 (2013) 434-445.
- [12] A. Ramadoss, G. S. Kim, and S. J. Kim Fabrication of reduced graphene oxide/TiO₂ nanorod/reduced graphene oxide hybrid nanostructures as electrode materials for supercapacitor applications. *CrystEngComm* 15(47) (2013) 10222-10229.
- [13] A. Ramadoss, and S. J. Kim, Vertically aligned TiO₂ nanorod arrays for electrochemical supercapacitor. *J. Alloys Comp.* 561 (2013) 262-267.

CHAPTER-III

Transition Metal Oxide /Hydroxides Based Hierarchical Nanostructure for Electrochemical Supercapacitors

It is well known that capacitance and the energy storage performance of supercapacitors depends on the electrode materials used. Therefore, much research has been carried out in recent years to improve the performance of supercapacitors by developing new electrode materials [1-5]. Among pseudocapacitive materials, metal oxides and hydroxides are inexpensive and environmentally friendly with good electrochemical performance, and those that possess multiple oxidative states or structures and can facilitate redox reactions are of particular interest [6]. Hydrated ruthenium oxide has shown the greatest specific capacitance and has excellent reversibility; however, the toxicity, scarceness and high cost of the Ru limits its commercial application [7,8]. Therefore, much efforts has been devoted to searching for alternative electrode materials with improved electrochemical behaviour.

In addition, even though some of other metal oxides exhibit higher specific capacitance and rate capabilities, but such performances cannot be transferred to bulk electrode materials because the ionic transport throughout the internal volume of the bulk electrode layer is largely limited due to poor conductivity. Therefore, it is desirable to shorten the diffusion path length of ion/electron transportation in the electrodes in order to improve the specific capacitance and rate capability.

Recently, the development of nanostructured materials (nanowires, nanotubes/rods, nanoaerogels, nanospheres, nanoplates etc.,) have been considered as competitive candidates for highly efficient electrodes of energy conversion/storage devices [9-13]. These nanostructured materials possess higher surface area (more

electro-active sites) and also they can provide short diffusion path lengths for transport of ions and electrons, leading to the fast kinetics and more efficient contact of electrolyte ions and more electroactive sites for faradaic energy storage, resulting in high charge/discharge rates even at high current densities. However, the functionalities of nanomaterials are largely affected by their structures, particularly in an electrode, the morphologies of nanomaterials directly affect their surface areas while interacting with the electrolyte. Therefore, in order to achieve high performance in supercapacitors, the electrode materials should be rationally manipulated so as to achieve fast kinetics, high capacity and stability.

Thus, significant effort has focused on further improvement of the electrochemical performance of supercapacitors, by using mixed metal oxides and binary metal oxide/ hydroxides with the rational manipulation of morphologies. In particular, well-defined hierarchical structures such as, vertically aligned one dimensional (1-D) wire-like, tubular and three dimensional (3-D) mesoporous topologies offer a low diffusion barrier, high areal density or active surface sites and a high strain/stress tolerance, ensuring enhanced cycling capacity. Hence, integrating nanostructures into conductive and highly porous frameworks can provide some advancement in this direction.

Based on the above analysis, hierarchical architecture with 1D nanostructured materials seem to be very promising for supercapacitor applications due to their short diffusion paths and higher specific surface areas. In this chapter, we focused on the development of smart design with different nanostructured morphologies onto FTO substrate to obtain a conducting additive-free and binder-less electrode for high-performance supercapacitors. Each sections were clearly discussed the motivation,

synthesis of nanostructure materials and investigation of potential application as electrodes in supercapacitors.

3.1. Synthesis and Electrochemical Performance of Vertically Aligned TiO₂ Nanorods

3.1.1. Introduction

TiO₂ is one of the most promising candidates because of its low cost, natural abundance, and environmental friendly nature. In recent years, titanium dioxide (TiO₂) have been used in various fields, such as pigments, self-cleaning, photochromic devices, sensors, dye-sensitized solar cells, lithium ion batteries, supercapacitor and especially used as photocatalyst to decompose organic contaminants from waste-water or air treatment [14-18]. Wang et al. [19] prepared TiO₂-B nanotubes by solvothermal reaction and the specific capacitance obtained was 17.7 F g⁻¹. Salari et al. [20] reported the TiO₂ nanotubes and TiO₂ nanopowder prepared by anodization and sol-gel techniques and the capacitance of 911 and 181 μF cm⁻² was obtained respectively at a scan rate of 1 mV s⁻¹. Lu et al. [21] synthesized hydrogenated TiO₂ nanotube arrays by anodic oxidation in a glycerol aqueous solution containing 0.75% NH₄F and the specific capacitance of H-TiO₂ and TiO₂ was 3.24 and 0.026 mF cm⁻² respectively at a scan rate of 100 mV s⁻¹. Salari et al. [22] reported that the self-organized TiO₂ nanotube array by anodic oxidation method with the specific capacitance of 19.2 F g⁻¹ at 1 mV s⁻¹. However, the specific capacitance and reversibility of these materials at higher current densities were not an ideal one.

Currently, researchers are mainly focused to enhance the electrochemical capacitance and stability of an electrode. The first approach is to develop the nanostructured electrodes with an extremely large surface area. One-dimensional

(1D) nanostructures (Nanotubes, nanowires, nanosheets, and mesoporous) with controlled size, shape, crystallinity and chemical composition could be considered in order to achieve the fast redox reactions, high surface area and short diffusion paths for electrons and ions than their bulk materials [23-29]. Therefore, much effort has been made to prepare 1D TiO₂ morphology. To the best of our knowledge, there are no reports on the capacitance of TiO₂ nanorod (NR) arrays. Vertically aligned TiO₂ NR arrays exhibited the high aspect ratio, chemical stability and high surface area facilitates the large number of ion transfer inside and/or outside of the electrode surface area.

In this section, we have demonstrated the vertically aligned TiO₂ Nanorod arrays as an electrode material prepared using a hydrothermal method for the supercapacitor applications. The structural and morphological information were obtained by XRD and FE-SEM. The electrochemical characterization of as-prepared electrodes were also examined using the cyclic voltammetry (CV), electrochemical impedance spectroscopy (EIS) and galvanostatic charge/discharge technique.

3.1.2. Experimental methods

3.1.2.1. Preparation of TiO₂ NR arrays by hydrothermal method

The rutile TiO₂ NR arrays were prepared by facile hydrothermal method using titanium tetra-n-butoxide and hydrochloric acid (HCl) as the precursors [30, 31]. The procedure to prepare TiO₂ NRs is as follows: Briefly, a 15 mL of deionized water was mixed with 15 mL of concentrated hydrochloric acid and allowed to vigorous stirring using Teflon coated magnetic bar for 5 min. After mixing the solution, 0.048M titanium tetra-n-butoxide was added to the mixture and stirred for another 30 min at room temperature. Then the solution mixture was transferred into a

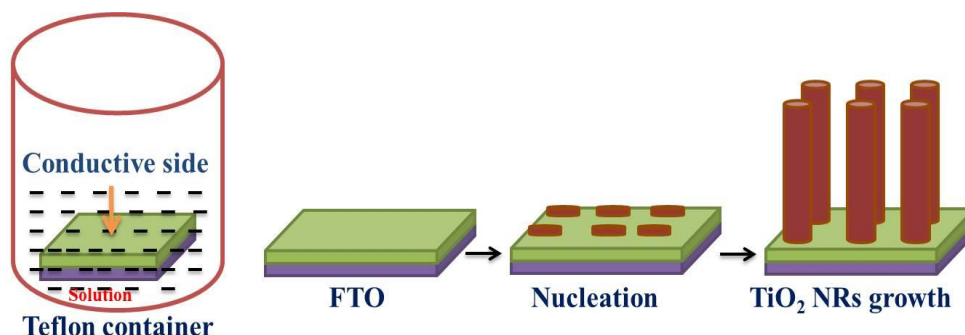
50 mL Teflon-lined stainless steel autoclave. A cleaned FTO glass was used as the substrate and was loaded into the same autoclave with the conducting side facing up position. Then, the autoclave was sealed and hydrothermally treated at 150 °C for 2 h in an electric oven. After synthesis, the Teflon reactor was cooled to room temperature naturally and then samples were taken out, rinsed extensively with deionized water and allowed to dry in ambient air. The as-prepared TiO₂ NR arrays were characterized by XRD, FT-IR, FE-SEM and EDX analysis.

3.1.2.2. Electrochemical characterization of TiO₂ NR arrays

The electrochemical experiments were investigated by using AUTOLAB PGSTAT302N electrochemical work station in 1 M Na₂SO₄ solution as an electrolyte. A typical three-electrode experimental cell equipped with a FTO glass coated with TiO₂ NR arrays served as the working electrode, a platinum foil as the counter electrode, and an Ag/AgCl as the reference electrode was used for measuring the electrochemical properties of working electrode. Cyclic voltammetry (CV) of the electrode was obtained at a different scan rates of 5, 10, 25, 50, 75, 100 and 125 mV s⁻¹ in the potential range of 0 to 0.8 V. Galvanostatic charge/discharge curves were measured in the potential range of 0 – 0.8 V at different current densities of 0.2, 0.3, 0.5 and 0.7 μA cm⁻². Electrochemical impedance spectroscopy (EIS) measurements were carried out at a dc bias of 0.1 V with a signal of 5 mV over the frequency range of 0.1 Hz to 100 kHz.

3.1.3. Results and discussion

3.1.3.1. Growth mechanism of TiO₂ NR arrays



Scheme 3.1.1 Schematic illustration of formation process of the vertically aligned TiO₂ nanorod arrays on the FTO substrate.

The possible growth mechanism of the vertically aligned TiO₂ NR arrays on FTO substrates (**Scheme 1**) as follows. Initially titanium tetra-n-butoxide was mixed with HCl solution at room temperature, titanium tetra-n-butoxide reacted with HCl and H₂O forming Ti⁴⁺. In the presence of FTO substrate, when the solution was heated, the Ti⁴⁺ precursors can hydrolyze with water at the interface of water/FTO substrate, resulting to the formation of a TiO₂ crystal nucleus. Then the nucleus grew vertically (TiO₂ nanorod arrays) with respect to the substrate surface with the continuous hydrolysis of Ti⁴⁺ precursor. In addition, HCl plays an important role throughout the synthesis process. Initially, the low pH value of the reaction solution delays the hydrolysis of Ti⁴⁺ precursor with water. Then the Cl⁻ ion can selectively adsorb onto the (110) crystal planes destroying further growth of the planes, ensuring the anisotropic growth along the (001) direction [32, 33]. Therefore, Cl⁻ could be a key factor for TiO₂ crystal growing along (001) direction to form a rod-like structure.

3.1.3.2. Structural properties of TiO₂ NR arrays

The crystal structure, purity and orientation of the as prepared TiO₂ NR arrays were examined by X-ray diffraction (XRD) pattern. **Figure 3.1.1a** shows the XRD pattern of TiO₂ NR arrays. It revealed that the NR arrays were crystallized in the tetragonal rutile phase with a preferred orientation of (002) plane at $2\theta = 62.31^\circ$. The observed data's are in a good agreement with the standard rutile phase TiO₂ (JCPDS card no: 21-1276). The other characteristics peaks found at 26.81° , 35.59° , 40.74° , 53.95° , and 69.44° , on the 2θ scale corresponds to the (110), (101), (111), (211), and (112), planes of rutile phase were also seen with comparatively lower intensities [34]. From **Figure 3.1.1a** asterisks symbol indicates the FTO substrate peaks. The sharp and narrow line width of the diffraction peaks suggests that the TiO₂ NR arrays have a high purity and high crystallinity. Furthermore, the predominant (002) peak indicates that TiO₂ NR arrays grow along with their c-axis orientation normal to the FTO glass surface during the hydrothermal process.

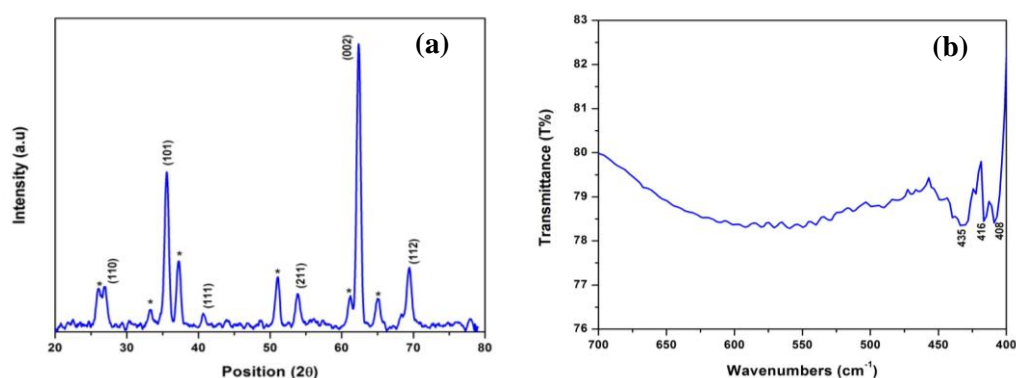


Figure 3.1.1 (a) XRD pattern of TiO₂ NR arrays synthesized by hydrothermal method (Peaks from the FTO substrate are indicated with asterisks symbol). (b) FT-IR spectrum of TiO₂ NR arrays.

FT-IR spectroscopy is an important technique for the direct monitoring of interaction between adsorbed molecules and the material. **Figure 3.1.1b** shows the

FT-IR spectrum of TiO₂ NR arrays. The spectrum was taken in the range of 400 to 1000 cm⁻¹. The absorption peaks at 408, 416 and 435 cm⁻¹ position correspond to the Ti-O vibration modes of rutile TiO₂ [35,36]. These bands are sharp and are having small intensity, which indicates the presence of rutile Ti-O bonds in the TiO₂ NR arrays. Thus the formation of rutile TiO₂ NR arrays is confirmed.

3.1.3.3. Morphological properties of TiO₂ NR arrays

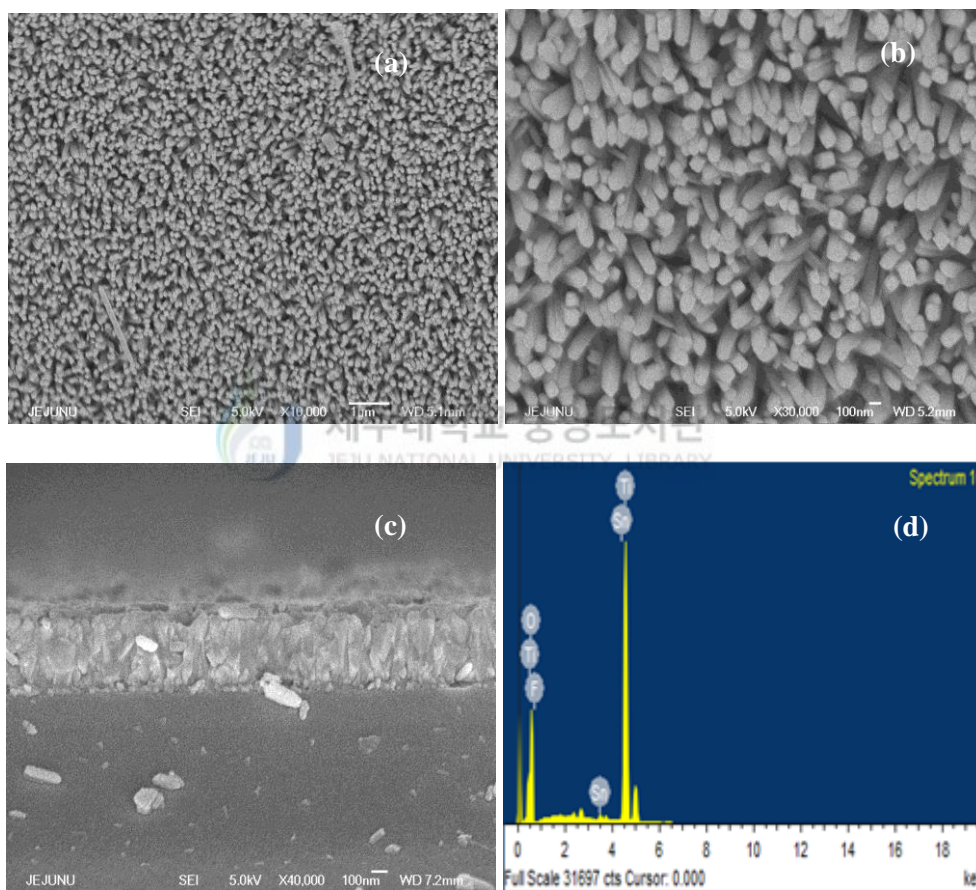


Figure 3.1.2 FE-SEM images of TiO₂ NR arrays with different magnification. (a-b) top view, (c) cross-sectional view and (d) EDS spectrum of TiO₂ NR arrays.

The general morphology of the as-synthesized TiO₂-NR arrays was examined by FE-SEM, which reveals that the obtained film have vertically aligned nanorod structures and are grown on FTO coated glass substrate at a high density. The FE-SEM images are taken at different locations and magnifications reveal that the whole

surface of the FTO glass substrate is covered uniformly and densely with TiO₂ nanorods. **Figure 3.1.2a and b** are the top-view of the aligned TiO₂ NRs. It can be seen that the obtained nanorods have a perfect tetragonal crystal structure and smooth facets on the top. **Figure 3.1.2c** is the cross-sectional view of the aligned TiO₂ NR arrays. It reveals that the sides of the TiO₂ nanorods are relatively smooth, vertically oriented and well-aligned on the surface of FTO substrate. The average size of the TiO₂ NRs is ~60-70 nm in width and 0.5 μm in uniform length. These results indicate an excellent adherence and connection between TiO₂ NRs and FTO substrate and it can be used for the growth of large quantities of single crystalline tetragonal-faceted surface with well-aligned TiO₂ nanorod arrays for supercapacitor electrode material. The EDS spectrum of the TiO₂ NR arrays is shown in **Figure 3.1.2d**. The chemical composition of TiO₂ NR arrays was found to be 1% for F, 1.5% for Sn, 57.5% for O and 40% for Ti.

3.1.3.4. Electrochemical characterization

The vertically aligned TiO₂ NR arrays were used as an electrode material for an electrochemical supercapacitor and its performance was tested using the cyclic voltammetry (CV), electrochemical impedance spectroscopy (EIS) and galvanostatic charge/discharge techniques. **Figure 3.1.3a** shows the CV curve of TiO₂ NR at a scan rate of 125 mVs⁻¹ in 1M Na₂SO₄ solution in the potential window of 0 to 0.8 V. The curve exhibits a quasi-rectangular shape, indicating an ideal capacitive behavior. Capacitance performance of the as prepared electrode was further used for the detailed measurements. **Figure 3.1.3b** shows the CV curves of TiO₂ NR electrode at the different scan rates of 5, 10, 25, 50, 75, 100 and 125 mV s⁻¹. All the CV curves are close to rectangular shape. In addition, the linear increase of the current with

increasing scan rate indicates that the charge is primarily non-faradic in nature. The specific capacitance (C_s), of the electrode was calculated using the equation (2.7). The calculated C_s of TiO_2 NR electrode at a scan rate of 5 mV s^{-1} is $85 \mu\text{Fcm}^{-2}$ (8.5 F g^{-1}).

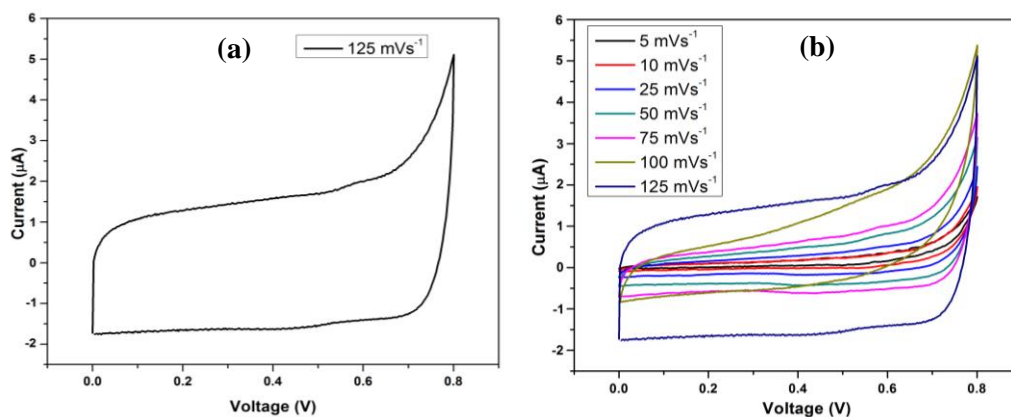


Figure 3.1.3 (a) Cyclic voltammogram curve of TiO_2 NR film at scan rate of 125 mVs^{-1} in $1\text{M Na}_2\text{SO}_4$ electrolyte solution. (b) Cyclic voltammogram curves of TiO_2 NR films at different scan rate from 5 to 125 mVs^{-1} in $1\text{M Na}_2\text{SO}_4$ solution.

The charge–discharge behavior of the TiO_2 NRs electrode was examined by galvanostatic charge–discharge method at a constant current density of $0.5 \mu\text{A cm}^{-2}$ in the potential range from 0 and 0.8 V . **Figure 3.1.4a** shows the typical galvanostatic charge–discharge curve of TiO_2 NRs electrode. It can be seen that the entire curve is linear and symmetrical, which indicates that the electrode has an ideal capacitive characteristics and excellent electrochemical reversibility. **Figure 3.1.4b** shows the typical galvanostatic charge/discharge curves of TiO_2 NR electrode at the different current densities of $0.2, 0.3, 0.5,$ and $0.7 \mu\text{A cm}^{-2}$. The specific capacitance of the electrode can also be calculated from the galvanostatic charge/discharge curve at different current densities using the equation (2.8) [21]. The specific capacitances of the vertically aligned TiO_2 NR arrays electrode are $47, 36, 23,$ and $21 \mu\text{F cm}^{-2}$ at

constant current densities of 0.2, 0.3, 0.5, and 0.7 $\mu\text{A cm}^{-2}$, respectively. As expected, the specific capacitance decreases with the increasing current density.

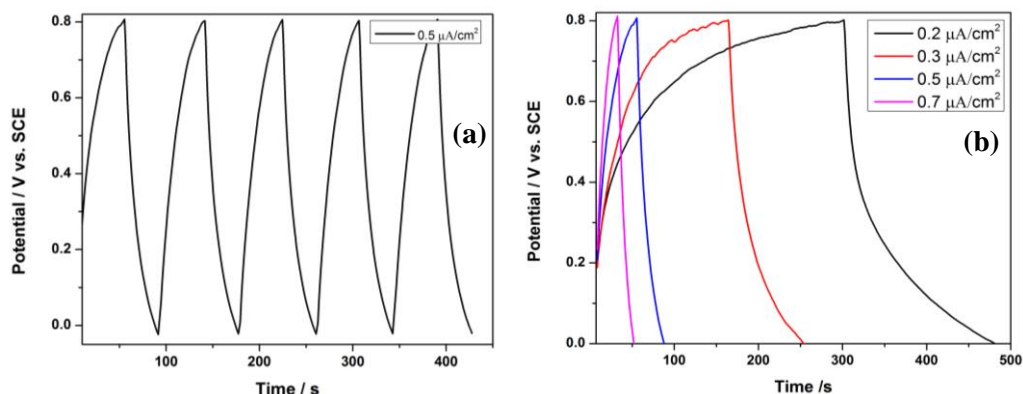


Figure 3.1.4 (a) Galvanostatic charge/discharge curve of TiO₂ NR films at 0.5 $\mu\text{A cm}^{-2}$ and (b) Galvanostatic charge/discharge curve of TiO₂ NR arrays at different current densities.

The electrochemical parameters such as energy density (E), power density (P) and coulomb efficiency ($\eta\%$) as an important parameters for the investigation of the capacitive behavior of electrochemical cells. The energy density, power density and coulomb efficiency can be calculated from the equations (2.4, 2.5, and 2.6). The calculated energy density, power density and energy efficiency of the electrode materials was 0.22 Wh kg^{-1} , 20 W kg^{-1} and 87%, respectively.

The long term cycle stability is an important parameter of supercapacitor for their practical applications. The cycle stability of the TiO₂ NRs electrode was also evaluated in this study by repeating the CV measurements between 0 to 0.8 V at a scan rate of 150 mV s^{-1} for 1000 cycles. The capacitance retention ratio as a function of cycle number is shown in **Figure 3.1.5a**. The electrode is found to exhibit excellent long cycle life over the entire cycle numbers. The capacitance decreases by 20% of the initial capacitance even after 1000 cycles, indicates a good cycling life of the electrode materials.

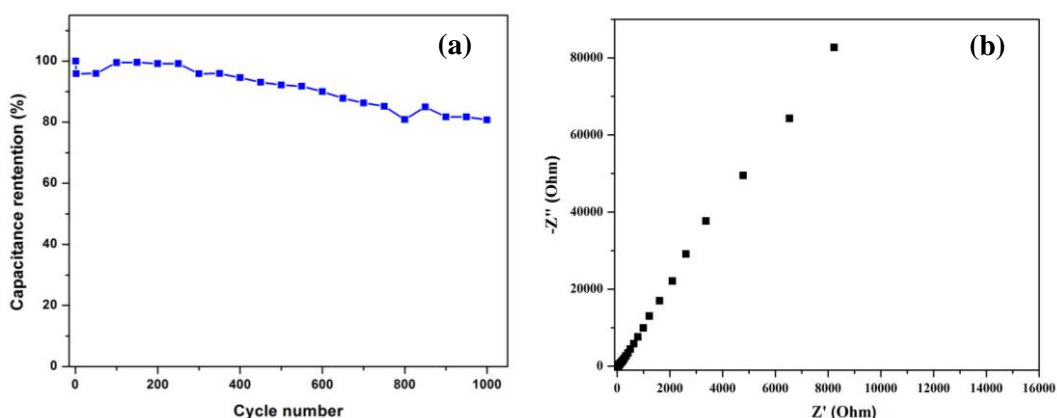


Figure 3.1.5 (a) Variation of the specific capacitance of TiO₂ NRs electrode as a function of cycle number measured at 150 mV s⁻¹ in 1 M Na₂SO₄ aqueous solution, and (b) Nyquist plot of TiO₂ NR films in 1M Na₂SO₄ electrolyte solution.

The electrochemical impedance spectroscopy is a powerful technique used to study the fundamental capacitive behavior of electrode materials for supercapacitor applications. The EIS measurements were carried out at the open-circuit potential in the frequency range of 0.1 Hz to 100 kHz with an ac perturbation of 10 mV. The EIS data were analyzed using Nyquist plots, which show the frequency response of the electrode/electrolyte system and are plotted using the data of the imaginary component ($-Z''$) of the impedance against the real component (Z'). **Figure 3.1.5b** shows the Nyquist plot of the TiO₂ NRs in 1M Na₂SO₄ electrolyte solution. The impedance plot is composed of a semicircle arc in the high frequency region followed by a relative linear response in the low frequency region. The high frequency region corresponds to the charge transfer limiting process and is ascribed to the double-layer capacitance (C_{dl}) in parallel with the charge transfer resistance (R_{ct}) at the contact interface structure between electrode surface and electrolyte solution [37]. However, as shown in **Figure 3.1.5b**, no semicircle arc was observed in the TiO₂ NRs electrode, which indicates that the charge transfer of these working electrodes is good enough to be used for electrochemical supercapacitor applications

and there is virtually no indication of electrical resistance. The linear part in the low frequency region is related to the Warburg resistance (diffusive resistance) of the electrolyte into the interior of the electrode surface and an ion diffusion/transport into the electrode surface. On the other hand, a line almost vertical to the real axis in the imaginary part of the impedance at the low-frequency region, representing the swift ion diffusion in electrolyte and the adsorption onto the electrode surface, suggested an ideal capacitive behavior of the electrodes [20].

From these results, we have demonstrated that the 1-D vertically aligned TiO₂ nanorods have many advantages such as high surface area, increased number of delocalized carriers, and an improved charge transport properties compared to the spherical nanoparticles in terms of their potential applications [38, 39]. Vertically aligned TiO₂ NR arrays offers the direct electron transfer pathways compared to the nanoparticles, which significantly increases the interparticle contact. Therefore, it can be concluded that the high surface area and highly active surface site will enhance the ion diffusion, charge transfer and capacitance values [40]. Further, the proposed vertically grown TiO₂ NR arrays are environmental friendly and low-cost, which could be used as an electrode material for high performance supercapacitor applications.

3.1.4. Conclusion

In summary, the vertically aligned TiO₂ NR arrays have been successfully prepared by a simple, green and inexpensive hydrothermal method and employed as a supercapacitor electrode. XRD and FT-IR results confirmed that the phase purity and nanocrystalline formation of TiO₂ NR arrays. FE-SEM image showed the TiO₂ NRs appears to be uniform, homogeneous, vertical oriented and well-aligned on FTO

substrate. The electrochemical tests showed that the as prepared TiO₂ NR electrode exhibited an ideal capacitive behavior with a maximum specific capacitance of 85 $\mu\text{F cm}^{-2}$ in 1M Na₂SO₄ solution at a scan rate of 5 mV s⁻¹. In addition, this electrode showed a good reversibility with 80% of capacitance retention even after 1000 cycles. These results demonstrate that hydrothermally prepared TiO₂ NR is good candidate and more attractive electrode material for the commercial supercapacitor applications.

3.1.5. References

- [1] M. Zhi, C. Xiang, J. Li, M. Li, and N. Wu, Nanostructured carbon–metal oxide composite electrodes for supercapacitors: a review. *Nanoscale* 5 (2013) 72-88.
- [2] S. Bose, T. Kuila, A. K. Mishra, R. Rajasekar, N. H. Kim and J. H. Lee, Carbon-based nanostructured materials and their composites as supercapacitor electrode. *J. Mater. Chem.* 22 (2012) 767-784.
- [3] L. L. Zhang, and X. S. Zhao, Carbon-based materials as supercapacitor electrodes. *Chem. Soc. Rev.* 38 (2009) 2520-2531.
- [4] X. Zhao, B. M. Sánchez, Peter J. Dobson, and Patrick S. Grant, The role of nanomaterials in redox-based supercapacitors for next generation energy storage devices. *Nanoscale*, 3 (2011) 839-855.
- [5] G. Wang, L. Zhang, and J. Zhang, A review of electrode materials for electrochemical supercapacitors. *Chem. Soc. Rev.* 41 (2012) 797-828.
- [6] M. C. Liu, L. B. Kong, C. Lu, X. J. Ma, X. M. Li, Y.C. Luo, and L. Kang, Design and synthesis of CoMoO₄–NiMoO₄·xH₂O bundles with improved

- electrochemical properties for supercapacitors. *J. Mater. Chem. A*, 1 (2013) 1380–1387.
- [7] C.-C. Hu, K.-H. Chang, M.-C. Lin and Y.-T. Wu, Design and tailoring of the nanotubular arrayed architecture of hydrous RuO_2 for next generation supercapacitors. *Nano Lett.* 6 (2006) 2690–2695.
- [8] S. Makino, Y. Yamauchi, and W. Sugimoto, Synthesis of electro-deposited ordered mesoporous RuO_x using lyotropic liquid crystal and application toward micro-supercapacitors. *J. Power Sources* 227 (2013) 153-160.
- [9] Q. Zhang and G. Cao, Nanostructured photoelectrodes for dye-sensitized solar cells. *Nano Today* 6 (2011) 91–109.
- [10] C. Cheng and H. J. Fan, Branched nanowires: Synthesis and energy applications. *Nano Today* 7 (2012) 327–343.
- [11] A. L. Reddy, S. R. Gowda, M. M. Shaijumon and P. M. Ajayan, Hybrid nanostructures for energy storage applications. *Adv. Mater.* 24 (2012) 5045–5064.
- [12] S. Campagna, Energy production and storage. Inorganic chemistry strategies for a warming world. Edited by Robert H. Crabtree. *Angew. Chem. Int. Ed.* 50 (2011) 8471–8472.
- [13] S. W. Lee, B. M. Gallant, H. R. Byon, P. T. Hammond and Y. Shao-Horn, Nanostructured carbon-based electrodes: bridging the gap between thin-film lithium-ion batteries and electrochemical capacitors. *Energy Environ. Sci.* 4 (2011) 1972–1985.

- [14] T. Brezesinski, J. Wang, J. Polleux, B. Dunn, and S. H. Tolbert, Templated nanocrystal-based porous TiO₂ films for next-generation electrochemical capacitors. *J. Am. Chem. Soc.* 131 (2009) 1802–1809.
- [15] P. Xiao, D. Liu, B. B. Garcia, S. Sepehri, Y. Zhang, and G. Cao, Electrochemical and photoelectrical properties of titania nanotube arrays annealed in different gases. *Sens. Actuators B* 134 (2008) 367–372.
- [16] G. Li, C. P. Richter, R. L. Milot, L. Cai, C. A. Schmittenmaer, R. H. Crabtree, G. W. Brudvig, and V. S. Batista, Synergistic effect between anatase and rutile TiO₂ nanoparticles in dye-sensitized solar cells. *Dalton Trans.* 45 (2009) 10078–10085.
- [17] C. S. Guo, M. Ge, L. Liu, G. D. Gao, Y. C. Feng and Y. Q. Wang, Directed synthesis of mesoporous TiO₂ microspheres: catalysts and their photocatalysis for bisphenol a degradation. *Environ. Sci. Technol.* 44 (2010) 419-425.
- [18] J. G. Yu, W. G. Wang, B. Cheng and B. L. Su, Enhancement of photocatalytic activity of mesoporous TiO₂ powders by hydrothermal surface fluorination treatment. *J. Phys. Chem. C* 113 (2009) 6743-6750.
- [19] G. Wang, Z.Y. Liu, J.N. Wu and Q. Lu, Preparation and electrochemical capacitance behavior of TiO₂-B nanotubes for hybrid supercapacitor. *Mater. Lett.* 71 (2012) 120-122.
- [20] M. Salari, S. H. Aboutalebi, K. Konstantinov and H.K. Liu, A highly ordered titania nanotube array as a supercapacitor electrode. *Phys. Chem. Chem. Phys.* 13 (2011) 5038–5041.

- [21] X. Lu, G. Wang, T. Zhai, M. Yu, J. Gan, Y. Tong and Y. Li, Hydrogenated TiO₂ nanotube arrays for supercapacitors. *Nano Lett.* 12 (2012) 1690–1696.
- [22] M. Salari, S. H. Aboutalebi, A. T. Chidembo, I. P. Nevirkovets, K. Konstantinov, and H. K. Liu, Enhancement of the electrochemical capacitance of TiO₂ nanotube arrays through controlled phase transformation of anatase to rutile. *Phys. Chem. Chem. Phys.* 14 (2012) 4770–4779.
- [23] M. Kaempgen, C. K. Chan, J. Ma, Y. Cui and G. Gruner, Printable thin film supercapacitors using single-walled carbon nanotubes. *Nano Lett.* 9 (5) (2009) 1872–1876.
- [24] X. H. Lu, D. Z. Zheng, T. Zhai, Z. Q. Liu, Y. Y. Huang, S. L. Xie and T. Y.X. Tong, Facile synthesis of large-area manganese oxide nanorod arrays as a high-performance electrochemical supercapacitor. *Energy Environ. Sci.* 4 (8) (2011) 2915–2921.
- [25] X. H. Xia, J. P. Tu, Y. J. Mai, X. L. Wang, C. D. Gu, and X. B. Zhao, Self-supported hydrothermal synthesized hollow Co₃O₄ nanowire arrays with high supercapacitor capacitance. *J. Mater. Chem.* 21 (2011) 9319–9325.
- [26] D. Feng, Y. Y. Lv, Z. X. Wu, Y. Q. Dou, L. Han, Z. K. Sun, Y. Y. Xia, G. F. Zheng, and D. Y. Zhao, Free-standing mesoporous carbon thin films with highly ordered pore architectures for nanodevices. *J. Am. Chem. Soc.* 133 (38) (2011) 15148–15156.
- [27] H. Jiang, L. Yang, C. Li, C. Yan, P. S. Lee, and J. Ma, High-rate electrochemical capacitors from highly graphitic carbon-tipped manganese oxide/mesoporous carbon/manganese oxide hybrid nanowires. *Energy Environ. Sci.* 4 (2011) 1813-1819.

- [28] S. J. Guo, S. J. Dong and E. K. Wang, Constructing carbon-nanotube/metal hybrid nanostructures using homogeneous TiO₂ as a spacer. *Small* 4 (2008) 1133-1138.
- [29] H. Jiang, T. Zhao, J. Ma, C. Y. Yan and C. Z. Li, Ultrafine manganese dioxide nanowire network for high-performance supercapacitors. *Chem. Commun.* 47 (2011) 1264-1266.
- [30] B. Liu and E.S. Aydil, Growth of oriented single-crystalline rutile TiO₂ nanorods on transparent conducting substrates for dye-sensitized solar cells. *J. Am. Chem. Soc.* 131 (2008) 3985-3990.
- [31] Y. Zhao, X. Gu and Y. Qiang, Influence of growth time and annealing on rutile TiO₂ single-crystal nanorod arrays synthesized by hydrothermal method in dye-sensitized solar cells. *Thin Solid Films* 520 (2012) 2814–2818.
- [32] J. H. Bang and P. V. Kamat, Solar Cells by Design: Photoelectrochemistry of TiO₂ nanorod arrays decorated with CdSe. *Adv. Funct. Mater.* 20 (2010) 1970–1976.
- [33] A. Moses Ezhil Raj, V. Agnes, V. Bena Jothy and C. Sanjeeviraja, Low temperature TiO₂ rutile phase thin film synthesis by chemical spray pyrolysis (CSP) of titanyl acetylacetonate. *Mater. Sci. Semiconduct. Proces.* 13 (2010) 389-394.
- [34] A. Sadeghzadeh Attar, Sh. Mirdamadi, F. Hajiesmaeilbaigi and M. Sasani Ghamsai, Growth of TiO₂ nanorods by sol-gel template process. *J. Mater. Sci. Technol.* 23 (2007) 611-613.
- [35] M. Adachi, Y. Murata, J. Takao, J. T. Jiu, M. Sakamoto and F. M. Wang, Highly efficient dye-sensitized solar cells with a titania thin-film electrode

- composed of a network structure of single-crystal-like TiO₂ nanowires made by the “oriented attachment” mechanism. *J. Am. Chem. Soc.* 126 (2004) 14943-14949.
- [36] J. Cai, J. Ye, S. Chen, X. Zhao, D. Zhang, S. Chen, Y. Ma, S. Jin, and L. Qi, Self-cleaning, broadband and quasi-omnidirectional antireflective structures based on mesocrystalline rutile TiO₂ nanorod arrays. *Energy Environ. Sci.* 5 (2012) 7575-7581.
- [37] K.K. Liu, Z.L. Hu, R. Xue, J.R. Zhang, and Z.J. Zhu, Electropolymerization of high stable poly(3,4-ethylenedioxythiophene) in ionic liquids and its potential applications in electrochemical capacitor. *J. Power Sources* 179 (2008) 858-862.
- [38] P. D. Cozzoli, A. Kornowski, and H. Weller, Low-temperature synthesis of soluble and processable organic-capped anatase TiO₂ nanorods. *J. Am. Chem. Soc.* 125 (2003) 14539-14548.
- [39] B. Koo, J. Park, Y. Kim, S. H. Choi, Y. E. Sung, and T. Hyeon. Simultaneous phase- and size-controlled synthesis of TiO₂ Nanorods via non-hydrolytic sol–gel reaction of syringe pump delivered precursors. *J. Phys. Chem. B* 110 (2006) 24318-24323.
- [40] B. Xu, F. Wu, R. Chen, G. Cao, S. Chen, Z. Zhou, and Y. Yang, Highly mesoporous and high surface area carbon: A high capacitance electrode material for EDLCs with various electrolytes. *Electrochem. Commun.* 10 (2008) 795–797.

3.2. Synthesis and Electrochemical Performance of TiO₂@MnO₂ Core-Shell Nanostructure

3.2.1. Introduction

Among the different transition metal oxides, manganese dioxide (MnO₂) and titanium dioxide (TiO₂) have been considered as potential pseudocapacitive materials, due to their low cost, low toxicity, natural abundance, and environmentally friendly nature [1-6]. Over the past few years, various manganese oxide nanomaterials with controlled morphologies and structures have been prepared as supercapacitor electrodes [7-11]. However, the specific capacitances are still far smaller than the theoretical value (1370 F g⁻¹) of manganese oxides. In particular, the poor electrical conductivity of manganese oxides results in the compromise of rate capability, largely limiting their applications in high-power supercapacitors [12]. In contrast, TiO₂ has higher electrical conductivity and electrochemical stability compared with MnO₂ [5]. In order to address these problems, designing complex nanoscale architectures with a combination of two types of materials and/or structures on a conducting substrate as binder-free electrodes is of much interest for improved electrochemical performance.

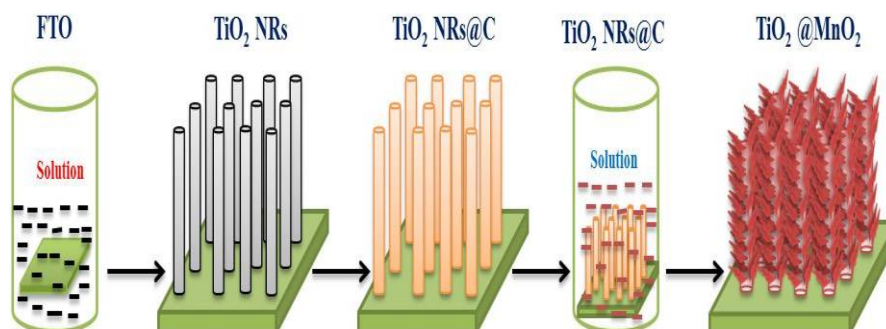
Recently, one-dimensional (1-D) and three-dimensional (3-D) architectures fabricated on conductive substrates have exhibited enhanced electrochemical performance, compared with their two-dimensional (2-D) counterparts, due to their larger surface area, and increased electroactive sites within a small footprint. Additionally, the nanostructure directly in contact with the current collector could serve as an easy path for fast ion and electron transport reactions, resulting in a reduced internal resistance and improved pseudocapacitive performance [5, 13-21].

A promising method to further enhance the capacitance and structural stability, is the integration of different active materials into self-supported core/shell nanoarray architectures [22, 23]. This hybrid core-shell structure utilizes the positive features of individual materials and may provide a combined synergistic effect, such as high capacitance, and long cycle life. Based on the above considerations, various core-shell nanoarchitectures with different morphological forms have been developed as electrodes for supercapacitors, including multi-walled carbon nanotubes as the core and graphene oxide nanoribbons (MWCNT@GONR) [24], CNT@RuO₂ [25], Co₃O₄@MnO₂ [26], SnO₂@MnO₂ [27], NiCo₂O₄@MnO₂ [28], Zn₂SnO₄@MnO₂ [29], ZnO@MnO₂ [7], TiO₂@MnO₂ [30], Co₃O₄@Au@MnO₂ [31], Co₃O₄@Pt@MnO₂ [32], CoO@NiHON [33], Fe₂O₃@MnO₂ [34], and WO_{3-x}@Au@MnO₂ [35]. However, the ultimate challenge facing researchers today is the design and fabrication of smart architectures to enhance fast-ion and electron transport, as well as electroactivity.

In this chapter, we describe the fabrication of a self-supported TiO₂@MnO₂ core-shell array electrode, using sacrificial reactive 3-D carbon template layers via a simple, green, low-cost, hydrothermal method. Here, the TiO₂ nanorod (NR) acts as a backbone for MnO₂ nanowall growth. The as-prepared TiO₂@MnO₂ core-shell electrode exhibited a high areal capacitance with long cycling stability in a 1-M Na₂SO₄ solution. Further, due to the intrinsic semiconductor nature of TiO₂ nanomaterials, it may be possible to further increase the electrical conductivity of TiO₂ NR array supported core-shell electrodes for more effective ion diffusion and electron transfer, and energy and power density enhancement.

3.2.2. Experimental methods

3.2.2.1. Preparation of $\text{TiO}_2@\text{MnO}_2$ core-shell nanostructures



Scheme 3.2.1 Schematic diagram illustrating the synthesis procedure of a $\text{TiO}_2@\text{MnO}_2$ core-shell array electrode on a fluorine-doped tin oxide (FTO) substrate.

A schematic illustration of the $\text{TiO}_2@\text{MnO}_2$ core-shell electrode fabrication process is shown in **Scheme 3.2.1**. First, TiO_2 NR arrays were grown on a fluorine-doped tin oxide (FTO) substrate, using a simple hydrothermal method (**Scheme 3.2.1**) [4]. The detail procedure was discussed in **Chapter 3.1**. To prepare a carbon modified TiO_2 NR array, the as-prepared NR arrays were dispersed into a 0.04 M aqueous glucose solution for 24 h, followed by carbonization at 450 °C in pure Ar gas for 3 h. Finally, to fabricate the $\text{TiO}_2@\text{MnO}_2$ core-shell nanowall structure, the carbon coated TiO_2 NR arrays were placed in a 0.03 M KMnO_4 solution in a sealed Teflon-lined stainless steel autoclave at 160 °C for 6, 8, and 10 h, using an electric oven. After synthesis, the Teflon reactor was cooled to room temperature. The samples were removed, rinsed extensively with deionized water and dried at 60 °C in a hot air oven to obtain the $\text{TiO}_2@\text{MnO}_2$ core-shell nanostructure. The geometrical area of the $\text{TiO}_2@\text{MnO}_2$ core-shell nanostructure coated surface is 1 x 1 cm². The $\text{TiO}_2@\text{MnO}_2$ core-shell nanostructure was characterized by using XRD, Raman, FE-SEM, TEM, EDS and XPS analysis.

3.2.2.2. Electrochemical measurements

The electrochemical properties of the electrodes were evaluated using cyclic voltammetry (CV), electrochemical impedance spectroscopy (EIS), and galvanostatic charge/discharge (GCD) testing, using an AUTOLAB PGSTAT302N electrochemical work station in a 1-M Na₂SO₄ electrolyte solution. The electrochemical studies of the electrodes were performed in a three electrode cell equipped with a working electrode, a counter electrode (platinum), and a reference electrode (Ag/AgCl). The CV measurement was carried out over a voltage range of 0 to 0.8 V at different scan rates ranging from 5 - 125 mV s⁻¹. The GCD tests were conducted in the potential range of 0 - 0.8 V at current densities ranging from 0.01 to 0.1 mA cm⁻². The EIS measurement was measured in the frequency range of 0.1 Hz to 100 kHz with an open-circuit potential and alternating current (AC) amplitude of 10 mV.

3.2.3. Results and discussion

The fabrication process for the TiO₂@MnO₂ core-shell nanostructure on the FTO substrate involved three steps, as illustrated in **Scheme 3.2.1**. First, vertically aligned TiO₂ NR arrays were grown on FTO via the simple hydrothermal method. In the second step, the as-grown TiO₂ NR arrays were subjected to immersion in a glucose solution, followed by post-annealing in Ar gas; this created a uniform amorphous carbon-layer coating on the NR surface. Finally, the MnO₂ outer shell layer was grown via a hydrothermal method, forming a TiO₂@MnO₂ core-shell nanostructure as the final product. The purpose of an amorphous carbon-layer coating on the TiO₂ NR surface is the formation of an interfacial reactive template for growing MnO₂ nanostructures [26]. In the absence of an amorphous carbon layer, it is difficult to grow a MnO₂ layer on the TiO₂ NR array surface. The reaction

between carbon and KMnO_4 could lead to *in situ* formation of porous ultrathin MnO_2 nanowalls on the TiO_2 NR array surface, based on the following reaction [36, 37]:



The above reaction shows that MnO_2 can be produced by the green reaction between KMnO_4 and carbonaceous materials, in the absence of any acid or base. Additionally, we extended this reaction to a 3-D ordered interface, using an amorphous carbon layer. Finally, the carbon layer confined the MnO_2 growth reaction on the NR surface, giving rise to a well-constructed 3-D hierarchical nanostructure. Hereafter, the as-prepared 6-, 8-, and 10-h core-shell nanostructure samples are referred to as TM-1, TM-2, and TM-3, respectively.

3.2.3.1. Structure, morphology and composition analysis

The crystalline phase of the as-prepared TiO_2 NRs, and TM-1, TM-2, and TM-3 core-shell nanostructures was characterized by XRD. The XRD pattern of bare TiO_2 NRs were fitted to the rutile phase of TiO_2 (JCPDS card no: 21-1276, denoted as ‘*’) and indexed, as shown in **Figure 3.2.1a**. Further, the core-shell nanostructure (MnO_2 rich; TM-3) confirmed the existence of the tetragonal phase MnO_2 (JCPDS card no: 65-2821, denoted as ‘#’) and rutile TiO_2 . The positions of the three main peaks at 27.3° , 36.1° , 62.7° and 69.8° corresponded to the (110), (101), (002), and (112) planes of the rutile phase. The other 2θ diffraction peaks at 38.3° , 41.2° and 68.8° corresponded to the (110), (200), and (310) planes of the tetragonal phase of MnO_2 . The symbol ‘s’ in the figure denotes the FTO substrate peaks. Due to the strong, sharp diffraction peaks of the FTO substrate, the other diffraction peaks corresponding to MnO_2 and TiO_2 were suppressed.

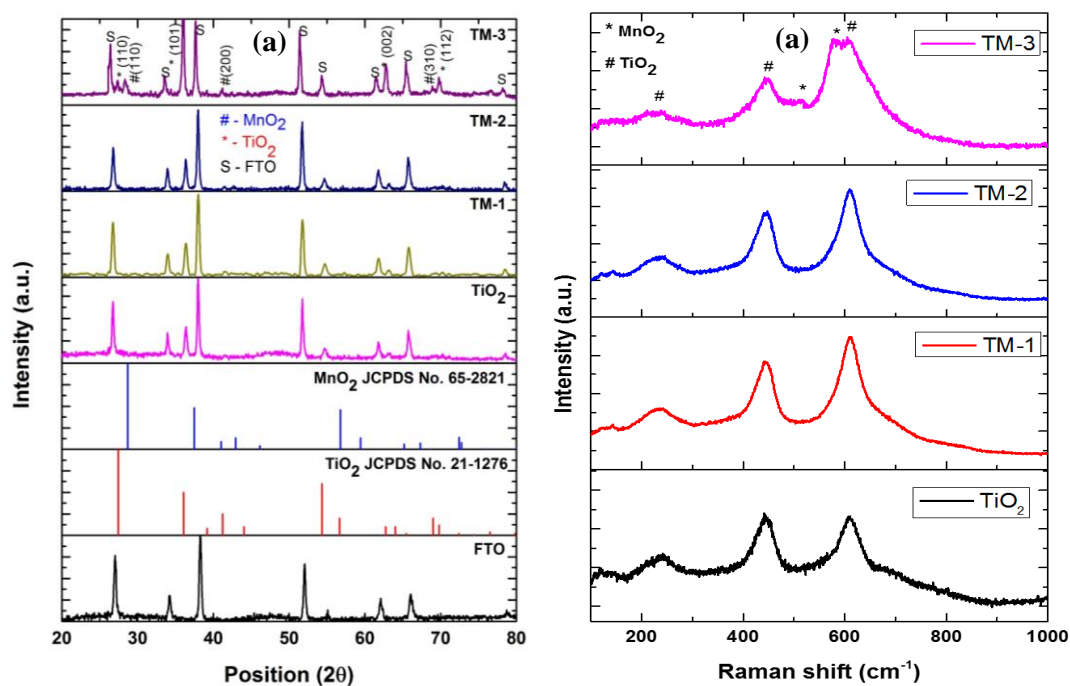


Figure 3.2.1 (a) X-ray diffraction (XRD) patterns of FTO, TiO₂ nanorod (NR) arrays, and TM-1, TM-2 and TM-3 core-shell nanostructures. TM-1, TM-2, and TM-3 correspond to the as- prepared 6-, 8-, and 10-h core-shell nanostructure samples. (b) Raman spectra of TiO₂ NR arrays, and TM-1, TM-2, and TM-3 core-shell nanostructures.

Raman spectroscopy was performed on the TiO₂ nanorod, and TM-1, TM-2, and TM-3 core-shell nanostructure samples, as shown in **Figure 3.2.1b**. The main peaks observed at 238, 445, and 615 cm⁻¹ (denoted as # in the **Figure 3.2.1b**) corresponded to a multi-photon process, E_g and the A_{1g} vibrational modes of rutile phase TiO₂, respectively [38]. The other Raman peaks appearing at 517 and 518 cm⁻¹ (denoted as * in the **Figure 3.2.1b**) in the TM-3 core-shell nanostructure sample were assigned to the oxygen vibrations of the tunnel -MnO₂ structure [39, 40]. The morphological properties of the as-fabricated electrodes were analyzed using FE-SEM at various magnifications, as shown in **Figure 3.2.2**. The vertically aligned TiO₂ NR arrays were uniformly grown on the FTO substrate (**Figure 3.2.2a and 3.2.2b**). The average diameters of the TiO₂ NR arrays were estimated to be 80-100

nm. **Figure 3.2.2c-3.2.3h** show the typical morphology of the TiO₂@MnO₂ (TM-1, TM-2, and TM-3) core-shell nanostructures. The MnO₂ nanowall shell uniformly covered the TiO₂ NR surface, forming a highly porous nanostructure morphology. After, MnO₂ nanowall growth on the TiO₂ NR surface, the diameter of the NR increased to ~150 nm. From this, we confirmed that the loading amount of MnO₂ (the shell thickness of the thin layer of MnO₂ on the TiO₂@MnO₂ core-shell nanostructure) increased (TM-3 > TM-2 > TM-1); this increase in layer thickness can be tailored by varying the deposition time of MnO₂.

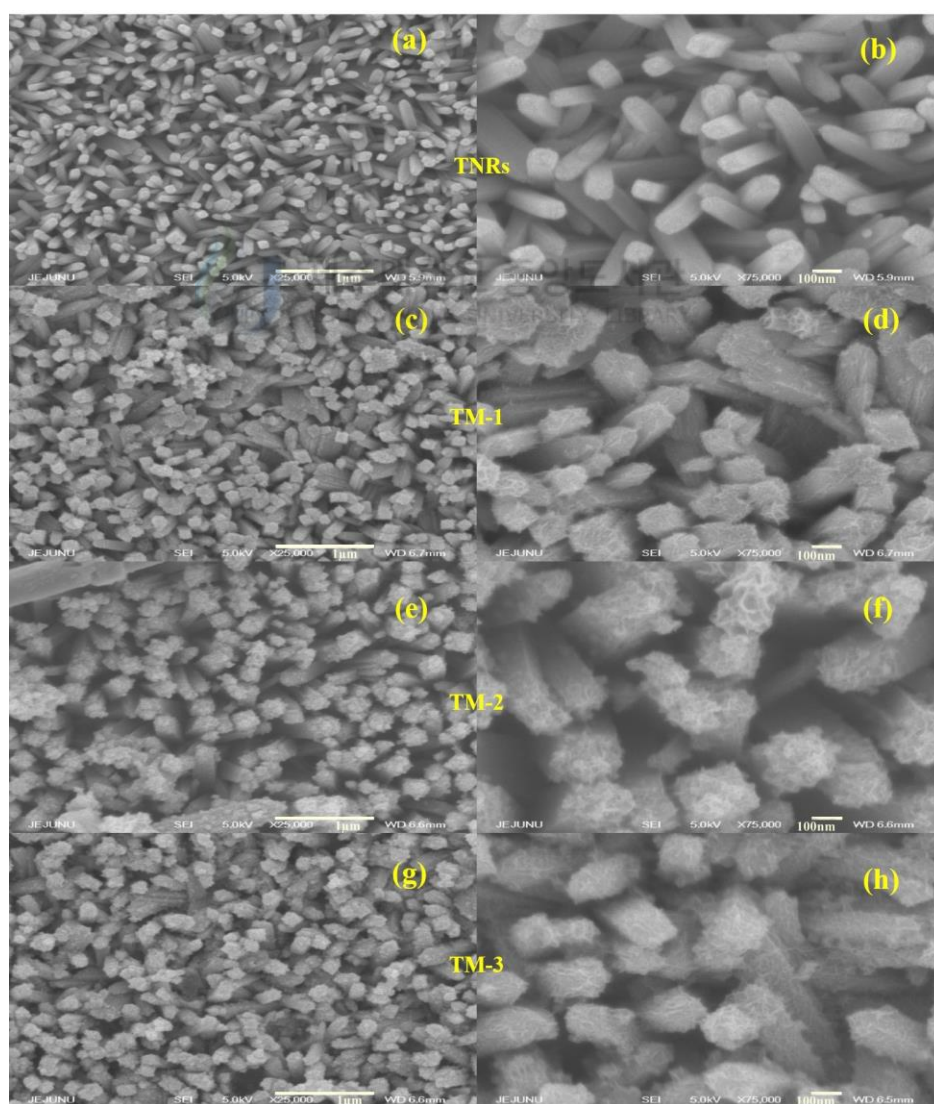


Figure 3.2.2 FE-SEM images of (a, b) TiO₂ NR arrays, and (c, d) TM-1, (e, f) TM-2 and (g-h) TM-3 core-shell nanostructures.

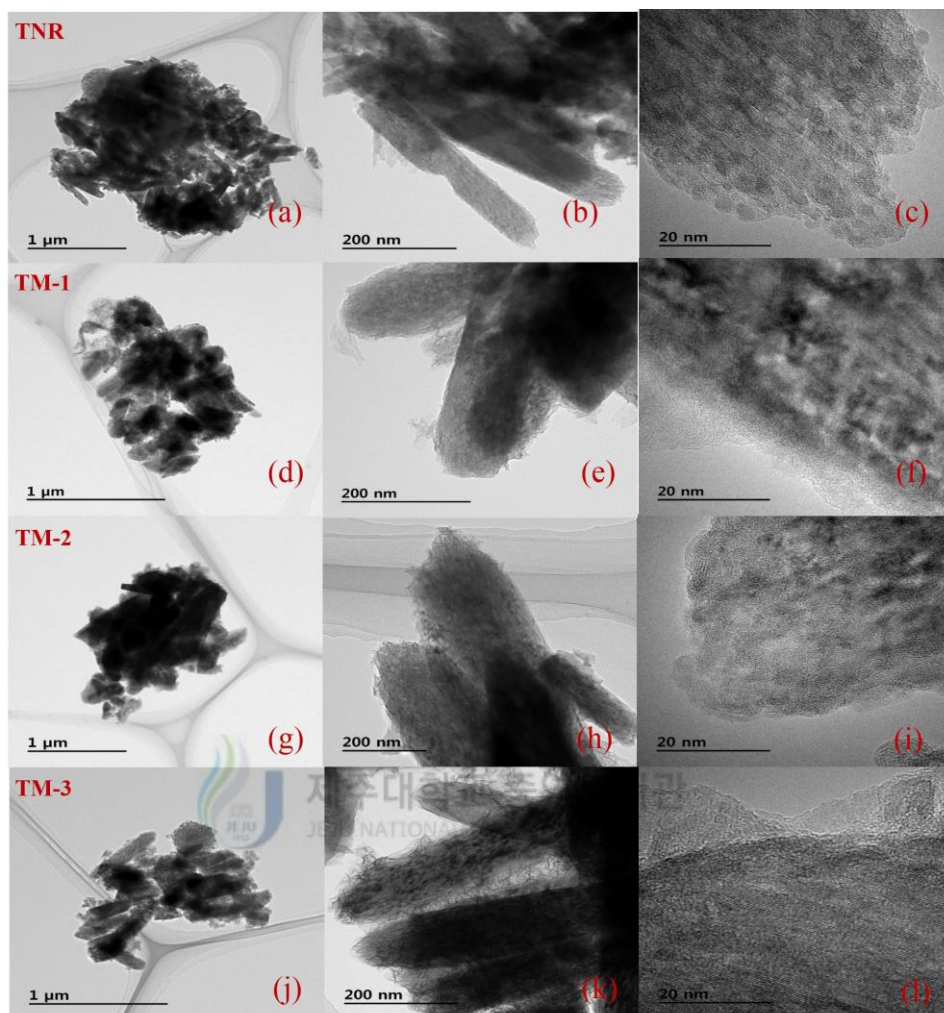


Figure 3.2.3 TEM images of (a-c) TiO₂ NR arrays, and (d-f) TM-1, (g-i) TM-2 and (j-l) TM-3 core-shell nanostructure at different magnifications.

The detailed microstructure of the TiO₂@MnO₂ core-shell nanostructure was elucidated by TEM. TEM samples were prepared by scratching the TiO₂@MnO₂ core-shell nanostructure from the FTO substrate, followed by dispersing them in ethanol solvent and casting them onto the TEM copper grids. TEM images of the TiO₂ NRs (**Figure 3.2.3a-3c**) indicated straight structures, with smooth sides and rough top surfaces, similar to those observed by FE-SEM. **Figure 3.2.3d-3l** show typical TEM images of the TiO₂@MnO₂ core-shell nanostructures (TM-1, TM-2, and

TM-3) at different magnifications indicating uniform coverage of the TiO₂ core NRs by the porous MnO₂ nanowalls (shell) in agreement with FE-SEM results. The diameter of the NRs increased from 80-100 nm (TiO₂) to 100-150 nm after MnO₂ deposition. The thickness of the MnO₂ shell layer was ~5-10 nm, further confirming the formation of core-shell nanostructures of the as-prepared samples.

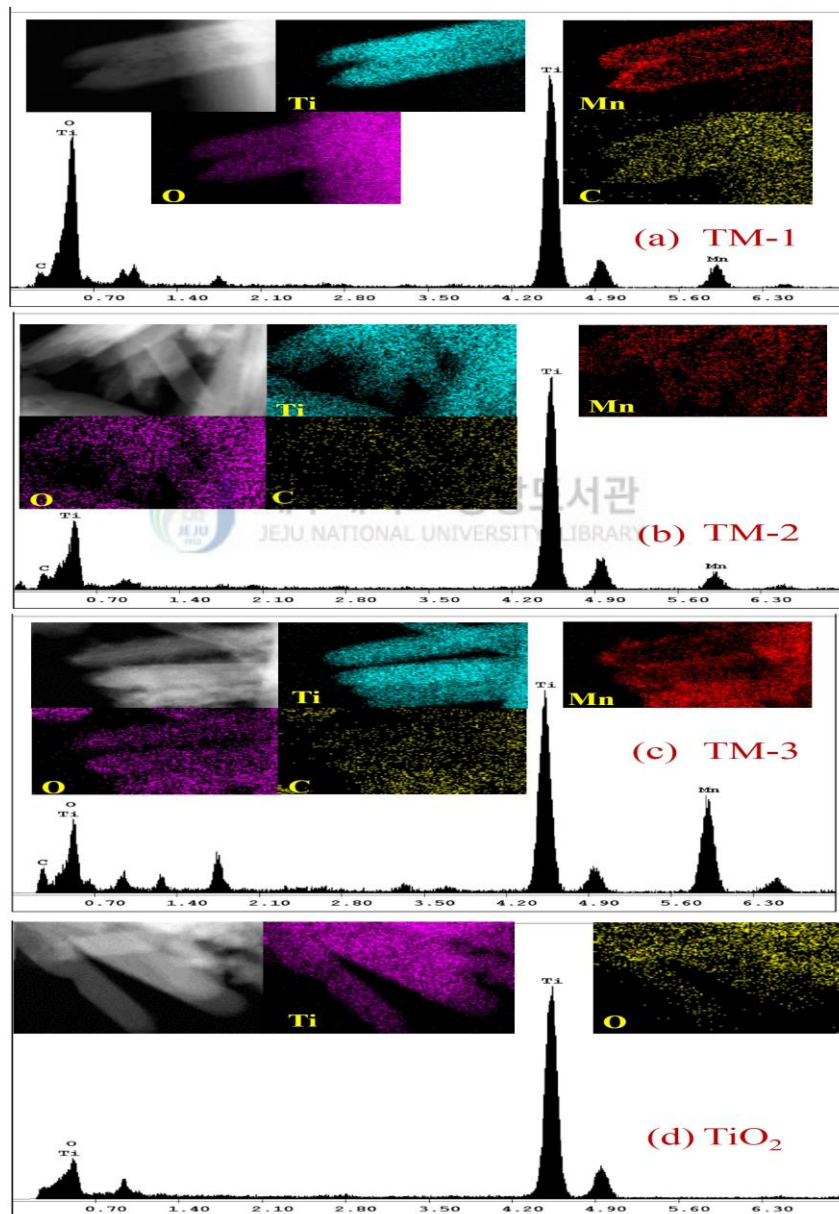


Figure 3.2.4 EDS spectra of (a) TM-1, (b) TM-2, and (c) TM-3 core-shell nanostructures and (d) TiO₂ NR arrays. The inset shows EDS mappings of Ti, Mn, O and C elements in the TiO₂@MnO₂ (a-c) core-shell arrays and (d) Ti and O elements in the TiO₂ NRs.

The elemental composition of the TiO₂ NRs and TiO₂@MnO₂ core-shell nanostructures was evaluated by EDS analysis. The EDS spectra of the TM-1, TM-2 and TM-3 core-shell nanostructures exhibited the characteristic peaks of the expected elements of Ti, Mn, O, and C, as shown in **Figure 3.2.4a - 4c**. The inset **Figure 3.2.4a - 4c** show the EDS mappings of Ti (blue color), Mn (red) O (magenta) and C (yellow) elements, confirming the core-shell hierarchical nanostructure of the TiO₂@MnO₂ nanostructure arrays. Additionally, the EDS spectra and mappings (inset) indicated the presence of Ti and O associated with the TiO₂ NRs, as shown in **Figure 3.2.4d**. The presence of the carbon peak signified that the amorphous carbon layer on the TiO₂ NR surface was not completely involved in the interfacial reaction, in agreement with XPS analysis described below.

XPS analysis was performed to examine the chemical composition of the TiO₂ and TiO₂@MnO₂ core-shell nanostructures. The typical XPS spectrum of TM-1, TM-2 and TM-3 core-shell nanostructures (**Figure 3.2.5a**) exhibited the characteristics peaks of Ti 2p, Mn 2p, O 1s, K 2p and C 1s with their corresponding binding energies. The TiO₂ survey spectrum (**Figure 3.2.5a**) displayed the Ti 2p, O 1s, and C 1s peaks; the presence of the carbon peak was discussed previously for the EDS results. **Figure 3.2.5b** shows a high-resolution, core-level spectrum of Ti 2p. The peaks at 458.2 and 464.2 eV were assigned to the Ti 2p_{3/2} and Ti 2p_{1/2} spin orbitals, respectively, indicating the formation of TiO₂ [14]. **Figure 3.2.5c** shows a high-resolution O 1s spectrum corresponding to the TiO₂ and TiO₂@MnO₂ core-shell nanostructure samples. The peaks at 530.1, and 531.9 eV, were attributed to M-O (M= Ti and Mn) and -OH bonds, respectively [5]. The core-level spectrum of Mn 2p

(Figure 3.2.5d) showed Mn 2p_{3/2} and Mn 2p_{1/2} peaks located at 642.5 and 654.1 eV, confirming the presence of Mn in the +4 oxidation state [41].

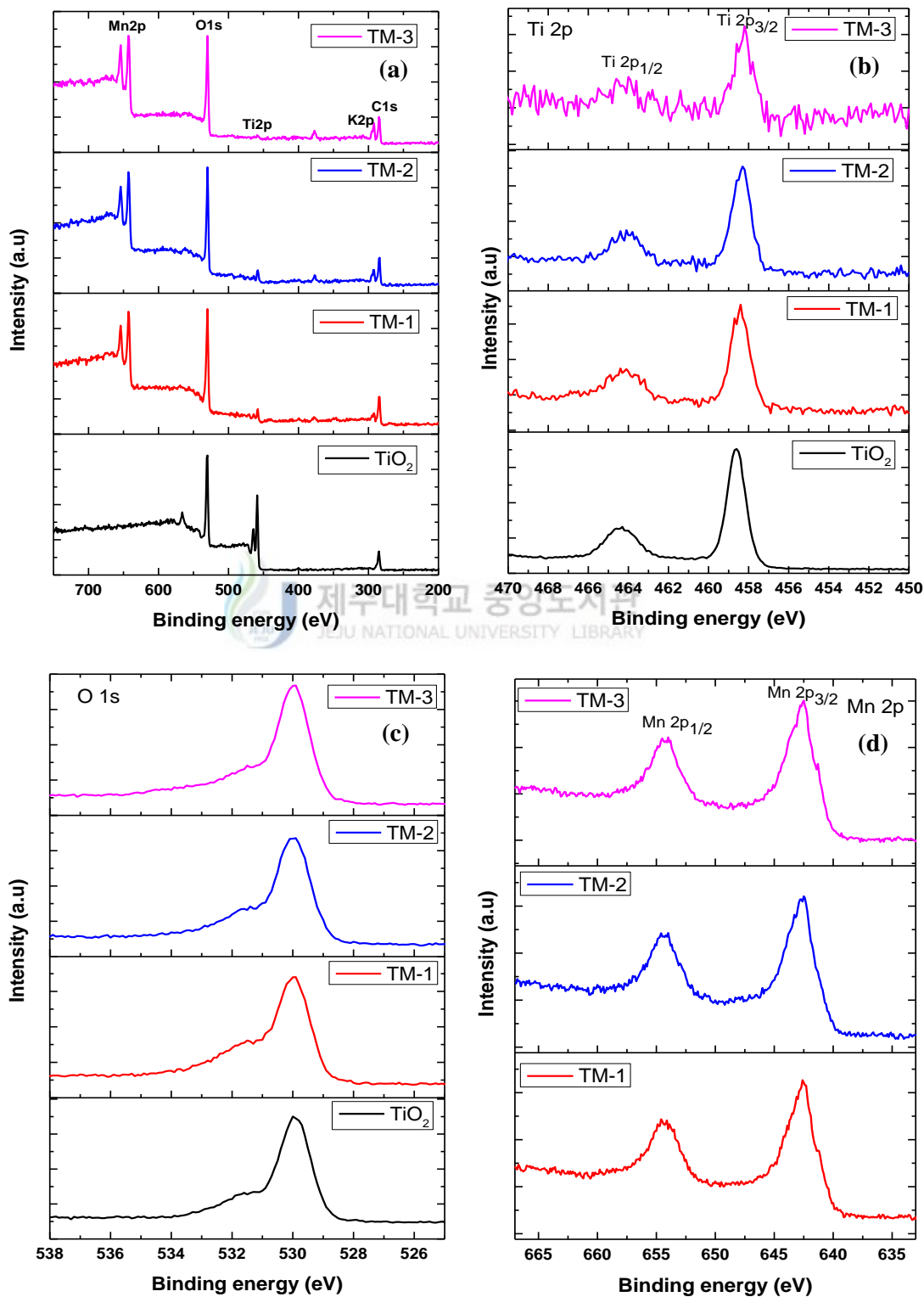
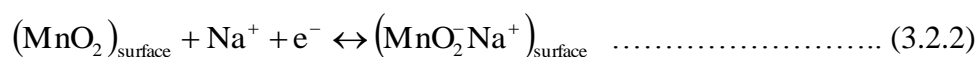


Figure 3.2.5 XPS spectra of TiO₂ NRs, and TM-1, TM-2, and TM-3 core-shell arrays for (a) the survey, (b) Ti 2p, (c) O 1s, and (d) Mn 2p.

3.2.3.2. Electrochemical characterization

The electrochemical performance of the TiO₂ NRs, and TM-1, TM-2, and TM-3 core-shell nanostructure electrodes were evaluated using CV, GCD testing and EIS. **Figure 3.2.6a** shows the typical CV curves of TiO₂ NRs, and TM-1, TM-2, and TM-3 core-shell electrodes in a 1-M Na₂SO₄ electrolyte over the voltage range 0 - 0.8 V and scan rate of 5 mV s⁻¹. All of the CV curves displayed a rectangular, symmetric shape with small redox peaks (Faradaic reaction), indicating the pseudocapacitive behavior of the electrodes. In comparison with TiO₂ NRs, the TiO₂@MnO₂ core-shell electrodes exhibited a larger CV integrated area, suggesting that a much higher areal capacitance was achieved in the TiO₂@MnO₂ (TM-3) core-shell electrode. The redox peaks observed at 0.45 and 0.47 V (versus Ag/AgCl) in the TiO₂@MnO₂ core-shell electrodes, corresponded to the reversible reaction of Mn (IV) / Mn(III) associated with the insertion/extraction of alkali cations C⁺ and the H₃O⁺ ion to/from the MnO₂ surface; this indicated that the capacitance of the core-shell nanostructure was mainly derived from pseudocapacitance. The proposed charge-storage mechanism of the MnO₂ surface in an aqueous electrolyte follows from the equation given below [3, 42]:



The above equation confirms that the charge storage occurred mainly on the surface of the MnO₂ through surface Faradaic (pseudocapacitive) reactions, involving surface adsorption of Na⁺ ions on the MnO₂ surface. Further, the core-shell nanostructure exhibited numerous electroactive sites (i.e., a large surface area) for the adsorption of Na⁺ ions, as well as enabled fast reversible Faradaic reaction by

shortening the ion diffusion path. As such, a higher specific capacitance and enhanced rate performance could be expected.

To further evaluate the electrochemical performance of the TM-1, TM-2, and TM-3 core-shell electrodes, an additional CV study was performed using scan rates ranging from 5 - 125 mV s^{-1} as shown in **Figure 3.2.6b - 6d**. All of the CV curves exhibited close to a rectangular shape, without any obvious change as the scan rate increased; this indicated ideal capacitive behavior, as well as the rapid charge-discharge behavior of the electrodes.

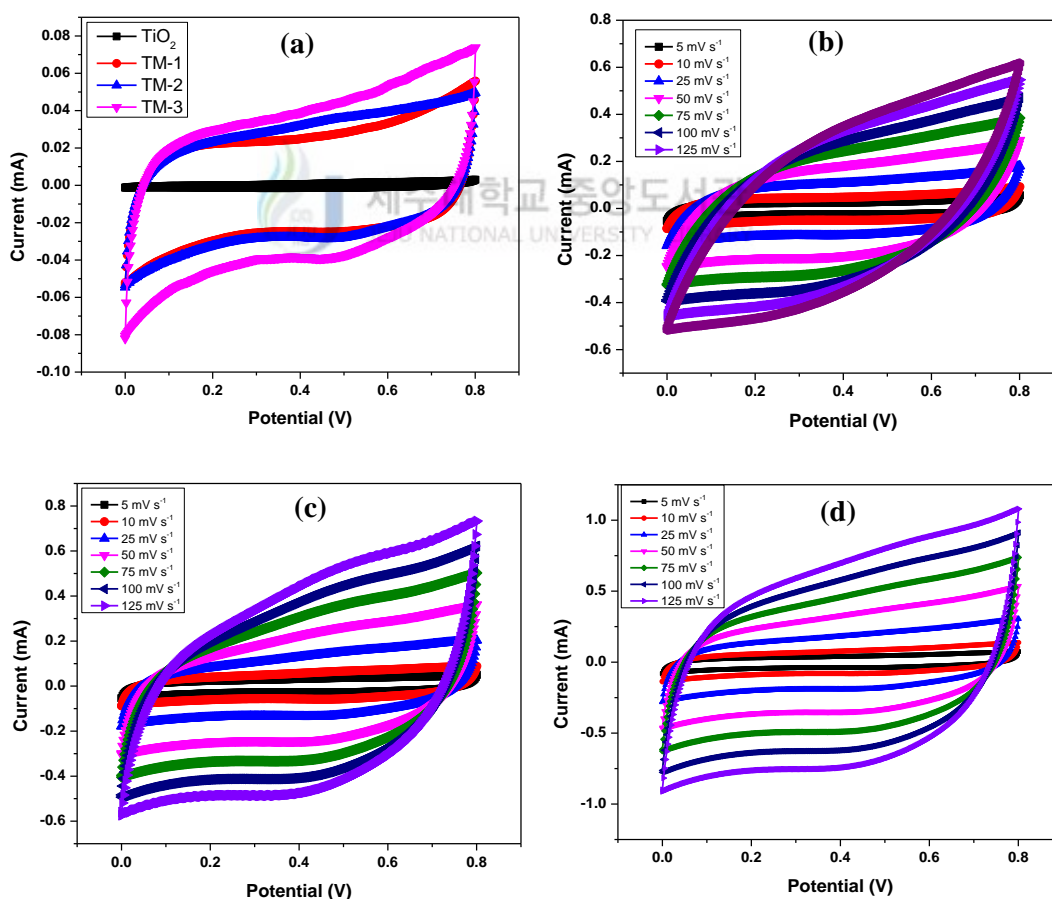


Figure 3.2.6 (a) Cyclic Voltammetry (CV) curves of TiO₂ NRs, and TM-1, TM-2, and TM-3 core-shell nanostructure electrodes at a scan rate of 5 mV s^{-1} in a 1-M Na₂SO₄ electrolyte solution. CV curves of (b) TM-1, (c) TM-2, and (d) TM-3 electrodes at different scan rates.

The areal capacitance (C_a (mF cm^{-2})) of the as-prepared electrodes was calculated from the CV curves using the equation (2.7). The calculated C_a of the TiO_2 NRs, and TM-1, TM-2, and TM-3 core-shell electrodes was 0.686, 14.36, 15.82 and 22.19 mF cm^{-2} at 5 mV s^{-1} , respectively. Among the $\text{TiO}_2@ \text{MnO}_2$ core-shell electrodes (TM-1, TM-2 and TM-3), the MnO_2 deposition prepared at 10 h (TM-3) demonstrated superior electrochemical performance, which was attributed to the combined merits of both high capacitance and the higher mass loading of MnO_2 .

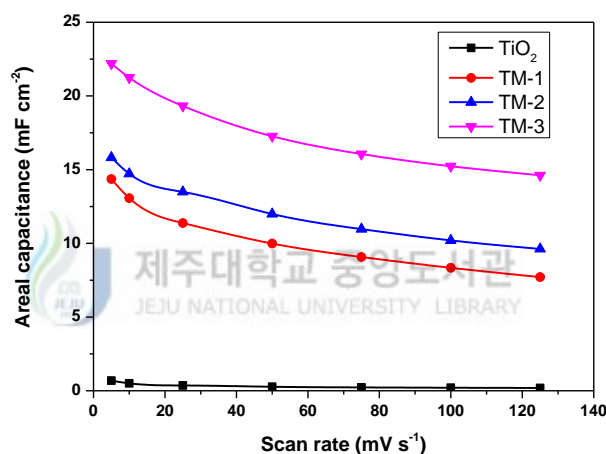


Figure 3.2.7 Areal capacitance of TiO_2 NRs, and TM-1, TM-2 and TM-3 electrodes as a function of scan rate.

Figure 3.2.7 shows a comparison of areal capacitance as a function of the scan rate for TiO_2 NRs, and TM-1, TM-2, and TM-3 core-shell electrodes; the core-shell electrodes exhibited higher areal capacitance than pure TiO_2 NRs as the scan rate varied from 5 to 125 mV s^{-1} . Moreover, the performance of the electrode dramatically decreased at a higher scan rate, due to the charge restive behavior of the material. The areal capacitance results obtained in this study are markedly better than those reported previously (TiO_2 NR arrays: $85 \mu\text{F cm}^{-2}$ at 5 mV s^{-1} [4]; untreated TiO_2 and hydrogenated TiO_2 nanotube arrays: 0.026 mF cm^{-2} and 3.24 mF cm^{-2} at 100 mV s^{-1}).

s^{-1} [6]; titania nanotubes and powder: $911 \mu F cm^{-2}$ and $181 \mu F cm^{-2}$ at $1 mV s^{-1}$ [43]; TiO_2 nanotubes heat-treated under argon atmosphere: $911 \mu F cm^{-2}$ at $1 mV s^{-1}$ [44]; self-organized titania (TiO_2) nanotube array: $2.6 mF cm^{-2}$ at $1 mV s^{-1}$ [45]; self-doped TiO_2 nanotube arrays: $1.84 mF cm^{-2}$ at $5 mV s^{-1}$ [46]; and H_2 treated bamboo-type TiO_2 nanotubes: $3.4 mF cm^{-2}$ at $10 mV s^{-1}$ [47]).

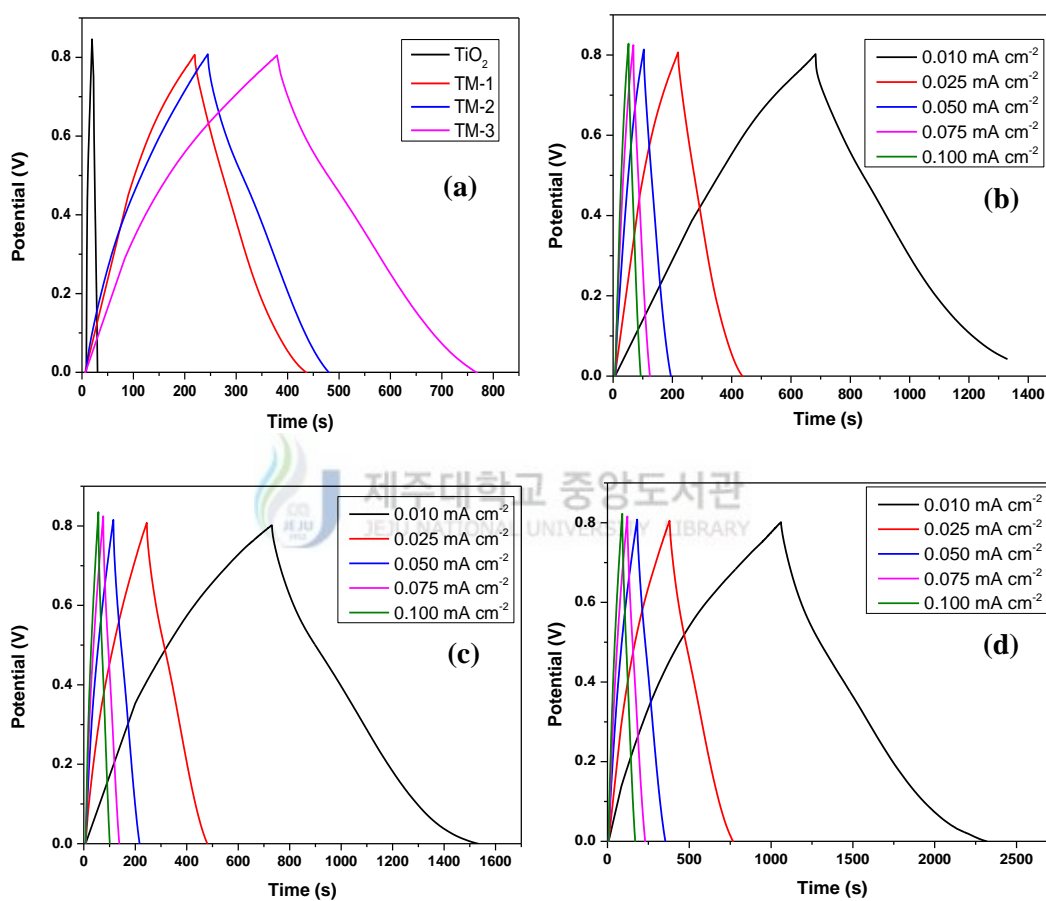


Figure 3.2.8 (a) Galvanostatic charge/discharge (GCD) curves of TiO_2 NRs, and TM-1, TM-2, and TM-3 core-shell nanostructure electrodes at a current density of $0.025 mA cm^{-2}$ in a $1-M Na_2SO_4$ aqueous solution. GCD curves of (b) TM-1, (c) TM-2, and (d) TM-3 electrodes as a function of current density.

The GCD behavior of the TiO_2 NRs, and TM-1, TM-2, and TM-3 core-shell nanostructure electrodes was measured at a current density of $0.025 mA cm^{-2}$ in $1 M Na_2SO_4$ solution as shown in **Figure 3.2.8a**. Compared with TiO_2 NR electrode, the hierarchical core-shell electrodes displayed symmetry, a fairly linear slope and long

discharge times, indicating improved electrochemical capacitive behavior and enhanced reversible redox reactions. The areal capacitance of the electrodes can be calculated from the GCD curve using the equation (2.8). The calculated areal capacitances of the TiO₂ NRs, and TM-1, TM-2 and TM-3 electrodes were ~0.27, 7.48, 9.66, and 15.32 mF cm⁻², respectively, for a current density of 0.01 mA cm⁻². The higher areal capacitance of the TM-3 electrode compared with TiO₂, TM-1, and TM-2 was due to the larger surface area, improved conductivity, and higher mass loading of MnO₂.

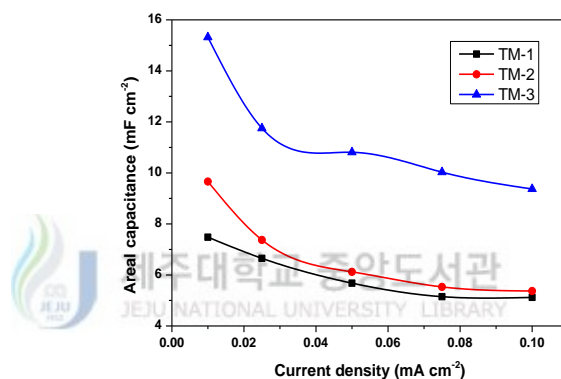


Figure 3.2.9 Areal capacitance of TM-1, TM-2, and TM-3 electrodes as a function of current density.

Additional estimations were performed to determine the electrochemical performance of the as-prepared TM-1, TM-2, and TM-3 core-shell electrodes for various current densities; the results are shown in **Figure 3.2.8b - 8d**. All of the GCD curves exhibited nearly symmetric, triangular shape, with a slight charge/ discharge plateau, indicating improved pseudocapacitive behavior and electrochemical reversibility of the as-fabricated electrodes. The current density versus areal capacitance of the TM-1, TM-2 and TM-3 electrodes are shown in **Figure 3.2.9**. Note that the areal capacitance decreased as the discharge current density increased. The TM-3 electrode delivered a higher areal capacitance than the TM-1 and TM-2

electrodes, within the current density range of 0.01 - 0.1 mA cm⁻². Additionally, at the highest current density of 0.1 mA cm⁻², the TM-3 electrode maintained its higher areal capacitance of 9.37 mF cm⁻² or 62% of the areal capacitance at 0.01 mA cm⁻². These results further confirmed that the superior rate capability and pseudocapacitive behavior of the electrode materials.

EIS measurements were carried out over the frequency range of 0.1 Hz to 100 kHz, to further evaluate the electrochemical behavior of the fabricated electrodes. The TM-1, TM-2 and TM-3 Nyquist curves (**Figure 3.2.10a**) exhibited a semicircular arc in the high-frequency region and a straight line in the low-frequency region. The diameter of the semicircular arc provided an approximate value for the charge-transfer resistance (R_{ct}) at the electrode-electrolyte interface. The 45° sloped portion in the low-frequency regions, demonstrated the Warburg impedance of the electrolyte into the interior of the electrode surface and ion diffusion/transport into the electrode surface [48]. The diameter of the semicircular arc in the curve of TM-3 was smaller than those of TM-2 and TM-1, indicating that the TM-3 core-shell electrode had a lower charge-transfer resistance (**Figure 3.2.10a**). The higher surface area and improved conductivity of the TM-3 electrode could explain the decrease in the charge transfer resistance. These results suggest better capacitive performance for the TM-3 electrode. Further, the inset of **Figure 3.2.10a** displays the Nyquist plot of TiO₂ NRs. The negligible semicircular arc in the high-frequency region indicated that the charge transfer of the working electrodes was sufficient for use in supercapacitor applications.

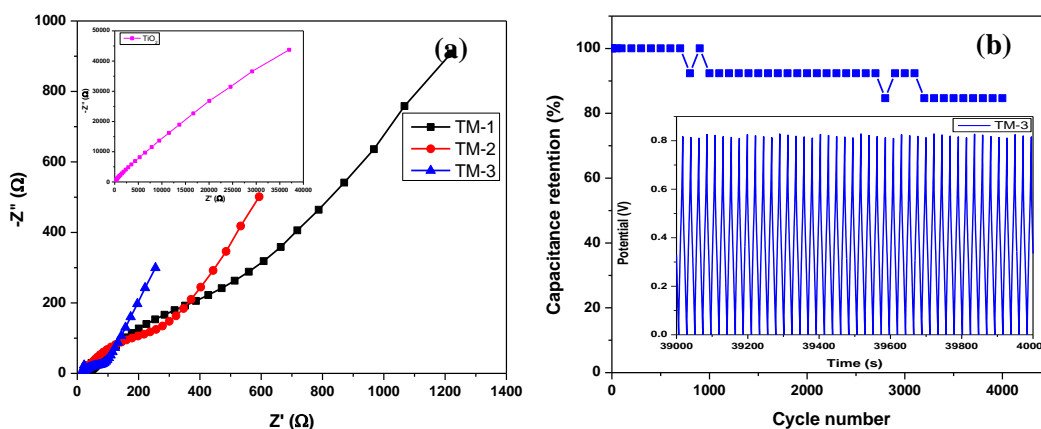


Figure 3.2.10 (a) Nyquist plots of TM-1, TM-2, and TM-3 core-shell electrodes; the inset shows the TiO₂ NR electrode. (b) Cycling performance of TM-3 core-shell electrode at a current density of 0.25 mA cm⁻² for 4000 cycles.

The long-term cycle stability of the electrode materials is an important parameter for its practical application. To evaluate the stability of the TiO₂@MnO₂ (TM-3) core-shell electrode, we repeated the GCD measurements between 0 - 0.8 V at a current density of 0.25 mA cm⁻² in a 1-M Na₂SO₄ electrolyte solution for 4000 cycles. **Figure 3.2.10b** displays the capacitance retention as a function of cycle number. We observed that the TM-3 core-shell electrode exhibited better long-term electrochemical stability (**Figure 3.2.10b**). The overall capacitance loss for the TM-3 core-shell electrode was ~15% even after 4000 cycles, indicating the excellent electrochemical stability of the fabricated electrodes, further confirming its adaptability for commercial applications.

The enhanced electrochemical performance of the TiO₂@MnO₂ core-shell electrode was attributed mainly to the following aspects: (1) By directly growing the TiO₂ NRs on the FTO current collector, the use of polymer binders and conductive additives was avoided, resulting in low interfacial resistance and a fast electrochemical reaction rate; (2) the MnO₂ nanowall-coated 1-D TiO₂ nanostructure created a highly porous morphology, as well as an ordered array geometry, which

provided a large surface area and increased number of electroactive sites; (3) the thin MnO₂ nanowalls reduced the diffusion path of the active species (here, Na⁺) and facilitated the fast diffusion of the electrolyte into the inner region of the electrode, resulting in an improved capacitance and rate capability [26, 49]; (4) the pseudocapacitive contribution (Faradaic reaction) from both the core and shell materials facilitated fast-ion transport; and finally; (5) the additional mass loading of MnO₂ enhanced the higher capacitance. These results are encouraging particularly when one considers that the hierarchical nanostructure electrode is completely conductive additive- and binder-free, thus, indicating its suitability for high-performance supercapacitors.

3.2.4. Conclusion

In summary, a simple, cost-effective approach was developed for fabrication of TiO₂@MnO₂ core-shell nanostructure electrodes, for their potential application as electrochemical supercapacitors. The resulting TM-3 core-shell electrode provided a high areal capacitance of 22.19 mF cm⁻² at a scan rate of 5 mV s⁻¹ with excellent long-term cycling stability (retaining 85% even after 4000 cycles), compared with that of pure TiO₂ NRs. The improved electrochemical performance of the electrode was attributed mainly to the high specific surface area, fast electron transport, and synergetic contribution from the core TiO₂ NR arrays and the shell MnO₂ nanowalls. These results clearly demonstrate the potential of the TiO₂@MnO₂ core-shell nanostructure as an electrode material for supercapacitor applications.

3.2.5. References

- [1] H. Jiang, L. P. Yang, C. Z. Li, C. Y. Yan, P. S. Lee, and J. Ma, High-rate electrochemical capacitors from highly graphitic carbon-tipped manganese oxide/mesoporous carbon/manganese oxide hybrid nanowires. *Energy Environ Sci.* 4 (2011)1813-1819.
- [2] W. F. Wei, X. W. Cui, W. X. Chen, and D. G. Ivey, Manganese oxide-based materials as electrochemical supercapacitor electrodes. *Chem. Soc. Rev.* 40 (2011) 1697-1721.
- [3] M. Toupin, T. Brousse, and D. Bélanger, Charge Storage Mechanism of MnO₂ electrode used in aqueous electrochemical capacitor. *Chem. Mater.* 16 (16) (2004) 3184-3190.
- [4] A. Ramadoss, and S. J. Kim, Vertically aligned TiO₂ nanorod arrays for electrochemical supercapacitor. *J. Alloys Compd.* 561 (2013) 262-267.
- [5] X. Lu, M. Yu, G. Wang, T. Zhai, S. Xie, Y. Ling, Y. Tong, and Y. H. Li, TiO₂@MnO₂/H-TiO₂@C core-shell nanowires for high performance and flexible asymmetric supercapacitors. *Adv. Mater.* 25 (2013) 267-272.
- [6] X. H. Lu, G. M. Wang, T. Zhai, M. H. Yu, J. Y. Gan, Y. X. Tong, and Y. Li, Hydrogenated TiO₂ nanotube arrays for supercapacitors. *Nano Lett.* 12 (2012) 1690-1696.
- [7] S. W. Zhang, and G. Z. Chen, Manganese oxide based materials for supercapacitors. *Energy Mater.* 3(3) (2008) 186-200.
- [8] M. S. Song, K. M. Lee, Y. R. Lee, I. Y. Kim, T. W. Kim, J. L. Gunjekar and S. J. Hwang, Porously assembled 2D nanosheets of alkali metal manganese

- oxides with highly reversible pseudocapacitance behaviors. *J. Phys. Chem. C* 114(50) (2010) 22134-22140.
- [9] C. Xu, F. Kang, B. Li and H. Du, Recent progress on manganese dioxide based supercapacitors. *J. Mater. Res.* 25(8) (2010) 1421-1432.
- [10] J. Zhang, J. Ma, J. Jiang and X. S. Zhao, Synthesis and capacitive properties of carbonaceous sphere@MnO₂ rattle-type hollow structures. *J. Mater. Res.* 25(8) (2010) 1476-1484.
- [11] J. T. Zhang, W. Chu, J. W. Jiang and X. S. Zhao, Synthesis, characterization and capacitive performance of hydrous manganese dioxide nanostructures. *Nanotechnology* 22(12) (2011) 125703-125712.
- [12] H. Y. Lee, and S. W. Kim, Expansion of active site area and improvement of kinetic reversibility in electrochemical pseudocapacitor electrode. *Electrochem. Solid-State Lett.* 4(3) (2001) A19-A22.
- [13] M. Yu, H. Sun, X. Sun, F. Lu, G. Wang, T. Hu, H. Qiu, and J. Lian, Hierarchical Al-doped and hydrogenated ZnO nanowire@MnO₂ ultra-thin nanosheet core/shell arrays for high-performance supercapacitor electrode. *Int. J. Electrochem. Sci.* 8 (2013) 2313-2329.
- [14] H. Zheng, T. Zhai, M. Yu, S. Xie, C. Liang, W. Zhao, S. C. Wang, Z. Zhang, and X. Lu, TiO₂@C core-shell nanowires for high-performance and flexible solid-state supercapacitors. *J. Mater. Chem. C* 1 (2013) 225-229.
- [15] L. Q. Mai, F. Yang, Y. L. Zhao, X. Xu, L. Xu, and Y. Z. Luo, Hierarchical MnMoO₄/CoMoO₄ heterostructured nanowires with enhanced supercapacitor performance. *Nat. Commun.* 2 (2011) 381-385.

- [16] H. Wei, X. Yan, S. Wu, Z. Luo, S. Wei, and Z. Guo, Electropolymerized polyaniline stabilized tungsten oxide nanocomposite films: Electrochromic behavior and electrochemical energy storage. *J. Phys. Chem. C* 116 (2012) 25052-25064.
- [17] X. Sun, Q. Li, Y. Lu, and Y. Mao, Three-dimensional ZnO@MnO₂ core@shell nanostructures for electrochemical energy storage. *Chem. Commun.* 49 (2013) 4456-4458.
- [18] J. P. Liu, C. W. Cheng, W. W. Zhou, H. X. Li, and H. J. Fan, Ultrathin nickel hydroxidenitrate nanoflakes branched on nanowire arrays for high-rate pseudocapacitive energy storage. *Chem. Commun.* 47 (2011) 3436-3438.
- [19] R. Liu, and S. B. Lee, MnO₂/Poly(3,4-ethylenedioxythiophene) coaxial nanowires by one-step coelectrodeposition for electrochemical energy storage. *J. Am. Chem. Soc.* 130 (2008) 2942-2943.
- [20] R. Liu, J. Duay, and S. B. Lee, Redox exchange induced MnO₂ nanoparticle enrichment in poly(3,4-ethylenedioxythiophene) nanowires for electrochemical energy storage. *ACS Nano* 4 (2010) 4299-4307.
- [21] X. H. Xia, J. P. Tu, Y. Q. Zhang, J. Chen, X. L. Wang, C. D. Gu, G. Guan, J. S. Luo, and H. F. Fan, Porous hydroxide nanosheets on preformed nanowires by electrodeposition: branched nanoarrays for electrochemical energy storage. *Chem. Mater.* 24 (2012) 3793-3799.
- [22] J. Rajeswari, P. S. Kishore, B. Viswanathan, and T. K. Varadarajan, One-dimensional MoO₂ nanorods for supercapacitor applications. *Electrochem. Commun.* 11 (2009) 572-575.

- [23] C. L. Sun, C. T. Chang, H. H. Lee, J. Zhou, J. Wang, T. K. Sham, and W. F. Pong, Microwave-assisted synthesis of a core-shell MWCNT/GONR heterostructure for the electrochemical detection of ascorbic acid, dopamine, and uric acid. *ACS Nano* 5(10) (2011) 7788-7795.
- [24] L. Y. Lin, M. H. Yeh, J. T. Tsai, Y. H. Huang, C. L. Sun, and K. C. Ho, A novel core-shell multi-walled carbon nanotube@graphene oxide nanoribbon heterostructure as a potential supercapacitor material. *J. Mater. Chem. A* 1 (2013) 11237-11245.
- [25] J. S. Ye, H. F. Cui, X. Liu, T. M. Lim, W. D. Zhang, and F. S. Sheu, Preparation and characterization of aligned carbon nanotube-ruthenium oxide nanocomposites for supercapacitors. *Small* 1 (2005) 560-565.
- [26] J. Liu, J. Jiang, C. Cheng, H. Li, J. Zhang, H. Gong, and H. J. Fan, Co_3O_4 nanowire@ MnO_2 ultrathin nanosheet core/shell arrays: a new class of high-performance pseudocapacitive materials. *Adv. Mater.* 23 (2011) 2076–2081.
- [27] J. Yan, E. Khoo, A. Sumboja, and P. S. Lee, Facile coating of manganese oxide on tin oxide nanowires with high-performance capacitive behavior. *ACS Nano* 4 (2010) 4247-4255.
- [28] L. Yu, G. Zhang, C. Yuan, and X. W. Lou, Hierarchical NiCo_2O_4 @ MnO_2 core-shell heterostructured nanowire arrays on Ni foam as high-performance supercapacitor electrodes. *Chem. Commun.* 49 (2013) 137–139.
- [29] L. Bao, J. Zang, and X. Li, Flexible Zn_2SnO_4 / MnO_2 core/shell nanocable-carbon microfiber hybrid composites for high-performance supercapacitor electrodes. *Nano Lett.* 11 (2011) 1215-1220.

- [30] Y. Luo, D. Kong, J. Luo, S. Chen, D. Zhang, K. Qiu, X. Qi, H. Zhang, C. M. Li, and T. Yu, Hierarchical TiO₂ nanobelts@MnO₂ ultrathin nanoflakes core-shell array electrode materials for supercapacitors. *RSC Adv.* 3 (2013) 14413–14422.
- [31] W. Li, G. Li, J. Sun, R. Zou, K. Xu, Y. Sun, Z. Chen, J. Yang, and J. Hu, Hierarchical heterostructures of MnO₂ nanosheets or nanorods grown on Au-coated Co₃O₄ porous nanowalls for high-performance pseudocapacitance. *Nanoscale* 5 (2013) 2901-2908.
- [32] H. Xia, D. Zhu, Z. Luo, Y. Yu, X. Shi, G. Yuan, and J. Xie, Hierarchically structured Co₃O₄@Pt@MnO₂ nanowire arrays for high-performance supercapacitors. *Sci. Rep.* 3 (2013) 2978-2985.
- [33] C. Guan, J. Liu, C. Cheng, H. Li, X. Li, W. Zhou, H. Zhang, and H. J. Fan, Hybrid structure of cobalt monoxide nanowire@nickel hydroxidenitrate nanoflake aligned on nickel foam for high-rate supercapacitor. *Energy Environ. Sci.* 4 (2011) 4496-4499.
- [34] D. Sarkar, G. G. Khan, A. K. Singh, and K. Mandal, High-performance pseudocapacitor electrodes based on α -Fe₂O₃/MnO₂ core-shell nanowire heterostructure arrays. *J. Phys. Chem. C* 117 (2013) 15523–15531.
- [35] X. Lu, T. Zhai, X. Zhang, Y. Shen, L. Yuan, B. Hu, L. Gong, J. Chen, Y. Gao, J. Zhou, Y. Tong, and Z. L. Wang, WO_{3-x}@Au@MnO₂ core-shell nanowires on carbon fabric for high-performance flexible supercapacitors. *Adv. Mater.* 24 (2012) 938–944.
- [36] X. Jin, W. Zhou, S. Zhang, and G. Z. Chen, Nanoscale microelectrochemical cells on carbon nanotubes. *Small* 3 (2007) 1513-1517.

- [37] S. W. Lee, J. Kim, S. Chen, P. T. Hammond, and S. H. Yang, Carbon nanotube/manganese oxide ultrathin film electrodes for electrochemical capacitors. *ACS Nano* 4 (2010) 3889-3896.
- [38] M. H. Yang, T. T. Chen, Y. S. Wang, H. T. Chiu, and C. Y. Lee, Electrochromism of rutile nanowires, vertically aligned along the [001] direction, due to alkali metal ion intercalation. *J. Mater. Chem.* 21 (2011) 18738-18743.
- [39] Y. Luo, J. Jiang, W. Zhou, H. Yang, J. Luo, X. Qi, H. Zhang, D. Y. W. Yu, C. M. Lid, and T. Yu, Self-assembly of well-ordered whisker-like manganese oxide arrays on carbon fiber paper and its application as electrode material for supercapacitors. *J. Mater. Chem.* 22 (2012) 8634-8640.
- [40] C. M. Julien, M. Massot, and C. Poinignon, Lattice vibrations of manganese oxides. Part I. Periodic structures. *Spectrochim Acta Part A* 60 (2004) 689-700.
- [41] P. Yang, X. Xiao, Y. Li, Y. Ding, P. Qiang, X. Tan, W. Mai, Z. Lin, W. Wu, T. Li, H. Jin, P. Liu, J. Zhou, C. P. Wong, and Z. L. Wang, Hydrogenated ZnO core-shell nanowires for flexible supercapacitors and self-powered systems. *ACS Nano* 7(3) (2013) 2617-2626.
- [42] G. Xiong, K. P. S. S. Hembram, R. G. Reifemberger, and T. S. Fisher, MnO₂-coated graphitic petals for supercapacitor electrodes. *J. Power Sources* 227 (2013) 254-259.
- [43] M. Salari, S. H. Aboutalebi, K. Konstantinov, and H. K. Liu, A highly ordered titania nanotube array as a supercapacitor electrode. *Phys. Chem. Chem. Phys.* 13 (2011) 5038-5041.

- [44] M. Salari, K. Konstantinov, and H. K. Liu, Enhancement of the capacitance in TiO₂ nanotubes through controlled introduction of oxygen vacancies. *J. Mater. Chem.* 21 (2011) 5128–5133.
- [45] M. Salari, S. H. Aboutalebi, A. T. Chidembo, I. P. Nevirkovets, K. Konstantinov, and H. K. Liu, Enhancement of the electrochemical capacitance of TiO₂ nanotube arrays through controlled phase transformation of anatase to rutile. *Phys. Chem. Chem. Phys.* 14 (2012) 4770–4779.
- [46] H. Zhou, and Y. Zhang, Electrochemically self-doped TiO₂ nanotube arrays for supercapacitors. *J. Phys. Chem. C* 118 (2014) 5626–5636.
- [47] B. Chen, J. Hou, and K. Lu, Formation mechanism of TiO₂ nanotubes and their applications in photoelectrochemical water splitting and supercapacitors. *Langmuir* 29 (2013) 5911–5919.
- [48] R. Kotz, and M. Carlen, Principles and applications of electrochemical capacitors. *Electrochimica Acta* 45 (2000) 2483–2498.
- [49] J. Jiang, Y. Y. Li, J. P. Liu, and X. T. Huang. Building one-dimensional oxide nanostructure arrays on conductive metal substrates for lithium-ion battery anodes. *Nanoscale* 3 (2011) 45-58.

3.3. Synthesis and Electrochemical Performance of TiO₂@CoO₃ Core-Shell Nanostructure

3.3.1. Introduction

Out of the metal oxides, cobalt oxides (Co₃O₄) has been demonstrated to be a promising electrode material for supercapacitors due to its high redox activity, great reversibility, practical availability, environmentally benign nature and lower cost [1–5]. The theoretical specific capacitance of Co₃O₄ is 3560 F g⁻¹ [6]. In addition, recent reports have proved that Co₃O₄ with different microstructure and morphology possessed excellent electrochemical behavior [7-10]. Therefore the morphology of electrode plays an important role in capacitance enhancement. However, still Co₃O₄ often result in low specific capacitance and poor rate capability due its poor conductivity [11-14]. Therefore, it is crucial to enhance charge the satisfactory electrochemical capacitive performance and high rate capability for high performance supercapacitors.

Recently, advanced nanoarchitecture with combination of two materials have attracted great interest in the application of anode and cathode materials for supercapacitors. These nanoarchitecture can provide high surface area for access large number of electroactive species and short diffusion path for ion transport, which leads to fast charge/discharge rates [15-17]. Inspired by this advancement, it would be interesting to prepare novel nanoarchitecture for high-performance supercapacitors.

In this chapter, the electroactive materials (TiO₂@Co₃O₄ core-shell nanostructure) were directly grown onto FTO substrate via a hydrothermal method to obtain a conducting additive-free and binder-less electrode with high utilization of

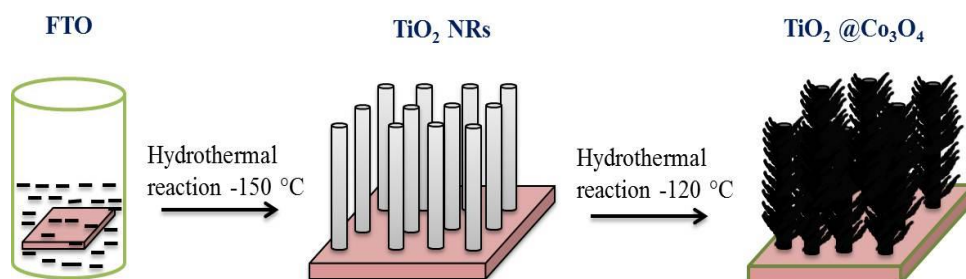
the electro-active material. Vertically aligned TiO₂ nanorod arrays serve as a core material and Co₃O₄ nanowall serve as a shell layer. TiO₂ is an inexpensive, non-toxic, high specific energy density, eco-friendly and electrochemically stable semiconducting material, which is commonly used as an electrode in electrochemical devices [18]. The Co₃O₄ nanowall grafted on the TiO₂ backbone are beneficial to enhance the electrochemical capacity and cycling stability of the electrode due to the high theoretical capacity of the Co₃O₄ shell and the low volume change of the TiO₂ core. The as-prepared core-shell nanostructure provide large surface area, fast ion and electron transfer as well as sufficient effective area between electrolyte ions and active materials for Faradaic reactions.

3.3.2. Experimental details

3.3.2.1. Preparation of TiO₂/Co₃O₄ core-shell nanostructure

All reagents used in these experiments were of analytical grade and were used directly without further purification. First, TiO₂ NRs were grown on FTO substrates using a hydrothermal deposition method, as described in previous **Chapter.3.1**. In the second step, Co₃O₄ nanowalls shell structure was grown over the TiO₂ NRs using a simple hydrothermal method. Briefly, an aqueous solution of 0.1 g Co(NO₃)₂, 0.5 g Co(NH₂)₂ and 0.37 g NH₄F was prepared to serve as a precursor solution for the shell growth. Then, the TiO₂ NR arrays coated FTO substrate were placed in the precursor solution in a sealed Teflon-lined stainless steel autoclave at 120 °C for 5 h, using an electric oven. After synthesis, the Teflon reactor was cooled to room temperature. The samples were removed, rinsed extensively with deionized water and dried at 60 °C in a hot air oven. Finally, to obtain the TiO₂@Co₃O₄ core-shell nanostructure, the prepared sample was calcined at 400 °C for 4 h in air. The

schematic illustration of $\text{TiO}_2@\text{Co}_3\text{O}_4$ core-shell nanostructure growth process is shown in **Scheme 3.3.1**. The crystal structure, morphology and composition of the samples was investigated using XRD, FE-SEM and XPS measurements.



Scheme 3.3.1 Schematic diagram illustrating the synthesis procedure of a $\text{TiO}_2@\text{Co}_3\text{O}_4$ core-shell array electrode on a fluorine-doped tin oxide (FTO) substrate.

3.3.2.2. Electrochemical characterization

All the electrochemical measurements were performed using an Autolab PGSTAT302N in a standard three-electrode system consisting of the $\text{TiO}_2/\text{Co}_3\text{O}_4$ core-shell nanostructured electrode as the working electrode, a saturated calomel electrode as the reference electrode, and a platinum counter electrode in a 2 M KOH electrolyte. The electrochemical behaviour of the as-prepared electrodes was characterised using CV, galvanostatic charge–discharge (GCD) and electrochemical impedance spectroscopy (EIS) tests. The CV was carried out in a potential range of 0.1 to 0.5 V at a range of scan rates. Constant-current charge–discharge tests were carried out at different current densities within a potential range of 0.1 to 0.5 V. The EIS measurement was measured in the frequency range of 0.1 Hz to 100 kHz with an open-circuit potential and alternating current (AC) amplitude of 10 mV.

3.3.3. Results and discussion

The fabrication process for the $\text{TiO}_2@\text{Co}_3\text{O}_4$ core-shell nanostructure on the FTO substrate involved two steps, as illustrated in **Scheme 3.3.1**. First, the core-

structure of vertically aligned TiO₂ NR arrays were grown on FTO via the simple hydrothermal method. In the second step, the Co₃O₄ outer shell layer was also grown via a hydrothermal method, forming a TiO₂@Co₃O₄ core-shell nanostructure as the final product.

3.3.3.1. Structure, morphology and compositional analysis

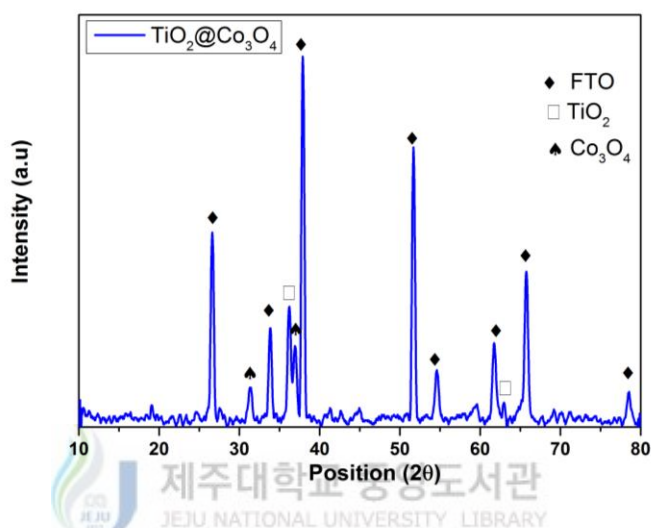


Figure 3.3.1 XRD pattern of TiO₂@Co₃O₄ core-shell nanostructure.

The crystal structure of the TiO₂@Co₃O₄ nanostructure was examined using XRD measurements. **Figure 3.3.1** shows a typical XRD pattern of the TiO₂@Co₃O₄ core-shell nanostructure. It can be clearly seen that the TiO₂@Co₃O₄ core-shell nanostructure exhibited a tetragonal rutile phase of TiO₂ NRs and cubic phase of the Co₃O₄ nanowall. The observed d-spacing values are well matched with standard JCPDS card no 021-1276 for TiO₂ and JCPDS card no 065-3103 for Co₃O₄. The peaks represented by diamond symbols in the figure correspond to the FTO substrate. **Figures 3.3.2a** shows FE-SEM image of the TiO₂ NRs. It can be clearly seen that the as-prepared TiO₂ NRs had a tetragonal structure, were highly uniform, and formed a densely packed array of vertically aligned NRs. The average diameter of the TiO₂

NRs was 100–150 nm. **Figures 3.3.2b - 2d** show typical FE-SEM images of $\text{TiO}_2@\text{Co}_3\text{O}_4$ core-shell nanostructure. The FE-SEM images showed the uniformly covered Co_3O_4 shell layer, over the TiO_2 NRs surface (core).

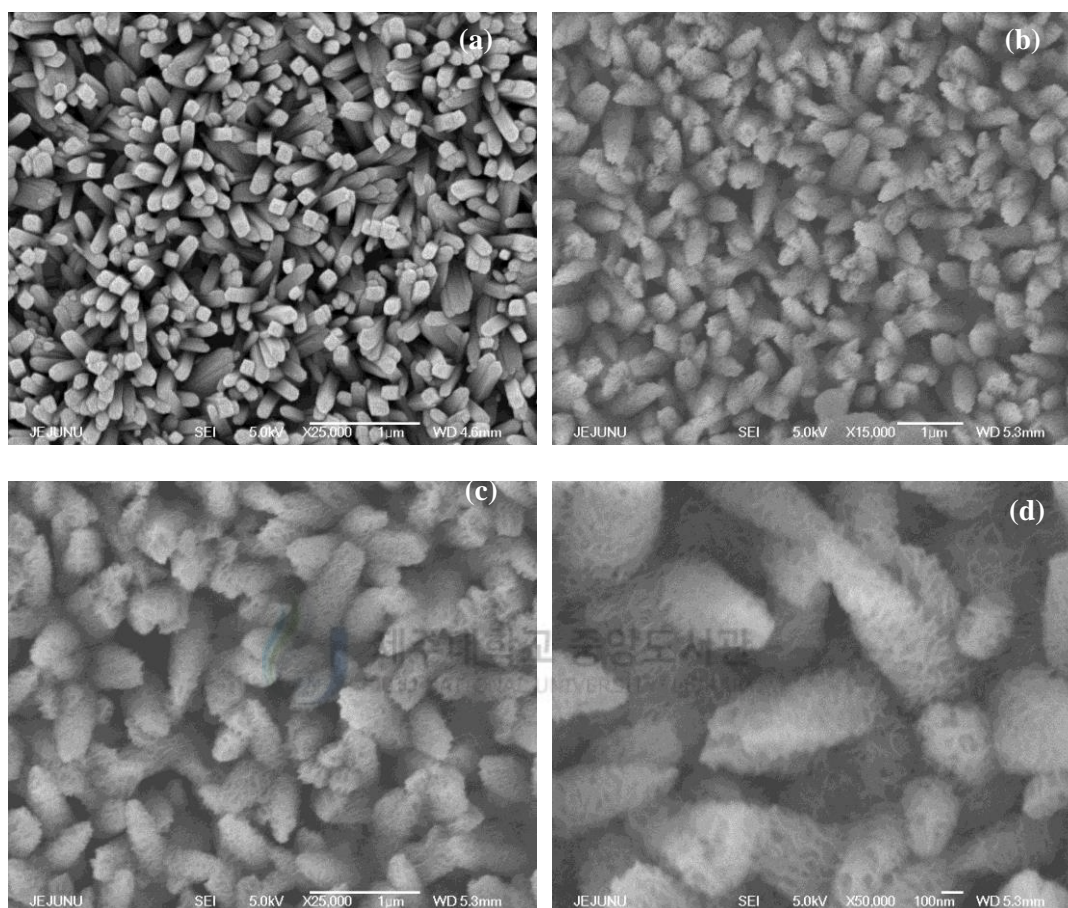


Figure 3.3.2 FE-SEM images (a) TiO_2 NR arrays, (b-d) $\text{TiO}_2@\text{Co}_3\text{O}_4$ core-shell nanostructure at different magnifications

The chemical composition of the $\text{TiO}_2@\text{Co}_3\text{O}_4$ core-shell nanostructure was examined using XPS analysis. The XPS survey spectrum (**Figure 3.3.3a**) exhibited the characteristic peaks of Ti 2p, Co 2p, O 1s, and C 1s with their corresponding binding energies. The peaks (**Figure 3.3.3b**) at 458.9 and 464.8 eV are assigned to the Ti 2p_{3/2} and Ti 2p_{1/2} spin orbital respectively, which indicating the formation of TiO_2 [19]. The core level spectrum of Co 2p (**Figure 3.3.3c**) exhibited the Co 2p_{3/2} and Co 2p_{1/2} peaks located at 781.2 and 797.4 eV, further suggesting the formation

of Co_3O_4 phase [20, 21]. **Figure 3.3.3d** shows a high-resolution spectrum of O 1s. The peak located at 530.5 eV was assigned to OH ions.

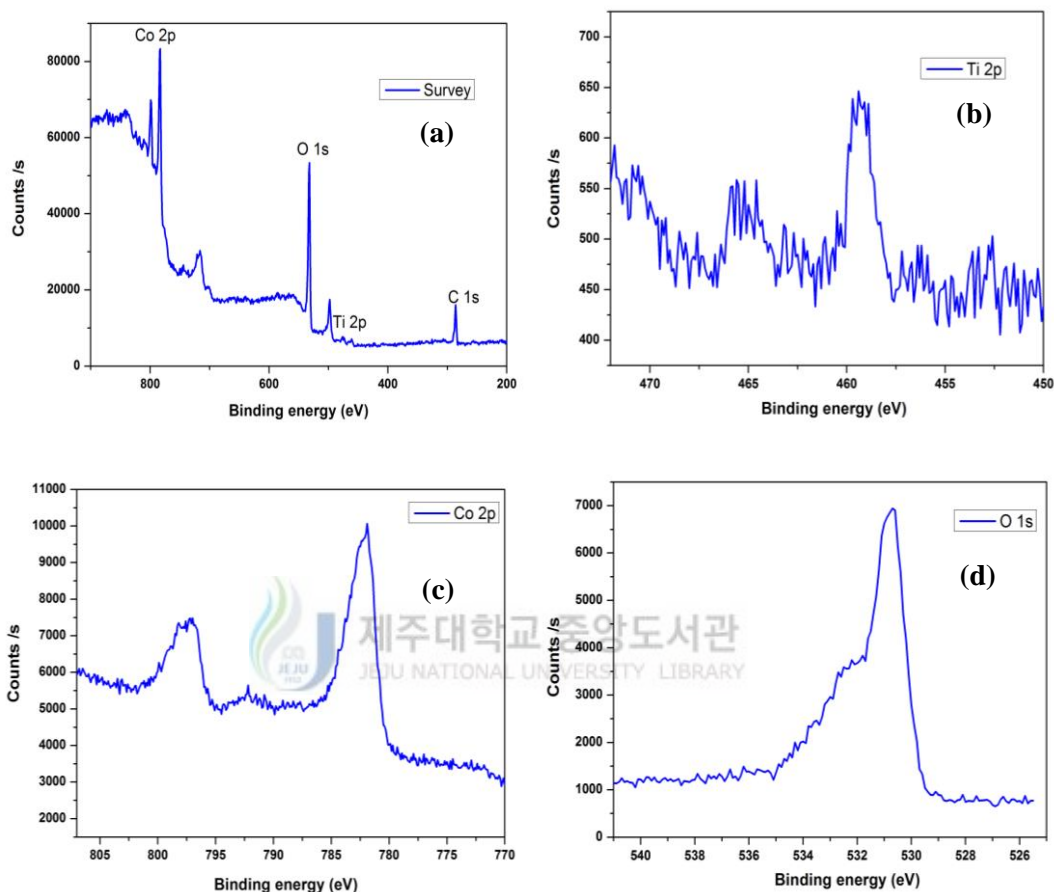


Figure 3.3.3 XPS spectra of $\text{TiO}_2@ \text{Co}_3\text{O}_4$ core-shell nanostructure (a) survey, (b) Ti 2p, (c) Co 2p and (d) O 1s.

3.3.3.2. Electrochemical characterizations

The capacitance behavior of as-prepared $\text{TiO}_2@ \text{Co}_3\text{O}_4$ core-shell nanostructure electrode were examined by cyclic voltammetry, galvanostatic charge-discharge, electrochemical impedance spectroscopy, techniques in 2 M KOH electrolyte solution. **Figure 3.3.4a** shows the CV curves of TiO_2 NR arrays and $\text{TiO}_2@ \text{Co}_3\text{O}_4$ core-shell nanostructure electrodes at a scan rate of 25 mV s^{-1} . It could be observed that $\text{TiO}_2@ \text{Co}_3\text{O}_4$ core-shell nanostructure electrode curve consist of a

pair of redox peaks, suggesting that the capacitance of the electrodes are mainly results from the pseudocapacitance which is based on faradic redox mechanism. The peaks observed at the anodic and cathodic direction corresponds to the redox transition of cobalt oxidation states at the $\text{TiO}_2@\text{Co}_3\text{O}_4$ /electrolyte interface, according the following equation [6].



Compared to TiO_2 NR arrays, the $\text{TiO}_2@\text{Co}_3\text{O}_4$ core-shell nanostructure electrode shows the increased redox current intensity, suggesting that core-shell nanostructure electrode has the highest specific capacitance.

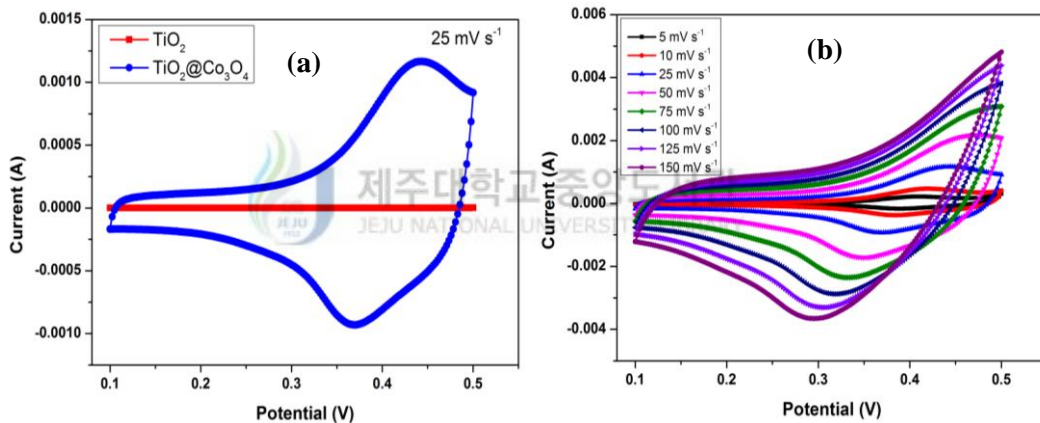


Figure 3.3.4 (a) CV curves of TiO_2 NR arrays and $\text{TiO}_2@\text{Co}_3\text{O}_4$ core-shell nanostructure electrodes. (b) CVs of $\text{TiO}_2@\text{Co}_3\text{O}_4$ core-shell nanostructure at different scan rates.

To further confirm the electrochemical performance of $\text{TiO}_2@\text{Co}_3\text{O}_4$ core-shell nanostructure electrode, the CV measurements of $\text{TiO}_2@\text{Co}_3\text{O}_4$ core-shell nanostructure were performed at various scan rates between 5 and 150 mV s^{-1} and are presented in **Figure 3.3.4b**. It should be noted that with an increase of scan rates, the position of anodic peaks shift toward high potential and cathodic peaks shift toward negative potential, which indicates the quasi-reversible feature of the redox couples [22].

Based on the CV curves, the areal capacitance (using equation 2) of the TiO₂ NR arrays and TiO₂@Co₃O₄ core-shell nanostructure electrode could be calculated to be 85 μF cm⁻² and 44 mF cm⁻² at the scan rate of 5 mV s⁻¹, respectively. Compared to TiO₂ NR arrays, the TiO₂@Co₃O₄ core-shell nanostructure electrode exhibited higher areal specific capacitance. The larger areal capacitance of the hierarchical nanostructured electrode is mainly attributed to its unique morphology. The core-shell nanostructure provides higher electro-active area for access large numbers of ions, finally which lead to the higher areal capacitance. **Figure 3.3.5a** showed the specific capacitance of TiO₂@Co₃O₄ core-shell nanostructure electrode as a function of scan rate. With increasing scan rate, the specific capacitance decreases gradually which is due to the some active surface areas becoming inaccessible for charge storage at higher scan rate. Noticeably, about 94% of the specific capacitance can be retained for a 30-time rising in scan rate, indicates the excellent capacitive behavior and high-rate capability of the TiO₂@Co₃O₄ core-shell nanostructure electrode.

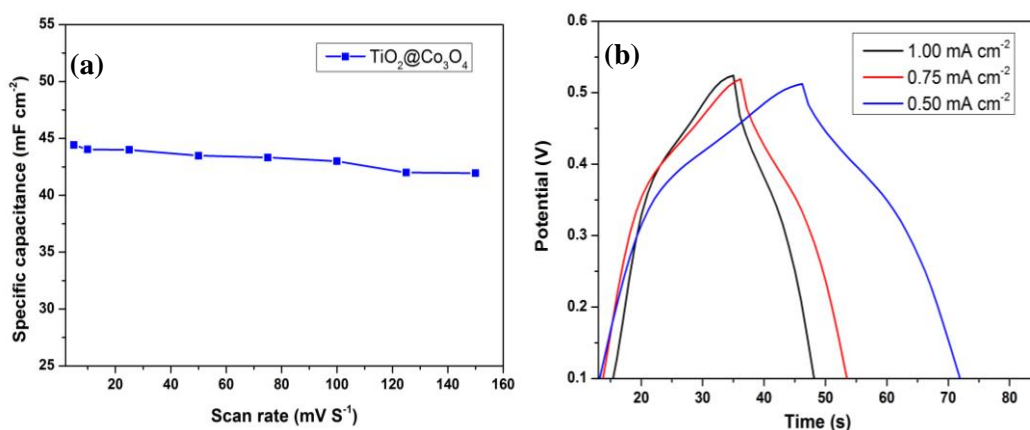


Figure 3.3.5 (a) Specific capacitance of TiO₂@Co₃O₄ core-shell nanostructure electrode at different scan rates. (b) GCD curves of TiO₂@Co₃O₄ core-shell nanostructure electrode at different discharge current densities.

Figure 3.3.5b shows the galvanostatic charge/discharge curves of TiO₂@Co₃O₄ core-shell nanostructure electrode at various current densities within

the potential window of 0.1-0.5 V. It could be observed that the shape of GCD curves is almost symmetric in all current densities, which suggesting their high coulombic efficiency. The discharge curve consists of two sections, a sudden potential drop followed by a potential decay, which indicates the internal resistance and the capacitive feature of the electrode. According to equation (3), the areal capacitance of the $\text{TiO}_2@\text{Co}_3\text{O}_4$ core-shell nanostructure electrode calculated from the discharge curves are 33, 32 and 26 mF cm^{-2} at the current density of 0.5, 0.75 and 1 mA cm^{-2} , respectively. The decrease of areal capacitance with the increase of discharge current density was due to the insufficient Faradic redox reaction of the active materials under higher discharge current densities [23].

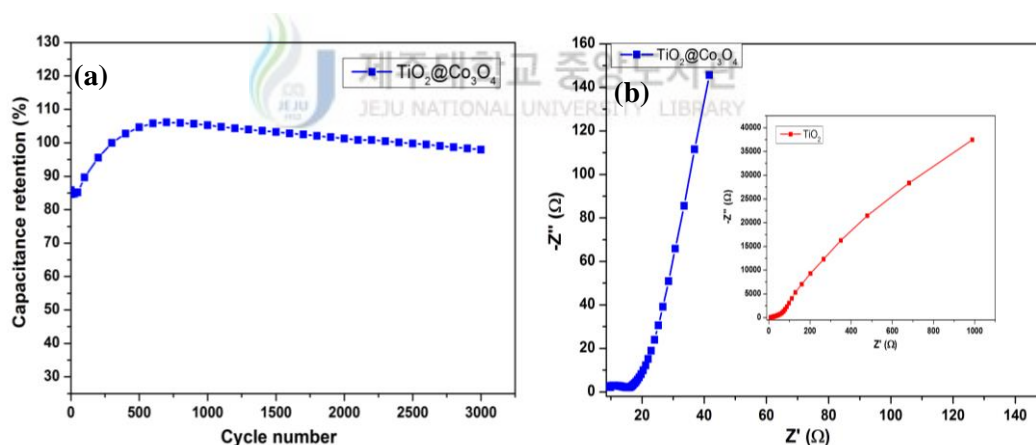


Figure 3.3.6 (a) Cycling stability of $\text{TiO}_2@\text{Co}_3\text{O}_4$ core-shell nanostructure electrode for 3000 cycles. (b) Nyquist plots of $\text{TiO}_2@\text{Co}_3\text{O}_4$ core-shell nanostructure electrode; the inset shows the TiO_2 NR arrays.

Further, the CV measurements were undertaken to investigate the cycling stability of $\text{TiO}_2@\text{Co}_3\text{O}_4$ core-shell nanostructure electrode, which is an important for energy storage practical applications. **Figure 3.3.6a** shows the cycling performance of $\text{TiO}_2@\text{Co}_3\text{O}_4$ core-shell nanostructure electrode for 3000 cycles at a scan rate of 200 mV s^{-1} . As shown in **Figure 3.3.6a** first 500 cycles, the capacitance

retention increases, which is result from the activation process of the electro-active material, after that it decreases subsequently. The $\text{TiO}_2@\text{Co}_3\text{O}_4$ core-shell nanostructure electrode exhibited better cycling stability, retaining 90% of its initial capacitance even after 3000 cycles, suggesting that the core-shell nanostructure electrode have the potential of being used as the electrode materials of supercapacitors.

Resistance is an important parameter for supercapacitor electrode, which was examined by EIS analysis. **Figure 3.3.6b** shows the Nyquist plot of $\text{TiO}_2@\text{Co}_3\text{O}_4$ core-shell nanostructure electrode; the inset shows the TiO_2 NR arrays electrode. Both the plots consists of semi-circle arc at high frequency region and a straight line at low frequency region. It is well-know that the semi-circle reflects the charge transfer resistance of the electrode/electrolyte interface and a line indicates the Warburg impedance related to the diffusion of electroactive species within the pores of the electrode [6, 23]. As shown in **Fig.3.3.6b**. the core-shell nanostructure electrode exhibited smaller charge transfer resistance compared to TiO_2 NRs arrays which indicating that the $\text{TiO}_2@\text{Co}_3\text{O}_4$ core-shell nanostructure electrode has better electronic conductivity and faster ion diffusion rate.

The advantage of $\text{TiO}_2@\text{Co}_3\text{O}_4$ core-shell nanostructure is (i) vertically aligned TiO_2 NRs can form good electrical contacts with the active materials and good mechanical adhesion to the current collector, leading to a decrease in the contact resistance without the use of any polymeric binders and conductive additives. (ii) The combination of TiO_2 NRs and Co_3O_4 nanowall arrays provides a large surface area to facilitate the penetration of the electrolyte into the electrode. (ii) The Co_3O_4 nanowalls reduced the diffusion path of the active species and facilitated the

fast diffusion of the electrolyte into the inner region of the electrode, resulting in an enhanced capacitance and rate capability. These results confirmed that as-fabricated core-shell electrode materials are suitable for high-performance supercapacitors.

3.3.4. Conclusion

We have reported a fabrication of $\text{TiO}_2@\text{Co}_3\text{O}_4$ core-shell nanostructure on a conductive substrate and comparatively investigated their electrochemical performance in energy storage applications. The as-fabricated samples were characterized by XRD, FE-SEM, and XPS. The pseudocapacitive performance of the electrode was investigated by CV and GCD measurements in 2 M KOH aqueous solution. The as-fabricated core-shell electrode delivered high areal capacitance as well as excellent cycle life and high capacitance retention, making them suitable for high-performance supercapacitor applications. Such fascinating capacitive behavior is attributed to the unique core-shell nanostructure and the synergistic effects of the combined pseudocapacitive contributions from the core TiO_2 nanorod array and the Co_3O_4 shell layer. This result demonstrated that as-fabricated core-shell electrode materials are suitable for high-performance supercapacitors.

3.3.5. References

- [1] M. J. Deng, F. L. Huang, I. W. Sun, W. T. Tsai, and J. K. Chang, An entirely electrochemical preparation of a nano-structured cobalt oxide electrode with superior redox activity. *Nanotechnology* 20 (2009) 175602-175606.
- [2] H. W. Wang, Z. A. Hu, Y. Q. Chang, Y. L. Chen, Z. Q. Lei, Z. Y. Zhang, and Y. Y. Yang, Facile solvothermal synthesis of a graphene nanosheet-bismuth oxide composite and its electrochemical characteristics. *Electrochim. Acta* 55 (2010) 8974-8980.
- [3] Y. Shan., and L. Gao, Formation and characterization of multi-walled carbon nanotubes/Co₃O₄ nanocomposites for supercapacitors. *Mater. Chem. Phys.* 103 (2007) 206-210.
- [4] C. Lin, J.A. Ritter, and B.N. Popov, Characterization of sol-gel-derived cobalt oxide xerogels as electrochemical capacitors. *J. Electrochem. Soc.* 145 (1998) 4097-4103.
- [5] G. Wang, L. Zhang and J. Zhang, A review of electrode materials for electrochemical supercapacitors. *Chem. Soc. Rev.* 41 (2012) 797-828.
- [6] Y. Y. Gao, S. L. Chen, D. X. Cao, G. L. Wang, and J. L. Yin, Electrochemical capacitance of Co₃O₄ nanowire arrays supported on nickel foam. *J. Power Sources* 195 (2010) 1757-1760.
- [7] J. Xu, L. Gao, J. Cao, W. Wang, and Z. Chen, Preparation and electrochemical capacitance of cobalt oxide (Co₃O₄) nanotubes as supercapacitor material. *Electrochim. Acta* 56 (2010) 732–736
- [8] V. R. Shinde, S. B. Mahadik, T. P. Gujar, and C. D. Lokhande, Supercapacitive cobalt oxide (Co₃O₄) thin films by spray pyrolysis. *Appl.*

Surf. Sci. 252 (2006) 7487-7492.

- [9] V. Srinivasan, and J. W. Weidner, Capacitance studies of cobalt oxide films formed via electrochemical precipitation. *J. Power Sources* 108 (2002) 15-20.
- [10] T.Y. Wei, C.H. Chen, K.H. Chang, S.Y. Lu, and C.C. Hu, Cobalt oxide aerogels of ideal supercapacitive properties prepared with an epoxide synthetic route. *Chem. Mater.* 21 (2009) 3228-3233.
- [11] W. Lu, R. Hartman, L. Qu, and L. Dai, Nanocomposite electrodes for high-performance supercapacitors. *J. Phys. Chem. Lett.* 2 (2011) 655-660.
- [12] A. Ghosh, E.J. Ra, M. Jin, H.-K. Jeong, T.H. Kim, C. Biswas, and Y.H. Lee, High pseudocapacitance from ultrathin V_2O_5 films electrodeposited on self-standing carbon-nanofiber paper. *Adv. Funct. Mater.* 21 (2011) 2541-2547.
- [13] W. Tang, L. Liu, S. Tian, L. Li, Y. Yue, Y. Wu, and K. Zhu, Aqueous supercapacitors of high energy density based on MoO_3 nanoplates as anode material. *Chem. Commun.* 47 (2011) 10058-10060.
- [14] Q. Qu, Y. Zhu, X. Gao, and Y. Wu, Core-shell structure of polypyrrole grown on V_2O_5 nanoribbon as high performance anode material for supercapacitors, *Adv. Energy Mater.* 2 (2012) 950-955.
- [15] C. D. Lokhande, D. P. Dubal, and O. S. Joo, Metal oxide thin film based supercapacitors. *Curr. Appl. Phys.* 11 (2011) 255-270.
- [16] X.H. Xia, J.P. Tu, X.L. Wang, C.D. Gu, and X.B. Zhao, Hierarchically porous NiO film grown by chemical bath deposition via a colloidal crystal template as an electrochemical pseudocapacitor material. *J. Mater. Chem.* 21 (2011) 671-679.
- [17] X.H. Xia, J.P. Tu, Y.J. Mai, X.L. Wang, C.D. Gu, and X.B. Zhao, Self-

- supported hydrothermal synthesized hollow Co_3O_4 nanowire arrays with high supercapacitor capacitance. *J. Mater. Chem.* 21 (2011) 9319-9325.
- [18] X. Lu, M. Yu, G. Wang, T. Zhai, S. Xie, Y. Ling, Y. Tong, and Y. H. Li, $\text{TiO}_2@ \text{MnO}_2//\text{H-TiO}_2@ \text{C}$ core-shell nanowires for high performance and flexible asymmetric supercapacitors. *Adv. Mater.* 25 (2013) 267-272.
- [19] H. Zheng, T. Zhai, M. Yu, S. Xie, C. Liang, W. Zhao, S. C. Wang, Z. Zhang, and X. Lu, $\text{TiO}_2@ \text{C}$ core-shell nanowires for high-performance and flexible solid-state supercapacitors. *J. Mater. Chem. C* 1 (2013) 225-229.
- [20] M. C. Biesinger, B. P. Payne, A. P. Grosvenor, L. W.M. Lau, A. R. Gerson, and St.C. Smart, Resolving surface chemical states in XPS analysis of first row transition metals, oxides and hydroxides: Cr, Mn, Fe, Co and Ni. *Appl. Surf. Sci.* 257 (2011) 2717-2730.
- [21] C. Xiang, M. Li, M. Zhi, A. Manivannan, and N. Wu, A reduced graphene oxide/ Co_3O_4 composite for supercapacitor electrode. *J. Power Sources* 226 (2013) 65-70.
- [22] L.B. Kong, J.W. Lang, M. Liu, Y.C. Luo, and L. Kang, Facile approach to prepare loose-packed cobalt hydroxide nano-flakes materials for electrochemical capacitors. *J. Power Sources* 194 (2009) 1194-1201.
- [23] J.B. Wu, Y. Lin, X.H. Xia, J.Y. Xu, and Q.Y. Shi, Pseudocapacitive properties of electrodeposited porous nanowall Co_3O_4 film, *Electrochim. Acta* 56 (2011) 7163- 7170.

3.4. Synthesis and Electrochemical Performance of TiO₂@Co(OH)₂ Core-Shell Nanostructure

3.4.1. Introduction

Titanium dioxide (TiO₂) and cobalt hydroxide (Co(OH)₂) are considered to be two of the most promising materials due their low cost, natural abundance, low toxicity, and relatively small environmental impact [1-3]. These materials have a wide range of existing and potential applications, including supercapacitors, lithium-ion batteries, gas sensors, electrocatalysts, and magnetic devices [1, 4, 5]. Co(OH)₂ has a high theoretical capacitance and excellent redox activity [6, 7], and TiO₂ is an electrochemically stable semiconductor and is commonly used as electrodes in electrochemical devices [8]. However, these materials may not provide high specific capacitance at higher current densities, and therefore much attention has been paid to improving the specific capacitance, structural stability, and electrochemical stability at high current densities.

One of the most promising approaches is to construct complex nanoscale architectures with a combination of two types of materials and/or structures on a conducting substrate as binder-free electrodes for high-performance supercapacitors. Hierarchical nano-architectures possess a large specific surface area and can exploit synergetic properties of materials and short ionic and electronic diffusion paths, which can lead to faster kinetics, more efficient contacts with the electrolyte ions, and more electroactive sites for Faradaic energy storage, resulting in high specific capacitance at high current densities [9, 10, 11]. Therefore, designing suitable electrodes with a suitable nanostructure is of much interest, and recently much effort

has been devoted to the synthesis of advanced hierarchical nano-architectures that combine two materials that exhibit improved electrochemical performance [12-16].

In this chapter, we describe a simple method to prepare TiO₂ nanorods (NRs)/porous Co(OH)₂ nanowall bilayer hierarchical nanostructures on fluorine-doped tin oxide (FTO) substrates. This synthetic approach is based on the combination of hydrothermal synthesis (the TiO₂ NR sub-structure) and electrodeposition methods (the Co(OH)₂ nanowall superstructure), which results in the unique structure and morphology. Compared with bare TiO₂ NR array electrodes, the bilayer hierarchical nanostructured electrode exhibited markedly improved electrochemical performance with a higher areal specific capacitance as well as better cycling stability. This hierarchical architecture provides a large surface area and large number of active sites to facilitate ion and electron transfer, which leads to the larger specific areal capacitance than the single-layer structure.

3.4.2. Experimental methods

3.4.2.1. Preparation of TiO₂/Co(OH)₂ hierarchical nanostructure

All reagents used in these experiments were of analytical grade and were used directly without further purification. TiO₂ NRs were grown on FTO substrates using a hydrothermal deposition method, as described in previous **Chapter.3.1**. Co(OH)₂ nanowalls were grown over the TiO₂ NRs by cathodic electrodeposition. Briefly, the electrolyte for electrodeposition was obtained by dissolving 6 g of Co(NO₃)₂ and 0.85 g of NaNO₃ in 100 mL of distilled water. Electrodeposition was carried out in a standard three-electrode system. The TiO₂ NRs were coated on the FTO substrate as the working electrode, Ag/AgCl was used as the reference electrode, and a platinum foil was used as the counter electrode. Electrodeposition was carried

out using a cyclic voltammetry (CV) system with an applied potential in the range of -0.4 to -1 V at a scan rate of 10 mV s^{-1} over four cycles. The deposited samples were removed and rinsed with distilled water, and then samples were dried in an oven for 1 hour at 60 °C. The mass of the $\text{TiO}_2/\text{Co}(\text{OH})_2$ hierarchical nanostructure was calculated from the difference in weight of the before and after deposition measured with a highly sensitively balance with precision down to $10 \text{ }\mu\text{g}$. The loading mass of the $\text{TiO}_2/\text{Co}(\text{OH})_2$ hierarchical nanostructure was 0.55 mg/cm^2 . The crystal structure, morphology and composition of the samples was investigated using XRD, FE-SEM and XPS measurements.

3.4.2.2. Electrochemical characterization

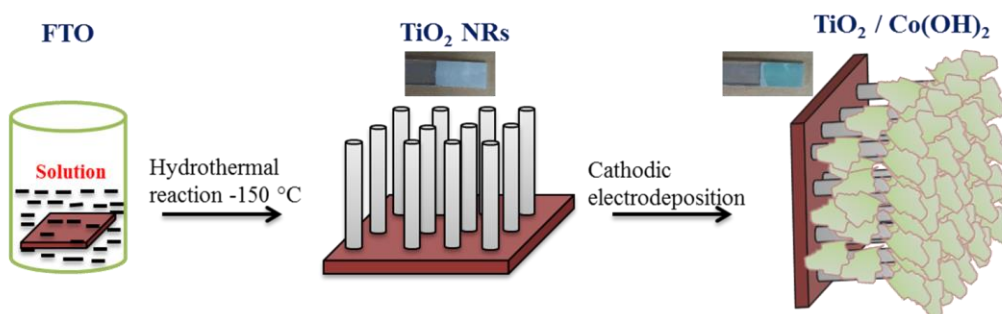
All the electrochemical measurements were performed using an Autolab PGSTAT302N in a standard three-electrode system consisting of the $\text{TiO}_2/\text{Co}(\text{OH})_2$ hierarchical nanostructured electrode as the working electrode, a saturated calomel electrode as the reference electrode, and a platinum counter electrode in a 2 M KOH electrolyte. The electrochemical behaviour of the as-prepared electrodes was characterised using CV and galvanostatic charge–discharge tests. The CV was carried out in a potential range of -0.1 to $+0.5$ V at a range of scan rates. Constant-current charge–discharge tests were carried out at different current densities within a potential range of -0.1 to $+0.5$ V.

3.4.3. Results and discussion

3.4.3.1. Synthesis and characterisation

Our approach to fabricate the $\text{TiO}_2/\text{Co}(\text{OH})_2$ hierarchical nanostructures involved two steps, as shown in **Scheme 3.4.1**. First, the sub-structure of vertically aligned TiO_2 NR arrays was grown on the FTO substrate using the hydrothermal

method. Second, the superstructure of $\text{Co}(\text{OH})_2$ nanowalls was deposited onto the top surface of the TiO_2 NRs using electrodeposition.



Scheme 3.4.1 Schematic diagram showing the $\text{TiO}_2/\text{Co}(\text{OH})_2$ hierarchical nanostructure growth process.

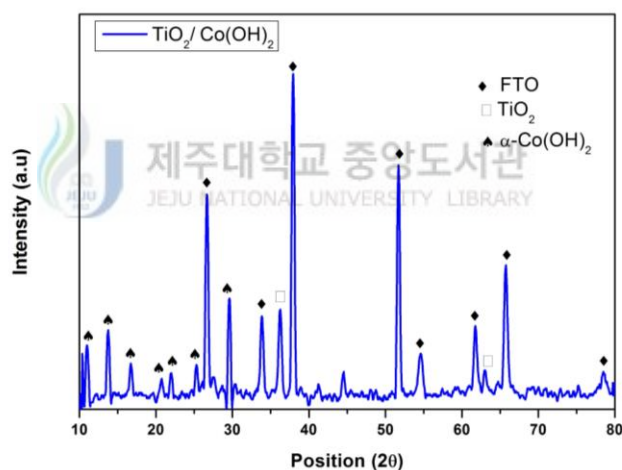


Figure 3.4.1 XRD pattern of the $\text{TiO}_2/\text{Co}(\text{OH})_2$ hierarchical nanostructure, showing the tetragonal rutile phase of TiO_2 NRs (JCPDS no:21-1276) and the α -phase of the $\text{Co}(\text{OH})_2$ nanowalls (JCPDS no:02-0925).

The crystal structure of the $\text{TiO}_2/\text{Co}(\text{OH})_2$ hierarchical nanostructure was examined using XRD measurements. **Figure 3.4.1** shows a typical XRD pattern of the $\text{TiO}_2/\text{Co}(\text{OH})_2$ hierarchical nanostructure. It can be clearly seen that the $\text{TiO}_2/\text{Co}(\text{OH})_2$ hierarchical nanostructure exhibited a tetragonal rutile phase of TiO_2 NRs and α -phase of the $\text{Co}(\text{OH})_2$ nanowall. The peaks represented by diamond symbols in the figure correspond to the FTO substrate.

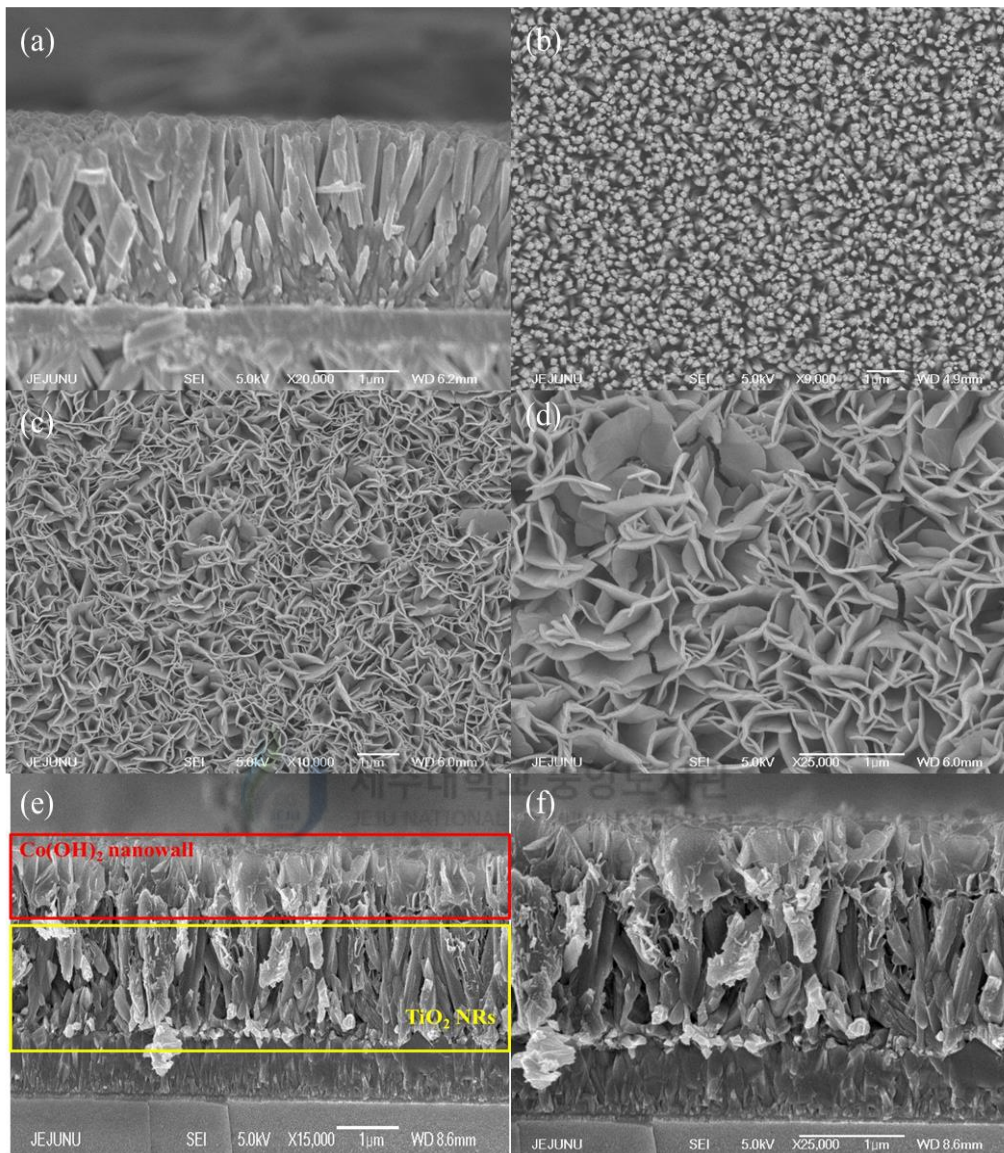


Figure 3.4.2 (a) Cross-sectional and (b) plan view FE-SEM images of the TiO_2 NR arrays; (c) and (d) show plan view FE-SEM images of the $\text{TiO}_2/\text{Co}(\text{OH})_2$ hierarchical nanostructure; and (e) and (f) show cross-sectional FE-SEM images of the $\text{TiO}_2/\text{Co}(\text{OH})_2$ hierarchical nanostructure.

Figures 3.4.2a shows cross-sectional field-enhanced scanning electron microscope (FE-SEM) images, and **Figure 3.4.2b** shows plan view FE-SEM images of the TiO_2 NRs. It can be clearly seen that the as-prepared TiO_2 NRs had a tetragonal structure, were highly uniform, and formed a densely packed array of vertically aligned NRs. The average diameter of the TiO_2 NRs was 100–150 nm, and

they were 1.2–1.8 μm long. **Figures 3.4.2c** and **2d** show typical FE-SEM images of hierarchical and nanowall-like structures of $\text{TiO}_2/\text{Co}(\text{OH})_2$ hierarchical nanostructures. The $\text{Co}(\text{OH})_2$ nanowalls, with an average diameter of 30 nm, uniformly covered the tip of the TiO_2 NRs. **Figures 3.4.2e** and **2f** show cross-sectional FE-SEM images of $\text{TiO}_2/\text{Co}(\text{OH})_2$ hierarchical nanostructures, revealing that the $\text{Co}(\text{OH})_2$ nanowalls were grown directly on the tips of the TiO_2 NRs. The length of the $\text{Co}(\text{OH})_2$ nanowalls was approximately 0.8–1 μm .

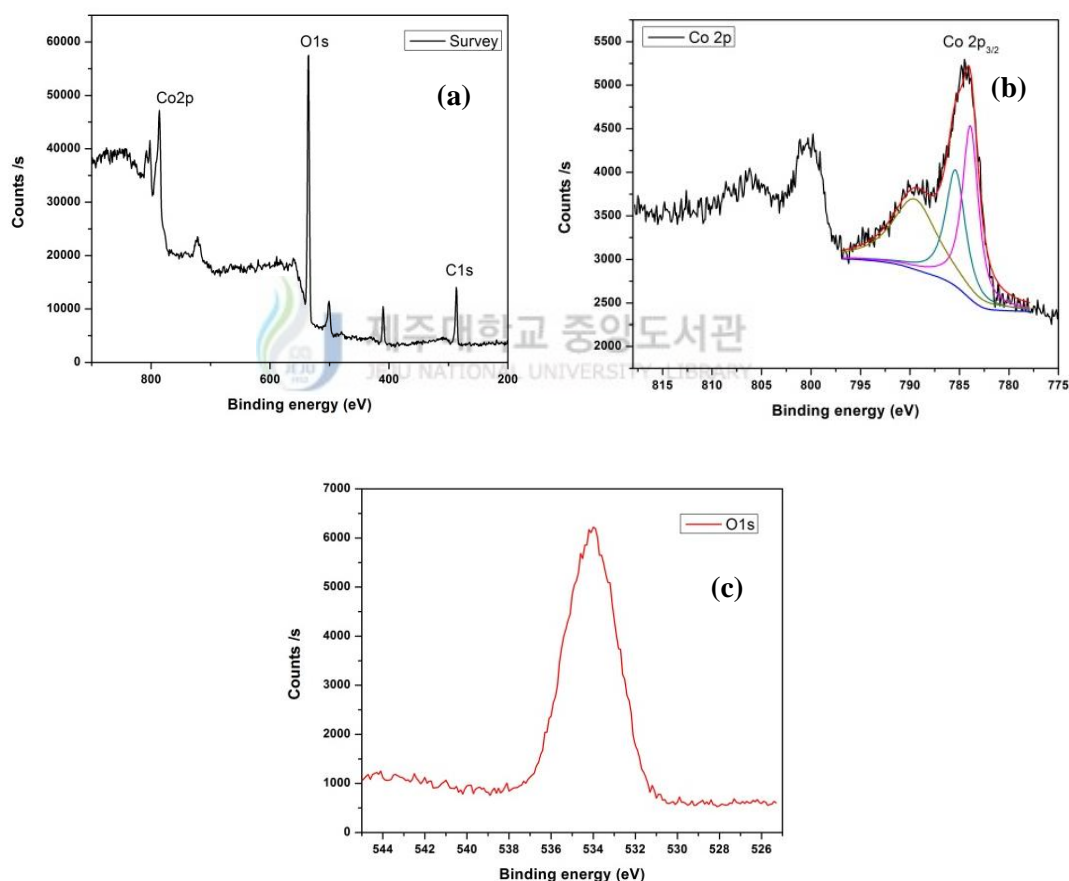


Figure 3.4.3 XPS spectra of the $\text{TiO}_2/\text{Co}(\text{OH})_2$ hierarchical nanostructure. (a) Survey, (b) Co 2p, and (c) O 1s.

The chemical composition of the $\text{TiO}_2/\text{Co}(\text{OH})_2$ hierarchical nanostructure was investigated using XPS analysis. As shown in **Figure 3.4.3a**, the XPS spectrum exhibited the characteristic peaks corresponding to Co 2p, O 1s, and C 1s [17]. No Ti

2p peaks were observed, which indicates that a TiO₂/Co(OH)₂ hybrid nanostructure was formed. The high-resolution spectrum of Co 2p shown in **Figure 3.4.3b** reveals splitting of the two spin-orbit components, namely the 2p 1/2 (799.8 eV) and 2p 3/2 (784.2 eV) levels, and both components were of the same magnitude [17, 18]. As shown in **Figure 3.4.3b**, the higher-intensity Co 2p bands were fitted using three Gaussians. The signal was deconvolved into peaks at 783.6, 785.5, and 789.6 eV, corresponding to cobalt hydroxide, which confirms the formation of Co(OH)₂ [17, 18]. **Figure 3.4.3c** shows a high-resolution spectrum of O 1s. The peak located at 530.5 eV was assigned to OH ions.

3.4.3.2. Electrochemical analysis

The electrochemical performance of the as-prepared electrodes was investigated using CV and galvanostatic charge–discharge measurements in a 2 M KOH electrolyte. **Figure 3.4.4a** shows CV curves of the TiO₂ NRs and the TiO₂/Co(OH)₂ hierarchical nanostructure at a scan rate of 5 mV s⁻¹ in the potential range from -0.1 to +0.5 V.

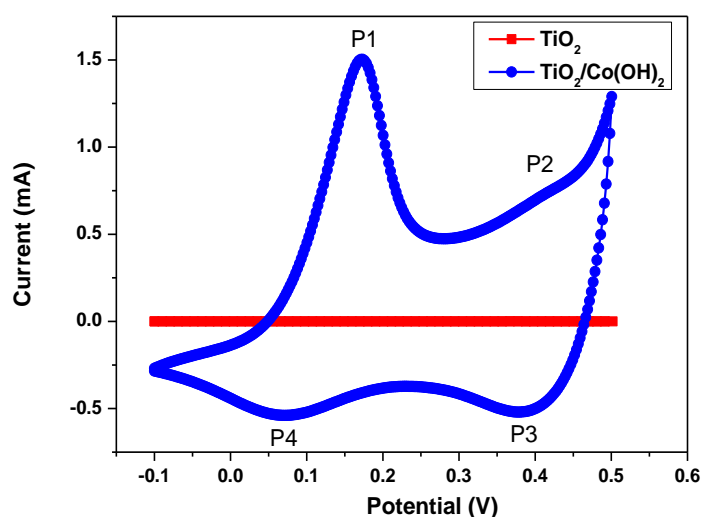
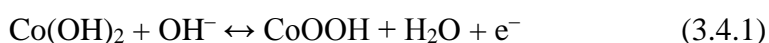


Figure 3.4.4 (a) CV curves of the TiO₂ NRs and TiO₂/Co(OH)₂ hierarchical nanostructured electrodes.

As shown in **Figure 3.4.4a**, the shape of the CV curves indicates pseudocapacitive behaviour. Furthermore, the CV curves exhibited two pairs of redox peaks (P1 vs P4 and P2 vs P3), as opposed to the ideal rectangular form. Two plausible electrochemical reactions corresponding to the redox peaks can be expressed as follows [19, 20]:

- (i) The first redox pair (P1 vs P4) corresponds to the conversion between Co(OH)_2 and CoOOH :



- (ii) The second redox pair (P2 vs P3) corresponds to the conversion between CoOOH and CoO_2 :



These two reactions explain the pseudocapacitive properties of the $\text{TiO}_2/\text{Co(OH)}_2$ hierarchical nanostructured electrode. Moreover, from the CV data, the total surface area of the hierarchical electrode was much larger than that of the TiO_2 NR electrode, which indicates that the hierarchical electrode has a higher electrochemical activity. This is attributed to the additional pseudocapacitance contribution of the Co(OH)_2 nanowalls.

Figure 3.4.5a shows CV curves of the $\text{TiO}_2/\text{Co(OH)}_2$ hierarchical nanostructured electrodes at scan rates in the range of 5–125 mV s^{-1} . As the scan rate increased, the anodic peaks shifted toward higher potentials, and cathodic peaks shifted towards larger negative potentials, which indicates quasi-reversible behaviour of the redox pairs [21]. Furthermore, the peak current increased with the scan rate, which indicates good reversibility of the charge–discharge reaction [22].

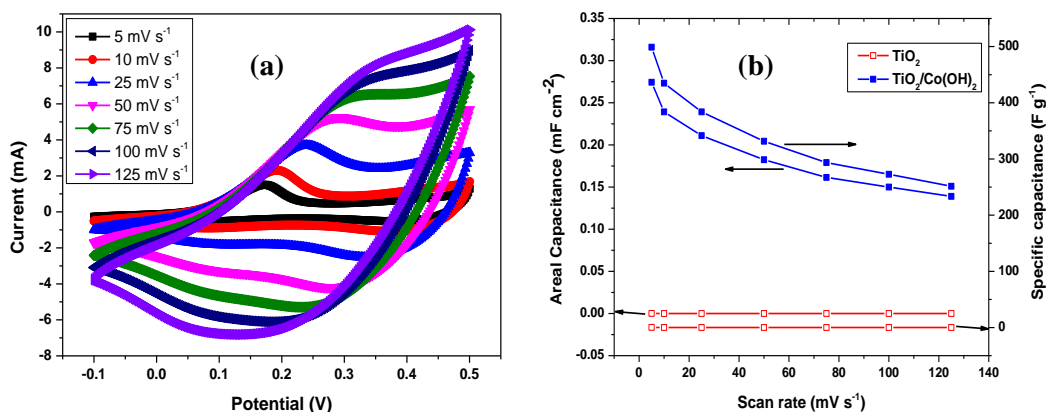


Figure 3.4.5 (a) CV curves of the $\text{TiO}_2/\text{Co}(\text{OH})_2$ hierarchical nanostructured electrode at different scan rates. (b) The areal capacitance and specific capacitance of the TiO_2 NRs and $\text{TiO}_2/\text{Co}(\text{OH})_2$ hierarchical nanostructured electrodes as a function of scan rate.

The areal capacitance of the electrodes, C_a , was calculated from the CV curves using the equation (2.7) [23]. **Figure 3.4.5b** shows the areal capacitances of the TiO_2 NRs and the $\text{TiO}_2/\text{Co}(\text{OH})_2$ hierarchical nanostructured electrodes as a function of the scan rate together with the corresponding specific capacitances for comparison. The areal capacitance of the hierarchical electrode was significantly higher than that of the TiO_2 NR electrode at all scan rates. The areal capacitance decreased with the scan rate in the range of 5–125 mV s^{-1} . This may be due to diffusion-limited behaviour, where only the outer surface was utilised for ion transfer reactions at higher scan rates (presence of inner active sites are inaccessible). At lower scan rates, all the electro-active area (including external and internal surfaces) can be utilised for charge storage and also allow more time for the ions to access the bulk of the oxide [24–26]. The maximum areal capacitance of the TiO_2 NR electrodes was 60.6 $\mu\text{F cm}^{-2}$ (Specific capacitance = 0.202 F g^{-1}) at 5 mV s^{-1} . The areal capacitance of hierarchical nanostructure electrode was 274.3 mF cm^{-2} to 139 mF cm^{-2} (Specific capacitance = 498.8 to 257 F g^{-1}) at a scan rate of 5 mV s^{-1} to 125 mV s^{-1} . This areal capacitance is significantly larger than that previously reported for TiO_2

nanostructures, including untreated TiO₂ and H-TiO₂ nanowire arrays (0.026 mF cm⁻² and 3.24 mF cm⁻² at 100 mV s⁻¹) [27], titania nanotubes and powder (911 μF cm⁻² and 181 μF cm⁻² at 1 mV s⁻¹) [28], TiO₂ nanotubes heat-treated under argon atmosphere (911 μF cm⁻² at 1 mV s⁻¹) [29], self-organized titania (TiO₂) nanotube array (2.6 mF cm⁻² at 1 mV s⁻¹) [30], NiO–ZnO/TiO₂ nanotubes (150 mF cm⁻² at 30 mV s⁻¹) [31], self-doped TiO₂ nanotube arrays (1.84 mF cm⁻² at 5 mV s⁻¹) [32], and H₂ treated bamboo-type TiO₂ nanotubes (3.4 mF cm⁻² at 10 mV s⁻¹) [33], TiO₂ NRs (85 μF cm⁻² at 5 mV s⁻¹) [34], TiO₂/C core/shell nanowire arrays (31.3 mF cm⁻² at 10 mV s⁻¹) [16]. The larger areal capacitance of the hierarchical nanostructured electrode is attributed to its unique morphology and large surface area, which lead to a large contact area between the electrode and electrolyte and to improved surface adsorption/desorption processes of the alkali cations.

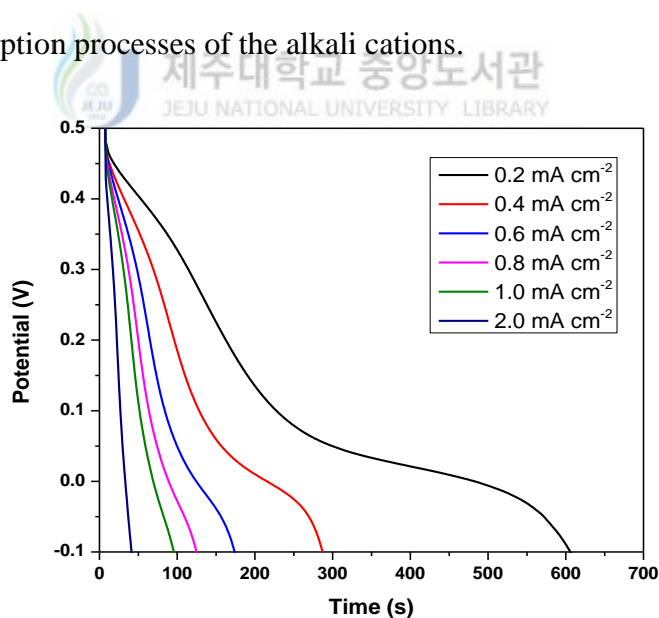


Figure 3.4.6 Discharge curves of the TiO₂/Co(OH)₂ hierarchical nanostructured electrodes at different discharge current densities.

The electrochemical performance of the TiO₂/Co(OH)₂ hierarchical nanostructured electrodes was also characterised using galvanostatic charge–discharge measurements. **Figure 3.4.6** shows the discharge curves of the

TiO₂/Co(OH)₂ hierarchical nanostructured electrode at various discharge current densities in a 2 M KOH electrolyte. The discharge curves exhibit two plateaus, which are consistent with the result of the CV analysis. The areal capacitance values of the hierarchical electrode calculated from the discharge curves were 199, 186, 166, 157, 148 and 113 mF cm⁻² at current densities of 0.2, 0.4, 0.6, 0.8, 1 and 2 mA cm⁻², respectively. The decrease of areal capacitance with increasing current density is explained by insufficient Faradic reactions of the electro-active materials at higher current densities [21, 35]. The results show that the TiO₂/Co(OH)₂ hierarchical nanostructured electrode maintained a high capacitance at large current density, which suggests that the hybrid nanostructured electrode may be suitable for high-energy-density devices.

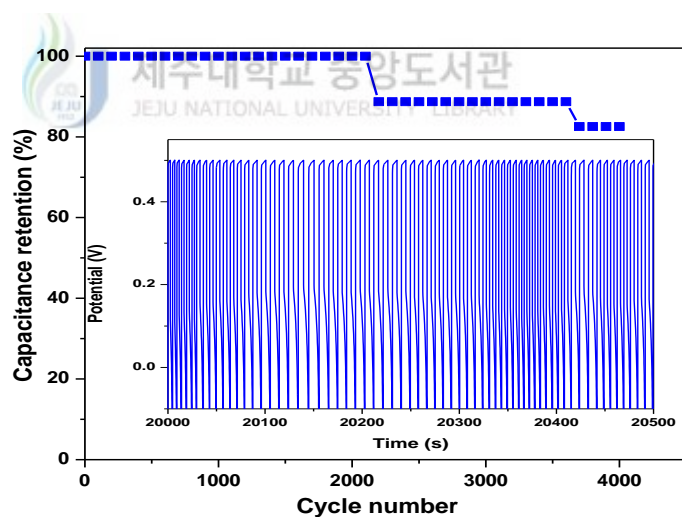


Figure 3.4.7 Cycling performance of TiO₂/Co(OH)₂ hierarchical nanostructured electrode at a current density of 2 mA cm⁻² for 4000 cycles in 2-M KOH solution.

The cycle stability of the TiO₂/Co(OH)₂ hierarchical nanostructured electrodes was evaluated using galvanostatic charge/discharge measurements at an increased current density of 2 mA cm⁻² for 4000 cycles. As shown in **Figure 3.4.7**, the hierarchical nanostructured electrodes exhibited good cycling stability and

reversibility, retaining 82.5% of the initial capacitance value after 4000 cycles and revealing better electrochemical stability than the as-prepared electrodes.

The enhanced electrochemical performance of the hierarchical nanostructured electrodes is attributed to the following factors [2, 8, 36]: First, the vertically aligned TiO₂ NRs can form good electrical contacts with the active materials and good mechanical adhesion to the current collector, leading to a decrease in the contact resistance without the use of any polymeric binders and conductive additives. Second, After cycling for 4000 cycles at current density of 2 mA cm⁻², the hierarchical structure still maintain their structure integrity (with little structural deformation) as well as keep the initial morphology (**Figure 3.4.8a**), which indicate that the hierarchical structure helps to alleviate the structure damage caused by volume expansion during the cycling process, finally resulting to the enhanced cycling stability [12, 37, 38]. Third, the combination of TiO₂ NRs and Co(OH)₂ nanowall arrays with a porous architecture and independent electroactivities in a combined hierarchical nanostructure (**Figure 3.4.8b**) provides a large surface area to facilitate the penetration of the electrolyte into the electrode. The short ionic and electronic diffusion pathways result in a small internal resistance. Fourth, the Co(OH)₂ nanowalls grafted on the TiO₂ NR (tip) backbone are useful for enhancing the electrochemical capacity and cycle stability of the electrode due to the high capacity of the Co(OH)₂ superstructure and the low volume change of the TiO₂ sub-structure. Fifth, the Co(OH)₂ nanowall superstructure is interconnected with the tip of the TiO₂ NR, but did not fully cover the TiO₂ NR array sub-structure. Therefore, almost all the sub-superstructure was accessible to the electrolyte, which facilitated a large areal

capacitance. Sixth, the porous hierarchical nano-architecture with a high surface area results in a large density of sites for ionic transport.

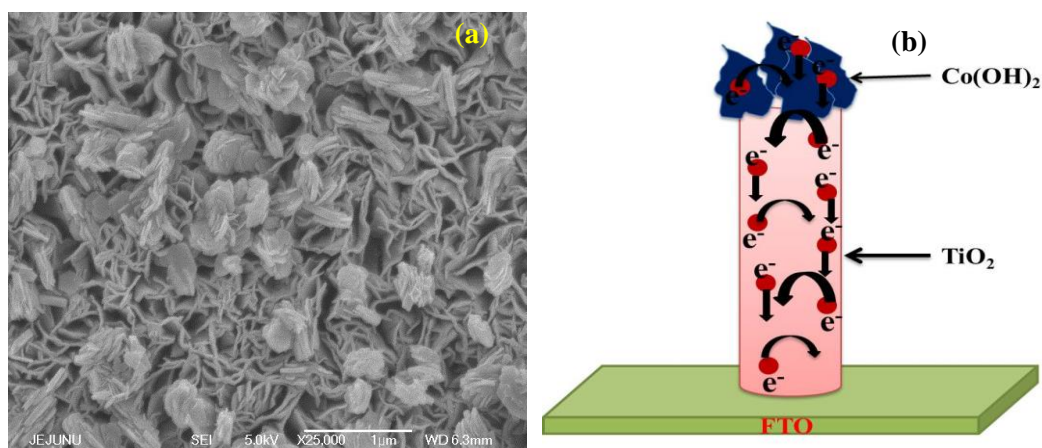


Figure 3.4.8 (a) FE-SEM image of the hierarchical nanostructure, after 4000 cycles. (b) Schematic representation of the direct electron transport path.

3.4.4. Conclusion



We have described a binder-free TiO₂ NR/porous Co(OH)₂ nanowall hierarchical nanostructure on an FTO substrate, which was fabricated using a combination of hydrothermal and electrodeposition techniques. The hierarchical nanostructured electrodes exhibited excellent pseudocapacitive behaviour with a high areal specific capacitance of 274.3 mF cm⁻² and good cycle stability. This electrochemical performance results from the porous bilayer structure, which provides a high surface area and fast ionic and electron transfer.

3.4.5. References

- [1] X. Chen, and S. S. Mao, Titanium dioxide nanomaterials: synthesis, properties, modifications, and applications. *Chem. Rev.* 107 (7) (2007) 2891-2959.
- [2] F. Cao, G.X. Pan, P.S. Tang, and H.F. Chen, Hydrothermal-synthesized $\text{Co}(\text{OH})_2$ nanocone arrays for supercapacitor application. *J. Power Sources*, 216 (2012) 395-399.
- [3] A.D. Jagadale, V.S. Kumbhar, D.S. Dhawale, and C.D. Lokhande, Performance evaluation of symmetric supercapacitor based on cobalt hydroxide [$\text{Co}(\text{OH})_2$] thin film electrodes. *Electrochimica Acta* 98 (2013) 32–38.
- [4] G. K. Mor, O. K. Varghese, M. Paulose, K. Shankar, and C. A. Grimes, A review on highly ordered, vertically oriented TiO_2 nanotube arrays: Fabrication, material properties, and solar energy applications. *Solar Energy Mater. Solar Cells* 90 (2006) 2011–2075.
- [5] C. Mondal, M. Ganguly, P.K. Manna, SM. Yusuf, and T. Pal, Fabrication of porous $\beta\text{-Co}(\text{OH})_2$ architecture at room temperature: A high performance supercapacitor. *Langmuir* 29 (2013) 9179-9187.
- [6] L. Cao, F. Xu, Y.Y. Liang, and H.L. Li, Preparation of the novel nanocomposite $\text{Co}(\text{OH})_2/\text{ultra-stable zeolite}$ and its application as a supercapacitor with high energy density. *Adv. Mater.* 16 (2004) 1853-1857.
- [7] C.C. Hu, and T.Y. Hsu, Effects of complex agents on the anodic deposition and electrochemical characteristics of cobalt oxides. *Electrochim. Acta* 53 (2008) 2386-2395.

- [8] X. Lu , M. Yu , G. Wang , T. Zhai , S. Xie , Y. Ling , Y. Tong , and Y. Li, H-TiO₂@MnO₂//H-TiO₂@C core-shell nanowires for high performance and flexible asymmetric supercapacitors. *Adv. Mater.* 25(2) (2013) 267-272.
- [9] G.Q. Zhang, H. B. Wu Harry E. Hoster, Mary B. Chan-Park, and X. Wen (David) Lou, Single-crystalline NiCo₂O₄ nanoneedle arrays grown on conductive substrates as binder-free electrodes for high-performance supercapacitors, *Energy Environ. Sci.* 5 (2012) 9453–9456.
- [10] J. H. Zhong, A. L. Wang, G. R. Li, J. W. Wang, Y. N. Ou, and Y. X. Tong, Co₃O₄/Ni(OH)₂ composite mesoporous nanosheet networks as a promising electrode for supercapacitor applications. *J. Mater. Chem.* 22 (2012) 5656–5665.
- [11] Y. Zhang, H. Feng, X. B. Wu, L. Wang, A. Zhang, T. Xia, H. Dong, X. Li, and L. Zhang, Progress of electrochemical capacitor electrode materials: A review. *Int J Hydrogen Energy* 34 (2009) 4889–4899.
- [12] X. Liu, S. Shi, Q. Xiong, L. Li, Y. Zhang, H. Tang, C. Gu, X. Wang, and J. Tu, Hierarchical NiCo₂O₄@NiCo₂O₄ core/shell nanoflake arrays as high-performance supercapacitor materials. *ACS Appl. Mater. Interfaces* 5 (17) (2013) 8790–8795.
- [13] J. B. Han, Y. B. Dou, J. W. Zhao, M. Wei, D. G. Evans, and X. Duan, Flexible CoAl LDH@PEDOT core/shell nanoplatelet array for high-performance energy storage. *Small* 9 (2013) 98–106.
- [14] X. H. Lu, T. Zhai, X. H. Zhang, Y. Q. Shen, L. Y. Yuan, B. Hu, L. Gong, J. Chen, Y. H. Gao, J. Zhou, Y. X. Tong, and Z. L. Wang, WO_{3-x}@Au@MnO₂

- core-shell nanowires on carbon fabric for high-performance flexible supercapacitors. *Adv. Mater.* 24 (2012) 938–944.
- [15] X. Xiao, T. P. Ding, L. Y. Yuan, Y. Q. Shen, Q. Zhong, X. H. Zhang, Y. Z. Cao, B. Hu, T. Zhai, L. Gong, J. Chen, Y. X. Tong, J. Zhou, and Z. L. Wang, $\text{WO}_{3-x}/\text{MoO}_{3-x}$ core/shell nanowires on carbon fabric as an anode for all-solid-state asymmetric supercapacitors. *Adv. Energy Mater.* 2 (2012) 1328–1332.
- [16] H. M. Zheng, T. Zhai, M. H. Yu, S. L. Xie, C. L. Liang, W. X. Zhao, S. C. I. Wang, Z. S. Zhang, and X. H. Lu, $\text{TiO}_2@\text{C}$ core-shell nanowires for high-performance and flexible solid-state supercapacitors. *J. Mater. Chem. C* 1 (2013) 225–229.
- [17] J. Yang, H. Liu, W. N. Martens, and R. L. Frost, Synthesis and characterization of cobalt hydroxide, cobalt oxyhydroxide, and cobalt oxide nanodiscs. *J. Phys. Chem. C* 114 (2010) 111–119.
- [18] M. C. Biesinger, B. P. Payne, A. P. Grosvenor, L. W.M. Lau, A. R. Gerson, and St.C. Smart, Resolving surface chemical states in XPS analysis of first row transition metals, oxides and hydroxides: Cr, Mn, Fe, Co and Ni. *Appl. Surf. Sci.* 257 (2011) 2717–2730.
- [19] F. Tao, Y. Shen, Y. Liang, and H. Li, Synthesis and characterization of $\text{Co}(\text{OH})_2/\text{TiO}_2$ nanotube composites as supercapacitor materials. *J Solid State Electrochem.* 11 (2007) 853–858.
- [20] L. Wang, Z. H. Dong, Z. G. Wang, F. X. Zhang, and J. Jin, Layered $\alpha\text{-Co}(\text{OH})_2$ nanocones as electrode materials for pseudocapacitors:

- Understanding the effect of interlayer space on electrochemical activity. *Adv. Funct. Mater.* 23 (2013) 2758–2764.
- [21] L.B. Kong, J.W. Lang, M. Liu, Y.C. Luo, and L. Kang, Facile approach to prepare loose-packed cobalt hydroxide nano-flakes materials for electrochemical capacitors. *J. Power Sources* 194 (2009) 1194-1201.
- [22] Q.H. Huang, X.Y. Wang, and J. Li, Characterization and performance of hydrous manganese oxide prepared by electrochemical method and its application for supercapacitors. *Electrochim. Acta* 52 (2007) 1758-1762.
- [23] K. Wang, H. Wu, Y. Meng, Y. Zhang, and Z. Wei, Integrated energy storage and electrochromic function in one flexible device: an energy storage smart window. *Energy Environ. Sci.* 5 (2012) 8384-8389.
- [24] J. Yan, T. Wei, W. Qiao, B. Shao, Q. Zhao, L. Zhang, and Z. Fan, Rapid microwave-assisted synthesis of graphene nanosheet/Co₃O₄ composite for supercapacitors, *Electrochimica Acta*, 55 (2010) 6973–6978.
- [25] S Park, and S Kim, Effect of carbon blacks filler addition on electrochemical behaviors of Co₃O₄/graphene nanosheets as a supercapacitor electrodes, *Electrochimica Acta*, 89 (2013) 516– 522.
- [26] C. D. Lokhande, T. P. Gujar, V.R. Shinde, R. S. Mane, and S. H. Han, Electrochemical supercapacitor application of perovskite thin films, *Electrochem. Comm.*, 9 (2007) 1805-1809.
- [27] X. Lu, G. Wang, T. Zhai, M. Yu, J. Gan, Y. Tong, and Y. Li, Hydrogenated TiO₂ nanotube arrays for supercapacitors. *Nano Lett.* 12 (2012) 1690-1696.

- [28] M. Salari, S.H. Aboutalebi, K. Konstantinov, and H.K. Liu, A highly ordered titania nanotube array as a supercapacitor electrode. *Phys. Chem. Chem. Phys.* 13 (2011) 5038-5041.
- [29] M. Salari, K. Konstantinov and H. K. Liu, Enhancement of the capacitance in TiO₂ nanotubes through controlled introduction of oxygen vacancies, *J. Mater. Chem.*, 21 (2011) 5128–5133
- [30] M. Salari, S. H. Aboutalebi, A. T. Chidembo, I. P. Nevirkovets, K. Konstantinov and H. K. Liu, Enhancement of the electrochemical capacitance of TiO₂ nanotube arrays through controlled phase transformation of anatase to rutile, *Phys. Chem. Chem. Phys.*, 14 (2012) 4770–4779.
- [31] F. Gobal and M. Faraji, Fabrication of nanoporous nickel oxide by de-zincification of Zn–Ni/(TiO₂-nanotubes) for use in electrochemical supercapacitors, *Electrochimica Acta* 100 (2013) 133– 139.
- [32] H. Zhou and Y. Zhang, Electrochemically self-doped TiO₂ nanotube arrays for supercapacitors, *J. Phys. Chem. C*, 118 (2014) 5626–5636.
- [33] B. Chen, J. Hou, and K. Lu, Formation mechanism of TiO₂ nanotubes and their applications in photoelectrochemical water splitting and supercapacitors, *Langmuir*, 29 (2013) 5911–5919.
- [34] A. Ramadoss, and S. J. Kim, Vertically aligned TiO₂ nanorod arrays for electrochemical supercapacitor. *J Alloys compd.* 561 (2013) 262-267.
- [35] L. B. Kong, M. C. Liu, and J. W. Lang, Porous cobalt hydroxide film electrodeposited on nickel foam with excellent electrochemical capacitive behavior. *J Solid State Electrochem*, 15 (2011) 571–577.

- [36] J. Liu, J. Jiang, C. Cheng, H. Li, J. Zhang, H. Gong, and H. J. Fan, Co_3O_4 Nanowire@ MnO_2 ultrathin nanosheet core/shell arrays: a new class of high-performance pseudocapacitive materials. *Adv. Mater.* 23 (2011) 2076–2081.
- [37] X. H. Xia, J. P. Tu, Y. J. Mai, X. L. Wang, C. D. Gu, and X. B. Zhao, Self-supported hydrothermal synthesized hollow Co_3O_4 nanowire arrays with high supercapacitor capacitance, *J. Mater. Chem.*, 21, (2011) 9319–9325.
- [38] X. Xia, J. Tu, Y. Zhang, J. Chen, X. Wang, C. Gu, C. Guan, J. Luo, and H. J. Fan, Porous hydroxide nanosheets on preformed nanowires by electrodeposition: Branched nanoarrays for electrochemical energy storage, *Chem. Mater.*, 24 (2012) 3793–3799.



CHAPTER-IV

Two Dimensional Nanomaterials for Electrochemical Supercapacitors

It is well-known that electrode materials play a crucial role in the development of high performance supercapacitors in terms of morphology, porosity, and size [1]. Recently, two dimensional (2-D) nanomaterials showing promising sign for construction of flexible energy storage devices compared to one dimensional (1-D) and three dimensional (3-D) materials due to the synergic advantages of high specific surface areas, high mechanical strength (originates from the large overlapping areas when they are stacked layer-by-layer to form a thin film structure) as well as enriched electrochemical performance [2-6]. In addition to that, 2-D nanomaterials exhibit fascinating mechanical properties, including bending/folding strength as well as excellent flexibility. Moreover, the high surface areas of the 2D nanomaterials provides lots of electro-active sites for electrochemical reactions and electron transport, which are of great advantage in enhancing the electrochemical performance of the supercapacitors. Based on the above considerations, finding new 2D nanomaterials with improved electrochemical performances would be the next essential step for flexible supercapacitors.

Recently, two-dimensional (2D) nanomaterials such as graphene [7-9] transition metal oxides [10-13] transition metal chalcogenides [14-16] and their composites [17-22] are widely attracted in numerous applications for next generation nano-electronic devices including supercapacitors and lithium-ion batteries. Their two dimensional nature has brought great advantages in achieving both high electrochemical performance and excellent high flexibility. Among the various

electrode materials, the graphene and molybdenum sulfides (MoS_2) shown more attention due to their high conductivity, high mechanical strength and high surface area providing numerous sites for reaction and fast electron/ion transport, finally leading to the enhanced capacitive performance.

Herein, we focus the synthesis and electrochemical performance of 2-D nanomaterials for electrochemical supercapacitors. In the first section, we describe the facile and low cost synthesis of MoS_2 nanosheets electrode materials for supercapacitors. In the last section, we describe the fabrication of graphene coated carbon fabric electrode for flexible supercapacitors. The obtained electrochemical performance results of binder-free graphene coated fabric electrode have shown promising signs as the best candidates for flexible supercapacitors.



4.1. Synthesis and Electrochemical Performance of MoS₂ Nanostructure

4.1.1. Introduction

Molybdenum disulfide (MoS₂) has layered structure like graphite with strong interlayer covalent bonds separated by a weak van der Waals force [23,24]. It exhibits the unique physical, optical, electrical properties and high surface area making them as promising materials in various fields such as catalysis, nano-electronics, optoelectronics, hydrogen storage, Li-ion batteries, and supercapacitors [25-28]. Due to its high surface area, electrical conductivity and sheet-like morphology exhibit the better capacitive properties for electrochemical double layers. The advantage of using MoS₂ over metal oxides and graphite for supercapacitor applications are mainly due to its higher intrinsic fast ionic conductivity than oxides and higher theoretical capacity than graphite [22,29,30]. In addition to electrochemical double layer capacitance, MoS₂ provides faradaic capacitance at lower scan rate due to diffusion of the electrolyte ions into the layered structure which could enhance the charge storage behavior [22].

In recent times, MoS₂ with specific morphologies and unique properties is of great attention to researchers exploring the design of MoS₂ materials. Therefore, various synthetic approaches has been developed to prepare MoS₂ nanostructures with different morphologies using sonochemical synthesis, gas-phase reactions, laser ablation, thermal decomposition, magnetron sputtering, electron-beam irradiation activation and microwave irradiation techniques [31-37]. Among the various synthesis methods, the hydrothermal method has been considered to be one of the most promising synthetic approaches, due to its facile, low cost, low temperature, high efficiency and good crystallinity of the product. Various morphologies such as

flower-like microspheres [38,39], nanospheres [40], nanorods [41], nanowires [42] and nanofibers [43] have been reported on the preparation of MoS₂ using hydrothermal method.

To the best our knowledge, there have been only very few reports available on MoS₂ nanostructures for supercapacitor applications. Soon et al. [44] prepared MoS₂ nanowall films by thermal evaporation method and obtained a maximum specific capacitance of 100 F g⁻¹ at a scan rate of 1 mV s⁻¹. Ma et al. [45] synthesized MoS₂ and polypyrrole/molybdenum disulfide nanocomposite, which exhibited a specific capacitance of 235 and 553.7 F g⁻¹ at 1 A g⁻¹ in a solution of 1 M KCl. Hu et al. [46] prepared tubular C/MoS₂ nanocomposite and delivered a specific capacitance of 210 F g⁻¹ at 1 A g⁻¹. However, the rate performance and cycling stability of the electrode materials are still unsatisfactory.

In this chapter, we have presented a novel mesoporous MoS₂ nanostructure synthesized via hydrothermal method for electrochemical supercapacitor. The structural, morphology and electrochemical performance of the electrode materials were investigated. The results confirmed that the as-prepared mesoporous MoS₂ nanostructure electrode exhibited an enhanced electrochemical behavior.

4.1.2. Experimental methods

4.1.2.1. Synthesis and characterization of mesoporous MoS₂ nanostructure

In a typical synthesis, 0.120 g sodium molybdate and 0.240 g thioacetamide was dissolved in to 80 mL of deionized (DI) water with continuous stirring. The as-obtained mixture was loaded into a Teflon-lined stainless steel autoclave and heated at 200 °C for 24 h. After synthesis, the Teflon reactor was cooled to room temperature naturally and then the mixture was washed with DI water for several

times and centrifuged at 10000 rpm for 10 minutes to remove the residuals and then dried at 60 °C for 10 h. The structure and morphology properties of the as-prepared samples were examined using XRD, FE-SEM, and HR-TEM. The chemical composition of the MoS₂ was obtained by EDX, and XPS. Nitrogen (N₂) adsorption/desorption isotherms of the as-prepared samples were collected with the assistance of Quantachrome's Quadasorb SI analyzer at 77 K. The Brunauer-Emmett-Teller (BET) and Barrett-Joyner-Halenda (BJH) method was used to calculate the surface area and pore size of the sample.

4.1.2.2. Electrochemical measurements

Electrochemical measurements were performed in 1 M Na₂SO₄ and KCl aqueous electrolyte solution under three electrode systems at room temperature. The working electrode was fabricated by mixing the as-prepared MoS₂, acetylene black, and polyvinylidene fluoride (PVDF) in the ratio of 80:10:10. A small amount of NMP was added to the mixture to produce a homogeneous paste, which was pressed onto stainless steel current collectors (1 cm × 1 cm) to make electrode. After that the electrode were dried in air at 120 °C for 12 h to remove the solvent. Cyclic voltammetry (CV) measurement was carried out at different scan rates from 1 to 100 mV s⁻¹. A galvanostatic charge-discharge (GCD) test was also conducted at different current densities (2.5, 5, 7.5 and 10 mA cm⁻²) for as-prepared electrodes. Electrochemical impedance spectroscopy (EIS) measurements were studied by applying an AC voltage with 10 mV amplitude in a frequency range from 0.1 Hz to 100 kHz.

4.1.3. Results and discussion

The synthesis of mesoporous MoS₂ nanostructure was conducted through a facile and low temperature hydrothermal method. Initially, Na₂MoO₄ and CH₃CSNH₂ react with each other in water to form MoS₂ nanoparticles through fast nucleation process under hydrothermal condition. Then, nucleated MoS₂ particles are further growing to form larger particles via Ostwald ripening process. By time goes on the aging process leads to the formation of sheet-like MoS₂ nanostructure through oriented aggregation. Further, the weak van der Waals force leads to form mesoporous MoS₂ nanostructure.

4.1.3.1. Structure, morphology and compositional analysis

The crystal structure and phase purity of the as-prepared samples were characterized by XRD. **Figure 4.1.1a** shows the XRD pattern of as-prepared mesoporous MoS₂ nanostructure sample. It could be observed that nearly all the diffraction peaks in the XRD pattern are well matched with that of MoS₂ (JCPDS 37-1492), indicating that pure hexagonal crystalline MoS₂ nanostructure were successfully synthesized. The corresponding reflection peaks for (002), (100), (103), (110), and (201) planes confirmed the formation of hexagonal structure of MoS₂ [47]. The composition of as-prepared MoS₂ samples were analyzed by EDX. **Figure 4.1.1b** shows the EDX image of mesoporous MoS₂ nanostructure. The EDX analysis confirmed that the mesoporous MoS₂ nanostructure was composed of Mo and S elements. Further no other elements were observed, which confirmed the purity of as-prepared samples.

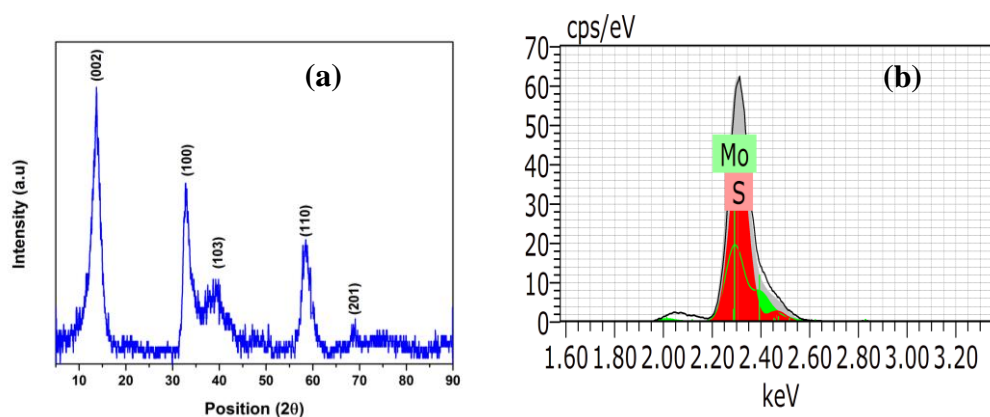


Figure 4.1.1 (a) XRD pattern and (b) EDS of the MoS₂ nanostructure.

The morphology and structural properties of the as-prepared MoS₂ samples were studied by FE-SEM, TEM and HR-TEM analysis as shown in **Figure 4.1.2a-e**. It could be seen that the FE-SEM images (**Figure 4.1.2a-b**) of MoS₂ sample revealed the mesoporous morphology. The MoS₂ nanostructures are composed of few MoS₂ layers to forming a self-assembled porous structure. TEM images (**Figure 4.1.2c**) also revealed mesoporous morphology; the results are consistent with the above FE-SEM results. This porous morphology will help to the enhancement of electrochemical performance because it would lead to the fast ion/electron transfer, sufficient contact between active materials and electrolyte. Therefore, enhanced electrode performances such as high-rate capability, and longer cycling life could be expected accordingly for MoS₂ nanostructure. Further, the HR-TEM images (**Figure 4.1.2d-e**) of the MoS₂ sample shows layer structure with the clear crystal lattice fringes were about 0.64 ± 0.05 nm corresponding to the standard spacing for (002) basal planes of the hexagonal MoS₂ structure. This confirms that the as-prepared sample was MoS₂. The crystallinity of the as-synthesized samples was further confirmed by selected-area electron diffraction (SAED) pattern. **Figure 4.1.2f** show the SAED pattern of mesoporous MoS₂ nanostructure, which exhibits clear ring

patterns, revealing the polycrystalline nature of the as-prepared samples. The rings can be indexed respectively to the (100) (103) (105) and (110) crystal diffractions of hexagonal MoS₂. The obtained HR-TEM image and SAED pattern of MoS₂ nanostructure results are consistent with the XRD result.

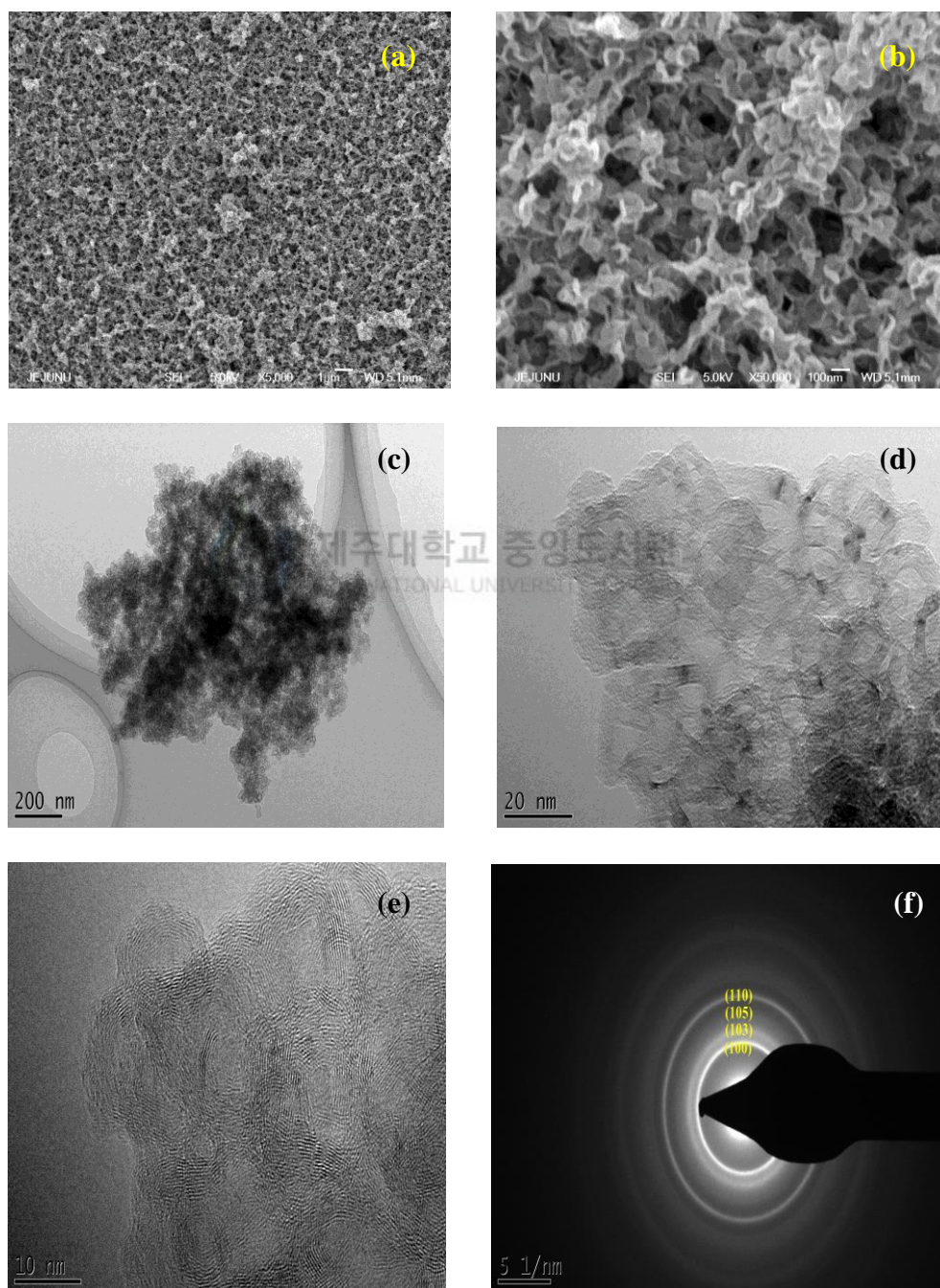


Figure 4.1.2 FE-SEM (a, b), TEM (c), HR-TEM images (d, e) and SAED pattern (f) of the MoS₂ nanostructure.

Nitrogen (N₂) adsorption-desorption isotherm measurement was carried out to determine the surface area and pore-size distribution of the as-prepared samples. **Figure 4.1.3** shows the corresponding N₂ adsorption/desorption isotherm and Barrett–Joyner–Halenda pore-size distribution plot for the MoS₂ sample. The calculated BET surface area of the mesoporous MoS₂ nanostructure is 93.55 m² g⁻¹. The pore-size distribution calculated by the BJH method and it confirms the presence of well-developed mesoporosity with very narrow pore-size distribution centered at 3.8 nm for MoS₂ sample. These results confirm that the high surface area and the formed mesoporosity facilitate the fast ion transports to enhance the electrochemical behavior of the electrodes.

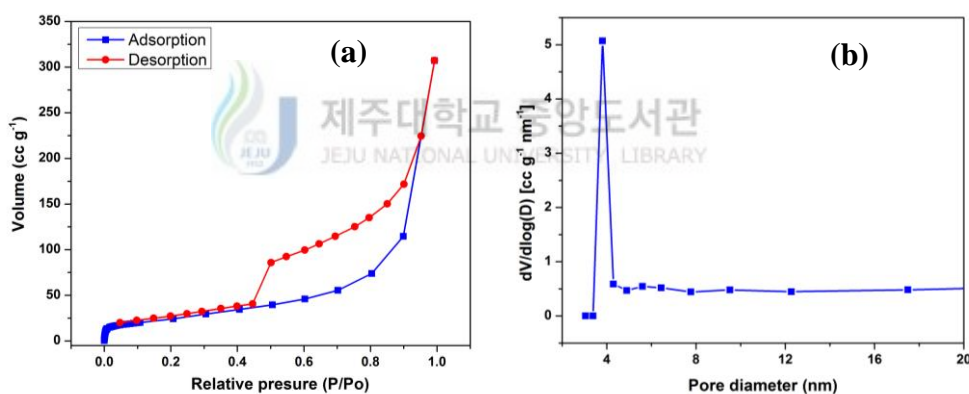


Figure 4.1.3 Nitrogen adsorption–desorption isotherm (a) and BJH pore-size distribution plot (b) of the MoS₂ nanostructure.

Further the composition of the as-prepared materials was confirmed by XPS analysis. The survey scan of MoS₂ nanostructure exhibited (**Figure 4.1.4a**) the characteristics peaks of Mo 3d, Mo 3p, S 2p, O 1s and C 1s with their corresponding binding energies [42]. The core-level spectrum of MoS₂ showed (**Figure 4.1.4b**) the two strong peaks located at 228.7 and 231.8 eV, which are attributed to the doublet of Mo 3d_{5/2} and Mo 3d_{3/2} spin orbital confirmed the formation of MoS₂ [27]. The

high resolution S 2p spectrum exhibited (**Figure 4.1.4c**) the peaks at 161.5 and 162.8 eV, which correspond to the S 2p_{3/2} and S 2p_{1/2} orbital of divalent sulfide ions (S²⁻) [48].

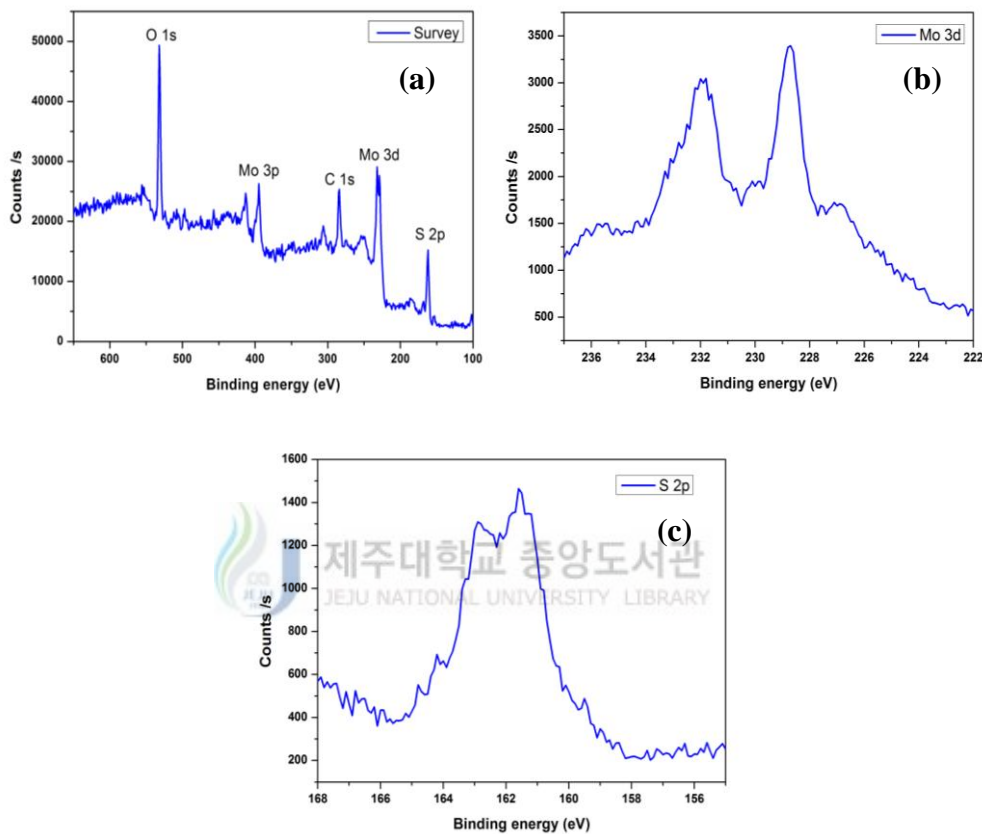


Figure 4.1.4 XPS spectra of MoS₂ nanostructure (a) survey scan, (b) Mo 3d, and (c) S 2p.

4.1.3.2. Electrochemical characterization of mesoporous MoS₂ nanostructure electrode

The capacitive performances of the mesoporous MoS₂ nanostructure electrodes were evaluated by cyclic voltammetry (CV) technique. **Figure 4.1.5a-b** shows the CV curves of MoS₂ nanostructure electrodes in 1M Na₂SO₄ (**Figure 4.1.5a**), and KCl (**Figure 4.1.5b**) electrolyte solution at different scan rates. It could be observed that the all the curves exhibited almost rectangular and symmetric in

shape indicates the non-faradaic charging (electrochemical double layer capacitance). In addition, CV curve area increases with increasing the scan rates from 1 to 100 mV s⁻¹, which reveals the capacitive behavior of the electrode. Further, the CV curves exhibited prominent reduction peaks, which occur during the cathodic scan. This may be due to the reduction of redox active species of Mo atoms at the edge of the porous walls suggesting the pseudocapacitance of MoS₂ [44,49].

There are two possible mechanism predicted [44]. First one is based on the pseudo-capacitive behavior due to faradaic charge transfer process. During the redox process the ions such as protons (H⁺) and or alkali metal cations (Li⁺, Na⁺ and K⁺) may diffuse into the interlayer of MoS₂ structure.



The non-faradaic process might be due to the formation of double layer at the electrode/electrolyte interface during the adsorption of protons or cations on the MoS₂ nanosheet.



The specific capacitance (C_s) of the as prepared electrodes were calculated from the CV curves by using the well-known equation [50]. The calculated C_s of the MoS₂ nanostructure electrodes were 376 and 403 F g⁻¹ at a scan rate of 1 mV s⁻¹ in 1M Na₂SO₄ and KCl electrolyte solution. The C_s as a function of scan rate for MoS₂ nanostructure electrodes are shown in **Figure 4.1.5c**. It could be observed that the C_s decreases with increasing the scan rate, which is due to the charge resistive behavior of the electrode material at higher scan rate.

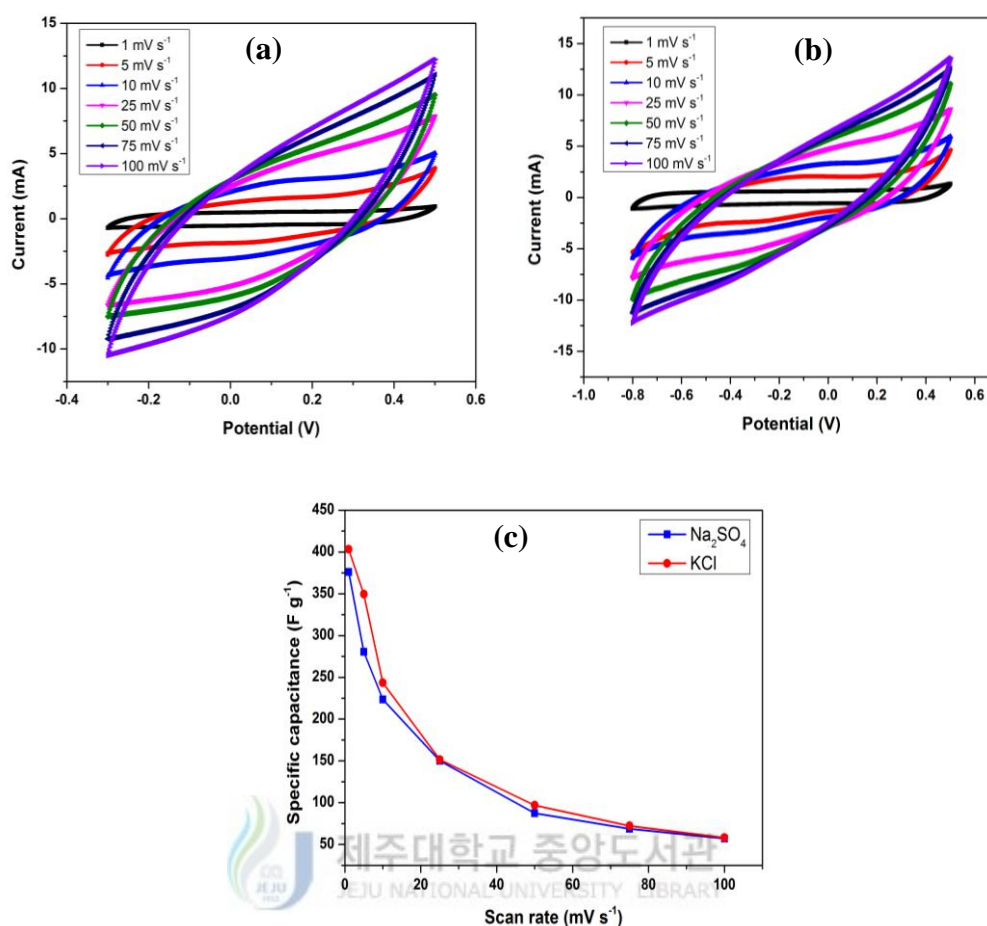


Figure 4.1.5 CV curves of MoS₂ nanostructure electrode at different scan rate in 1M (a) Na₂SO₄, and (b) KCl electrolyte solution. (c) Specific capacitance of MoS₂ nanostructure electrode at different scan rates from 1 to 100 mV s⁻¹.

The obtained C_s value is higher than that of the previously reported by Soon et al. (100 F g⁻¹ at 1 mV s⁻¹) [44]. The higher specific capacitance of MoS₂ nanostructure electrodes in comparison with previous report was mainly due to the porous morphology. This porous morphology could provide a large surface area, and effectively reduce the ion diffusion path which enables the fast electron transports between the electrode and electrolytes, which lead to the improved capacity. From the observed results, the specific capacitance of 1 M KCl electrolyte solution was found to be highest in all scan rates as compared to that of 1 M Na₂SO₄ electrolyte solution, which may be due to the smallest hydrated ionic radius and highest ionic

conductivity of K^+ ions ($0.33 \text{ nm}, 73.5 \text{ cm}^2 \Omega^{-1} \text{ mol}^{-1}$) than the Na^+ ions ($0.358 \text{ nm}, 50.1 \text{ cm}^2 \Omega^{-1} \text{ mol}^{-1}$) [51, 52]. This smallest hydrated ionic radius and highest ionic conductivity of K^+ ions could easily access to the inner surface of the MoS_2 nanostructure electrode than that of Na^+ ions, finally which leads to the higher specific capacitance.

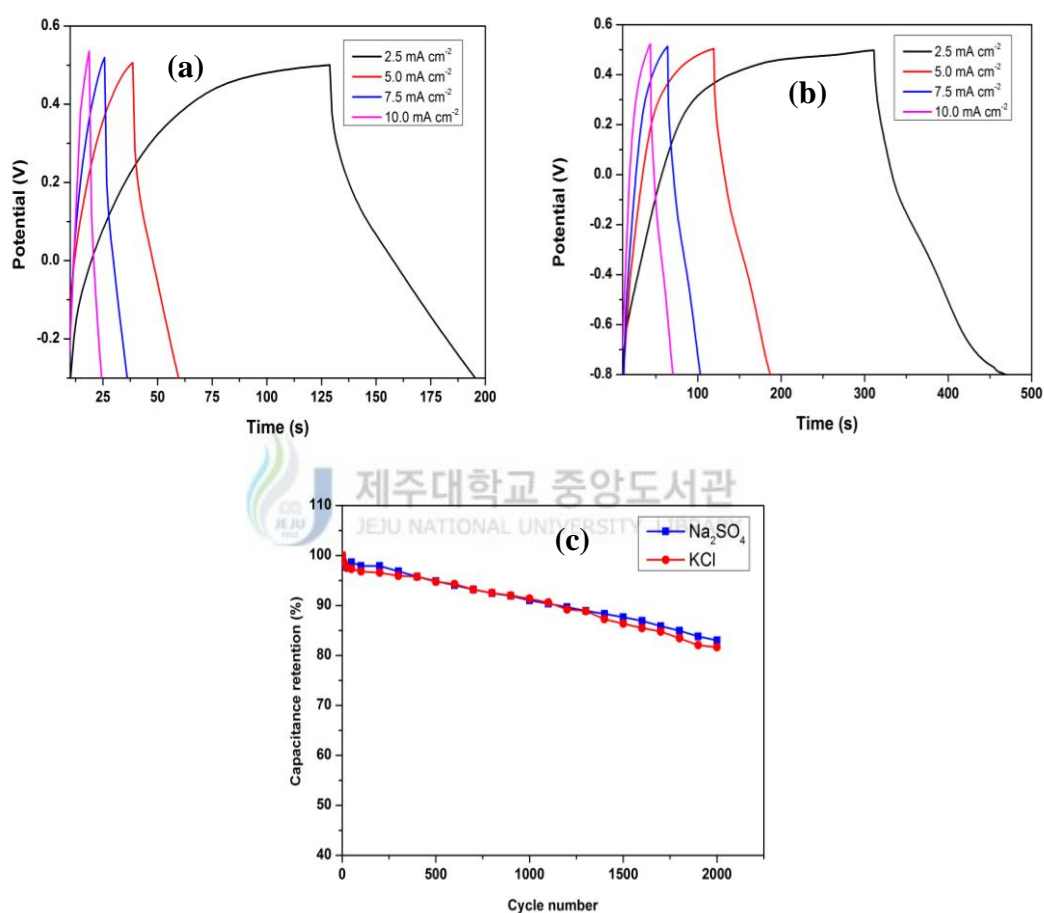


Figure 4.1.6 Galvanostatic charge/discharge curve of MoS_2 nanostructure electrode at different current densities in 1M (d) Na_2SO_4 , and (e) KCl electrolyte solution. (f) Variation of the specific capacitance of MoS_2 nanostructure electrode as a function of cycle number measured at 150 mVs^{-1} in 1M Na_2SO_4 and KCl aqueous solution.

The galvanostatic charge-discharge curves of MoS_2 nanostructure electrodes were measured at different current densities (2.5, 5, 7.5 and 10 mA cm^{-2}) in 1M Na_2SO_4 and KCl solutions is shown in **Figure 4.1.6a-b** Both the curves exhibited almost symmetric and triangular in shape, indicates the capacitive behavior of the

electrode. In the case of **Figure 4.1.5b** the plots exhibited two plateaus in discharge process, which are consistent with the result of the CV analysis. However the electrode exhibited a more pronounced potential drop (IR drop) at the beginning of the discharge process, which is due to the internal resistance of the electrode material [53]. The specific capacitance (C_s) can also be calculated from the galvanostatic charge-discharge curves by using the familiar equation [18]. The specific capacitance calculated are found to be in 1M Na₂SO₄ solution are 98, 85, 41, and 30 F g⁻¹ and in 1M KCl solution are 124, 109, 95, and 89 F g⁻¹ obtained at current densities of 2.5, 5, 7.5 and 10 mA cm⁻², respectively, implying relatively good specific capacitance retention ratio of the electrode at the current density ranging from 2.5 to 10 mA cm⁻².

The cycling stability of the MoS₂ nanostructure electrodes were investigated by repeating the CV measurement at a scan rate of 150 mV s⁻¹ for 2000 cycles. As shown in **Figure 4.1.6c** the capacitance retention of MoS₂ in both electrolyte is around 80% even after 2000 cycles, which indicates a good cycling stability of the electrode materials. The enhanced electrochemical performance of the MoS₂ electrode is mainly due to the porous morphology, which provided the large surface area, and efficient pathway for faster electron transport.

Figure 4.1.7 shows Nyquist plots of the EIS data obtained for MoS₂ nanostructure electrode, after the 1st and 2000th cycles in 1M Na₂SO₄ (**Figure 4.1.7a**) and KCl (**Figure 4.1.7b**) electrolyte solution. Both the impedance spectra are almost similar in shape, composed of semicircle at high frequency region and followed by a vertical line in the low frequency region, which reveals its capacitive behavior due to the non-faradaic charge storage mechanism. After 2000 cycles, the charge transfer resistance of the electrode was increased from 7.2 to 16.7 Ω and from 4 to 11.4 Ω

in 1M Na₂SO₄ and KCl electrolyte solution, respectively. This might be due to the loss of adhesion of some active material with the current collector during the long term charge/discharge cycling [54]. In addition, the increased Warburg impedance after 2000 cycles indicates the increased ion diffusion path lengths and the obstruction of ion movement during the charge/discharge processes [55].

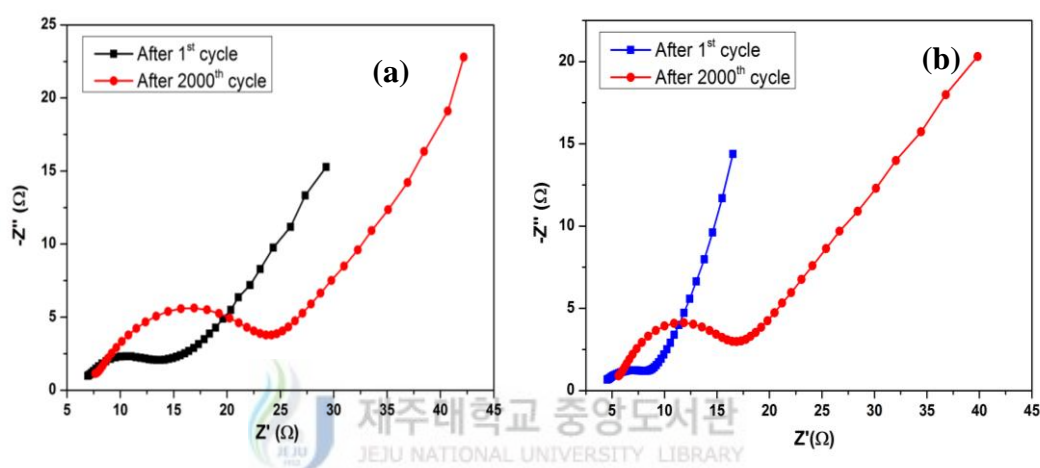


Figure 4.1.7 Nyquist plots for MoS₂ nanostructure electrode measured during the cycle life testing in 1M (a) Na₂SO₄ and (b) KCl electrolyte solution.

4.1.4. Conclusion

In summary, mesoporous MoS₂ nanostructure was prepared by a facile and effective hydrothermal approach for electrochemical supercapacitors. XRD pattern confirmed the hexagonal phase of the as-prepared MoS₂ samples. The MoS₂ nanostructure electrode exhibited an enhanced specific capacitance of 376 and 403 Fg⁻¹ at a scan rate of 1 mV s⁻¹ with an excellent long term cycling stability retaining 80% even after 2000 cycles. From these results, we have concluded that the cost effective preparation of MoS₂ nanostructure could be a promising electrode material for supercapacitors.

4.1.5. References

- [1] H. Jiang, J. Ma and C. Li, Hierarchical porous NiCo₂O₄ nanowires for high-rate supercapacitors. *Chem. Commun.* 48 (2012) 4465-4467.
- [2] S. Guo and S. Dong, Graphene nanosheet: synthesis, molecular engineering, thin film, hybrids, and energy and analytical applications. *Chem. Soc. Rev.* 40 (2011) 2644–2672.
- [3] X. Huang, Z. Yin, S. Wu, X. Qi, Q. He, Q. Zhang, Q. Yan, F. Boey and H. Zhang, Graphene-based materials: Synthesis, characterization, properties, and applications. *Small* 7 (2011) 1876–1902.
- [4] M. Xu, T. Liang, M. Shi and H. Chen, Graphene-like two-dimensional materials. *Chem. Rev.* 113 (2013) 3766–3798.
- [5] S. Z. Butler, S. M. Hollen, L. Cao, Y. Cui, J. A. Gupta, H. R. Gutierrez, T. F. Heinz, S. S. Hong, J. Huang, A. F. Ismach, E. Johnston-Halperin, M. Kuno, V. V. Plashnitsa, R. D. Robinson, R. S. Ruoff, S. Salahuddin, J. Shan, L. Shi, M. G. Spencer, M. Terrones, W. Windl and J. E. Goldberger, Progress, challenges, and opportunities in two-dimensional materials beyond graphene. *ACS Nano* 7 (2013) 2898–2926.
- [6] X. Peng, L. Peng, C. Wu and Y. Xie, Two dimensional nanomaterials for flexible supercapacitors, *Chem. Soc. Rev.* 43 (2014) 3303-3323.
- [7] A. Naoi, W. Naoi, S. Aoyagi, J. I. Miyamoto and T. Kamino, New generation “Nanohybrid supercapacitor”. *Acc. Chem. Res.* 46 (2013) 1075-1083.
- [8] A. Sumboja, C. Y. Foo, X. Wang and P. S. Lee, Large areal mass, flexible and free-standing reduced graphene oxide/manganese dioxide paper for asymmetric supercapacitor device. *Adv. Mater.* 25 (2013) 2809-2815.

- [9] A. Ramadoss and S. J. Kim, Improved activity of a graphene–TiO₂ hybrid electrode in an electrochemical supercapacitor. *Carbon* 63 (2013) 434-445.
- [10] X. C. Dong, H. Xu, X. W. Wang, Y. X. Huang, M. B. Chan-Park, H. Zhang, L. H. Wang, W. Huang and P. Chen, 3D graphene–cobalt oxide electrode for high-performance supercapacitor and enzymeless glucose detection. *ACS Nano* 6 (2012) 3206-3213.
- [11] G. Zhang, X. W. Lou, General solution growth of mesoporous NiCo₂O₄ nanosheets on various conductive substrates as high-performance electrodes for supercapacitors. *Adv. Mater.* 25 (2013) 976-979.
- [12] L. Mai, H. Li, Y. Zhao, L. Xu, X. Xu, Y. Luo, Z. Zhang, W. Ke, C. Niu and Q. Zhang, Fast ionic diffusion-enabled nanoflake electrode by spontaneous electrochemical pre-Intercalation for high-performance supercapacitor. *Sci. Reports* 3 (1718) (2013) 1-8.
- [13] A. Ramadoss and S. J. Kim, Vertically aligned TiO₂ nanorod arrays for electrochemical supercapacitor. *J. Alloys Comp.* 561 (2013) 262-267.
- [14] L. Cao, S. Yang, W. Gao, Z. Liu, Y. Gong, L. Ma, G. Shi, S. Lei, Y. Zhang, S. Zhang, R. Vajtai, and P. M. Ajayan, Direct Laser-Patterned Micro-Supercapacitors from Paintable MoS₂ Films. *Small* 9 (2013) 2905-2910.
- [15] L. Zhang, H. B. Wu and X. W. Lou, Unusual CoS₂ ellipsoids with anisotropic tube-like cavities and their application in supercapacitors. *Chem. Commun.* 48 (2012) 6912-6914.
- [16] J. Yang, X. Duan, Q. Qin and W. Zheng, Solvothermal synthesis of hierarchical flower-like β-NiS with excellent electrochemical performance for supercapacitors. *J. Mater. Chem. A* 1 (2013) 7880-7884.

- [17] H. Zhang, X. Yu, D. Guo, B. Qu, M. Zhang, Q. Li, and T. Wang, Synthesis of bacteria promoted reduced graphene oxide-nickel sulfide networks for advanced supercapacitors. *ACS Appl. Mater. Interfaces* 5 (2013) 7335-7340.
- [18] A. Ramadoss, G. S. Kim and S. J. Kim, Fabrication of reduced graphene oxide/TiO₂ nanorod/reduced graphene oxide hybrid nanostructures as electrode materials for supercapacitor applications. *Cryst. Eng. Comm.* 15 (2013) 10222-10229.
- [19] A. Ramadoss and S.J. Kim, Facile preparation and electrochemical characterization of graphene/ZnO nanocomposite for supercapacitor applications. *Mater. Chem. Phys.* 140 (2013) 405-411.
- [20] B. Wang, J. Park, D. Su, C. Wang, H. Ahnb, and G. Wang, Solvothermal synthesis of CoS₂-graphene nanocomposite material for high-performance supercapacitors. *J. Mater. Chem.* 22 (2012) 15750-15756.
- [21] S. Ratha and C. S. Rout, Supercapacitor electrodes based on layered tungsten disulfide-reduced graphene oxide hybrids synthesized by a facile hydrothermal method. *ACS Appl. Mater. Interfaces* 5 (2013) 11427-11433.
- [22] K. J. Huang, L. Wang, Y. J. Liu, Y. M. Liu, H. B. Wang, T. Gan and L. L. Wang, Layered MoS₂-graphene composites for supercapacitor applications with enhanced capacitive performance. *Int. J. Hydrogen Energy* 38 (2013) 14027-14034.
- [23] K. H. Hu, X. G. Hu, Y. F. Xu and J. D. Sun, Synthesis of nano-MoS₂ /TiO₂ composite and its catalytic degradation effect on methyl orange. *J. Mater. Sci.* 45 (2012) 2640-2648.

- [24] J. Zhao, Z. Zhang, S. Yang, H. Zheng and Y. Li, Facile synthesis of MoS₂ nanosheet-silver nanoparticles composite for surface enhanced Raman scattering and electrochemical activity. *J. Alloys Comp.* 559 (2013) 87-91.
- [25] B. Radisavljevic, A. Radenovic, J. Brivio, V. Giacometti and A. Kis, Single-layer MoS₂ transistors. *Nat. Nanotechnol.* 6 (2011) 147-150.
- [26] H. Hwang, H. Kim and J. Cho, MoS₂ nanoplates consisting of disordered graphene-like layers for high rate lithium battery anode materials. *Nano Lett.* 11 (2011) 4826-4830.
- [27] Y. Liang, R. Feng, S. Yang, H. Ma, J. Liang and J. Chen, Rechargeable Mg batteries with graphene-like MoS₂ cathode and ultrasmall Mg nanoparticle anode. *Adv. Mater.* 23 (2011) 640-643.
- [28] B. Jacopo, T. L. A. Duncan and K. Andras, Ripples and layers in ultrathin MoS₂ membranes. *Nano Lett.* 11 (2011) 5148-5153.
- [29] N. Zheng, X. Bu and P. Feng, Synthetic design of crystalline inorganic chalcogenides exhibiting fast-ion conductivity. *Nature* 426 (2003) 428-432.
- [30] J. Xiao, D. Choi, L. Cosimbescu, P. Koech, J. Liu and J. P. Lemmon, Exfoliated MoS₂ nanocomposite as an anode material for lithium ion batteries. *Chem. Mater.* 22 (2010) 4522-4524.
- [31] M. M. Millan, T. Hyeon and K. S. Suslick, Sonochemical synthesis of nanostructured molybdenum sulfide *J. Am. Chem. Soc.* 120 (1998) 6189-6190.
- [32] Y. Feldman, E. Wasserman, D. J. Srolovitz and R. Tenne, High-rate, gas-phase growth of MoS₂ nested inorganic fullerenes and nanotubes. *Science* 267 (1995) 222-225.

- [33] J. J. Hu, J. S. Zabinski, J. H. Sanders, J. E. Bultman and A. A. Voevodin, Pulsed laser syntheses of layer-structured WS₂ nanomaterials in water. *J. Phys. Chem. B* 110 (2006) 8914-8916.
- [34] C. M. Zelenski and P. K. Dorhout, Template synthesis of near-monodisperse¹ microscale nanofibers and nanotubules of MoS₂. *J. Am. Chem. Soc.* 120 (1998) 734-742.
- [35] K. Ellmer, R. Mientus, S. Seeger, and V. Weib, Highly (001)-textured WS_{2-x} films prepared by reactive radio frequency magnetron sputtering. *Phys. Status Solidi A* 201 (2004) R97-R100.
- [36] M. Chhowalla, and G. A. J. Amaratunga, Thin films of fullerene-like MoS₂ nanoparticles with ultra-low friction and wear. *Nature* 407 (2000) 164-167.
- [37] D Vollath and D.V Szabó, Synthesis of nanocrystalline MoS₂ and WS₂ in a microwave plasma. *Mater. Lett.* 35 (1998) 236-244.
- [38] G. Tang, Y. Wang, W. Chen, H. Tang and C. Li, Hydrothermal synthesis and characterization of novel flowerlike MoS₂ hollow microspheres. *Mater. Lett.* 100 (2013) 15-18.
- [39] L. Ma, W. Chen, H. Li, Y. Zheng and Z. Xu, Ionic liquid-assisted hydrothermal synthesis of MoS₂ microspheres. *Mater. Lett.* 62 (2008) 797-799.
- [40] Y. Tian, X. Zhao, L. Shen, F. Meng, L. Tang, Y. Deng and Z. Wang, Synthesis of amorphous MoS₂ nanospheres by hydrothermal reaction. *Mater. Lett.* 60 (2006) 527-529.
- [41] Y. Tian, J. Zhao, W. Fu, Y. Liu, Y. Zhu, Z. Wang, A facile route to synthesis of MoS₂ nanorods. *Mater. Lett.* 59 (2005) 3452-3455.

- [42] W. J. Li, E. W. Shi, J. M. Ko, Z. Chen, H. Ogino and T. Fukuda, Hydrothermal synthesis of MoS₂ nanowires. *J. Cryst. Growth* 250 (2003) 418-422.
- [43] G. Nagaraju, C. N. Tharamani, G. T. Chandrappa and J. Livage, Hydrothermal synthesis of amorphous MoS₂ nanofiber bundles via acidification of ammonium heptamolybdate tetrahydrate. *Nanoscale Res. Lett.* 2 (2007) 461-468.
- [44] J. M. Soon and K. P. Loh, Electrochemical double-layer capacitance of MoS₂ nanowall films. *Electrochem. Solid State Lett.* 10 (11) (2007) A250-A254.
- [45] G. Ma, H. Peng, J. Mu, H. Huang, X. Zhou and Z. Lei, In situ intercalative polymerization of pyrrole in graphene analogue of MoS₂ as advanced electrode material in supercapacitor. *J. Power Sources* 229 (2012) 72-78.
- [46] B. Hu, X. Qin, A. M. Asiri, K. A. Alamry, A. O. Al-Youbi, and X. Sun, Synthesis of porous tubular C/MoS₂ nanocomposites and their application as a novel electrode material for supercapacitors with excellent cycling stability. *Electrochimica Acta* 100 (2013) 24-28.
- [47] H. Luo, C. Xu, D. Zou, L. Wang and T. Ying, Hydrothermal synthesis of hollow MoS₂ microspheres in ionic liquids/water binary emulsions. *Mater. Lett.* 62 (2008) 3558.
- [48] H. Lin, X. Chen, H. Li, M. Yang and Y. Qi, Hydrothermal synthesis and characterization of MoS₂ nanorods. *Mater. Lett.* 64 (2010) 1748-1750.
- [49] S. P. Vincent, Oxidation--reduction potentials of molybdenum and iron--sulphur centres in nitrate reductase from *Escherichia coli*. *Biochem. J.* 177 (1979) 757-759.

- [50] J.W. Lee, A. S. Hall, J. D. Kim and T. E. Mallouk, A facile and template-free hydrothermal synthesis of Mn_3O_4 nanorods on graphene sheets for supercapacitor electrodes with long cycle stability. *Chem. Mater.* 24 (2012) 1158-1164.
- [51] R. N. Reddy and R. G. Reddy, Sol-gel MnO_2 as an electrode material for electrochemical capacitors. *J. Power Sources* 124 (2003) 330-337.
- [52] Q. Qu, P. Zhang, B. Wang, Y. Chen, S. Tian, Y. Wu, and R. Holze, Electrochemical performance of MnO_2 nanorods in neutral aqueous electrolytes as a cathode for asymmetric supercapacitors. *J. Phys. Chem. C* 113 (2009) 14020-14027.
- [53] J. Zhang, J. Jiang and X. S. Zhao, Synthesis and capacitive properties of manganese oxide nanosheets dispersed on functionalized graphene sheets. *J. Phys. Chem. C* 115 (2011) 6448-6454.
- [54] J. Yan, Z. Fan, T. Wei, W. Qian, M. Zhang and F. Wei, Reduction of graphene oxide by an in-situ photoelectrochemical method in a dye-sensitized solar cell assembly. *Carbon* 48 (2010) 3825-3833.
- [55] M. Pasta, F. L. Mantia, L. Hu, H. D. Deshazer and Y. Cui, Aqueous supercapacitors on conductive cotton. *Nano. Res.* 3 (2010) 452-458.

4.2. Synthesis and Electrochemical Performance of Graphene Coated Fabrics

4.2.1. Introduction

The rapid growth of technology and the introduction of nanotechnology have enabled device miniaturisation and lowered their operating power requirements; this has encouraged the development of self-powered wearable and portable devices [1–6]. For this application, the power sources (energy conversion/storage devices) such as the battery and supercapacitor should be flexible, stretchable, and lightweight. Recently, two dimensional (2-D) materials such as graphene and inorganic graphene-like materials have concerned much attention for fabricating high-performance flexible supercapacitors because of their high specific surface areas, high mechanical flexibility. Among them, 2-D graphene is composed of carbon atoms arranged in a two-dimensional, atomic-layer-thick, honeycomb structure. The exceptional electrical, thermal conductivity, optical, and mechanical properties of graphene have enabled its use in a diverse range of applications [7–10]. The high electrical conductivity, surface area ($2600 \text{ m}^2 \text{ g}^{-1}$), and excellent mechanical flexibility makes graphene appealing as an electric double-layer capacitor electrode material for energy storage applications [11–20]. However, the reported specific capacitance, energy density, and power density values of graphene-based supercapacitors are lower than the expected values because of the restacking of graphene sheets. Hence, regulating strong sheet-to-sheet van der Waals interaction to a reasonable degree is immediately needed.

Several methods have been developed for the preparation of graphene, such as chemical vapour deposition, micromechanical exfoliation of graphite,

solvothermal synthesis, epitaxial growth, and the reduction of graphene oxide (GO) [21–26]. However, those approaches suffer from low productivity and use hazardous reductants. Recently, GO has been reduced using thermal treatment methods that are considered more eco-friendly and do not use any hazardous reductants [27].

Herein, we fabricated flexible graphene-coated fabric electrodes by using a simple-cost effective dip-coating method followed by thermal reduction at 170°C in Ar for 2 h. The carbon fabric, used as a current collector, has the advantages of being inexpensive, has good chemical stability, is flexible, and has a high conductivity. These features enable the design of highly flexible and lightweight devices. Additionally, directly growing graphene nanosheets on the fabric without the need for a binder or a conductive additive avoids the issue of inactive surfaces with conventional binder electrodes and allows for more efficient charge transport. The graphene-coated fabric exhibited excellent electrochemical performance. Furthermore, we fabricated a solid-state, flexible, symmetric supercapacitor (SSC) based on a graphene nanosheet hybrid structure.

4.2.2. Experimental Section

4.2.2.1. Synthesis of graphene oxide (GO)

Commercially available conducting fabric was cleaned in ethanol, acetone, and deionised water in a sonicating bath. First, GO was synthesised from commercial graphite powder using a modified Hummers method. In a typical synthesis, 4 g of graphite powder was dissolved in 100 ml concentrated sulfuric acid with 2 g of sodium nitrate. The mixer was stirred for 30 min in ice bath. After 30 min acid treatment, 14 g of potassium permanganate was added slowly over a period of 30 min and the reaction was continued under constant stirring for overnight. Afterwards,

the reaction mixture was diluted by the adding 200 ml of deionized water. Further, the unreacted reactant was removed by the addition of 3% hydrogen peroxide (10 ml). The solution was allowed to settle after the addition of 5% HCl and decanted. Further, the prepared graphene oxide was purified by the repeated washing and centrifuge using deionized water and ethanol. The purified graphene oxide solution was sonicated for one hour by using a probe sonicator. The sonicated GO solution was centrifuged at higher RPM (10,000) and the supernant and settled samples were separated. Further, the separated supernant solution was diluted with deionized water and sonicated for 30 min. The sonicated graphene oxide solution was used for further applications.

4.2.2.2. Fabrication of the graphene-coated fabric

The prepared GO solution was used to coat the clean conducting fabric by repeated dip-coating. After each coating, the GO-coated fabric was dried at 60°C for 30 min; this process was repeated five times. The GO-coated fabric was reduced to a graphene-coated fabric by thermal treatment at 170°C in Ar for 2 h. The graphene-coated fabric were characterised by Raman, FT-IR, XPS and FE-SEM measurements.

4.2.2.3. Electrochemical measurements of graphene-coated fabric electrode

Electrochemical testing of the as-fabricated binder-free graphene-coated fabric electrode was performed in a three-electrode cell, in which a Pt sheet and a Ag/AgCl electrode were used as the counter and reference electrodes, respectively. The mass loading of the graphene on the fabric was ca. 0.6–0.8 mg cm⁻². Cyclic voltammetry (CV) measurements were carried out in 1 M H₃PO₄ electrolyte solution at scan rates from 5–125 mV s⁻¹ with a potential window of 0–1 V. Galvanostatic charge/discharge (GCD) tests were performed from 0–1 V at current densities

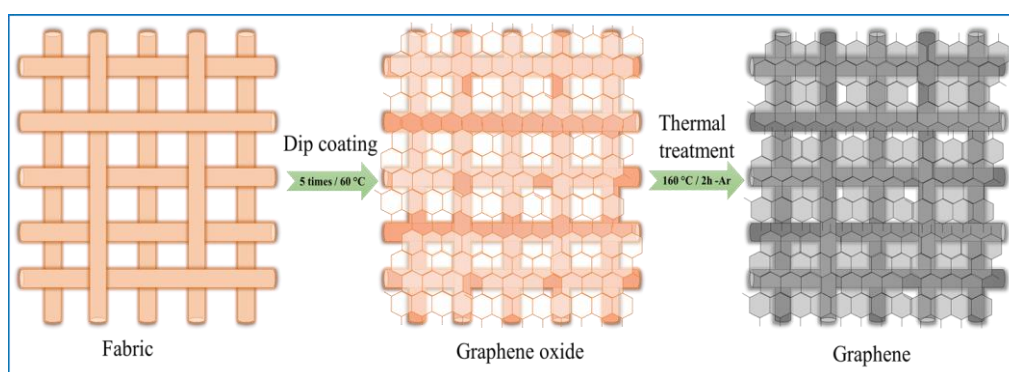
ranging from 0.5–5 mA cm⁻². Electrochemical impedance spectroscopy (EIS) measurements were recorded from 10 mHz to 100 kHz with an alternate current (AC) amplitude of 5 mV. Cycle-life testing was carried out using GCD at a current density of 2.5 mA cm⁻² for 1000 cycles.

4.2.2.4. Fabrication of a flexible solid-state SSC

A flexible solid-state SSC was assembled by separating two pieces of graphene-coated fabric electrodes with a filter paper separator. H₃PO₄/PVA gel was prepared by mixing 3 g of polyvinyl alcohol (PVA) and 3 g of phosphoric acid (H₃PO₄) in 30 mL of deionised water and heating at 85°C for 1 h under vigorous stirring until a homogeneous sticky solution formed. Cooling the solution to room temperature provided a clear and transparent gel. Prior to the assembling, the electrodes and the separator were immersed in the H₃PO₄/PVA gel electrolyte for 3 min and then allowed to solidify at room temperature over 6 h. Finally, they were assembled together and dried at room temperature for 12 h to remove the excess water in the electrolyte. The electrochemical performance of this solid-state SSC was investigated by CV and GCD measurements.

4.2.3. Results and discussion

The graphene-coated fabric was made in two-steps; the process is shown schematically in **Scheme 4.2.1**. First, GO was deposited by simple dip-coating in a GO solution and drying at 60°C for 30 min. Second, the GO coating was reduced to a graphene coating by thermal treatment at 170°C in Ar for 2 h.



Scheme 4.2.1 Schematic representation of the formation of the graphene nanosheets.

4.2.3.1. Characterisation of the graphene-coated fabric

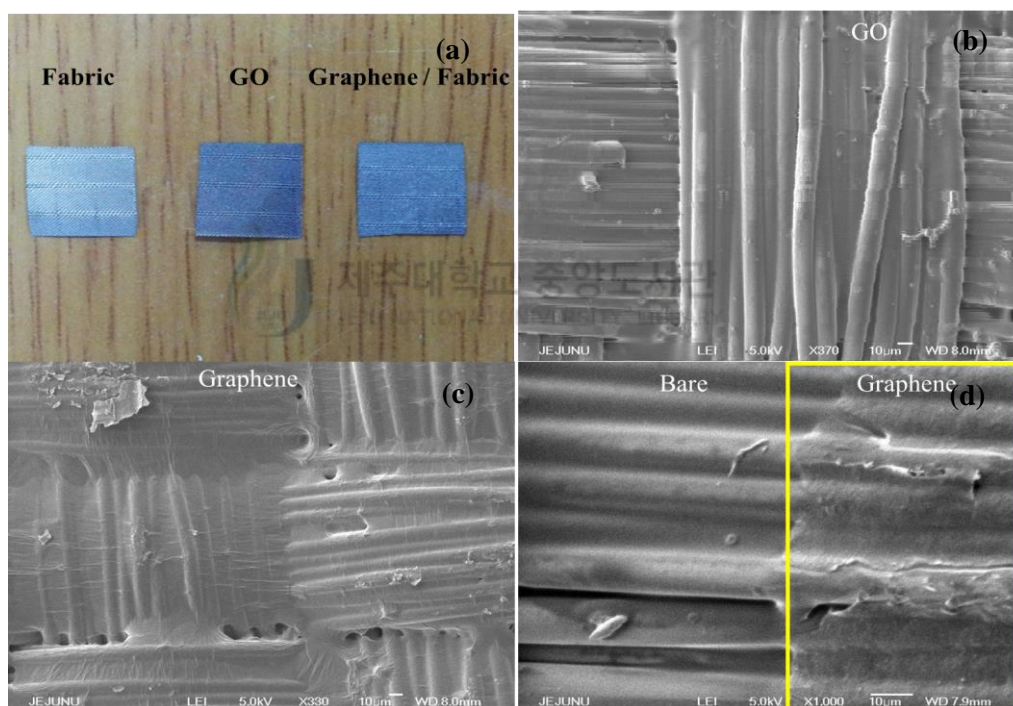


Figure 4.2.1 (a) Photographs of the conductive fabric substrate, and the GO- and graphene-coated fabrics. FE-SEM images of the (b) GO- and (c, d) graphene-coated fabrics.

Figure 4.2.1a shows photographs of the bare fabric, and the GO- and graphene-coated carbon fabrics. The graphene coating appeared as a uniformly grey film on the surface of the fabric after the thermal treatment. The morphologies of the as-prepared GO- and graphene-coated fabrics were characterised by FE-SEM

(Figure 4.2.1b-d). The image (Figure 4.2.1b) of the GO-coated fabric clearly shows that a thin layer of GO on the surface of the fabric. Figure 4.2.1c provides an FE-SEM image of the graphene-coated fabric. It is clear that the graphene nanosheets were uniformly deposited over the fabric surface. Figure 4.2.1d shows the surface of the bare fabric as well as the graphene-coated fabric, which confirmed the deposition of graphene nanosheets.

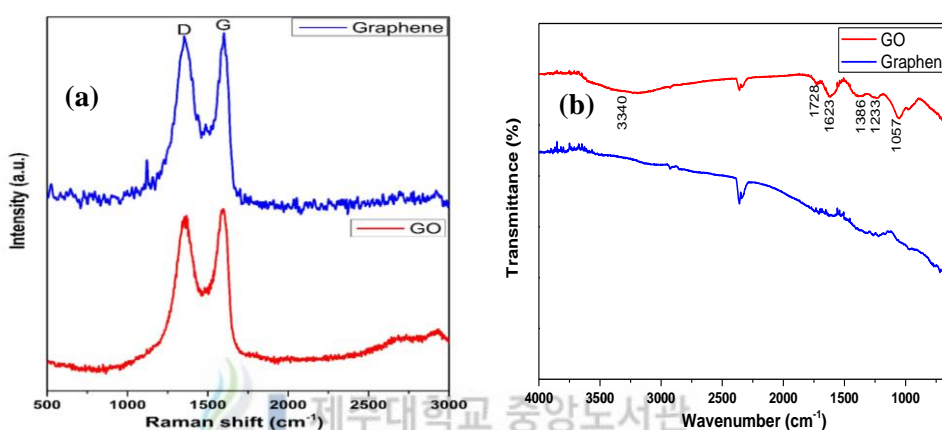


Figure 4.2.2 (a) Raman spectra of the GO- and graphene-coated fabrics. The inset is an optical image of the latter. (b) FT-IR spectra of the GO- and graphene-coated fabrics.

Raman spectroscopy is a non-destructive technique used to provide structural information of carbon-based materials. Figure 4.2.2a shows the Raman spectra of the GO- and graphene-coated fabrics. The characteristic G- and D-bands of the Raman spectra of graphitic-carbon-based materials were observed at ca. 1602 and 1354 cm^{-1} , respectively. These bands correspond to defects and disorder in the hexagonal graphitic layers and relate to the optical E_{2g} mode in-plane vibration phonon at the Brillouin zone centre [11, 13, 28]. The G- and D-bands in the graphene Raman spectrum were shifted to lower wavenumbers, which indicated the reduction of GO. The intensity ratio (I_D/I_G) for GO and graphene were ca. 0.95 and 0.97, respectively. The higher I_D/I_G ratio for graphene indicated that the thermal reduction

had altered the structure of the GO and had introduced structural defects [25]. FT-IR spectroscopy was used to demonstrate the reduction of oxygen-bearing functional groups in GO. **Figure 4.2.2b** displays the ATR-FT-IR spectra of the GO- and graphene-coated fabrics. The presence of various oxygen-containing groups in GO was confirmed by the observation of absorption bands at 3340 (O–H stretching vibration), 1728 (C=O stretching vibration), 1623 (skeletal vibration of unoxidised graphitic domains), 1386 (O–H deformation of C–OH groups), 1233 (C–OH stretching vibration), and 1057 cm^{-1} (C–O stretching vibration) [29]. The intensities of the oxygen-bearing-group vibrations were greatly reduced after the reduction step (**Figure 4.2.2b**), which confirmed the reduction of the GO into graphene.

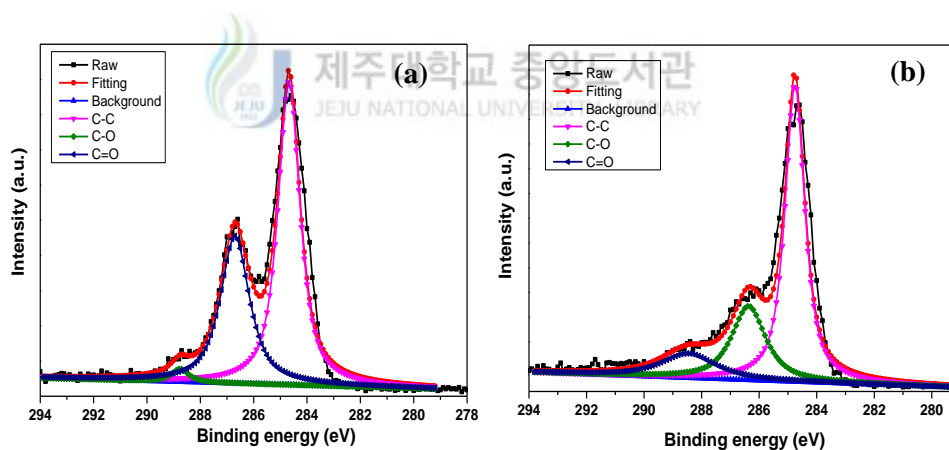


Figure 4.2.3 The C 1s XPS spectra of the (c) GO- and (d) graphene-coated fabrics.

XPS analysis was performed to further study the reduction of the GO-coated fabric. **Figure 4.2.3a-b** shows the C1s XPS spectra of the GO- and graphene-coated fabrics. In **Figure 4.2.3a**, the C1s spectrum of the former consists of three peaks centred at 284.6, 286.4, and 288.6 eV, which correspond to C=C/C–C (aromatic rings), C–O (hydroxyl and epoxy), and C=O (carbonyl) groups, respectively [11, 13]. The dominant C–C and C–O peaks indicated a considerable degree of oxidation of

the GO-coated fabric. The peak intensities of the oxygen-containing groups were lower after reduction by the thermal treatment (**Figure 4.2.3b**), which indicated that most of the oxygen functional groups had been converted. This result demonstrated that the carbon atoms in the as-synthesised graphene-coated fabric were partially transformed from sp^3 to sp^2 hybridisation [30].

4.2.3.2. Electrochemical performance of the graphene-coated fabric electrode

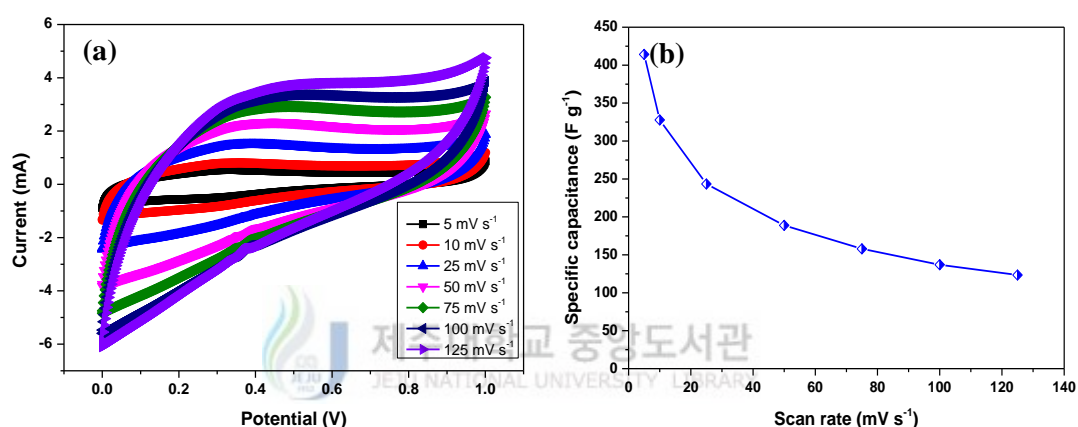


Figure 4.2.4 (a) CV curves of the graphene-coated fabric electrode at various scan rates with a potential window of 0–1 V in 1 M H₃PO₄ solution. (b) Specific capacitance of the graphene-coated fabric at different scan rates.

The electrochemical performance of the as-prepared graphene-coated fabric electrode was measured in a three-electrode system using 1 M H₃PO₄ as the electrolyte. **Figure 4.2.4a** shows the CV curves of the graphene-coated fabric electrode for various sweeps rates from 5 to 125 mV s⁻¹. The rectangular-like shape of the CV curves clearly indicated electrochemical double-layer capacitance characteristics. Even at higher scan rates, the CV curves maintained their slightly distorted rectangular-like shape. **Figure 4.2.4b** shows the specific capacitance of the graphene-coated fabric plotted as a function of scan rate. The high specific capacitance of 414 F g⁻¹ at a scan rate of 5 mV s⁻¹ dropped at higher scan rates. This

was attributed to a reduction in the ion-accessible area at the graphene surface; as the scan rate increased, charge diffusion in graphene was interrupted because of the time constraint for fast charging/discharging. That led to activation of only the outer surface of the graphene nanosheets, thereby resulting in decreased capacitance at high scan rates [31].

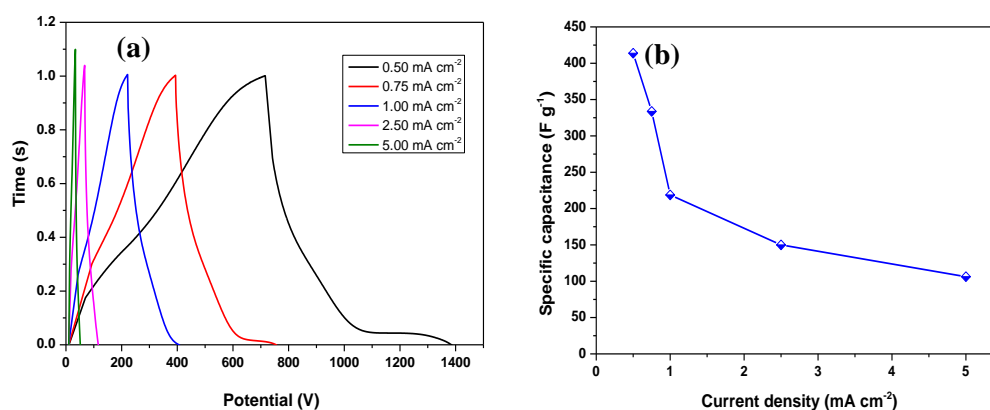


Figure 4.2.5 (a) GCD curves of the graphene-coated fabric at different current densities. (b) Specific capacitance calculated from the charge/discharge curves as a function of current density.

Figure 4.2.5a displays the GCD profiles for different current densities. All of the GCD curves were linear and symmetric, which further verified capacitive behaviour. The variation in the specific capacitance of the fabric electrode as a function of current density is plotted in **Figure 4.2.5b**. The calculated specific capacitance of the graphene-coated electrode was 413 F g⁻¹ at a current density of 0.5 mA cm⁻². When the current density was increased to 5 mA cm⁻², the specific capacitance decreased to 106 F g⁻¹, which was 26% of its initial capacitance at 0.5 mA cm⁻². This was an improved rate capability for the electrode. These values are comparable to but higher than previously reported values [11–16]. The enhanced specific capacitance and rate capability of the graphene fabric electrode was attributed to a shorter diffusion path for both electrolyte ions and electrons, a highly

activated surface, and improved electrical conductivity following the thermal reduction.

The long-term cycle stability of the graphene-coated fabric electrode was evaluated by repeating the GCD process at a current density of 2.5 mA cm^{-2} for 1000 cycles in $1 \text{ M H}_3\text{PO}_4$ electrolyte solution (**Figure 4.2.6a**). The electrode retained 93% of its initial capacitance after 1000 charge/discharge cycles, demonstrating the reliable long-term performance required for supercapacitor applications. EIS was also used to evaluate the electrochemical performance of the graphene-coated fabric electrode. **Figure 4.2.6b** shows the EIS spectrum for the electrode before and after the cycling stability test; the real (Z') and imaginary ($-Z''$) parts of the frequency-dependent impedance are used in these Nyquist plots. The graphs are nearly linear and vertical at low frequencies, indicating ideal capacitive behaviour of the electrode and illustrative of ion diffusion in the structure of the electrode. The semi-circular arc in the high-frequency region indicates charge-transfer resistance at the electrode–electrolyte interface [13]. The EIS spectra were virtually unchanged even after 1000 cycles, which indicated good cycling stability of the graphene-coated fabric electrode.

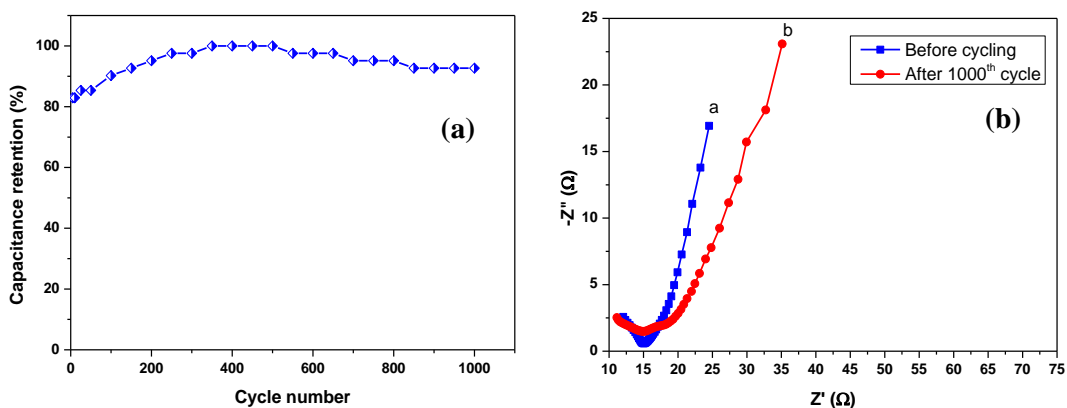


Figure 4.2.6 (a) Capacitance retention ratio as a function of cycle number. (b) Nyquist plots of the graphene-coated fabric electrode before and after 1000 cycles.

4.2.3.3. Electrochemical performance of the flexible solid-state SSC

A solid-state SSC was fabricated by sandwiching a $\text{H}_3\text{PO}_4/\text{PVA}$ gel electrolyte and filter paper between two pieces of the graphene-coated fabric electrodes. The electrochemical properties of this supercapacitor were characterised by CV and GCD techniques. **Figure 4.2.7a** shows the CV curves of the solid-state supercapacitor device measured at various scan rates. All of the CV curves had slightly distorted rectangular-like shapes even at high scan rates, which demonstrated the ideal capacitive and fast charge/discharge behaviour of the supercapacitor device. **Figure 4.2.7b** shows the specific capacitance of the device calculated from the CV curves. The calculated specific capacitance of the single electrode decreased from 281 to 54 F g^{-1} as the scan rate increased from 5 to 125 mV s^{-1} . This decrease was attributed to inefficient diffusion of ions at higher scan rates. The calculated specific capacitance of the cell (flexible supercapacitor) was 70.4 F g^{-1} at 5 mV s^{-1} .

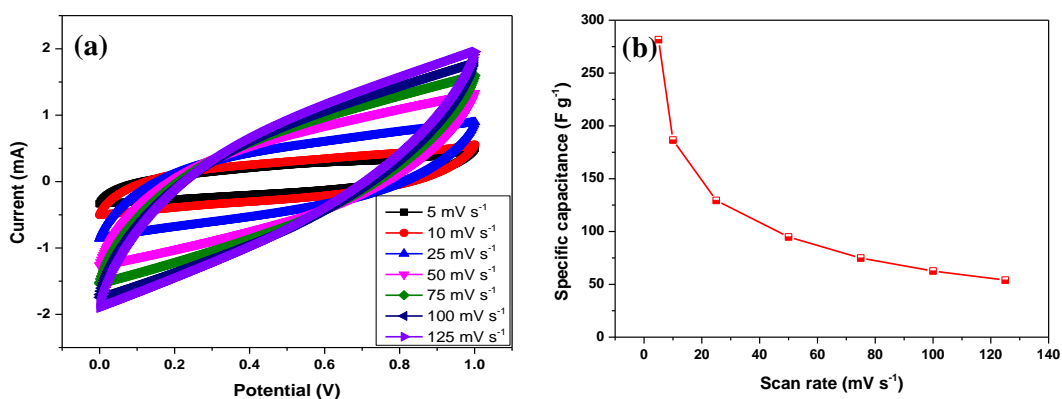


Figure 4.2.7 (a) CV curves of the graphene-coated fabric SSC measured at different scan rates over 0–1 V in $\text{PVA}/\text{H}_3\text{PO}_4$ gel electrolyte. (b) Specific capacitance of the graphene-coated fabric SSC at different scan rates.

GCD curves at different current densities were also recorded to further evaluate the performance of the device. **Figure 4.2.8a** shows that the charging curves

of the supercapacitor device were relatively symmetric with their corresponding discharging counterparts, further confirming the good capacitive behaviour of the device. Based on the GCD curves, the specific capacitance of the fabricated solid-state device was calculated using Equations 2 and 3. The specific capacitance of the flexible supercapacitor device was 42.1 F g^{-1} at 0.1 mA cm^{-2} . **Figure 4.2.8b** shows the specific capacitance as a function of current density. The highest specific capacitance (single electrode) of 169 F g^{-1} was achieved at a current density of 0.1 mA cm^{-2} ; this value is comparable to those previously reported for solid-state [12, 17, 18] and aqueous [11, 15] supercapacitors. Additionally, at the higher current density of 1 mA cm^{-2} , the specific capacitance retained ca. 25% of its value (43 F g^{-1}), indicating improved rate capability of the device. The suitability of this solid-state device for supercapacitor applications was further estimated by examining its power and energy densities. These densities were calculated using Equations 4 and 5 and the charge/discharge curves at different current densities. The energy density of the solid-state device reached 5.8 W h kg^{-1} at a power density of 27.7 kW kg^{-1} and sustained 1.5 W h kg^{-1} at a power density of 277.6 kW kg^{-1} .

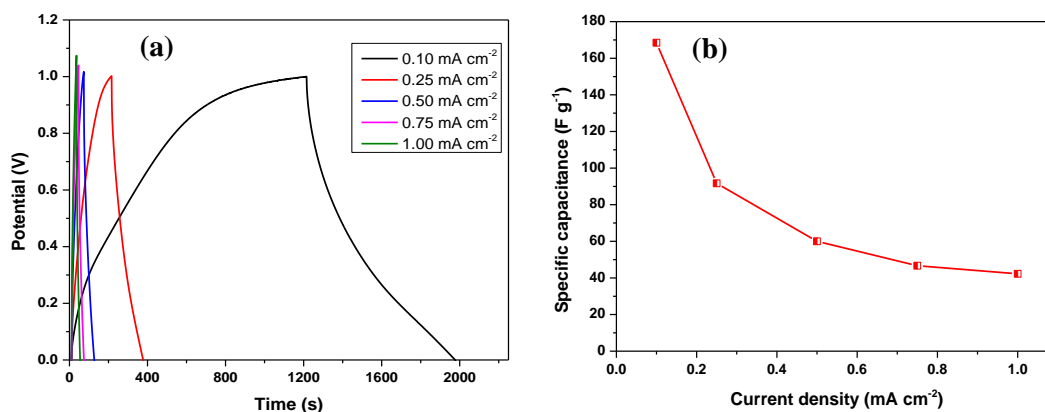


Figure 4.2.8 (a) GCD curves of the graphene-coated fabric SSC at various current densities. (b) Specific capacitance of the graphene-coated fabric SSC as a function of current density.

CV tests were conducted for the fabric supercapacitor under normal and bent conditions to explore the feasibility of using the device in flexible and wearable energy storage applications. **Figure 4.2.9a** displays the CV results. Bending did not cause any significant changes in the electrochemical performance of the device. The inset of **Figure 4.2.9a** shows photographs of the two test conditions. The as-fabricated supercapacitor demonstrated excellent flexibility and could be strongly bent without destroying the structural integrity of the device. Finally, to show the capability of the solid-state supercapacitor, five supercapacitors were assembled in serial to drive a light-emitting diode (LED). The charged supercapacitor device powered a green (**Figure 4.2.9b**) and a red LED (**Figure 4.2.9c**) for more than 15 min.

The excellent electrochemical performance of the eco-friendly solid-state SSC device was attributed to the following factors: (1) graphene nanosheets directly deposited on the conductive fabric formed an integrated electrode (binder-free device), which helped to improve the electrical conductivity between the electroactive material and the current collector, thereby reducing the contact resistance and facilitating a fast electrochemical reaction rate; (2) the graphene nanosheets provided a large accessible surface area and allowed abundant access of ions (adsorption/desorption), leading to more efficient charge transport; (3) the highly conducting graphene provided an effective pathway for charge transport; (4) the graphene-coated fabrics had excellent mechanical stability when bent. These various performance attributes suggest that graphene-nanosheet-coated fabrics hold great promise for flexible energy storage devices.

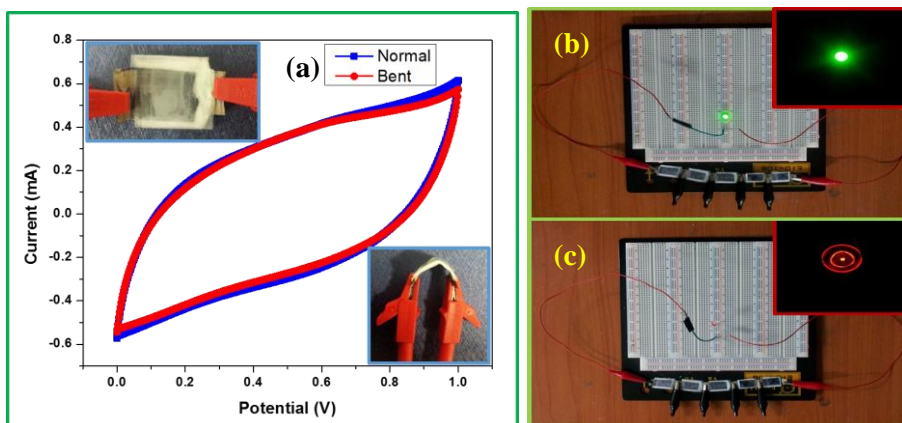


Figure 4.2.9 (a) Comparison of CV curves at 10 mV s^{-1} for the flexible graphene-coated fabric SSC measured as normal and bent. Photographs of (b) green and (c) red LEDs powered by graphene-coated fabric SSC devices connected in series. The insets are magnified images of the green and red LED glows.

4.2.4. Conclusion

Summarising, a graphene-coated fabric was generated using simple dip-coating followed by thermal treatment. A flexible solid-state graphene-coated fabric SSC exhibited excellent electrochemical performance with an energy density of 5.8 W h kg^{-1} at a power density of 27.7 kW kg^{-1} . The present method is simple and scalable to fabrication of graphene nanosheets on conductive cotton fabrics, which have considerable advantages as freestanding and binder-free electrodes for flexible and wearable supercapacitors.

4.2.5. References

- [1] J. F. Ihlefeld, P. G. Clem, B. L. Doyle, P. G. Kotula, K. R. Fenton, and C. A. Appleton, Fast lithium-ion conducting thin-film electrolytes integrated directly on flexible substrates for high-power solid-state batteries, *Adv. Mater.* 23 (2011) 5663–5667.
- [2] D. J. Lipomi, M. Vosgueritchian, B. C. Tee, S. L. Hellstrom, J. A. Lee, C. H. Fox, and Z. Bao, Skin-like pressure and strain sensors based on transparent elastic films of carbon nanotubes. *Nat. Nanotechnol.* 6 (2011) 788–792.
- [3] X. Zhang, L. Gong, K. Liu, Y. Cao, X. Xiao, W. Sun, X. Hu, Y. Gao, J. Chen, J. Zhou, and Z. L. Wang, Tungsten oxide nanowires grown on carbon cloth as a flexible cold cathode. *Adv. Mater.* 22 (2010) 5292–5296.
- [4] L. Yuan, X. Xiao, T. Ding, J. Zhong, X. Zhang, Y. Shen, B. Hu, Y. Huang, J. Zhou, and Z. L. Wang, Paper-based supercapacitors for self-powered nanosystems, *Angew. Chem. Int. Edit.* 5 (2012) 4934–4938.
- [5] C. Xu, C. Pan, Y. Liu, and Z. L. Wang, Hybrid cells for simultaneously harvesting multi-type energies for self-powered micro/nanosystems, *Nano Energy*, 1(2) (2012) 259–272.
- [6] L. G. H. Staaf, P. Lundgren, and P. Enoksson, Present and future supercapacitor carbon electrode materials for improved energy storage used in intelligent wireless sensor systems, *Nano Energy*, 9 (2014) 128–141.
- [7] D. Li, R. and B. Kaner, Graphene-based materials, *Science* 320(5880) (2008) 1170–1171.

- [8] S. Stankovich, D. A. Dikin, G. H. B. Dommett, K. M. Kohlhaas, E. J. Zimney, E. A. Stach, R. D. Piner, S. T. Nguyen, and R. S. Ruoff, Graphene-based composite materials, *Nature* 442(7100) (2006) 282–286.
- [9] Y. B. Tan, and J. M. Lee, Graphene for supercapacitor applications, *J. Mater. Chem. A* 1 (2013) 14814–14843.
- [10] C. Xu, B. Xu, Y. Gu, Z. Xiong, J. Sun, and X. S. Zhao, Graphene-based electrodes for electrochemical energy storage, *Energy Environ. Sci.* 6 (2013) 1388–1414.
- [11] D. Sun, X. Yan, J. Lang, and Q. Xue, High-performance supercapacitor electrode based on graphene paper via flame-induced reduction of graphene oxide paper, *J. Power Sources* 222 (2013) 52–58.
- [12] M. Kaempgen, C. K. Chan, J. Ma, Y. Cui, and G. Gruner, Printable thin film supercapacitors using single-walled carbon nanotubes, *Nano Lett.* 9 (5) (2009) 1872–1876.
- [13] D. Zhang, X. Zhang, Y. Chen, C. Wang, and Y. Ma, An environment-friendly route to synthesize reduced graphene oxide as a supercapacitor electrode material, *Electrochim. Acta*, 69 (2012) 364–370.
- [14] Y. Li, M. V. Zijl, S. Chiang, and N. Pan, KOH modified graphene nanosheets for supercapacitor electrodes, *J. Power Sources* 196 (2011) 6003–6006.
- [15] C. Liu, Z. Yu, D. Neff, A. Zhamu, and B. Z. Jang, Graphene-based supercapacitor with an ultrahigh energy density, *Nano Lett.* 10 (12) (2010) 4863–4868.

- [16] Y. Zhu, S. Murali, M. D. Stoller, A. Velamakanni, R. D. Piner, and R. S. Ruoff, Microwave assisted exfoliation and reduction of graphite oxide for ultracapacitors, *Carbon* 48(7) (2010) 2118–2122.
- [17] Y. Xu, Z. Lin, X. Huang, Y. Liu, Y. Huang, and X. Duan, Flexible solid-state supercapacitors based on three-dimensional graphene hydrogel films, *ACS Nano* 7(5) (2013) 4042–4049.
- [18] A. Yu, I. Roes, A. Davies, and Z. Chen, Ultrathin, transparent, and flexible graphene films for supercapacitor application, *Appl. Phys. Lett.* 96 (2010) 253105–253107.
- [19] X. Cao, Z. Yin, and H. Zhang, Three-dimensional graphene materials: preparation, structures and application in supercapacitors, *Energy Environ. Sci.* 7 (2014) 1850–1865.
- [20] Z. K. Wu, Z. Lin, L. Li, B. Song, K. Moon, S. L. Bai, and C. P. Wong, Flexible micro-supercapacitor based on in-situ assembled graphene on metal template at room temperature, *Nano Energy*, 10 (2014) 222–228.
- [21] K. S. Kim, Y. Zhao, H. Jang, S. Y. Lee, J. M. Kim, K. S. Kim, J. H. Anh, P. Kim, J. Y. Choi, and B. H. Hong, Large scale pattern growth of graphene films for stretchable transparent electrodes, *Nature* 457(7230) (2009) 706–710.
- [22] X. Lu, M. Yu, H. Huang, and R. S. Ruoff, Tailoring graphite with the goal of achieving single sheets, *Nanotechnology* 10(3) (1999) 269–272.
- [23] C. Berger, Z. Song, X. Li, X. Wu, N. Brown, C. Naud, D. Mayou, T. Li, J. Hass, A. N. Marchenkov, E. H. Conrad, P. N. First, and W. A. D. Heer,

- Electronic confinement and coherence in patterned epitaxial graphene, *Science* 312(5777) (2006) 1191–1196.
- [24] M. Choucair, P. Thordarson, and J. A. Stride, Gram-scale production of graphene based on solvothermal synthesis and sonication, *Nat. Nanotechnol.* 4(1) (2009) 30–33.
- [25] S. Stankovich, Synthesis of graphene-based nanosheets via chemical reduction of exfoliated graphite oxide, *Carbon* 45(3) (2007) 1558–1565.
- [26] S. Park, and R. S. Ruoff, Chemical methods for the production of graphenes, *Nat. Nanotechnol.* 29(4) (2009) 217–224.
- [27] M. J. McAllister, J. L. Li, D. H. Adamson, H. C. Schnlepp, A. A. Abdalam, J. Liu, and I. A. Aksay, Single sheet functionalized graphene by oxidation and thermal expansion of graphite, *Chem. Mater.* 19 (2007) 4396–4404.
- [28] F. Tuinstra, and J. L. Koenig, Raman spectrum of graphite, *J. Chem. Phys.* 53 (1970) 1126–130.
- [29] C. Chen, M. Long, M. Xia, C. Zhang, and W. Cai, Reduction of graphene oxide by an in-situ photoelectrochemical method in a dye-sensitized solar cell assembly, *Nanoscale Res. Lett.* 7 (2012) 101–105.
- [30] G. Eda, and M. Chhowalla, Chemically derived graphene oxide: towards large-area thin-film electronics and optoelectronics, *Adv. Mater.* 22 (2010) 2392–2415.
- [31] A Ramadoss, and S. J. Kim, Improved activity of a graphene–TiO₂ hybrid electrode in an electrochemical supercapacitor, *Carbon* 63 (2013) 434–445.

CHAPTER-V

Graphene-Based Composites for Electrochemical Supercapacitors

It is well known that, the supercapacitors can be divided into two types of charge-storage mechanisms [1-5]. The first are electrical double-layer capacitors (EDLCs), which are based on charge-separation at the electrode / electrolyte interface. Typical EDLC materials are activated carbon, carbon nanotubes, and graphene-based active materials with high surface area. The second are pseudocapacitors, which are based on Faradic redox reactions of electroactive materials, including transition metal oxides and conductive polymers [6,7]. The limited charge accumulation in the electrical double layer limits the specific capacitance and energy density of EDLCs [8]. In contrast, pseudocapacitors generally have higher specific capacitance and energy density that tends to gradually decrease as a result of poor electrical conductivity [9]. Also the strain developed in the pure metal oxide during the charge–discharge processes causes the cracking of the electrode, leading to poor long-term stability. Therefore metal oxides and carbon materials may not be employed alone as the supercapacitor electrodes for practical purpose.

To improve the specific capacitance and the energy density, develop a hybridize electrode containing both carbon and transition metal oxide as the supercapacitor electrode, which combines the merits and mitigate the shortcomings of both the components [8]. In such hybrid nanostructure electrode, the carbon nanostructure serve as the physical support of metal oxides and the high electrical conductivity benefits to the high rate capability and power density at higher

charge/discharge current. The metal oxides in hybrid nanostructure electrode contribute to the high specific capacitance and high energy density.

In recent years, graphene materials are attractive to researchers in various areas due to their wide potential applications (especially in energy storage), such as lithium-ion batteries [10], supercapacitors [11], solar cells [12], hydrogen storage [13], nanoelectronics [14], sensors [15], and nanocomposites [16]. Graphene, a single layer of carbon atoms tightly packed into a two-dimensional honeycomb sp^2 carbon lattice [17]. Due to its good conductivity, excellent chemical stability, large surface-to-volume ratio, high mobility of charge carriers, suitable pore size distribution and good capacitive performance, graphene has to be used as the electrode material for electrochemical supercapacitor (ESCs) [18-20].

Improving the capacitive performance of graphene-based energy storage materials by growing redox-active materials on the graphene nanosheets has thus become a topic of major interest. Recently, transition metal oxide such as RuO_2 , IrO_2 , MnO_2 , and NiO_x can improve the electrochemical performance of carbon-based supercapacitors, as they can contribute pseudocapacitance to the total capacitance apart from the double-layer capacitance provided by carbon materials [21-26]. This work is one of the most important ongoing fields of research in advanced energy-storage devices. However, most of them suffer the low abundance and high cost. Therefore, it is necessary to explore more desirable materials for the application in the field of ESCs.

Hence, the aim of research on the graphene-metal oxide composite electrodes is to develop electrodes that simultaneously possess high power density, high energy density as well as good rate capability, cyclic stability, low cost and environmentally

free. This chapter is organized into four sections: In the first section, synthesis and electrochemical performance of graphene-ZnO electrode was discussed. In the second section, we described the fabrication and testing of graphene/TiO₂ NRs /graphene hybrid nanostructure electrode for supercapacitor. In the next section, we discussed about the G-TiO₂ nanocomposite electrode for high performance supercapacitors. In the last section, we described the synthesis and electrochemical performance of G-V₂O₅ nanocomposites electrodes. Finally, the solid state devices were fabricated using the graphene based composites and demonstrate the LED driven experiments for practical applications.



5.1. Synthesis and Electrochemical Performance of Graphene-ZnO Nanocomposites

5.1.1. Introduction

Zinc oxide (ZnO) has triggered worldwide research interest as a wide-band-gap (3.37 eV) semiconductor material [27,28] for its tremendous potential applications in electronic and optoelectronic devices, such as photodetectors [29], light emitting diodes [30], electroluminescence devices [31], solar cells [32], gas sensors [33], flat display devices [34], piezoelectric nanogenerators [35], nanolasers [36], and so on. It is also a well-known battery active material having high energy density of 650 A/g [37]. Because of its good electrochemical activity and eco-friendly nature, researchers have begun to study ZnO to be a promising electrode material for the supercapacitor applications.

To the best of our knowledge, there are few reports on the graphene-ZnO composite as electrode materials for supercapacitors. Wang et al. [38] have prepared and studied their electrochemical performance of GNS/ZnO composites. Lu et al. [23] synthesized graphene/ZnO composite electrode materials by ultrasonic spray pyrolysis, which showed a specific capacitance of 61.7 F/g in 1 M KCl solution. Guo et al. [39] fabricated sandwiched type of reduced graphene oxide/ZnO nanorods/reduced graphene oxide on flexible PET substrate for supercapacitor applications, and the capacitance of 51.6 F g⁻¹ was obtained at a scan rate of 10 mV s⁻¹. Lu et al. [40] reported the specific capacitance of 146 F g⁻¹ at a scan rate of 2 mV s⁻¹ for graphene/ZnO nanocomposite prepared by microwave assisted synthesis. Y. Zhang et al. [26] reported graphene/ZnO composite for supercapacitor electrode using ultrasonic spray pyrolysis method, which exhibited a specific capacitance of 11.3 Fg⁻¹ in 1 M KCl electrolyte solution. However, the specific capacitance and

reversibility of these materials at higher current densities was not an ideal one and still need to be enhanced.

In this work, graphene-ZnO nanocomposite has been prepared as an electrode material for the electrochemical supercapacitor. First, graphene oxide (GO) was synthesized by a well-known modified Hummer's method, then GO-Zn(OH)₂ were prepared by sonochemical process. Finally, graphene-ZnO nanocomposites were synthesized by microwave-assisted method. The electrochemical properties of this composite were investigated by cyclic voltammetry and electrochemical impedance spectroscopy.

5.1.2. Experimental methods

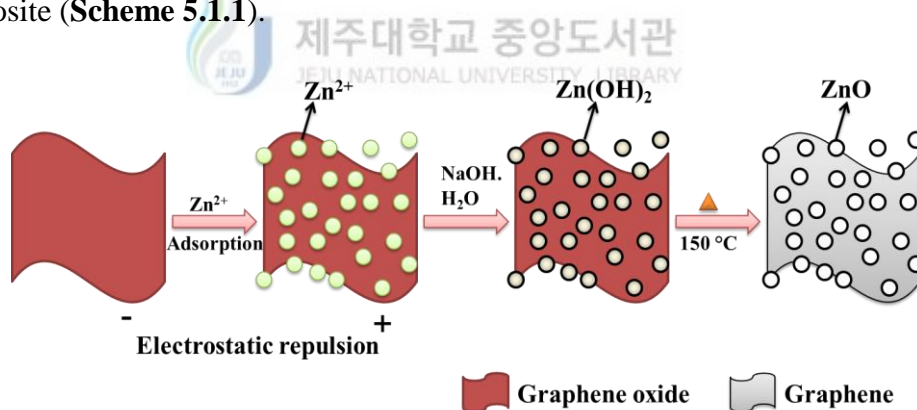
5.1.2.1. Synthesis of graphene oxide

Graphene oxide was successfully synthesized from expandable graphite powder by the modified Hummer's method [41]. Briefly, expandable graphite powder (2 g) was added into the concentrated H₂SO₄ (40 mL) solution with stirring for 2 h. KMnO₄ (6 g) was added slowly into the above solution with stirring while keeping the temperature of reaction less than 20 °C. The mixture was then stirred at 35-40 °C for 30 min, and then at 65-80 °C for 45 min. The resulting solution was diluted by adding 50 mL of water and the mixture was heated at 90 °C for 30 min, leads to the formation of dark brown solution. After additional stirring for 2 h, the dark brown solution was further diluted with distilled water (150 mL) and then H₂O₂ (10 mL) was added slowly and the color of the mixture was turned into brilliant yellow. The mixture was washed by repeated centrifugation and filtration, first with 5% HCl aqueous solution, and then with distilled water until the pH of the solution becomes neutral. Finally, 150 mL of water was added to the resulting precipitate and

sonicated well in a probe type sonicator nearly 1 h to obtain a uniform suspension of graphene oxide. After centrifuging and drying at 60 °C in hot air oven, the GO was obtained as a gray powder.

5.1.2.2. Synthesis of GO-Zn(OH)₂ composite

The GO-Zn(OH)₂ composite was achieved by sonochemical process. Briefly, 50 mg of GO was dispersed into a 20 mL of double distilled water and then sonicated for 30 min. 0.01 M of Zn(NO₃)₂ was dissolved in 10 mL of DI water. The above solution was dropwise added into the GO solution with the continuous sonication for 30 min to produce uniform dispersion. Afterwards a dilute NaOH solution was dropped into the solution to form a brownish black suspension with a pH value of the solution reached to 9. Finally, the obtained product is the formation of GO-Zn(OH)₂ composite (Scheme 5.1.1).



Scheme 5.1.1 Schematic representation of the growth process of the graphene-ZnO nanocomposite.

5.1.2.3. Synthesis of graphene-ZnO nanocomposite

The GO-Zn(OH)₂ composites and 10 μL of hydrazine were used as the precursor to subject into an automated focused household microwave synthesis system and treated for 2 min at 150 °C. It was observed that the color of suspension had changed from brown into black, indicating the successful chemical reduction of

GO [42]. The as-synthesized product was washed thoroughly with the distilled water and centrifuged at 10000 rpm for 10 minutes to remove the residuals. The obtained final product was dried in a hot air oven at 100 °C for 3 h, resulting to the formation of graphene-ZnO nanocomposite. The as-prepared samples were characterized by XRD, XPS, FE-SEM, FT-IR, Raman and UV-VIS analysis.

5.1.2.4. Preparation of electrodes and electrochemical characterization

The obtained graphene-ZnO nanocomposite solution was mixed with methanol. After the addition of methanol, some graphene-ZnO sheets were aggregated. The mixed solution was then subjected to centrifugation in order to remove aggregation. To prepare the graphene and graphene-ZnO nanocomposite electrode, a certain amount of the obtained solution were deposited onto the indium tin oxide (ITO) glass substrate (current collector) by dropwise addition (drop-casting method) with the aid of a micropipette. Finally, the deposited samples were dried at 80 °C in air for 1 hr.

The electrochemical experiments were investigated by using AUTOLAB PGSTAT302N electrochemical work station in 1 M KCl solution as an electrolyte. A typical three-electrode experimental cell equipped with a working electrode, a platinum foil as a counter electrode, and an Ag/AgCl as reference electrode was used for measuring the electrochemical properties of the working electrode. Cyclic voltammetry (CV) of the electrode was obtained at a scan rate of 10 mV s⁻¹ in the potential range of -0.5 to 0.5 V. Electrochemical impedance spectroscopy (EIS) measurements were carried out at a dc bias of 0.1 V with a signal of 5 mV over the frequency range of 0.1 Hz to 100 kHz.

5.1.3. Results and discussion

5.1.3.1. Structural analysis

Figure 5.1.1a shows the XRD pattern of graphene-ZnO nanocomposite. Graphene nanosheets exhibited a weak (100) diffraction peak at 44.5° . The ZnO nanoparticles were crystallized with the wurzite hexagonal structure with a preferred orientation of (101) plane. The observed d values are in good agreement with the standard d values of JCPDS card no: 89-1397. The other diffraction peaks at 31.3° , 34.1° , 35.8° , 47.2° , 56.2° , 62.5° , and 67.6° correspond to (100), (002), (101), (102), (110), (103), (112) planes of ZnO respectively. The average crystallite size of the ZnO NPs was calculated to be 24 nm by using a well-known Scherrer's formula [43].

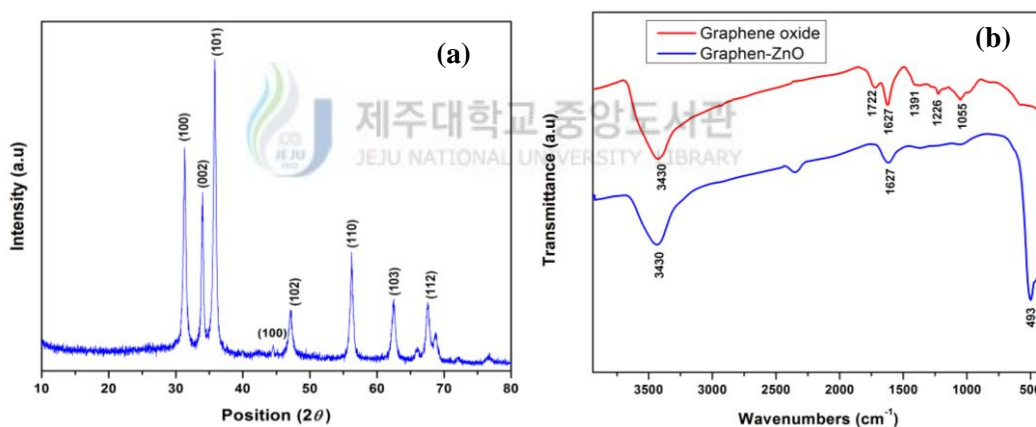


Figure 5.1.1 (a) X-ray diffraction pattern of graphene-ZnO nanocomposite. (b) FT-IR spectra of GO and graphene-ZnO nanocomposite.

FT-IR spectroscopy was used to confirm the reduction of oxygen-containing groups of graphene oxide. **Figure 5.1.1b** shows the FT-IR spectra of GO and graphene-ZnO nanocomposite. The presence of different types of oxygen functionalities in GO was confirmed from the characteristics bands at 1055 cm^{-1} for C-O stretching vibration of alkoxy, 1226 cm^{-1} for C-OH stretching vibration, 1391 cm^{-1} for O-H ($\nu(\text{carboxyl})$) and 1722 cm^{-1} for stretching vibrations from C=O [44].

The broad peak appeared at 3430 cm^{-1} is attributed to the stretching vibration of the O–H bond indicating the presence of small amount of water molecules absorbed on the surface. The peak at 1627 cm^{-1} is assigned to the vibration of the adsorbed water molecules and the contributions from the vibration of aromatic C=C [44]. For the ZnO NPs, an absorption band at 493 cm^{-1} is observed in the FT-IR spectrum, which is due to the formation of Zn-O bond [45]. The results showed that the most of the oxygen-containing functional groups of GO were significantly reduced in the graphene-ZnO nanocomposite curve.

The Raman studies are sensitive towards the crystallization, structural disorders and defects in nanostructures. Therefore, Raman-scattering studies have been performed for the as synthesized graphene-ZnO nanocomposite and the spectrum is shown in **Figure 5.1.2a**. It is also used to study the bonding nature of various carbon materials such as graphene, graphene oxide and carbon nanotubes. Raman spectrum of graphene-ZnO nanocomposite exhibited the characteristics peaks of graphene such as G band at 1589 cm^{-1} which corresponds to the first order scattering of the E_{1g} phonon mode of the sp^2 carbon atoms, and D band at 1348 cm^{-1} which is attributed to the breathing mode of κ -point phonons of A_{1g} symmetry [46, 47]. The D/G intensity ratio of graphene is larger than the graphene oxide, indicating the conversion from GO to graphene. These results are in consistent with the previously reported data [48].

In case of ZnO, the obtained Raman spectrum (**Figure 5.1.2a**) exhibits the three characteristic peaks at 323, 437 and 571 cm^{-1} [49]. The band at 323 cm^{-1} is attributed to the second-order Raman process. The peak at 437 cm^{-1} corresponds to the to the optical phonon E_2 (high) mode of wurtzite hexagonal phase ZnO [50]. The

weak peak at 571 cm^{-1} is positioned between A_1 (LO) and E_1 (LO) modes, which is in good agreement with the theoretical calculations of Fonoberov and Balandin [51].

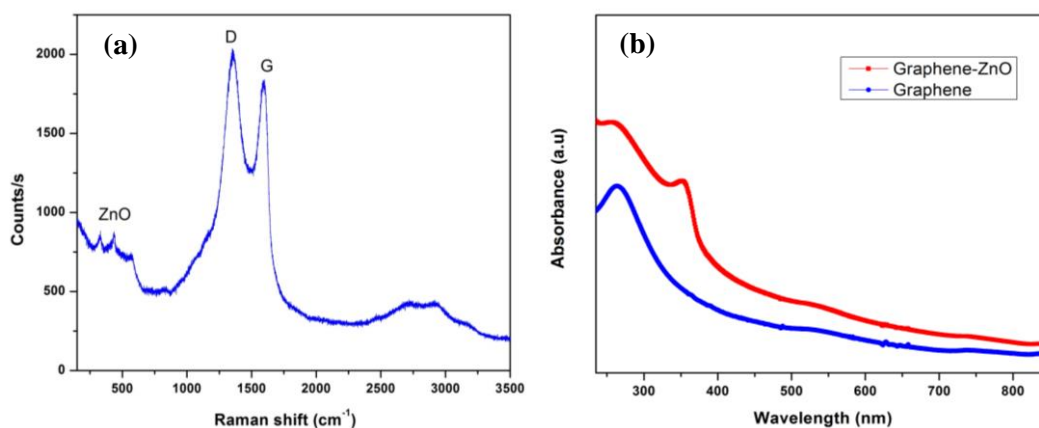


Figure 5.1.2 (a) Laser Raman spectrum of graphene-ZnO nanocomposite. (b) UV-visible absorbance spectra of graphene-ZnO nanocomposite.

Figure 5.1.2b shows the UV-visible absorption spectra of graphene and graphene-ZnO nanocomposite dispersed in water. The spectrum showed a high peak at 262 nm corresponds to the excitation of π - plasmon of graphitic structure [52]. Another peak at 355 nm corresponds to the wurzite hexagonal phase of ZnO. This indicates that the observed absorption peak is blue shifted from that of bulk ZnO. This is because of the quantum size-effect of ultrafine particles with nanometer size [53].

5.1.3.2. Morphology and compositional analysis

Figure 5.1.3 shows the FE-SEM image of graphene-ZnO nanocomposite. It is clearly seen that the graphene nanosheets are covered by densely packed and irregularly shaped ZnO nanograins, spread over the large-scale. The nanoparticle seems to be agglomerated. The agglomeration of nanoparticles is due to the high surface interaction between nanoparticles, which have a large specific surface area

and high surface energy [54]. The aggregation occurred probably during the drying process.

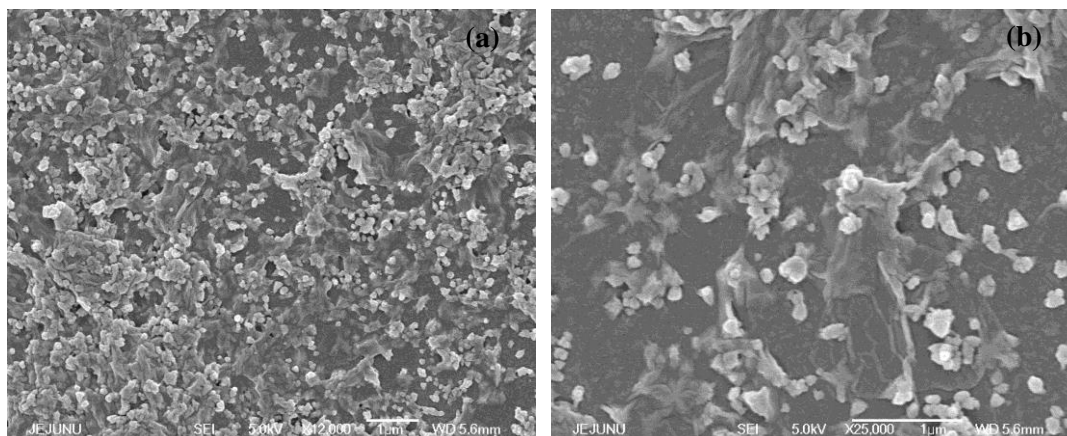


Figure 5.1.3 FE-SEM image of graphene-ZnO nanocomposite.

XPS was used to provide further evidence for the successful reduction degree of GO and the chemical composition of graphene-ZnO nanocomposite. The graphene-ZnO nanocomposite survey spectrum (**Figure 5.1.4a**) exhibited the characteristics peaks of Zn 2p_{1/2}, Zn 2p_{3/2}, Zn 3p, O 1s and C 1s with the corresponding binding energies of 1045.2, 1022.9, 90.7, 531.4, and 285.6 eV respectively [55]. The high resolution of Zn 2p spectrum (**Figure 5.1.4b**) exhibited the two major peaks with the binding energies at 1022.1 and 1045.22 eV, corresponding to Zn 2p_{3/2} and Zn 2p_{1/2} respectively, with a spin energy separation of 23.1 eV which is the characteristics of ZnO phase and in good agreement with the previous reported data of ZnO [56]. **Figure 5.1.4c** shows the high resolution spectra of O 1s. The deconvoluted peaks observed at 531.2 and 532.4 eV corresponds to the Zn-O and OH ions, respectively. The C1s spectrum of graphene-ZnO nanocomposite is shown in **Figure 5.1.4d**. The C1s spectrum shows suppressed carbon peaks corresponding to the oxygen-containing groups, indicating the success of the

reduction process [57, 1]. These results indicated the successful deposition of ZnO on the graphene surfaces and also the removal of the oxygenated functional groups.

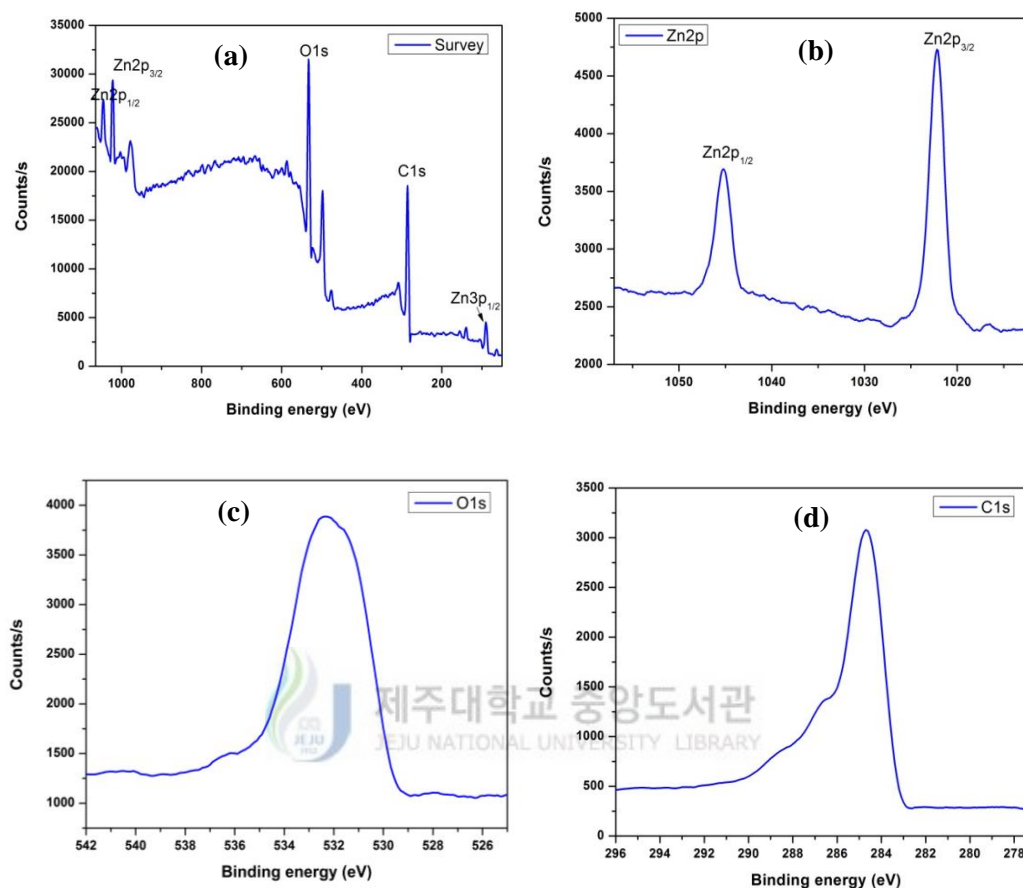


Figure 5.1.4 XPS spectra of graphene-ZnO nanocomposite (a) survey, (b) Zn 2p, (c) O 1s and (d) C 1s.

5.1.3.3. Electrochemical analysis

The electrochemical properties of the as prepared graphene and graphene-ZnO nanocomposite electrodes were investigated by cyclic voltammetry (CV) and electrochemical impedance spectroscopy (EIS) in 1 M KCl electrolyte solution.

Figure 5.1.5a shows the CV curves of graphene and graphene-ZnO nanocomposite at a scan rate of 10 mV s^{-1} . It can be seen that both of the CV curves have a similar and close to rectangular shape, indicating an ideal SC behavior of the electrode. The capacitive performance of graphene-ZnO electrode is obviously better than the

graphene electrode. To get more details on the capacitance performance of the as prepared graphene-ZnO nanocomposites electrode was used for the detailed measurements. **Figure 5.1.5b** shows the CV curves of graphene-ZnO electrode at the different scan rates of 5, 10, 25, and 50 mV s^{-1} in 1 M KCl electrolyte. All the CV curves are close to the rectangular shape, indicating an ideal capacitive property and an excellent reversibility of this electrode.

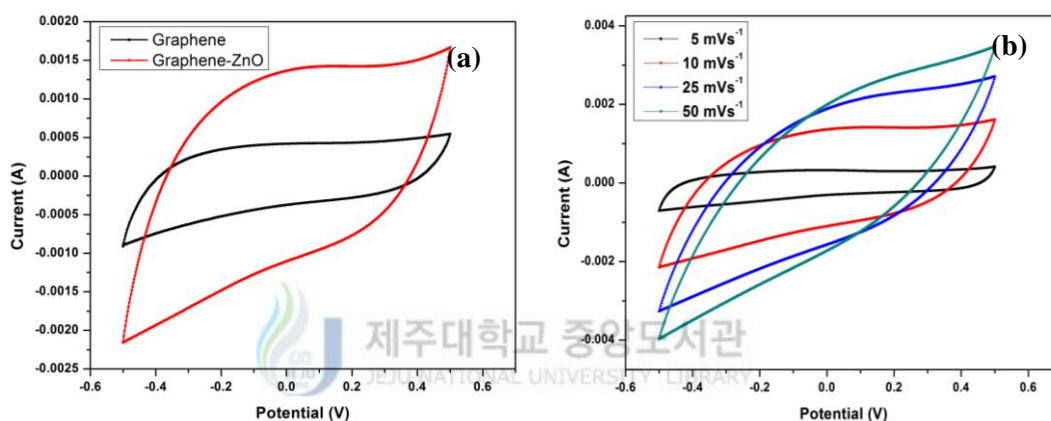


Figure 5.1.5 (a) CV curves of graphene and graphene-ZnO electrodes at scan rate of 10 mV s^{-1} in 1 M KCl electrolyte. (b) CV curves of graphene– ZnO composite at different scan rates of 5, 10, 25 and 50 mV s^{-1} .

The specific capacitance of the both electrodes were calculated from the CV curves according to the following equation (2.1). The calculated C_s values of graphene and graphene-ZnO electrodes from CV curve at a scan rate of 5 mV s^{-1} are 54 and 109 F g^{-1} . The obtained C_s value of graphene-ZnO nanocomposite is higher than the graphene electrode. The improved electrochemical performance of graphene-ZnO electrodes compared to the graphene is mainly attributed to the pseudocapacitance of ZnO phase and partially due to intrinsic electrical double layer capacitance of graphene. Therefore, it is reasonable to believe that the capacitance

behavior of graphene-ZnO electrodes is much better than that of graphene due to the fact that higher ZnO loading brings more pseudocapacitive contribution.

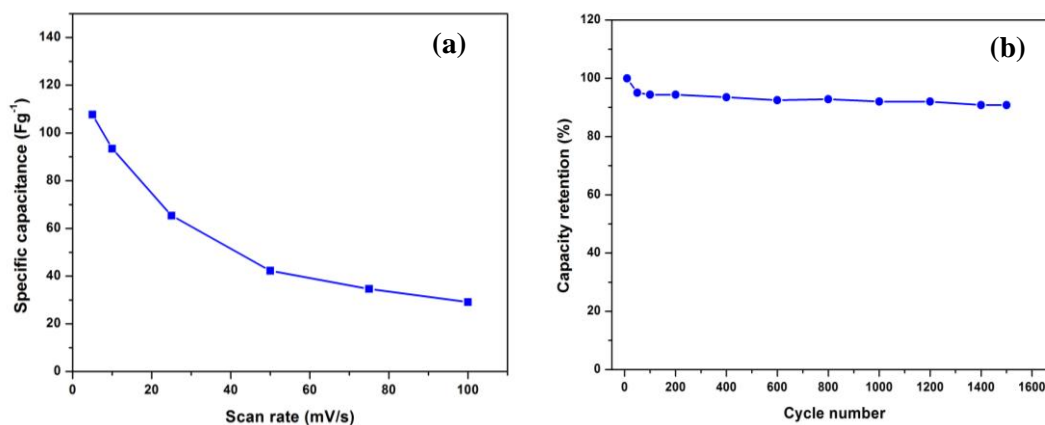


Figure 5.1.6 (a) Specific capacitance at different scan rates of graphene-ZnO nanocomposite. (b) Cycling stability of the graphene-ZnO nanocomposite electrode measured at 150 mV s^{-1} in 1 M KCl electrolyte.

Figure 5.1.6a shows the variation in the specific capacitance of the as-prepared graphene-ZnO nanocomposite samples as a function of scan rates. It could be found that the specific capacitance for nanocomposite electrode decreases with the increasing of scan rates from 5 to 100 mV s^{-1} . It is a common phenomenon and is caused by the insufficient time available for an ion diffusion and adsorption inside the smallest pores within large particles due to the diffusion limit at higher scan rates [58]. The cycle stability of supercapacitors is also an important parameter for their practical applications. The long-term cycle stability of the graphene-ZnO nanocomposite was evaluated using CV measurement at a scan rate of 150 mV s^{-1} for 1500 cycles. The capacitance retention ratio as a function of cycle number is shown in **Figure 5.1.6b**. The electrode exhibited an excellent long cycle life over the entire cycle numbers. The capacitance of the electrode only decreases by 6.8% of the initial

capacitance even after 1500 cycles, demonstrating an excellent cycle stability with a high degree of reversibility in the repetitive charge/discharge cycling.

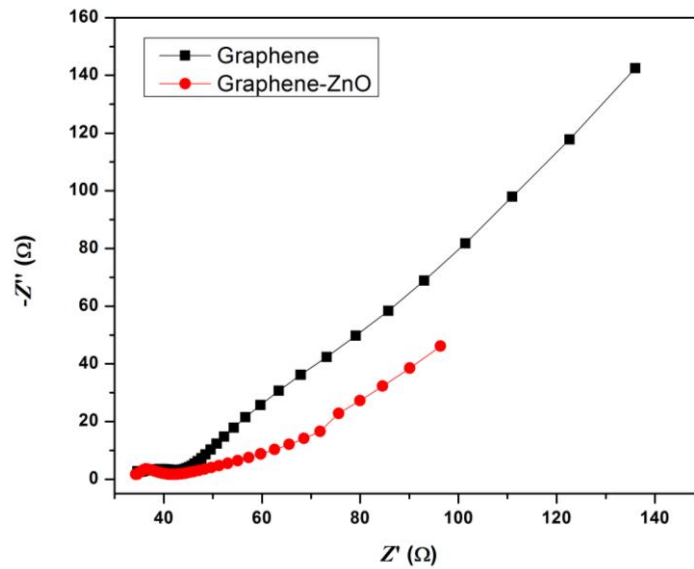


Figure 5.1.7 Nyquist plots of graphene and graphene-ZnO electrodes in 1 M KCl electrolyte.

The EIS analysis is used to study the fundamental behavior of electrode materials for the supercapacitors. The EIS experiments were conducted at a frequency range of 0.1 Hz to 100 kHz. The EIS data were analyzed using Nyquist plots, which show the frequency response of the electrode/electrolyte system and are plotted with the imaginary component ($-Z''$) of the impedance against the real component (Z'). **Figure 5.1.7** shows the Nyquist plot of the graphene and graphene-ZnO nanocomposite. Both the impedance plots are composed of a semicircle arc in the high frequency range and a straight line in the low frequency range. The high-frequency arc corresponds to the charge transfer limiting process and is ascribed to the double-layer capacitance (C_{dl}) in parallel with the charge transfer resistance (R_{ct}) at the contact interface between electrode and electrolyte solution. R_{ct} can be directly

measured as the semicircle diameter. The charge-transfer resistance (R_{ct}) caused by the Faradaic reactions and the doublelayer capacitance (C_{dl}) on the grain surface. It is found that the graphene-ZnO has a low R_{ct} (6.5 Ω) value compared to graphene (9.8 Ω), indicating that the incorporation of ZnO improves the charge transfer performance of graphene electrodes. The straight line in the low frequency range is related to the diffusive resistance (Warburg resistance) of the electrolyte into the interior of the electrode and ion diffusion/transport into the electrode surface. The almost vertical shape, representing the swift ion diffusion in electrolyte and the adsorption onto the electrode surface, suggested an ideally capacitive behavior of the electrodes.

5.1.4. Conclusion

In summary, graphene-ZnO nanocomposites were synthesized by microwave-assisted method and its structural, morphological, composition and electrochemical performance were investigated. The graphene-ZnO nanocomposite exhibited an enhanced electrode performance with the higher specific capacitance, higher electrochemical stability and higher energy density than the graphene electrodes. Graphene-ZnO nanocomposite achieves a high capacitance value of 109 F g⁻¹ at 10 mV s⁻¹ in the potential range of -0.5 to 0.5 V and also has a good reversible charge/discharge ability compared to the graphene electrode. The improved supercapacitance of graphene-ZnO nanocomposites compared to graphene is mainly attributed to the pseudocapacitance behavior of ZnO phase and partially from intrinsic electrical double layer capacitance of graphene nanosheets.

5.1.5. References

- [1] W. Yang, Z. Gao, J. Wang, B. Wang, Q. Liu, Z. Li, T. Manna, P. Yang, M. Zhang, and L. Liu, Synthesis of reduced graphene nanosheet/urchin-like manganese dioxide composite and high performance as supercapacitor electrode. *Electrochim. Acta* 69 (2012) 112-119.
- [2] L. L. Zhang, and X. S. Zhao, Carbon-based materials as supercapacitor electrodes. *Chem. Soc. Rev.* 38 (2009) 2520-2531.
- [3] Q. Qu, S. Yang, and X. Feng, 2D Sandwich-like sheets of iron oxide grown on graphene as high energy anode material for supercapacitors. *Adv. Mater.* 23 (2011) 5574-5580.
- [4] S. Murali, D. R. Dreyer, P. Valle-Vigon, M. D. Stoller, Y. Zhu, C. Morales, A. B. Furtés, C. W. Bielawski, and R. S. Ruoff, Mesoporous carbon capsules as electrode materials in electrochemical double layer capacitors. *Phys. Chem. Chem. Phys.* 13 (2011) 2652-2655.
- [5] P. J. Hall, M. Mirzaeian, S. I. Fletcher, F. B. Sillars, A. J. R. Rennie, G. O. Shitta-Bey, G. Wilson, A. Cruden, and R. Carter, Energy storage in electrochemical capacitors: designing functional materials to improve performance. *Energy Environ. Sci.* 3 (2010) 1238-1251.
- [6] L. Li, K. H. Seng, Z. Chen, H. Liu, I. P. Nevirkovets, and Z. Guo, Synthesis of Mn_3O_4 -anchored graphene sheet nanocomposites via a facile, fast microwave hydrothermal method and their supercapacitive behavior. *Electrochim. Acta* 87 (2013) 801-808.

- [7] X. Zhao, B. M. Sanchez, P. J. Dobson, and P. S. Grant, The role of nanomaterials in redox-based supercapacitors for next generation energy storage devices. *Nanoscale* 3 (2011) 839-855.
- [8] M. Zhi, C. Xiang, J. Li, M. Li, and N. Wu, Nanostructured carbon–metal oxide composite electrodes for supercapacitors: a review. *Nanoscale*, 5 (2013) 72–88.
- [9] X. Lu, G. Wang, T. Zhai, M. Yu, J. Gan, Y. Tong, and Y. Li, Hydrogenated TiO₂ nanotube arrays for supercapacitors. *Nano Lett.* 12 (2012) 1690-1696.
- [10] E.J. Yoo, J. Kim, E. Hosono, H.S. Zhou, T. Kudo, and I. Honma, Large reversible Li storage of graphene nanosheet families for use in rechargeable lithium ion batteries. *Nano Lett.* 8 (2008) 2277-2282.
- [11] M.D. Stoller, S. Park, Y. Zhu, J. An, and R.S. Ruoff, Graphene-based ultracapacitors. *Nano Lett.* 8 (2008) 3498-3502.
- [12] X. Wang, L. Zhi, and K. Mullen, Transparent, conductive graphene electrodes for dye-sensitized solar cells. *Nano Lett.* 8 (2008) 323-327.
- [13] L.P. Ma, Z.S. Wu, J. Li, E.D. Wu, W.C. Ren, and H.M. Cheng, Hydrogen adsorption behavior of graphene above critical temperature. *Int. J. Hydrogen Energy* 34 (2009) 2329-2332.
- [14] P. Blake, P.D. Brimicombe, P.R. Nair, T.J. Booth, D. Jiang, F. Schedin, L.A. Ponomarenko, L.V. Morozov, H.F. Gleeson, E.W. Hill, A.K. Geim, and K.S. Novoselov, Graphene-based liquid crystal device. *Nano Lett.* 8 (2008) 1704-1708.
- [15] H.B. Heersche, P. Jarillo-Herrero, J.B. Oostinga, L.M.K. Vandersypen, and A.F. Morpurgo, Bipolar supercurrent in graphene. *Nature* 446 (2007) 56-59.

- [16] D. Li, and R.B. Kaner, Graphene-based materials. *Science* 320 (2008) 1170-1171.
- [17] A.K. Geim, and K.S. Novoselov, The rise of graphene. *Nat. Mater.* 6 (2007) 183-191.
- [18] S. Guo, and S. Dong, Graphene nanosheet: synthesis, molecular engineering, thin film, hybrids, and energy and analytical applications. *Chem. Soc. Rev.* 40 (2011) 2644-2672.
- [19] X. Zhang, X. Sun, Y. Chen, D. Zhang, and Y. Ma, One-step solvothermal synthesis of graphene/Mn₃O₄ nanocomposites and their electrochemical properties for supercapacitors. *Mater. Lett.* 68 (2012) 336-339.
- [20] K.S. Novoselov, A.K. Geim, S.V. Morozov, D. Jiang, Y. Zhang, S.V. Dubonos, I.V. Grigorieva, and A.A. Firsov, Electric field effect in atomically thin carbon films. *Science* 306 (2004) 666-669.
- [21] S. Chen, J. Zhu, X. Wu, Q. Han, and X. Wang, Graphene oxide–MnO₂ nanocomposites for supercapacitors. *ACS Nano* 4 (2010) 2822-2830.
- [22] B.J. Lee, S.R. Sivakkumar, J.M. Ko, J.H. Kim, S.M. Jo, and D.Y. Kim, Carbon nanofibre/hydrous RuO₂ nanocomposite electrodes for supercapacitors. *J. Power Sources* 168 (2007) 546-552.
- [23] T. Lu, Y. Zhang, H. Li, L. Pan, Y. Li, and Z. Sun, Electrochemical behaviors of graphene–ZnO and graphene–SnO₂ composite films for supercapacitors. *Electrochim. Acta* 55 (2010) 4170-4173.
- [24] Y. Shan, and L. Gao, Formation and characterization of multi-walled carbon nanotubes/Co₃O₄ nanocomposites for supercapacitors. *Mater. Chem. Phys.* 103 (2007) 206-210.

- [25] J. Yan, Z. Fan, T. Wei, W. Qian, M. Zhang, and F. Wei, Fast and reversible surface redox reaction of graphene-MnO₂ composites as supercapacitor electrodes. *Carbon* 48 (2010) 3825-3833.
- [26] Y. P. Zhang, H. B. Li, L. K. Pan, T. Lu, and Z. Sun, Capacitive behavior of graphene– ZnO composite film for supercapacitors. *J. Electroanal. Chem.* 634 (2009) 68-71.
- [27] G.C. Yi, C. Wang, and W.I. Park, ZnO nanorods: synthesis, characterization and applications. *Semicond. Sci. Technol.* 20 (2005) S22-S34.
- [28] F. Lu, W. Cai, and Y. Zhang, ZnO Hierarchical micro/nanoarchitectures: Solvothermal synthesis and structurally enhanced photocatalytic performance. *Adv. Funct. Mater.* 18 (2008)1047-1056.
- [29] C.Y. Lu, S.J. Chang, S.P. Chang, C.T. Lee, C.F. Kuo, H.M. Chang, H.Z. Chiou, C.L. Hsu, and I.C. Chen, Ultraviolet photodetectors with ZnO nanowires prepared on ZnO: Ga/glass templates. *Appl. Phys. Lett.* 89 (2006) 153101-153103.
- [30] J.H. Na, M. Kitamura, M. Arita, and Y. Arakawa, Hybrid p-n junction light-emitting diodes based on sputtered ZnO and organic semiconductors. *Appl. Phys. Lett.* 95 (2009) 253303-253305.
- [31] W.I. Park, and G.C. Yi, Electroluminescence in n-ZnO Nanorod Arrays Vertically Grown on p-GaN. *Adv. Mater.* 16 (2004) 87-90.
- [32] P. Sudhagar, R.S. Kumar, J.H. Jung, W. Cho, R. Sathyamoorthy, J. Won, and Y.S. Kang, Facile synthesis of highly branched jacks-like ZnO nanorods and their applications in dye-sensitized solar cells. *Mater. Res. Bull.* 46 (2011) 1473-1479.

- [33] J. Xu, J. Han, Y. Zhang, Ya. Sun, and B. Xie, Studies on alcohol sensing mechanism of ZnO based gas sensors. *Sen. Actua. B-Chem.* 132 (2008) 334-339.
- [34] S.B. Park, B.G. Kim, J.Y. Kim, T.H. Jung, D.G. Lim, J.H. Park, and J.G. Park, Field-emission properties of patterned ZnO nanowires on 2.5D MEMS substrate. *Appl. Phys. A* 102 (2011) 169-172.
- [35] Z.L. Wang, R. Yang, J. Zhou, Y. Qin, C. Xu, Y. Hu, and S. Xu, Lateral nanowire/nanobelt based nanogenerators, piezotronics and piezo-phototronics. *Mater. Sci. Eng. R-Rep.* 70 (2010) 320-329.
- [36] M.H. Huang, S. Mao, H. Feick, H. Yan, Y. Wu, H. Kind, E. Webber, R. Russo, and P. Yang, Room-temperature ultraviolet nanowire nanolasers. *Science* 292 (2001) 1897-1899.
- [37] Y. Ito, M. Nyce, R. Plivelich, M. Klein, D. Steingart, and S. Banerjee, Zinc morphology in zinc–nickel flow assisted batteries and impact on performance. *J. Power Sources* 196 (2011) 2340-2345.
- [38] J. Wang, Z. Gao, Z. Li, B. Wang, Y. Yan, Q. Liu, T. Mann, M. Zhang, and Z. Jiang, Green synthesis of graphene nanosheets/ZnO composites and electrochemical properties. *J. Solid State Chem.* 184 (2011) 1421-1427.
- [39] G. Guo, L. Huang, Q. Chang, L. Ji, Y. Liu, Y. Xie, W. Shi, and N. Jia, Flexible and transparent supercapacitor based on In₂O₃ nanowire/carbon nanotube heterogeneous films. *Appl. Phys. Lett.* 99 (2011) 83111-83113.
- [40] T. Lu, L. Pan, H. Li, G. Zhu, T. Lv, X. Liu, Z. Sun, T. Chen, and D. H.C. Chua, Microwave-assisted synthesis of graphene–ZnO nanocomposite for electrochemical supercapacitors. *J. Alloy. Comp.* 509 (2011) 5488–5492.

- [41] K. Krishnamoorthy, R. Mohan, and S.J. Kim, Graphene oxide as a photocatalytic material. *Appl. Phys. Lett.* 98 (2011) 244101-244103.
- [42] H.A. Becerril, J. Mao, Z. Liu, R.M. Stoltenberg, Z. Bao, and Y. Chen, Evaluation of solution-processed reduced graphene oxide films as transparent conductors.. *ACS Nano* 2 (2008) 463-470.
- [43] A. Ramadoss, K. Krishnamoorthy, and S.J. Kim, Facile synthesis of hafnium oxide nanoparticles via precipitation method. *Mater. Lett.* 75 (2012) 215-217.
- [44] Q. Shou, J. Cheng, L. Zhang, B.J. Nelson, and X. Zhang, Synthesis and characterization of a nanocomposite of goethite nanorods and reduced graphene oxide for electrochemical capacitors. *J. Solid State Chem.* 185 (2012) 191-197.
- [45] M.A. Gondal, Q.A. Drmash, Z.H. Yamani, and T.A. Saleh, Synthesis of ZnO₂ nanoparticles by laser ablation in liquid and their annealing transformation into ZnO nanoparticles. *Appl. Surf. Sci.* 256 (2009) 298-304.
- [46] V. Singh, D. Joung, L. Zhai, S. Das, S.I. Khondaker, and S. Seal, Graphene based materials: past, present and future. *Prog. Mater. Sci.* 56 (2011)1178-1271.
- [47] L.G. Cancado, M.A. Pimenta, B.R.A. Neves, M.S.S. Dantas, and A. Jorio, Influence of the atomic structure on the Raman spectra of graphite edges. *Phys. Rev. Lett.* 93 (2004) 247401-247404.
- [48] X.Y. Peng, X.X. Liu, D. Diamond, and K.T. Lau, Synthesis of electrochemically-reduced graphene oxide film with controllable size and thickness and its use in supercapacitor. *Carbon* 49 (2011) 3488-3496.

- [49] R.Y. Sato-Berru, A. Va´zquez-Olmos, A.L. Ferna´ndez-Osorio, and S. Sotres-Marti´nez, Micro-Raman investigation of transition-metal-doped ZnO nanoparticles. *J. Raman Spectrosc.* 38 (2007) 1073-1076.
- [50] K.A. Alim, V.A. Fonoberov, M. Shamsa, and A.A. Balandin, Micro-Raman investigation of optical phonons in ZnO nanocrystals. *J. Appl. Phys.* 97 (2005) 124313-124317.
- [51] V.A. Fonoberov, and A.A. Balandin, Interface and confined optical phonons in wurtzite nanocrystals. *Phys. Rev. B* 70 (2004) 233205-233208.
- [52] X. Wang, L.J. Zhi, N. Tsao, J.L. Tomovic, and K. Mullen, Transparent carbon films as electrodes in organic solar cells. *Angew. Chem. Int. Ed.* 47 (2008) 2990-2992.
- [53] X.M. Yang, Z.Z. Gu, Z.H. Lu, and Y. Wei, Atomic force microscopy and UV-visible absorption-spectroscopy studies of ZnO nanometer colloidal particles supported on graphite. *Appl. Phys. A* 59 (1994) 115-117.
- [54] S. Mohseni Meybodi, S.A. Hosseini, M. Rezaee, S.K. Sadrnezhaad, and D. Mohammadyani, Synthesis of wide band gap nanocrystalline NiO powder via a sonochemical method. *Ultrasonic Sonochem.* 19 (2012) 841-845.
- [55] Y. Zhang, W. Zhang, and H. Zheng, Fabrication and photoluminescence properties of ZnO:Zn hollow microspheres. *Scripta Materialia* 57 (2007) 313-316.
- [56] R. Escudero, and R. Escamilla, Ferromagnetic behavior of high-purity ZnO nanoparticles, *Solid State Commun.* 151 (2011) 97-102.

- [57] C. Chen, M. Long, M. Xia, C. Zhang, and W. Cai, Reduction of graphene oxide by an in-situ photoelectrochemical method in a dye-sensitized solar cell assembly. *Nanoscale Res. Lett.* 7 (2012) 101-109.
- [58] J. Yan, T. Wei, W. Qiao, B. Shao, Q. Zhao, L. Zhang, and Z. Fan, Rapid microwave-assisted synthesis of graphene nanosheet/Co₃O₄ composite for supercapacitors. *Electrochim Acta*, 55 (23) (2010) 6973-6978.



5.2. Synthesis and Electrochemical Performance of TiO₂/rGO/TiO₂ Hybrid Nanostructure

5.2.1. Introduction

Among these metal oxides, titanium dioxide (TiO₂) is considered one of the most promising candidates for use in supercapacitors due to its low cost, electrochemical stability, natural abundance, high surface area, low toxicity, and ease of preparation in defined nanoscale dimensions [1,2]. Furthermore, TiO₂ is an n-type semiconductor, and surface charges are greater than in other regions due to a positively charged depletion region [3]. Hence, TiO₂ is suitable for low-cost electrode materials in supercapacitor applications. However, there are a limited number of available reports that describe TiO₂-based supercapacitors. Each of these describes a different method of TiO₂ preparation, resulting in considerable variation with regard to morphology and supercapacitor performance. However, the specific capacitance and rate capability of these materials were still low at higher current densities. This may be due to an inherently lower electrical conductivity.

A new approach is needed to overcome these problems and to improve the capacitive performance and stability of TiO₂ electrodes. One possible approach is to fabricate the nanostructured electrodes with an extremely large surface area. One-dimensional (1D) nanostructures, such as nanotubes, nanowires, and nanosheets, provide a much higher surface area than their bulk counterparts [4]. In addition, 1D nanostructures offers a direct pathway for electron transfer between the electrode and electrolyte and a shortened diffusion path for the intercalation / de-intercalation of electro-active species resulting in higher capacitance [5]. Another approach is the mixing of highly conductive materials with metal oxide electrode materials to increase the overall electrical conductivity of the electrodes. Recently, graphene or

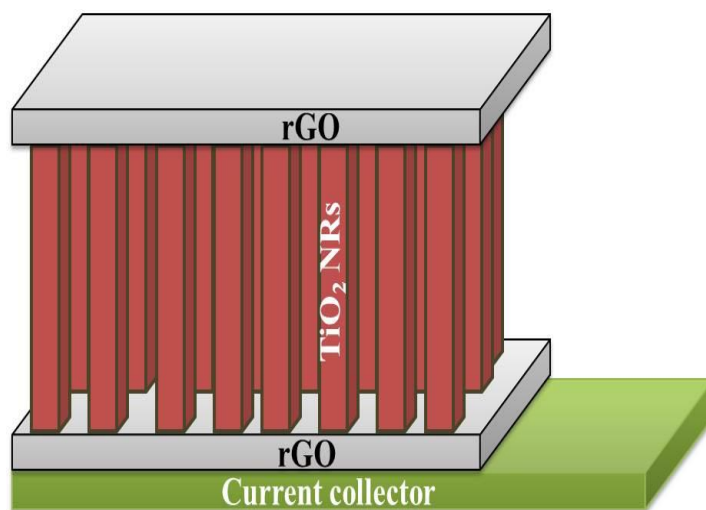
reduced graphene oxide sheets which boost high specific area, high conductivity, flexibility, thermal stability, chemical stability, and appropriate mechanical properties have been considered as promising candidates for use in supercapacitor applications [6-9]. Combining the unique properties of graphene with 1D nanostructured materials with high specific surface area and fast electron transfer opens new avenues for research in energy conversion and storage.

This chapter describes the two-dimensional (2D) reduced graphene oxide / TiO₂ nanorod array / reduced graphene oxide (rGO / TiO₂ NR / rGO) electrodes fabricated on the surface of fluorine-doped tin oxide (FTO) substrates for use in supercapacitor applications. The porous hybrid structure of these materials exhibited a high specific surface area and a fast ion diffusion process that could enhance specific capacitance and rate capability.

5.2.2. Experimental methods

5.2.2.1. Preparation and characterization of rGO / TiO₂ NR / rGO electrode

A schematic diagram of the rGO / TiO₂ NR / rGO structure is shown in **Scheme 5.2.1**. Graphene oxide (GO) was successfully synthesized from expandable graphite powder using a modified Hummer's method and reduction with hydrazine [10]. After reduction of GO, the solution was washed thoroughly with distilled water and centrifuged at 10,000 rpm for 10 minutes to remove any aggregates. As-prepared rGO sheets were re-dispersed in dimethylformamide (DMF) to a concentration of ~1 mg/mL to make the rGO solution.



Scheme 5.2.1 Schematic diagram of an rGO / TiO₂ NR / rGO electrode.

To prepare rGO thin films, rGO solution was dropped onto FTO-coated glass substrates and the samples were spin-coated at 3,000 rpm for 20 s. After deposition, the samples were dried at 80°C in air for 1 hr. The thickness of the rGO layer was controlled by repeating the spin coating process for 20 cycles. The same procedure was used to deposit rGO coatings on top of TiO₂ NR arrays. Vertically aligned TiO₂ NR arrays were prepared using a simple hydrothermal method with titanium tetra-n-butoxide and HCl as the precursors [11]. RGO-coated substrates were loaded into the same autoclave with the coating side facing up. The autoclave was sealed and hydrothermal treatment commenced at 150 °C for 3 h in an electric oven. After synthesis, the Teflon reactor was cooled to room temperature under ambient conditions. The samples were then removed, rinsed extensively with deionized water, and allowed to dry in ambient air. The crystal structure, morphology and chemical composition of the resulting hybrid material was determined using a XRD, Raman, FE-SEM, and XPS techniques.

5.2.2.2. Electrochemical characterization of rGO / TiO₂ NR / rGO electrodes

Electrochemical experiments were performed at an AUTOLAB PGSTAT302N electrochemical workstation in 1 M Na₂SO₄ as the electrolyte. A typical three-electrode experimental cell, equipped with platinum as the counter electrode and an Ag/AgCl reference electrode, was used for measuring the electrochemical properties of the working electrode. The effective electrode area of the active material was 1 cm x 1 cm. Cyclic voltammograms of the working electrode were measured at different scan rates of 5, 10, 25, 50, 75, 100, and 125 mV s⁻¹ from 0 to 0.8 V. EIS measurements were performed with a DC bias of 0.1 V and a signal of 5 mV from 0.1 Hz to 100 kHz. GCD curves were measured from 0 to -0.8 V at current densities of 0.010, 0.025, 0.050, 0.075 and 0.100 mA cm⁻².

5.2.3. Results and discussion

The crystal structure and orientation of the as-prepared samples were studied by XRD. The diffractogram of rGO in **Figure 5.2.1a** shows a broad diffraction peak around $2\theta = 24.68^\circ$, which corresponds to the (002) reflection of rGO sheets. A diffractogram of an rGO / TiO₂ NR / rGO hybrid nanostructure is shown in **Figure 5.2.1b**. It contains a peak characteristic of a tetragonal rutile phase with a preferred orientation of the (002) plane at $2\theta = 62.77^\circ$. The observed data are in a good agreement with the standard rutile phase of TiO₂ (JCPDS card number 21-1276). Other characteristic peaks of relatively lesser intensity at 27.06° , 35.98° , 54.29° , and 69.72° , on the 2θ scale correspond to the (110), (101), (211), and (112), planes of the rutile phase [12]. The high intensity of the (002) peak indicates that TiO₂ NR arrays grew with their c-axes orientated orthogonal to the rGO-coated substrate surface. Moreover, peaks indicated by the box symbol correspond to X-ray diffraction from

the FTO substrate. Notably, no diffraction peaks corresponding to rGO were observed in the hybrid structure. This is because the main characteristic peak of rGO at 24.68° has a low intensity and can overlap with the FTO substrate peak at 25.3° .

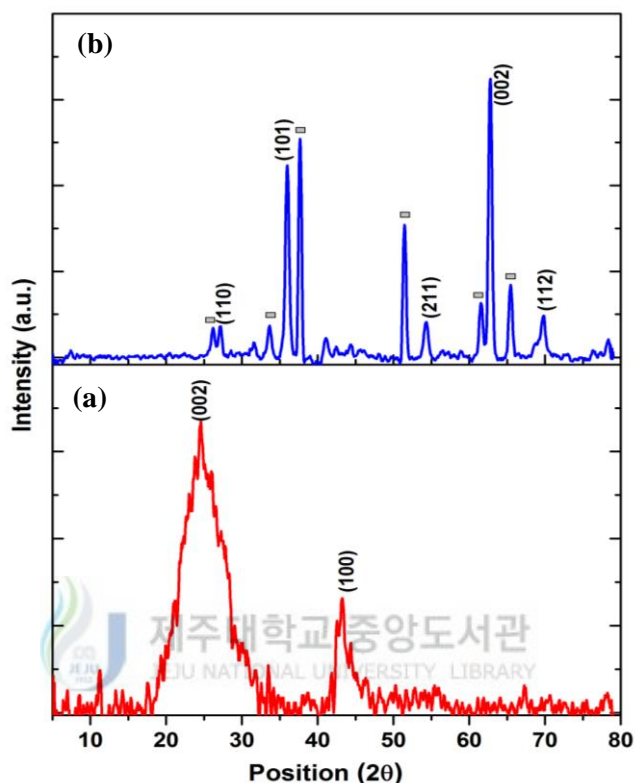


Figure 5.2.1 XRD diffraction patterns of (a) pure rGO and (b) the rGO / TiO₂ NR / rGO hybrid nanostructure.

Raman spectroscopy is widely used to characterize crystal structure, disorder, and defects in graphene-based materials. **Figure 5.2.2** shows Raman spectra of pure rGO and an rGO / TiO₂ NR / rGO hybrid nanostructure from 100 to 3000 cm⁻¹. As shown in **Figure 5.2.2** characteristic peaks at 1342 and 1593 cm⁻¹ were ascribed to sp³ (D band) and sp² (G band) hybridized carbon atoms, respectively [13]. The inset of **Figure 5.2.2** shows symmetric 2D and S3 bands of rGO sheets [14]. Moreover, the D/G band intensity ratio after hydrazine reduction increased relative to that of GO. This suggests a decrease in the average size of sp² domains upon hydrazine

reduction [15,16]. This provides further evidence that GO was reduced to graphene. Furthermore, the obtained Raman spectrum in **Figure 5.2.2b** contains four characteristic peaks at 130, 240, 444 and 613 cm^{-1} , which correspond to the B_{1g} , E_g , and A_{1g} modes of rutile TiO_2 NRs, respectively [17].

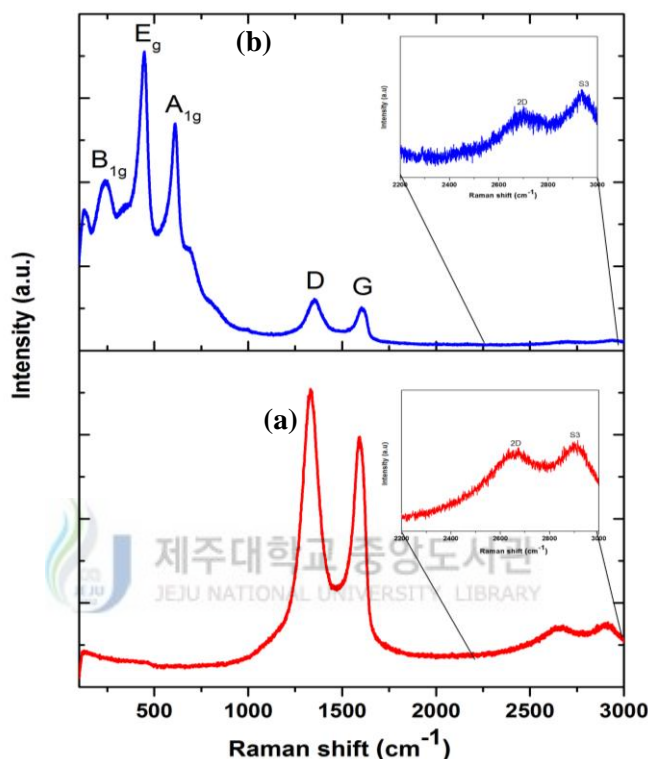


Figure 5.2.2 Raman spectra of (a) pure rGO and (b) the rGO / TiO_2 NR / rGO hybrid nanostructure.

Figures 5.2.3a through 5.2.3b. show the FE-SEM images of a rGO / TiO_2 NR / rGO electrode. Note that the TiO_2 NR arrays completely cover the rGO sheets. The rGO sheets are supported by the TiO_2 NRs and do not restack into a 2D plane, but instead form a porous structure. The porous hybrid structure allows for electrolyte penetration, which is favorable for ion diffusion, charge transfer, and capacitance, and increases the overall surface area of the electrode. **Figures 5.2.3c and 5.2.3d** show cross-sectional views of vertically aligned TiO_2 NR arrays. Note

that the sides of the TiO₂ nanorods are relatively smooth, vertically oriented, and aligned along the rGO-coated FTO substrate. The TiO₂ NRs averaged 80-150 nm in width with a uniform length of 1.5-2 μm.

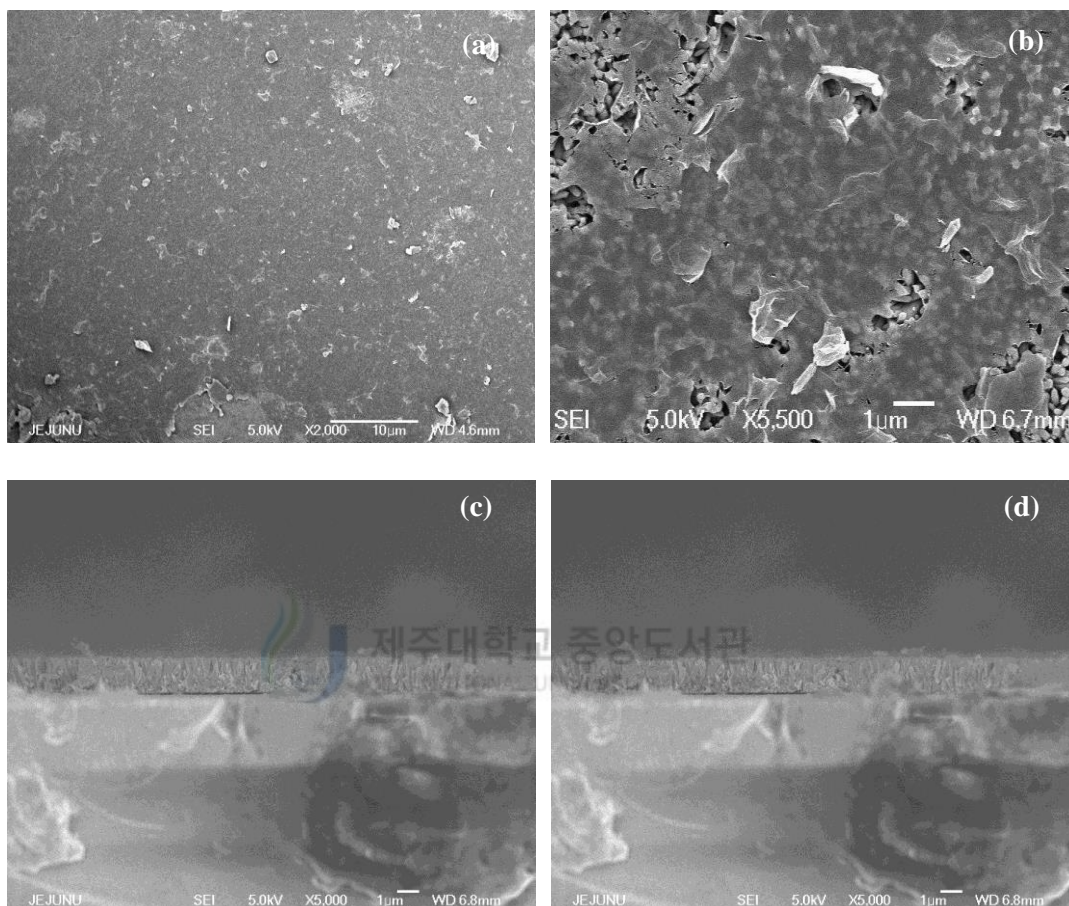


Figure 5.2.3 (a-b) Top view FE-SEM images of the rGO / TiO₂ NR / rGO porous hybrid structure. (c-d) Cross-sectional views of the hybrid structure.

XPS spectra, shown in **Figure 5.2.4** were acquired to determine oxidation levels and the nature of chemical bonding in the rGO / TiO₂ NR / rGO electrode. **Figure 5.2.4a** shows a wide-scan spectrum Ti 2p, O 1s and C 1s peaks were detected at binding energies of 459.1, 530.5, and 284.6 eV, respectively. **Figure 5.2.4b** shows a high-resolution spectrum of the Ti 2p peak which consists of a doublet with peaks at 459.1 and 464.8 eV, corresponding to the Ti 2p_{3/2} and Ti 2p_{1/2} core levels of TiO₂ respectively [14]. The observed splitting width of 5.68 eV is in good agreement with

earlier data [18]. **Figure 5.2.4c** shows a high-resolution O 1s spectrum of the as-prepared samples. Two peaks at 530.6 and 532.4 eV, correspond to the TiO₂ phase and an –OH group, respectively. The high-resolution C 1s spectrum can be deconvoluted into four components (**Figure 5.2.4d**) corresponding to carbon species in different functional groups: (i) non-oxygenated carbon (C-C) at 284.4 eV, (ii) carbon in C-O (hydroxyl and epoxy groups) at 285.3 eV, (iii) C=O (carbonyl groups) at 286.2 eV, and O-C=O (carboxyl groups) at 288.3 eV [19]. The smaller intensities of these peaks indicate the reduction of GO [20].

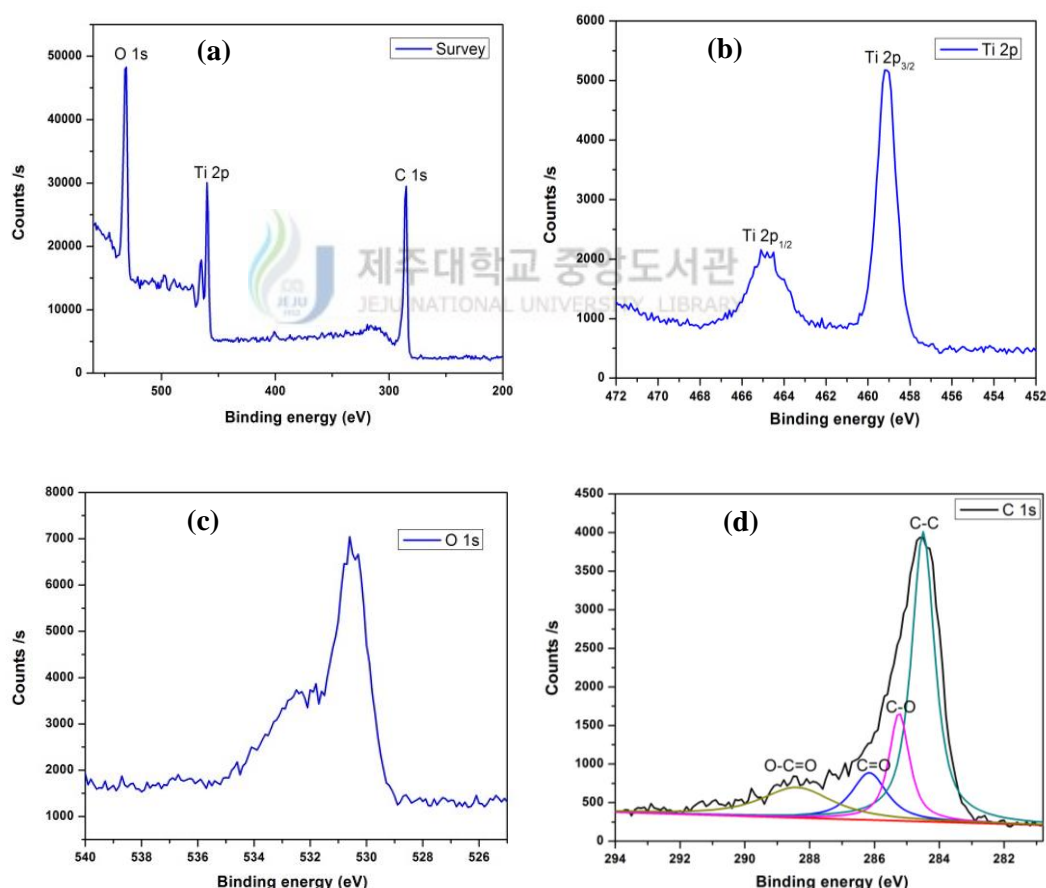


Figure 5.2.4 XPS spectra of an rGO / TiO₂ NR / rGO electrode (a) wide scan survey, (b) Ti 2p, (c) O 1s, and (d) C 1s.

The electrochemical performance of the as-prepared TiO₂ NRs, rGO, and rGO / TiO₂ NR / rGO electrodes was evaluated by CV, EIS, and GCD measurements

in 1 M Na₂SO₄. **Figure 5.2.5a** shows typical CVs between 0 and 0.8 V at a scan rate of 5 mV s⁻¹. The CV of the rGO / TiO₂ NR / rGO electrode approximates an ideal rectangle with a greater area and a more symmetrical shape, than CVs acquired with rGO and TiO₂ NRs. This indicates the greater capacitive nature of the hybrid material. **Figure 5.2.5b** displays the CV of an as-prepared electrode scan rates from 5 to 125 mV s⁻¹. The area defined by the CV increased with the scan rate, and maintained a rectangular shape without obvious distortion, even at scan rates of up to 125 mV s⁻¹.

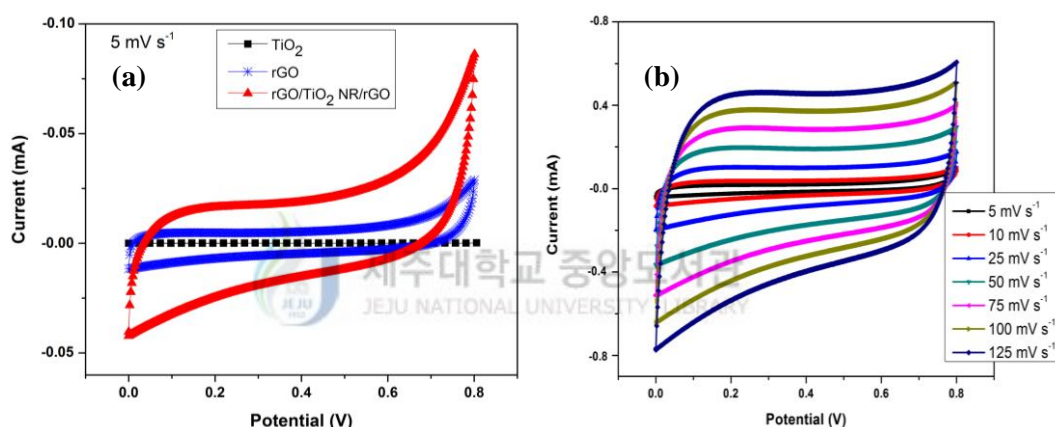


Figure 5.2.5 (a) Cyclic voltammograms (CVs) curves of as-prepared TiO₂ NRs, rGO and an rGO / TiO₂ NR / rGO electrode at a scan rate of 5 mV s⁻¹ in 1 M Na₂SO₄ electrolyte solution. (b) CVs of an rGO / TiO₂ NR / rGO electrode at scan rates from 5 to 125 mV s⁻¹.

The specific capacitance (C_s) of the electrode can be calculated from the CVs using equation (2.1)[20,21]. The maximum specific capacitance of the rGO /TiO₂ NR / rGO electrode was 114.5 F g⁻¹ (13.74 mF cm⁻²) at a scan rate of 5 mV s⁻¹. The C_s values of rGO and the TiO₂ NR arrays were 75.3 F g⁻¹ (7.51 mF cm⁻²) and 0.13 F g⁻¹ (13.45 μF cm⁻²) at a scan rate of 5 mV s⁻¹. The capacitance of the rGO and TiO₂ electrodes were less than that of the rGO / TiO₂ NR / rGO electrode. In addition, the C_s of the hybrid electrode was much higher than those reported for pure TiO₂ by Lu *et al.* [4] (H-TiO₂:3.24 mF cm⁻² and untreated TiO₂:0.026 mF cm⁻² at 100 mV s⁻¹),

Salari *et al.* [22] (Titania nanotubes: $911 \mu\text{F cm}^{-2}$ and powder: $181 \mu\text{F cm}^{-2}$ at 1 mV s^{-1}), Wang *et al.* [23] (TiO_2 -B nanotubes: 17.7 F g^{-1} at 10 mV s^{-1}), Ramadoss *et al.* [11] (TiO_2 NRs: 8.5 F g^{-1} at 5 mV s^{-1}), Salari *et al.* [24] (TiO_2 nanotubes: 19.2 F g^{-1} at 1 mV s^{-1}) and Sun *et al.* [25] (TiO_2 -G: 84 F g^{-1} at 10 mV s^{-1}). This confirms that the porous hybrid electrode exhibited improved electrochemical performance with the enhancement most likely due to the hybrid structure of the rGO / TiO_2 NR / rGO electrode as follows. (1) Vertically aligned TiO_2 NR arrays provide direct electron transport pathways that facilitate ion diffusion and enable fast and reversible Faradic reaction, which lead to enhanced capacitance and a higher rate capability. (2) The intrinsic EDLC of graphene is high. (3) The high specific surface area and high conductivity of graphene improves the electrical conductivity of the electrode, and facilitates ion diffusion and electrolyte interactions, during charge and discharge.

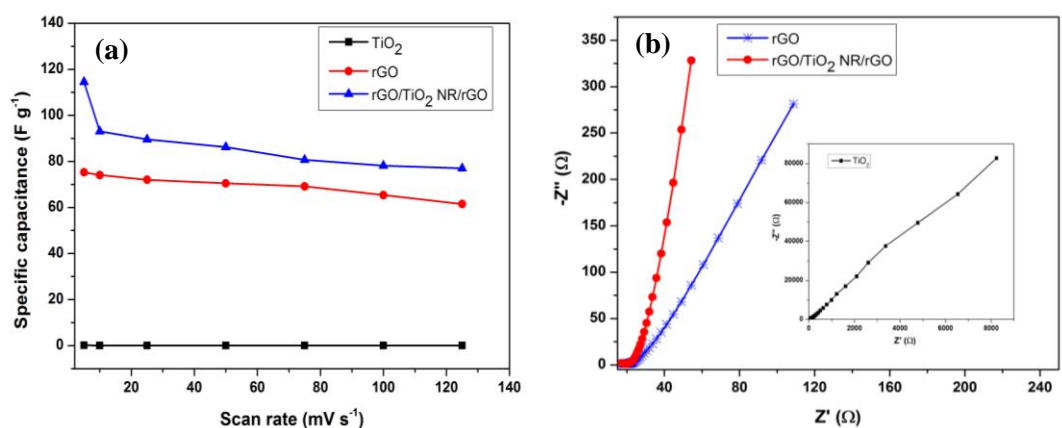


Figure 5.2.6 (a) Specific capacitance, as calculate from the CVs in Fig.6, of TiO_2 NRs, rGO and an rGO / TiO_2 NR / rGO electrode at various scan rates. (b) Nyquist plots for rGO and an rGO / TiO_2 NR / rGO electrode. The inset shows the Nyquist plot of a TiO_2 NR electrode.

Figure 5.2.6a shows the variation in specific capacitance as a funtion of scan rate. The hybrid nanostructure electrode consistently demonstrated a specific capacitance that was higher than those of pure rGO and TiO_2 electrodes at scan rates

from 5 to 125 mV s⁻¹. Furthermore, specific capacitance decreased with increasing scan rate. The decrease in C_s at higher scan rates was attributed to the presence of inner active sites that cannot sustain the redox transitions, possibly due to diffusion of ions within the electrode. The decreasing trend in capacitance indicates that part of the electrode surface are inaccessible at high charging–discharging rates [26,27].

EIS experiments were conducted from 0.01 Hz–100 kHz in order to investigate the internal resistance and capacity of the electrode material. **Figure 5.2.6b** shows Nyquist plots obtained with rGO /TiO₂ NR / rGO and pure rGO electrodes. Each Nyquist plot shows a semicircle in the high-frequency region and a straight line in the low-frequency region. In general, the semicircle arc in the high-frequency region is related to electronic resistance and the vertical line in the low-frequency region indicates pure capacitive behavior [28]. The inset of **Figure 5.2.6b** shows a Nyquist plot of the TiO₂ NR arrays. Note that the TiO₂ Nyquist plot does not contain a semicircle region. This is probably due to the low Faradaic resistances of the electrode and the high electrical conductivity between the nanorods and the current collector [22]. The charge transfer resistance (R_{ct}) was 2.5 and 4.0 Ω for the rGO / TiO₂ NR / rGO and pure rGO electrodes, respectively. The R_{ct} of the rGO / TiO₂ NR / rGO electrode was less than that of the rGO electrode, indicating that the former exhibits lower resistance and higher capacitance. This small R_{ct} value was due to the following. (i) The vertically aligned TiO₂ nanorods were in direct contact with highly conductive rGO nanosheets, which minimized the interfacial resistance of the charge transfer process. (ii) Aggregation of graphene nanosheets was prevented by the TiO₂ nanorods. (iii) The hybrid rGO / TiO₂ NR / rGO porous nanostructure facilitated fast electron transfer between the active materials and the current collector.

These results demonstrate that the nanostructured electrode enhances the electrochemical performance of the hybrid material, indicating a synergistic effect between the TiO₂ nanorods and the rGO sheets.

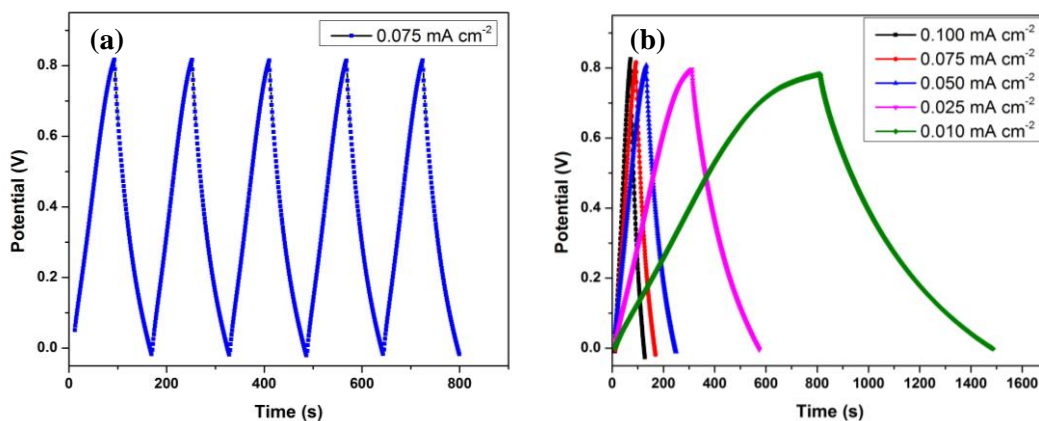


Figure 5.2.7 (a) Galvanostatic charge-discharge curve of an rGO / TiO₂ NR / rGO electrode at a constant current density of 0.075 mA cm⁻² in 1 M Na₂SO₄. (b) Galvanostatic charge-discharge curves of an rGO / TiO₂ NR / rGO electrode at different current densities.

Figure 5.2.7a shows galvanostatic charge / discharge curves obtained with an rGO / TiO₂ NR / rGO electrode in 1 M Na₂SO₄ at a current density of 0.075 mA cm⁻² from 0 to 0.8 V. The curve is symmetric and resembles an equilateral triangle. This is indicative of a highly efficient (high rate capability) charge / discharge process. The GCD curves of the electrode in 1 M Na₂SO₄ at current densities from 0.010 to 0.100 mA cm⁻² are shown in **Figure 5.2.7b**. All of the curves are symmetric. Using the charge/discharge curve, the specific capacitance of the electrode can be calculated by using equation (2.2) [20]. The calculated C_s values of the rGO / TiO₂ NR / rGO electrode were 78.9, 77.8, 67.4, 65.7, and 64.3 F g⁻¹ at 0.010, 0.025, 0.050, 0.075 and 0.10 mA cm⁻², respectively.

The Coulombic efficiency (η), energy density (E) and a power density (P) of the electrode were calculated from charge / discharge curves using the following

equations (2.4, 2.5, and 2.6) [29, 30]. The values for η , E , P of the electrode were 89%, 6.30 Wh kg⁻¹, and 190 W kg⁻¹, respectively.

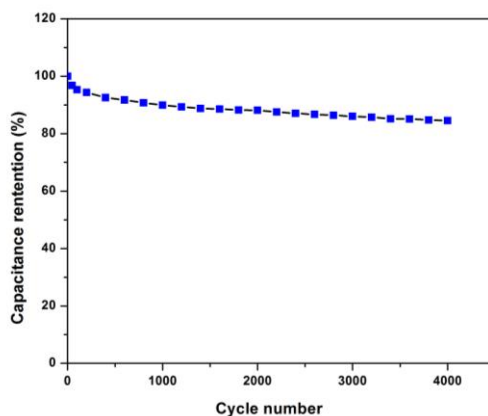


Figure 5.2.8 Variation of the specific capacitance of an rGO / TiO₂ NR / rGO electrode as a function of cycle number measured at 200 mV s⁻¹ in 1 M Na₂SO₄.

Electrochemical stability is one of the most important factors determining the usefulness of supercapacitors in commercial applications. CVs were acquired from 0 to 0.8 V for 4000 cycles at a scan rate of 200 mV s⁻¹ in 1 M Na₂SO₄. **Figure 5.2.8** shows that the specific capacitance retention ratio of the rGO / TiO₂ NR / rGO electrode was 85% even after 4000 cycles, indicating excellent cyclability. Within the rGO / TiO₂ NR / rGO electrode, reduced graphene nanosheets act as an interconnector and improve the internal electrical conductivity. In addition, the enhanced specific surface area of the electrode improves the charge capacity. The TiO₂ NR arrays act as infrastructure that bridge the graphene nanosheets and prevent them from severe swelling and shrinking during the cycling process.

5.2.4. Conclusion

Two-dimensional rGO / TiO₂ NR / rGO porous hybrid structure electrodes were fabricated for supercapacitor applications. The electrode material exhibited a maximum specific capacitance of 114.5 F g⁻¹ at a scan rate of 5 mV s⁻¹ in 1 M

Na_2SO_4 aqueous electrolyte. The enhanced specific capacitance was due to the effective pseudocapacitance of the TiO_2 NRs, the intrinsically high EDLC of graphene, a higher specific surface area, faster electron transport, and the larger mesoporous volume of 2D graphene. In addition, the hybrid electrodes exhibited high electrochemical stability with 85% capacitance retention after 4000 cycles. These results suggest that rGO / TiO_2 NR / rGO electrode is suitable for the electrode material in supercapacitor applications.



5.2.5. References

- [1] G. Li, C. P. Richter, R. L. Milot, L. Cai, C. A. Schmuttenmaer, R. H. Crabtree, G. W. Brudvig, and V. S. Batista, Synergistic effect between anatase and rutile TiO₂ nanoparticles in dye-sensitized solar cells. *Dalton Trans.* 45 (2009) 10078-10085.
- [2] C. S. Guo, M. Ge, L. Liu, G. D. Gao, Y. C. Feng, and Y. Q. Wang, Directed synthesis of mesoporous TiO₂ microspheres: catalysts and their photocatalysis for bisphenol A degradation. *Environ. Sci. Technol.* 44 (2010) 419-425.
- [3] M. Jayalakshmi, and K. Balasubramanian, Simple capacitors to supercapacitors - An overview. *Int. J Electrochem. Sci.* 3 (2008) 1196-1217.
- [4] X. Lu, G. Wang, T. Zhai, M. Yu, J. Gan, Y. Tong, and Y. Li, Hydrogenated TiO₂ nanotube arrays for supercapacitors. *Nano Lett.* 12 (2012) 1690-1696.
- [5] H. Zheng, T. Zhai, M. Yu, S. Xie, C. Liang, W. Zhao, S. C. Wang, Z. Zhang, and X. Lu, TiO₂@C core-shell nanowires for high-performance and flexible solid-state supercapacitors. *J. Mater. Chem. C*, 1 (2013) 225-229.
- [6] Y. Sun, Q. Wu, and G. Shi, Graphene based new energy materials. *Energy Environ. Sci.* 4 (2011) 1113-1132.
- [7] M. D. Stoller, S. Park, Y. Zhu, J. An, and R. S. Ruoff, Graphene-based ultracapacitors. *Nano Lett.* 8 (2008) 3498-3502.
- [8] Y. Wang, Z. Shi, Y. Huang, Y. Ma, C. Wang, M. Chen, and Y. Chen, Supercapacitor devices based on graphene materials. *J. Phys. Chem. C* 113 (2009) 13103-13107.

- [9] Y. Bai, R. B. Rakhi, W. Chen, and H.N. Alshareef, Effect of pH-induced chemical modification of hydrothermally reduced graphene oxide on supercapacitor performance. *J. Power Sources* 233 (2013) 313-319.
- [10] B. Saravanakumar, R. Mohan, and S. J. Kim, Facile synthesis of graphene/ZnO nanocomposites by low temperature hydrothermal method. *Mater. Res. Bullet.* 48 (2013) 878-883.
- [11] A. Ramadoss, and S. J. Kim, Vertically aligned TiO₂ nanorod arrays for electrochemical supercapacitor. *J Alloys compd.* 561 (2013) 262.
- [12] J. H. Bang, and P. V. Kamat, Solar Cells by Design: Photoelectrochemistry of TiO₂ nanorod arrays decorated with CdSe. *Adv. Funct. Mater.* 20 (2010) 1970-1976.
- [13] S. Stankovich, D. A. Dikin, R. D. Piner, K. A. Kohlhaas, A. Kleinhammes, Y. Jia, Y. Wu, S. T. Nguyen, and R. S. Ruoff, Synthesis of graphene-based nanosheets via chemical reduction of exfoliated graphite oxide. *Carbon* 45 (2007) 1558-1565.
- [14] M. Selim Arif Sher Shah, A. Reum Park, K. Zhang, J. H. Park, and P. J. Yoo, Green synthesis of biphasic TiO₂-reduced graphene oxide nanocomposites with highly enhanced photocatalytic activity. *ACS Appl. Mater. Interfaces* 4 (2012) 3893-3901.
- [15] F. Tuinstra, and J. L. Koenig, Raman spectrum of graphite. *J Chem. Phys.* 53(3) (1970) 1126-1130.
- [16] C. Xiang, M. Li, M. Zhi, A. Manivannan, and N. Wu, A reduced graphene oxide/Co₃O₄ composite for supercapacitor electrode. *J. Power Sources* 226 (2013) 65-70.

- [17] V. Swamy, and B. C. Muddle, Size-dependent modifications of the Raman spectrum of rutile TiO₂. *Appl. Phys. Lett.* 89 (2006) 163118-163120.
- [18] L. Sun, Z. Zhao, Y. Zhou, and L. Liu, Anatase TiO₂ nanocrystals with exposed {001} facets on graphene sheets via molecular grafting for enhanced photocatalytic activity. *Nanoscale* 4 (2012) 613-620.
- [19] Y. Wu, S. Liu, H. Wang, X. Wang, X. Zhang, and G. Jin, A novel solvothermal synthesis of Mn₃O₄/graphene composites for supercapacitors. *Electrochim. Acta* 90 (2013) 210-218.
- [20] J. W. Lee, A. S. Hall, J. D. Kim, and D. T. E. Mallouk, A facile and template-free hydrothermal synthesis of Mn₃O₄ nanorods on graphene sheets for supercapacitor electrodes with long cycle stability. *Chem. Mater.* 24 (2012) 1158-1164.
- [21] J. Yan, W. Sun, T. Wei, Q. Zhang, Z. Fan, and F. Wei, Fabrication and electrochemical performances of hierarchical porous Ni(OH)₂ nanoflakes anchored on graphene sheets. *J. Mater. Chem.* 22 (2012) 11494-11502.
- [22] M. Salari, S. H. Aboutalebi, K. Konstantinov, and H. K. Liu, A highly ordered titania nanotube array as a supercapacitor electrode. *Phys. Chem. Chem. Phys.* 13 (2011) 5038-5041.
- [23] G. Wang, Z. Y. Liu, J. N. Wu, and Q. Lu, Preparation and electrochemical capacitance behavior of TiO₂-B nanotubes for hybrid supercapacitor. *Mater. Lett.* 71 (2012) 120-122.
- [24] M. Salari, S. H. Aboutalebi, A. T. Chidembo, I. P. Nevirkovets, K. Konstantinov, and H. K. Liu, Enhancement of the electrochemical

- capacitance of TiO₂ nanotube arrays through controlled phase transformation of anatase to rutile. *Phys. Chem. Chem. Phys.* 14 (2012) 4770-4779.
- [25] X. Sun, M. Xie, G. Wang, H. Sun, A. S. Cavanagh, J. J. Travis, S. M. George, and J. Lian, Atomic layer deposition of TiO₂ on graphene for supercapacitors. *J Electrochem. Soc.* 159 (4) (2012) A364-A369.
- [26] D. S. Dhawale, D. P. Dubal, V. S. Jamadade, R. R. Salunkhe, and C. D. Lokhande, Fuzzy nanofibrous network of polyaniline electrode for supercapacitor application. *Synth. Met.* 160 (2010) 519-522.
- [27] J. Wang, Z. Gao, Z. Li, B. Wang, Y. Yan, Q. Liu, T. Mann, M. Zhang, and Z. Jiang, Green synthesis of graphene nanosheets/ZnO composites and electrochemical properties. *J Solid State Chem.* 184 (2011) 1421-1427.
- [28] J. Li, W. Zhao, F. Huang, A. Manivannan, and N. Q. Wu, Single-crystalline Ni(OH)₂ and NiO nanoplatelet arrays as supercapacitor electrodes. *Nanoscale* 3 (2011) 5103-5109.
- [29] X. Xia, Q. Hao, W. Lei, W. Wang, H. Wang, and X. Wang, Reduced-graphene oxide/molybdenum oxide/polyaniline ternary composite for high energy density supercapacitors: Synthesis and properties. *J. Mater. Chem.* 22 (2012) 8314-8320.
- [30] H. Sun, L. Cao, and L. Lu, Bacteria promoted hierarchical carbon materials for high-performance supercapacitor. *Energy Environ. Sc.* 5 (2012) 6206-6213.

5.3. Synthesis and Electrochemical Performance of Graphene-TiO₂ Nanocomposites

5.3.1. Introduction

A recent trend in supercapacitor research has focused on inexpensive electrode materials with high energy density, which maintain a high power density and cycling stability. One of the ways to improve the performance of supercapacitors is to combine pseudocapacitance materials with a double-layer capacitor. Graphene has become one of the most promising electrode materials for electrochemical double layer capacitors. Specifically, graphene can be used as an ideal platform to build graphene-based composites with metals, metal oxides, and conducting polymers for energy storage applications [1].

Different types of approaches have been used to obtain graphene nanosheets [2]. However, in practical applications, graphene nanosheets usually suffer from agglomeration or restacking due to strong van der Waals interactions, which lead to the loss of surface area and capacitance. Metal/metal oxide or metal hydroxide nanoparticles are currently introduced into the interlayers of graphene nanosheets to prevent agglomeration [3]. These nanoparticles enlarge the interplanar spacing, maintain the high surface area of the graphene nanosheets, and make both sides of the nanosheets readily accessible.

Transition metal oxides, such as RuO₂, MnO₂, NiO, Co₃O₄, and SnO₂, contribute pseudocapacitance [4], although, most of them suffer from low abundance, a high cost for their raw materials, low electrical conductivity, and poor rate capability and reversibility during the charge-discharge process. Hence, both theoretical and experimental efforts have been applied to seek alternative inexpensive

electrode materials. There are several materials to be considered in this regard, such as TiO_2 , ZnO , and Fe_2O_3 . Among the transition metal oxides, TiO_2 is considered to be a promising material for supercapacitors, due to its high specific energy density, low cost, non-toxicity, eco-friendliness, and abundant availability. Additionally, TiO_2 is an n-type semiconductor; the charge density on the surface is greater than that on other regions due to the attractive contribution of the positively-charged depletion region [5]. Hence, it can be used as an inexpensive electrode material for supercapacitor applications.

Very recently, Xiang et al. [6] reported on reduced graphene oxide (rGO)- TiO_2 nanobelts and nanoparticles for supercapacitor electrodes using the hydrothermal method, which exhibited a specific capacitance of 200 and 60 F g^{-1} at a scan rate of 2 mV s^{-1} , but only 56.2 and 18.4 F g^{-1} at a scan rate of 100 mV s^{-1} , respectively. Additionally, the TiO_2 nanoparticle coating on graphene sheets fabricated by Sun et al. [7] demonstrated a specific capacitance of 75 F g^{-1} at a scan rate of 10 mV s^{-1} using atomic layer deposition. However, these materials were limited by a low specific capacitance and poor stability (10% loss after 1000 cycles) for the graphene/ TiO_2 nanoparticle composite; other disadvantages included a long reaction time, high cost, and a high processing temperature, which would impede large-scale production.

This chapter presents a simple method to synthesize a graphene- TiO_2 hybrid nanostructure as an electrode material for supercapacitor applications. Initially, graphene oxide (GO) was synthesized using the well-known modified Hummer's method. After that, a graphene- TiO_2 hybrid nanostructure has been synthesized using the microwave-assisted method [8]. Compared with conventional methods, the

microwave reduction method has the following advantages: a short processing time, low cost, homogeneous heating, and, in general, heat generation within the material [9]. Moreover, the method is environmentally friendly, and the particle size is smaller and more uniform, which improved the physical and chemical properties of the graphene–TiO₂ hybrid nanostructure.

5.3.2. Experimental methods

5.3.2.1. Synthesis of TiO₂ nanoparticles

The TiO₂ nanoparticles were synthesized by the precipitation method using titanium (IV)-n-butoxide, acetic acid, and ethanol as starting precursors. Briefly, 20 mL of titanium (IV)-n-butoxide were dissolved in 50 mL of ethanol, and the reaction mixture was stirred for 30 min to obtain a solution, referred to as Solution A. Then, 10 mL of deionized water and 25 mL acetic acid were added to 35 mL of the ethanol solution (A) and stirred for 30 min to obtain Solution B. Both solutions (A and B) were produced at room temperature. Solution B was then slowly added drop-wise to Solution A and stirred vigorously using a Teflon-coated magnetic bar at 40°C for the hydrolysis of titanium (IV)-n-butoxide. Finally, the obtained solution was dried in a hot air oven at 100°C for 24 h and further calcined at 500°C for 2 h resulting in the formation of anatase TiO₂ nanoparticles.

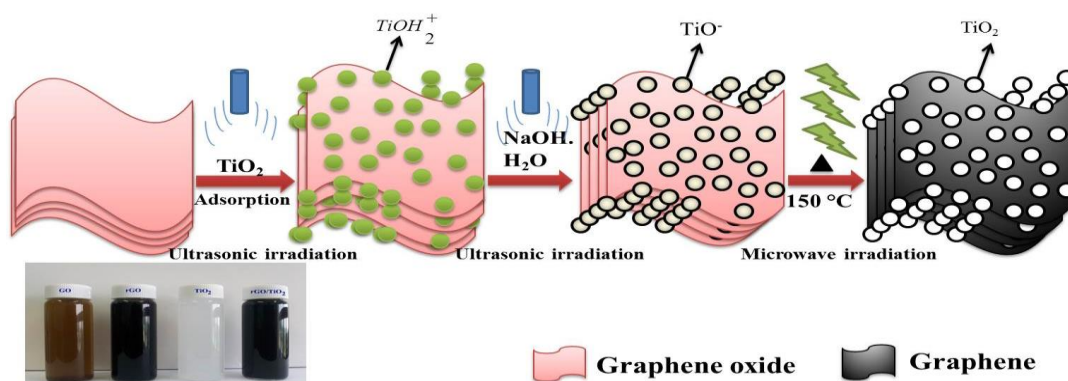
5.3.2.2. Synthesis of reduced graphene oxide

GO was successfully synthesized from expandable graphite powder using the well-known modified Hummer's method [10], which was described in previous **Chapter**. As-synthesized GO (50 mg) was dispersed in 100 mL double-distilled water; the dispersion was brown in color. The dispersed GO was exfoliated, using sonication for 1 h. The pH of the solution was adjusted to 10 using a sodium

hydroxide solution, which turned the suspension dark brown. The mixture was then placed in a microwave oven for 10 min at 150°C. After irradiation, the color of the suspension changed from dark brown to black, which indicated GO reduction. The product obtained was filtered and washed several times with the distilled water and then centrifuged at 10,000 rpm for 10 min to remove the residuals. Finally, the sample was dried at 60 °C for 5 h in a hot air oven.

5.3.2.3. Synthesis of the graphene–TiO₂ hybrid nanostructure

The graphene–TiO₂ hybrid nanostructure was synthesized using a microwave-assisted technique [8]. Briefly, 90 mg of GO were dispersed into 50 mL of double-distilled water and then sonicated for 30 min (**Scheme 5.3.1**). Then, 40 mg of as-synthesized anatase TiO₂ nanoparticles were added to the GO solution under continuous sonication for 30 min to create a uniform dispersion. The weight ratio of GO to TiO₂ nanoparticles was 2:1. Afterwards, a dilute NaOH solution was added to the solution to form a brownish-black suspension with a pH of ~9. Finally, the resulting solution of GO/TiO₂ (**Scheme 5.3.1**) was transferred to an automated household microwave oven and treated for 10 min at 150 °C. After exposure, the color of the suspension changed from brown to grayish-black, which indicated the reduction of GO (**Scheme 5.3.1**). The as-synthesized product was washed thoroughly with distilled water and then centrifuged at 10,000 rpm for 10 min to remove the residuals. The obtained final product was dried in a hot air oven (at 100°C) for 3 h to produce the graphene–TiO₂ hybrid nanostructure. The crystal structure, morphology and composition of the as prepared samples were measured by XRD, Raman, FT-IR, FE-SEM, TEM, EDS and XPS techniques.



Scheme 5.3.1 Schematic representation of the formation process of the graphene–TiO₂ hybrid nanostructure. The inset shows photographs of graphene oxide (GO), graphene, TiO₂, and graphene–TiO₂ hybrid nanostructure.

5.3.2.4. Preparation of electrodes and electrochemical characterization

The working electrodes were prepared by the following procedure. Briefly, the as-prepared samples, carbon black, and poly (tetrafluoroethylene) (PTFE) were mixed in a mass ratio of 75:20:5 and dispersed in the ethanol solution, resulting in a homogeneous paste. The resulting solution mixture was coated onto a nickel foam substrate (1 cm × 1 cm) with a spatula for the fabrication of the electrodes. The electrodes were then dried at 100 °C for 12 h in a vacuum oven. The loading mass of the electrode active material was ~3-4 mg cm⁻².

All of the electrochemical experiments were investigated using an AUTOLAB PGSTAT302N electrochemical work station. 1 M Na₂SO₄ solution was used as the electrolyte at room temperature. A typical three-electrode experimental cell, equipped with a working electrode, platinum foil as a counter electrode, and an Ag/AgCl reference electrode, was used for measuring the electrochemical properties of the working electrode (Ni foam-coated TiO₂, graphene, and the graphene–TiO₂ hybrid nanostructure). The cyclic voltammetry (CV) data of the electrode were obtained by changing the scan rates: 5, 10, 25, 50, 75, 100, and 125 mV s⁻¹.

Electrochemical impedance spectroscopy (EIS) measurements were carried out using a direct current (dc) bias of 0.1 V with a signal of 10 mV over the frequency range of 0.1 Hz to 100 kHz. The galvanostatic charge-discharge curves were obtained at various current densities.

5.3.2.5. Electrochemical measurements in two electrode system

The symmetric supercapacitor was assembled by a two piece of G-TiO₂ (positive and negative) electrodes on Ni foam with filter paper separator in middle. The each electrode contained 3 mg of electroactive material and had a geometric surface area of about 1 cm². The electrochemical measurements of the symmetric supercapacitors were carried out in 1M Na₂SO₄ aqueous electrolyte using the electrochemical work station in a two electrode cell at room temperature.

5.3.3. Results and discussion

5.3.3.1. Material characterizations

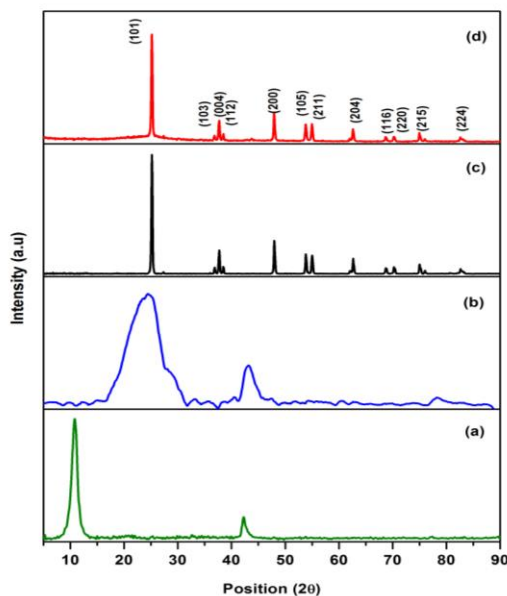


Figure 5.3.1 Typical XRD pattern of (a) GO, (b) graphene, (c) TiO₂ and (d) the graphene-TiO₂ hybrid nanostructure.

The crystalline structure, purity, and size of the resultant materials were determined by powder X-ray diffraction (XRD) measurements. **Figure 5.3.1** shows the XRD pattern of the as-prepared GO, graphene, TiO₂, and graphene–TiO₂ hybrid nanostructure. The XRD pattern of GO has a dominant peak centered at a 2θ value of 10.8°, which was assigned to the (001) reflection (**Figure 5.3.1a**). The interplanar spacing, determined to be 8.1 Å, agreed well with previous reports [4]. After reduction, although the GO peak at 10.8° had completely disappeared, a strong and broad peak appeared at a 2θ value of 25°, which corresponded to the (002) plane (**Figure 5.3.1b**); this signified the formation of rGO [11]. Also, the XRD pattern of pure TiO₂ (**Figure 5.3.1c**) exhibited the anatase phase with preferential orientation of the (101) plane. All of the peaks observed in the XRD pattern matched the anatase TiO₂ phase (JCPDS card No: 21-1272). No other diffraction peaks were observed, which clearly indicated the purity of the samples.

From the XRD pattern of the graphene–TiO₂ hybrid nanostructure (**Figure 5.3.1d**), the peaks are readily indexed to the anatase phase of TiO₂, without GO diffraction peaks. These results indicate that GO is completely reduced to a graphene sheet. Notably, no typical diffraction peaks corresponding to graphene were observed in the graphene–TiO₂ hybrid nanostructure. This is because the main characteristic peak of rGO at 25.0° has a low diffraction intensity, which can overlap with the (101) peak of anatase TiO₂ at 25.1° [12]. The average crystallite size of the graphene–TiO₂ hybrid nanostructure was calculated to be ~35 nm for the (101) plane, using the well-known Scherrer's formula [13]. This value is consistent with FE-SEM and TEM results as shown below.

To further confirm the formation of the samples, Raman detection was performed. Fig. 3 shows a comparison of the Raman spectra of GO, graphene, TiO₂ and the graphene–TiO₂ hybrid nanostructure. In **Figure 5.3.2a**, the Raman spectra of the GO samples showed two prominent peaks at 1354 and 1596 cm⁻¹, which corresponded to the well-documented D and G bands, respectively. The D band is a common feature for sp³ defects or disorder in carbon, and the G band provides useful information on in-plane vibrations of sp²-bonded carbon atoms in a 2-D hexagonal lattice [14]. After reduction (**Figure 5.3.2b**), the D band (1345 cm⁻¹) and G band (1586 cm⁻¹) values shifted towards the lower values, which indicated the formation of rGO [14]. The D/G intensity ratio of rGO was larger than that for GO, indicating the conversion of GO into rGO [15]. Pure TiO₂ (**Figure 5.3.2c**) exhibited the characteristic peaks of the anatase TiO₂ phase.

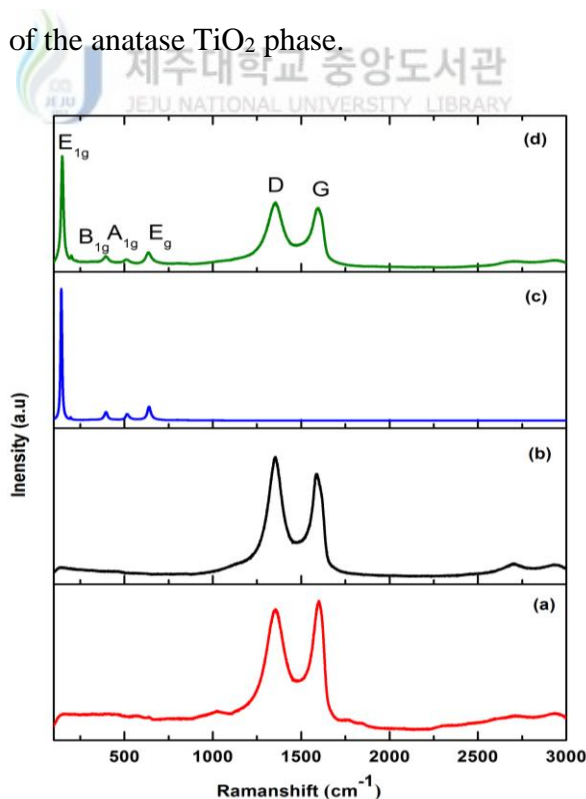


Figure 5.3.2 Raman spectra of (a) GO, (b) graphene, (c) TiO₂, and (d) the graphene–TiO₂ hybrid nanostructure.

The Raman spectrum of the graphene–TiO₂ hybrid nanostructure is shown in **Figure 5.3.2d**. A very intense Raman band can be seen at ~148 cm⁻¹, which was attributed to the main E_g anatase vibrational mode. Additionally, three strong vibrational peaks at 391 (B_{1g}), 509 (A_{1g}), and 635 cm⁻¹ (E_g) were observed, indicating that the anatase TiO₂ crystallites were the major species [16]. Significantly, two bands at ~1348 (D band) and 1588 cm⁻¹ (G band) for the graphitized structures were also observed, confirming the presence of graphene [17]. Moreover, the observed D and G bands of the graphene–TiO₂ hybrid nanostructure samples were slightly shifted compared with the D band (1354 cm⁻¹) and G band (1596 cm⁻¹) of GO, which indicated the reduction of GO. Further observation showed that the graphene–TiO₂ hybrid nanostructure had a larger D/G intensity ratio (I_D/I_G = 1.19) compared with that of pristine GO (I_D/I_G = 0.94). This change suggested a decrease in the average size of the in-plane sp² domains upon reduction of the exfoliated GO, confirming the existence of graphene sheets in the graphene–TiO₂ hybrid nanostructure, similar to that observed in chemically-reduced GO [17].

The FT-IR spectra of GO, graphene, pure TiO₂, and the graphene–TiO₂ hybrid nanostructure are shown in **Figure 5.3.3**. **Figure 5.3.3a** shows a strong, broad peak at 3424 cm⁻¹ for all of the samples, indicating the presence of surface O–H stretching vibrations of the C–OH groups and water. The other peaks corresponded to oxygen functional groups, such as, carboxyl C=O stretching of COOH groups (1739 cm⁻¹), aromatic stretching C=C (1627 cm⁻¹), tertiary C–OH group stretching (1382 cm⁻¹), epoxy C–O group stretching (1215 cm⁻¹), and alkoxy C–OH group stretching vibrations (1047 cm⁻¹) [18]. In **Figure 5.3.3b**, compared with GO, the intensities of the peaks corresponding to epoxide and ether groups disappeared in the

FT-IR spectrum of rGO, indicating that the oxygen-containing functional groups in GO were completely removed from GO. In the case of pure TiO₂ (**Figure 5.3.3c**), the peak observed at 607 cm⁻¹ correspond to the Ti–O–Ti vibration of the TiO₂ phase [19]. For the graphene–TiO₂ hybrid nanostructure (**Figure 5.3.3d**), the intensities of the bands corresponding to the oxygen functional groups were reduced compared with GO, signifying the reduction of oxygen in the as-prepared graphene–TiO₂ hybrid nanostructure. The strong band observed at 588 cm⁻¹ indicated the Ti–O–C vibration [19]. Further, the graphene skeleton peak appeared at 1617 cm⁻¹, (C–C), indicating the formation of Ti–O–C bonds (i.e. the anchoring of TiO₂ nanoparticles to the graphene sheets) [20]. The presence of the Ti–O–C bonds confirmed the formation of chemical bonding between the graphene nanosheets and TiO₂ during the microwave radiation process.

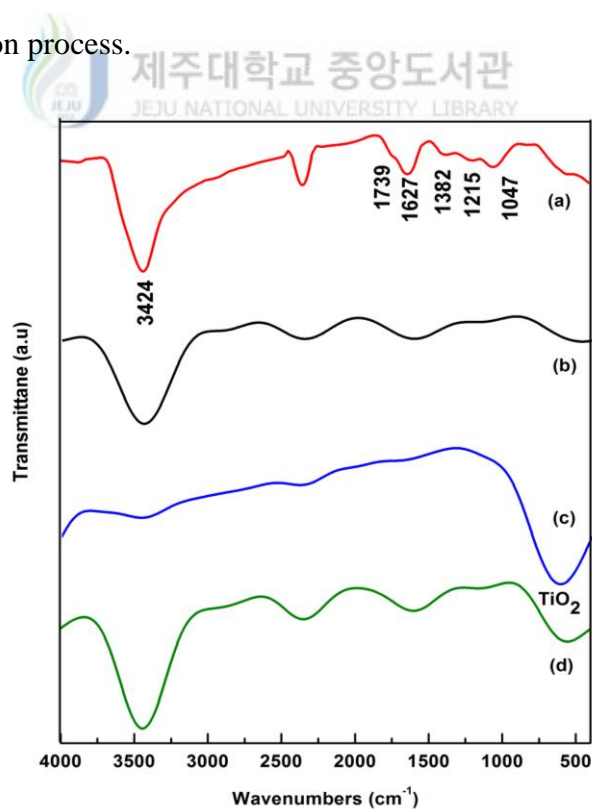


Figure 5.3.3 FT-IR spectra of (a) GO, (b) graphene, (c) TiO₂, and (d) the graphene–TiO₂ hybrid nanostructure.

To investigate the degree of reduction of GO and the chemical composition of the graphene–TiO₂ hybrid nanostructure, the samples were further characterized by XPS; the results are shown in **Figure 5.3.4**. **Figure 5.3.4a** shows the XPS spectra of the survey scan, Ti 2p, C 1s, and O 1s for the different samples (GO, graphene, TiO₂ and the graphene–TiO₂ hybrid nanostructure). According to the XPS survey spectrum (as shown in **Figure 5.3.4a**), the graphene–TiO₂ hybrid nanostructure exhibited the Ti 2p (457.4 eV), O 1s (532.2 eV), and C 1s (284.7 eV) peaks with their corresponding binding energies [21]. Both the C 1s and O 1s peaks were observed in all XPS spectra. The high resolution of the Ti 2p spectrum of graphene–TiO₂ (**Figure 5.3.4b**) showed two major peaks, with binding energies of 459.7 and 465.4 eV, corresponding to the Ti 2p_{3/2} and Ti 2p_{1/2} spin orbits, respectively; note that the spin-energy separation of 5.7 eV (Ti⁴⁺ chemical state), is characteristic of a TiO₂ phase and in good agreement with previously reported data [22]. Compared with pure TiO₂, the Ti 2p spectrum of graphene–TiO₂ exhibited a higher energy shift of 0.4 eV, which was attributed to the interaction of Ti ions with the oxygen centers of rGO. Because oxygen is a highly electronegative element, it removes the electron density from the Ti of the graphene–TiO₂ composites, which results in an increase in the binding energy of Ti in the composite, compared with pure TiO₂ [23, 24]. The high-resolution C 1s spectra of GO, graphene, TiO₂ and the graphene–TiO₂ hybrid nanostructure are shown in **Figure 5.3.4c**. The C 1s GO spectrum (**Figure 5.3.4c**) can be deconvoluted into five components, corresponding to the carbon species in different oxygen containing functional groups: (i) the C–C (aromatic) group at 284.6 eV, (ii) C–OH at 285.5 eV, (iii) C (epoxy/alkoxy) at 286.5 eV, (iv) C=O at 287.2 eV, and (v) C(O)O (carboxyl carbon) at 288.4 eV [25].

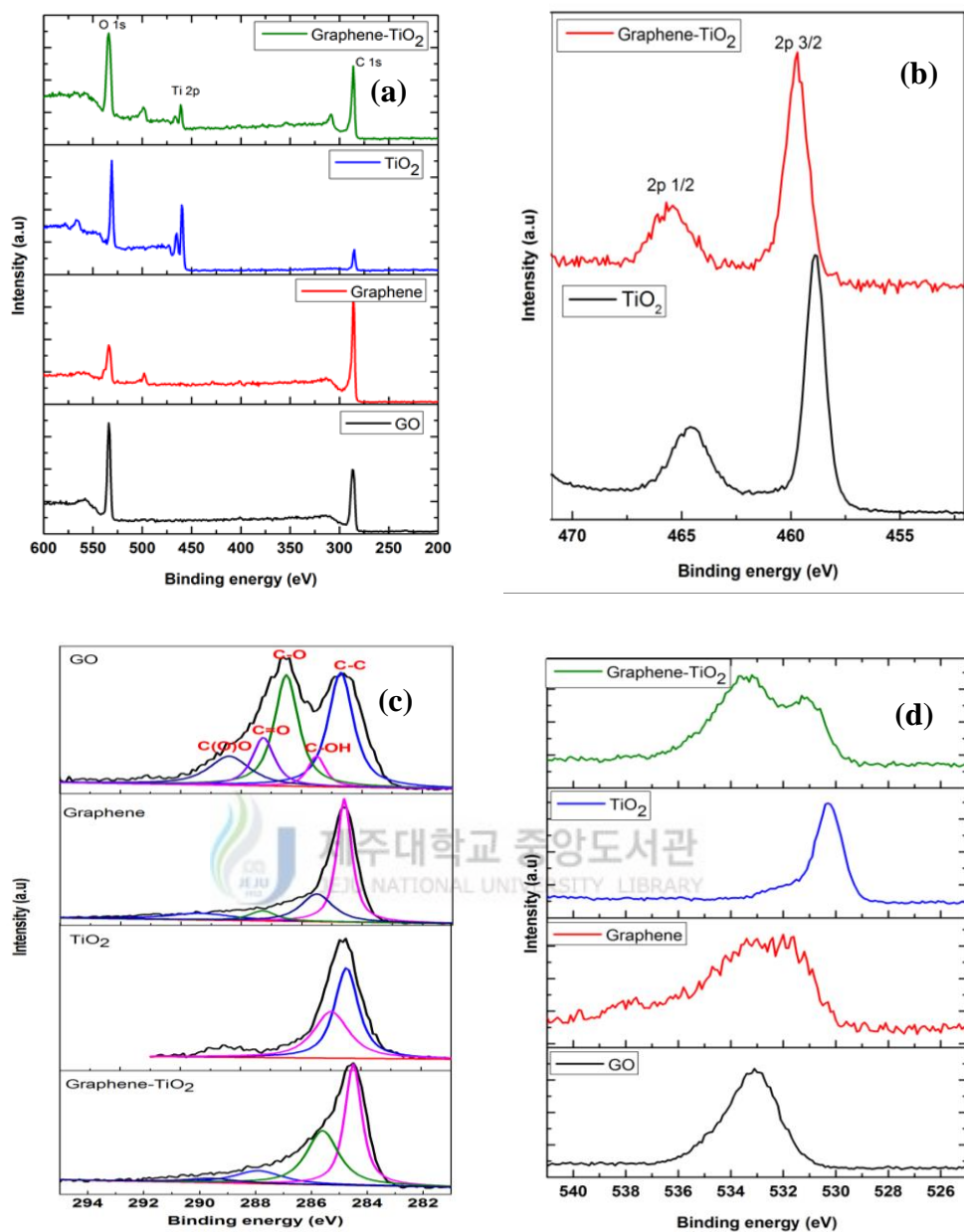


Figure 5.3.4 XPS spectra of GO, graphene, TiO₂, and the graphene–TiO₂ hybrid nanostructure for (a) the survey scan, (b) Ti 2p, (c) C 1s, and (d) O 1s.

Compared with the GO spectrum, the C 1s spectra of graphene and the graphene–TiO₂ hybrid nanostructure obtained after the microwave reduction process, exhibited greatly suppressed peaks corresponding to the epoxide, hydroxyl, and carboxyl functional groups; this indicated the successful reduction [25]. Additionally, the high-resolution O 1s spectra of the four samples exhibited different peaks as

shown in **Figure 5.3.4d**. For GO, the O 1s peak at 533 eV was related to the presence of hydroxyl groups on the surface of GO. The O 1s spectrum of rGO showed a peak at 532.4 eV corresponding to the –OH group. Compared with GO (O 1s), the peak intensity of graphene was reduced, which indicated the reduction of GO. The strong O 1s peak at 530.2 eV in the TiO₂ sample was mainly attributed to TiO₂ formation. The O 1s XPS spectrum of the graphene–TiO₂ hybrid nanostructure exhibited two peaks at 531.1 and 533.3 eV, which were assigned to the TiO₂ phase and –OH group, respectively [26]. All of these results further confirm the successful incorporation of TiO₂ nanoparticles into the graphene nanosheets.

The morphology and microstructure of the as-prepared graphene–TiO₂ hybrid nanostructure were investigated by FE-SEM and TEM. **Figure 5.3.5a and 5.3.5b** shows the FE-SEM images of the graphene–TiO₂ hybrid nanostructure; the 2-D graphene sheets and spherical nanostructure of the TiO₂ nanoparticles were clearly visible. From the images, we determined that the TiO₂ nanoparticles were uniformly anchored to large sections of the graphene nanosheets; these particles were densely and homogeneously deposited. The TEM images (**Figure 5c–d**) also revealed that the TiO₂ nanoparticles were uniformly distributed on the surface of the graphene sheets. As can be seen from the FE-SEM and TEM images, the average size of the TiO₂ nanoparticles was in the range of 35–45 nm, which was in good agreement with XRD measurements. The selected-area electron diffraction (SAED) pattern of the graphene–TiO₂ hybrid nanostructure (**Figure 5.3.5e**) confirmed the anatase phase, which was also consistent with the obtained TiO₂ XRD pattern, as shown in **Figure 5.3.1**. The EDS spectrum of the graphene–TiO₂ hybrid nanostructure is shown in Fig.6f. The spectrum clearly showed the presence of carbon (C), titanium (Ti), and

oxygen (O) elements in the graphene–TiO₂ hybrid nanostructure. The Ti and O elements originated from the TiO₂ nanoparticles, and the C was contributed by the graphene nanosheets.

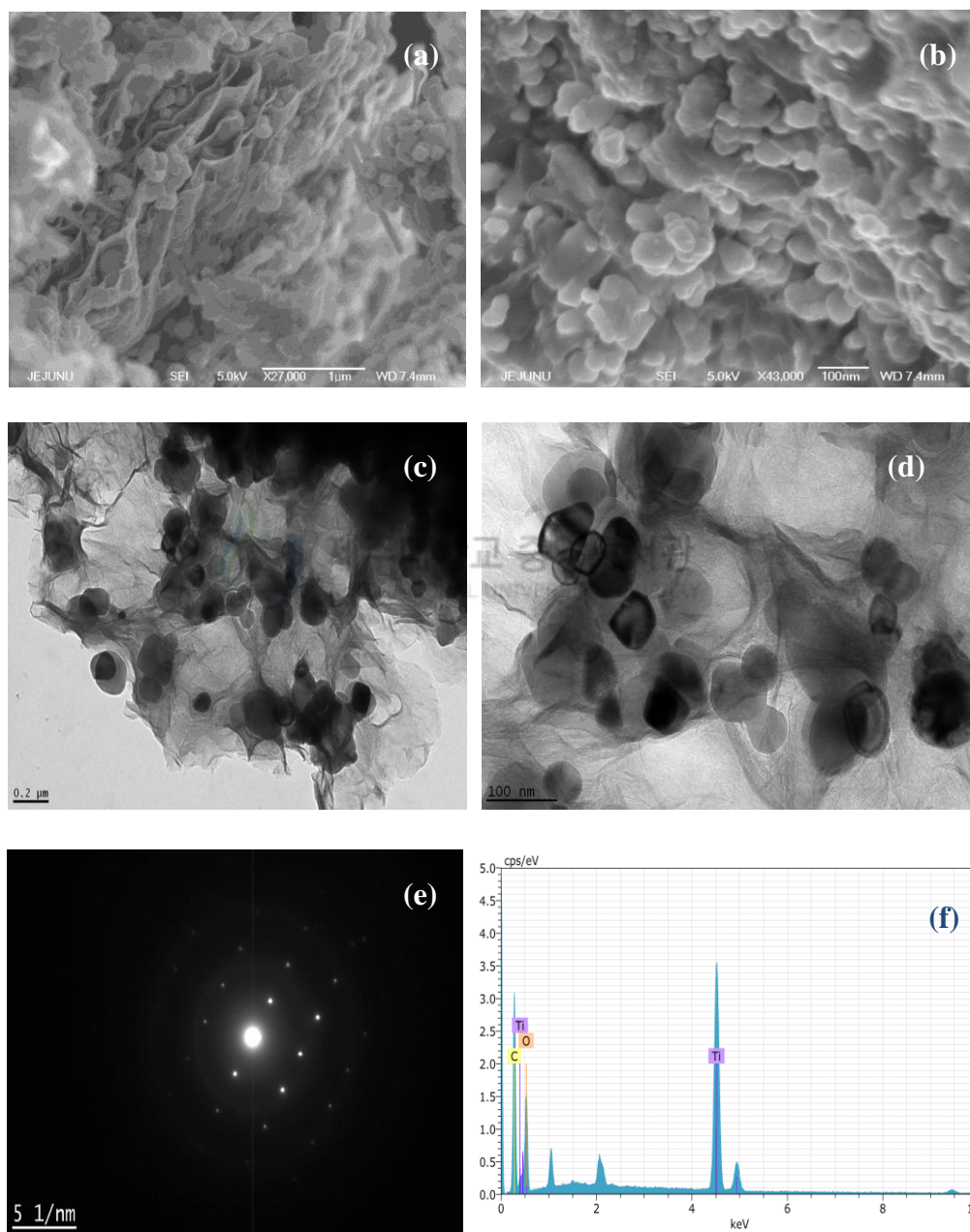


Figure 5.3.5 (a–d) Different magnification of FE-SEM images, (c–d) TEM images, (e) SAED pattern, and (f) EDS image of the graphene–TiO₂ hybrid nanostructure.

5.3.3.2. Electrochemical studies

The capacitive performance of TiO₂, graphene and the graphene–TiO₂ hybrid electrode was evaluated by various electrochemical tests, including CV, EIS and galvanostatic charge–discharge techniques. **Figure 5.3.6a** shows the CV curves of as-prepared TiO₂, graphene and the graphene–TiO₂ hybrid electrode at a scan rate of 5 mV s⁻¹ in 1 M Na₂SO₄ electrolyte solution. We observed that all of the CV curves had a similar and ideal rectangular shape, which indicated the ideal electrochemical double-layer capacitive behavior of the electrode. Additionally, the graphene–TiO₂ hybrid electrode showed a higher integrated area than that for TiO₂, or a graphene electrode at the same scan rate, confirming excellent electrochemical performance for the graphene–TiO₂ hybrid electrode. The specific capacitance (C_s) of the electrodes can be calculated from the CV curves according to the equation (2.1) [27]. The calculated C_s values of TiO₂, graphene, and the graphene–TiO₂ hybrid electrode are 20, 110 and 165 F g⁻¹, respectively, at a scan rate of 5 mV s⁻¹. The specific capacitance of the graphene–TiO₂ hybrid electrode was much higher than that of the rGO and TiO₂ electrodes. The graphene–TiO₂ hybrid electrode, which exhibited a specific capacitance value of 165 F g⁻¹ at a scan rate of 5 mV s⁻¹ was almost two times higher than that previously reported by Xiang et al. [6] and Sun et al. [7] This higher capacitance value was due to the smaller particle size (~35 nm) and large specific surface area compared with that previously reported for the rGO–TiO₂ composite (having a nanoparticle size of ~138 nm). Moreover, the microwave synthesis method was a simple, efficient approach and required less preparation time, compared with the hydrothermal method.

The higher C_s of the graphene–TiO₂ hybrid electrode compared with that for rGO was mainly attributed to both the faradaic contribution (pseudocapacitance) due to the charge transfer process with the surface atoms and the non-faradaic contribution from the double-layer effect (arising from graphene). Additionally, by decreasing the TiO₂ particle size to nanoscale dimensions, both types of capacitance (pseudocapacitance and double-layer charging) have a considerable effect due to the high surface area [28,29]. The pseudocapacitance behavior of TiO₂ arises from the reversible redox transition involving the exchange of protons and/or cations with the electrolyte (Na₂SO₄). The proposed mechanism is explained based on the following equation (Eq. (2)):



where C⁺ indicates the protons and alkali metal cations (Na⁺, Li⁺, and K⁺) in the electrolyte. The above equation suggests that both protons and alkali metal cations are involved in the redox process. Moreover, it is evident that when the TiO₂ particle size is reduced to nanometer dimensions, the surface area and electro-active sites increase, which effectively reduces the diffusion length of the Na⁺ ion in the electrode matrix. Moreover, the graphene in the hybrid electrode provides better electronic conductivity and excellent interfacial contact between TiO₂ and graphene, which results in the fast transportation of electrons throughout the entire electrode matrix [30,14]. These results further support the contention that charge stored at the surface of TiO₂ from the pseudocapacitance storage mechanism can be an important factor in achieving high values for the gravimetric energy density.

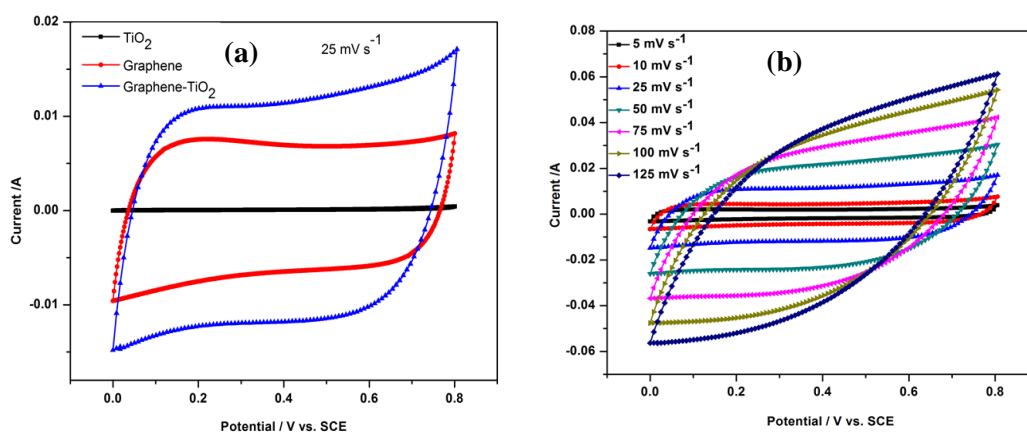


Figure 5.3.6 (a) CV curves of the as-prepared TiO₂, graphene and the graphene–TiO₂ hybrid electrode at a scan rate of 25 mV s⁻¹ in 1 M Na₂SO₄ electrolyte solution. (b) CV curves of the graphene–TiO₂ hybrid electrode at different scan rates from 5 to 125 mV s⁻¹.

To obtain more detailed information on the capacitance performance of the as prepared graphene–TiO₂ hybrid nanostructure, additional CV studies were performed. **Figure 5.3.6b** shows the CV curves of the graphene–TiO₂ hybrid electrode at different scan rates of 5, 10, 25, 50, 75, 100 and 125 mV s⁻¹ in 1 M Na₂SO₄ electrolyte solution. All of the CV curves are approximately rectangular in shape even at very high scan rates, indicating ideal capacitive properties and excellent reversibility of this electrode. The specific capacitance of graphene and graphene–TiO₂ hybrid electrodes at various scan rates is shown in **Figure 5.3.7a**. We observed that the specific capacitance for both electrodes decreased with an increase in the scan rate from 5 to 125 mV s⁻¹. This is a common phenomenon and is caused by the insufficient time available for ion diffusion and adsorption inside the smallest pores within a large particle at high scan rates [31]. The C_s of the graphene–TiO₂ hybrid electrode was much higher than that of a pure graphene electrode, for all of the scan rates tested.

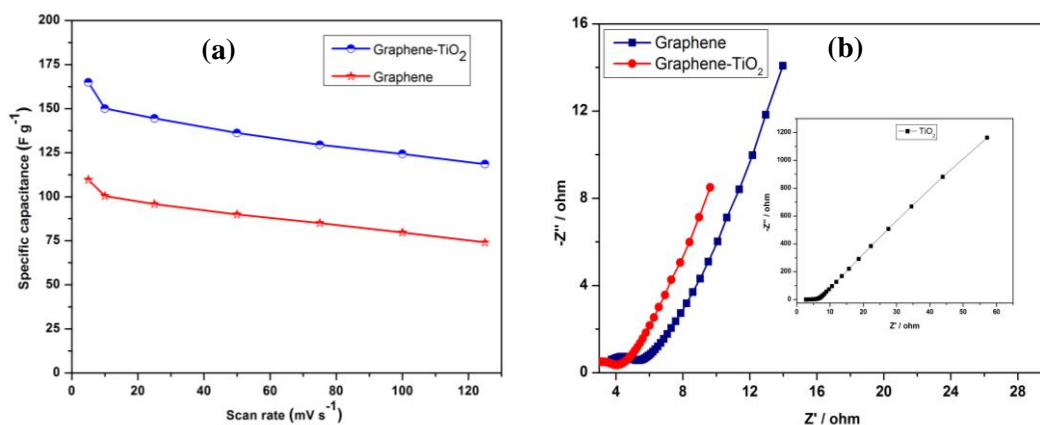


Figure 5.3.7 (a) Specific capacitance of graphene and the graphene-TiO₂ hybrid electrode at different scan rates calculated from CV curves. (b) Nyquist plots for graphene and the graphene-TiO₂ hybrid electrode in 1 M Na₂SO₄ electrolyte solution; the inset shows the Nyquist plot for TiO₂.

EIS analysis was used to study the fundamental behavior of the electrode materials for supercapacitors [41]. The EIS experiments were conducted in the frequency range of 0.1 Hz to 100 kHz using an open circuit potential with an AC perturbation of 10 mV. Typical Nyquist plots of the TiO₂, graphene and the graphene-TiO₂ hybrid electrode are shown in **Figure 5.3.7b**. The three impedance spectra were composed of a semi-circular arc in the high-frequency range and a straight line in the low-frequency range. The arc for the very high-frequency range corresponded to the charge transfer limiting process and was ascribed to the double-layer capacitance (C_{dl}) in parallel with the charge transfer resistance (R_{ct}) at the contact interface between the electrode and electrolyte solution [32]. The straight line in the low-frequency range is called the Warburg resistance, which is caused by the frequency dependence of ion diffusion/transport from the electrolyte to the electrode surfaces [32]. Moreover, the vertical line in the low-frequency range which represents swift ion diffusion in the electrolyte and adsorption onto the electrode surface, suggests the ideally pure capacitive behavior of the electrodes; this was

evident in the semicircular arc, which decreases in the following order: TiO₂, graphene and the graphene–TiO₂ hybrid nanostructure. R_{ct} can be directly measured from the Nyquist plots as the semicircular arc diameter. The calculated R_{ct} values for TiO₂, graphene, and graphene–TiO₂ hybrid electrodes are 4.1, 2.0 and 0.8 Ω , respectively. The graphene–TiO₂ hybrid electrode had a low R_{ct} value compared with the other electrodes, which indicated the incorporation of TiO₂ nanoparticles into the graphene nanosheets, resulting in an improved charge transfer performance for the electrode. The equivalent series resistance (ESR) of the electrode can be obtained from the intersection of the high–frequency region with the real x-axis of the Nyquist plots, which determines the charge–discharge rate for the electrode (i.e., its power capability). The ESR values obtained for graphene and graphene–TiO₂ hybrid electrodes were 3.5 and 3.0 Ω , respectively. The ESR value of the graphene–TiO₂ hybrid electrode was smaller than those of the other electrodes, because the composite structure facilitated efficient transport of electrolyte ions to the surfaces of TiO₂ and graphene.

To further evaluate the specific capacitance of our graphene–TiO₂ hybrid electrode, galvanostatic charge–discharge measurements (**Figure 5.3.8a**) were performed in the potential range of 0–0.8 V. **Figure 5.3.8b** shows the typical galvanostatic charge–discharge curves of the graphene–TiO₂ hybrid electrode for current densities of 2.5, 5, 7.5, and 10 mA cm⁻². It can be seen that all of the curves were linear and exhibited a typical triangular shape, which indicated good electrochemical capacitive characteristics. The specific capacitances of the graphene–TiO₂ hybrid electrode are 136, 125, 121, and 113 F g⁻¹ at the current densities of 2.5,

5, 7.5 and 10 mA cm⁻², respectively. As expected, the specific capacitance values decreased with increasing current density.

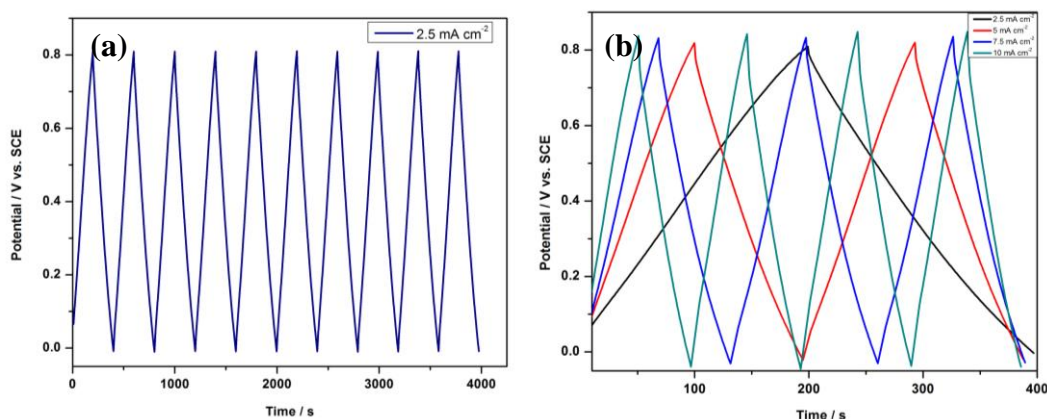


Figure 5.3.8 (a) Galvanostatic charge–discharge curve of the graphene–TiO₂ hybrid electrode at a constant current density of 2.5 mA cm⁻² in 1 M Na₂SO₄ electrolyte solution. (b) Galvanostatic charge–discharge curves of the graphene–TiO₂ hybrid electrode at different current densities (2.5, 5, 7.5 and 10 mA cm⁻²).

Long cycle life for the supercapacitors is an important parameter for their practical application. The cycle stability of the graphene–TiO₂ hybrid electrode was further evaluated by repeating the CV measurements between 0 and 0.8 V at a scan rate of 100 mV s⁻¹ for 5000 cycles. **Figure 5.3.9a** shows the capacitance retention ratio as a function of cycle number. We observed that the specific capacitance decreased by only 9.0 % with respect to the initial capacitance after 5000 cycles, indicating an excellent cycle life for supercapacitor applications. The better electrochemical performance of the as-prepared electrode can be attributed to the following aspects: (1) graphene in the hybrid structure can act as a conducting agent, which greatly improves the electrical conductivity of the hybrid structure; (2) well dispersed TiO₂ nanoparticles can effectively prevent the agglomeration and restacking of the graphene nanosheets, resulting in an EDLC for the overall specific capacitance; (3) graphene nanosheet with a large surface area in the hybrid structure

not only provided double-layer capacitance to the overall energy storage, but also effectively inhibited the aggregation of TiO₂ nanoparticles, resulting in fast electron transfer throughout the entire electrode matrix as well as an overall improvement in the electrochemical performance; and (4) the nanometer sized smaller particle facilitates faster charge–discharge rates, because the faradaic reaction replaced the diffusion-controlled Na⁺ ion intercalation process which usually occurs at the TiO₂ surface [30, 14]. Therefore, the overall charge–discharge rates are much faster for the smaller nanoparticles compared with the larger particles previously synthesized using the hydrothermal method [6].

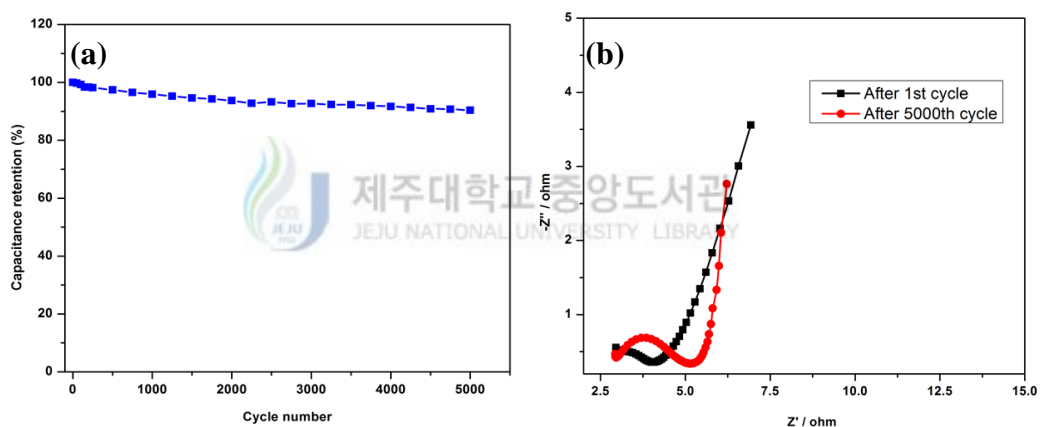


Figure 5.3.9 (a) Variation of the specific capacitance of the graphene–TiO₂ hybrid electrode as a function of cycle number measured at 100 mV s⁻¹ in a 1 M Na₂SO₄ aqueous solution. (b) Nyquist plots of the graphene–TiO₂ hybrid electrodes after the 1st and 5000th cycles.

To further study the cyclic stability of the as prepared electrode materials, we compared the EIS of the 1st and 5000th cycles. We observed that the impedance spectra (**Figure 5.3.9b**) were similar in shape, composed of semicircular arc in high–frequency region, followed by a vertical line in the low–frequency region; this further indicated the long-term electrochemical stability of this hybrid electrode material. A noticeable difference between the two impedance spectra occurred, after 5,000 cycles; the calculated charge-transfer resistance for the electrode increased from 0.8 to 2.6 Ω. This result could

be caused by the loss of adhesion between the active material and the current collector, or it may be due to the dissolution of a small amount of TiO_2 during the charge–discharge process [30,14,33].

5.3.3.3. Electrochemical performance in two-electrode system

To completely investigate the electrochemical performance of the G- TiO_2 electrode material, the G- $\text{TiO}_2/\text{G-TiO}_2$ supercapacitor was studied in 1 M Na_2SO_4 aqueous solution.

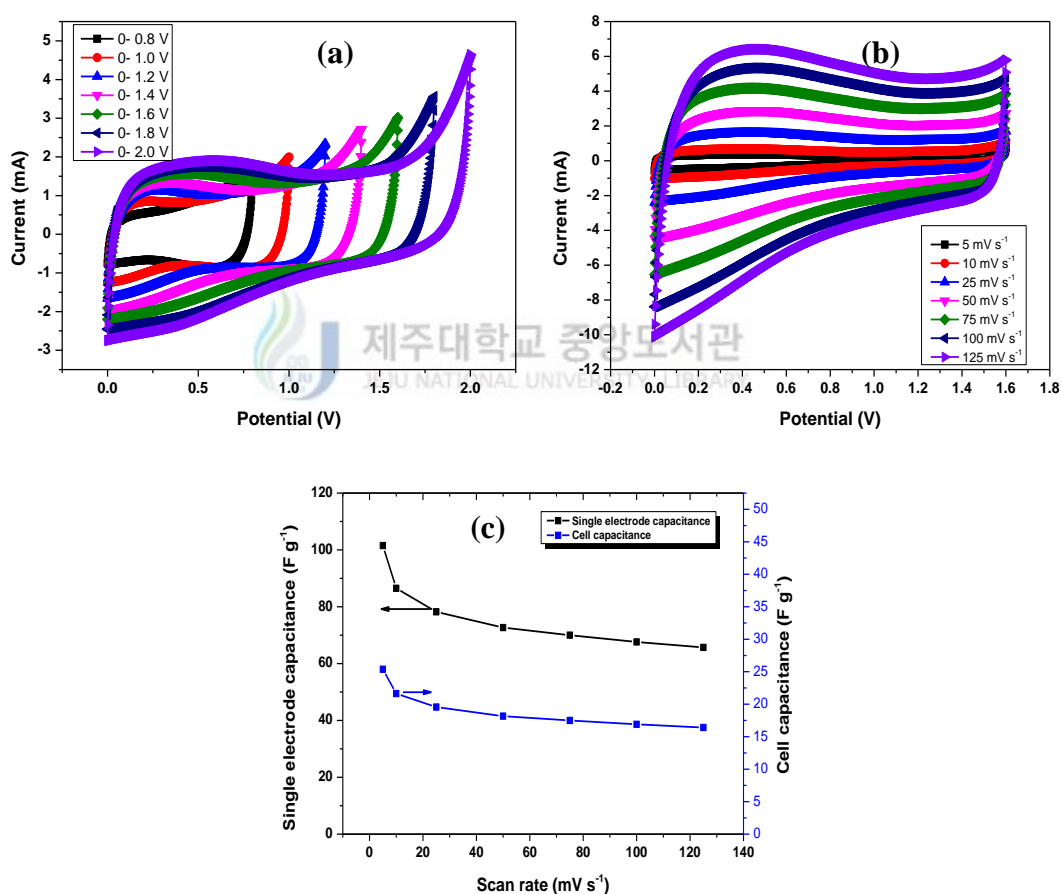


Figure 5.3.10 (a) CVs of symmetric G- TiO_2 supercapacitor with different potential windows. (b) CVs of symmetric G- TiO_2 supercapacitor between 0.0 to 1.6 V at various scan rates. (c) The cell and single electrode capacitance of symmetric supercapacitor as a function of scan rate.

The CVs of a symmetric supercapacitor with different potential windows at a scan rate of 25 mV s^{-1} are shown in **Figure 5.3.10a**. It could be observed that the CV

exhibits a rectangular shape characteristics for a low value of upper potential limit of 1.6 V, indicating the pure capacitive behavior. When the upper potential limit increases over 1.6 V, a current leap at the end of potential window was observed, which might be due to the gas evolution from the positive and/or the negative electrode. Further, CV curves (**Figure 5.3.10b**) of the symmetric supercapacitor device measured at various scan rates with potential windows ranging from 0 to 1.6 V. The cell exhibit rectangular-like shapes even at a higher scan rates, revealing the ideal capacitive and a fast charge/discharge property. **Figure 5.3.10c** shows the specific capacitance of the cell and single electrode in the cell as a function of scan rate based on the CV curves. The symmetric supercapacitor device achieved the maximum specific capacitance of 25.3 F g⁻¹ at a scan rate of 5 mV s⁻¹. The calculated specific capacitance of single electrode in the cell is 101 F g⁻¹ at a scan rate of 5 mV s⁻¹. Moreover, the symmetric supercapacitor shows good rate capacitance, with 65% of cell capacitance retained when the scan rate increased from 5 to 125 mV s⁻¹.

The electrochemical performance of the symmetric supercapacitor was further confirmed by galvanostatic charge/discharge measurements. **Figure 5.3.11a** shows the GCD curves of a symmetric supercapacitor with different voltage windows at a current density of 0.5 A g⁻¹. The GCD curves reveal the linear voltage-time relation, confirming the ideal capacitive behavior. Further, the GCD curves of symmetric supercapacitor collected at different current densities, as shown in **Figure 5.3.11b**. Almost all of the GCD curves are exhibited in symmetric with a good linear relation of discharge/charge voltage versus time. This again confirming the good capacitive behavior and fast charge-discharge behavior of the fabricated symmetric supercapacitor device. The specific capacitance of the full cell can be calculated from

the GCD curves using the equation (2.2). **Figure 5.3.11c** shows the specific capacitance versus current densities. The calculated cell capacitance and single electrode capacitance in cell are 9 F g^{-1} and 37 F g^{-1} , at a current density of 0.1 A g^{-1} , respectively.

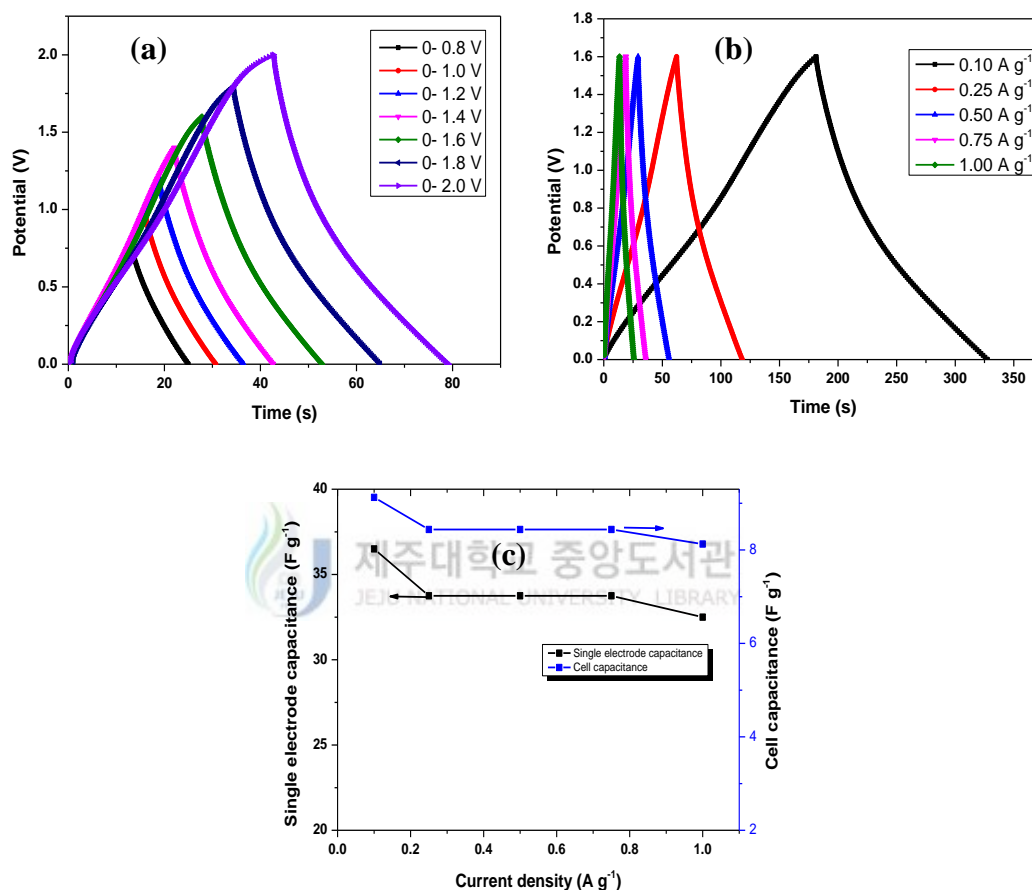


Figure 5.3.11 (a) Galvanostatic charge/discharge curves of symmetric G-TiO₂ supercapacitor with different potential windows. (b) GCD curves of symmetric G-TiO₂ supercapacitor between 0.0 to 1.6 V at various current densities. (c) The cell and single electrode capacitance of symmetric supercapacitor as a function of current density.

The electrochemical parameters, such as the energy (E), and power density (P) are important parameters for the investigation of the capacitive behavior of electrochemical cells. The energy density and power density of the electrode can be further evaluated from the GCD curves at different current densities using the equations (2.5 and 2.6). The calculated energy density and power density of the

graphene–TiO₂ symmetric supercapacitors (**Figure 5.3.12a**) were 3.2 Wh kg⁻¹ and 79.9 kW kg⁻¹, respectively, at 0.1 A g⁻¹. From these results, we concluded that the graphene–TiO₂ hybrid electrode materials showed a higher specific capacitance, better rate capability, and were also highly efficient. Therefore, our results on the graphene–TiO₂ hybrid electrode show that it is a promising candidate for supercapacitor applications.

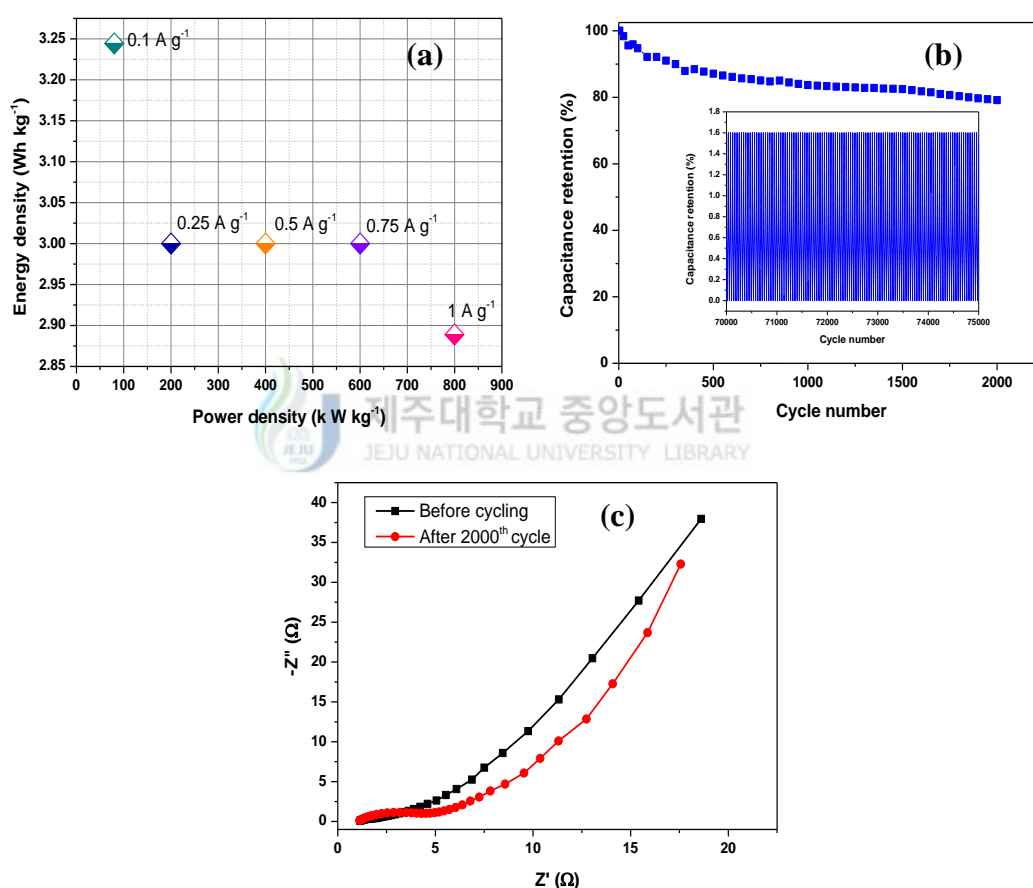


Figure 5.3.12 (a) Ragone plot of symmetric supercapacitor at various current densities. (b) The cycle performance of the symmetric supercapacitor in the potential window between 0.0 to 1.6 V at 0.5 A g⁻¹ for 2000 cycles; the inset shows the GCD cycles. (c) Nyquist plots of symmetric supercapacitor before and after 2000 cycles.

Electrochemical stability is one of the most important factors determining the usefulness of supercapacitors in commercial applications. The long-term cycle stability of the symmetric supercapacitor was evaluated using GCD measurement

from 0 to 1.6 V for 2000 cycles at a current density of 0.5 A g^{-1} in 1 M Na_2SO_4 . The capacitance retention ratio as a function of cycle number is shown in **Figure 5.3.12b**. The electrode exhibited an excellent long cycle life over the entire cycle numbers. The capacitance of the electrode only decreases by 20% of the initial capacitance even after 2000 cycles, demonstrating an excellent cycle stability with a high degree of reversibility in the repetitive charge/discharge cycling.

To further study the cyclic stability of the symmetric supercapacitor, we compared the EIS of the before and after cycles in 1 M Na_2SO_4 solution. Both the impedance spectra (**Figure 5.3.12c**) are almost similar in shape, composed of semicircle at high frequency region and followed by a vertical line in the low frequency region, which indicated good cycling stability of the symmetric supercapacitor. After 2000 cycles, the charge transfer resistance of the supercapacitor was increased. This might be due to the loss of adhesion of some active material with the current collector during the long term charge/discharge cycling.

5.3.3.4. Performance of solid-state supercapacitor devices

In order to demonstrate the potential application of as-prepared electrode material, we have fabricated all-solid-state symmetric supercapacitor by sandwiching two pieces of G- TiO_2 electrode with a polymer-gel electrolyte separator in a middle. We have connected two supercapacitors in series, and found that the device could power (**Figure 5.3.13**) a green, red and blue light-emitting diode (LED) for about 5 min.

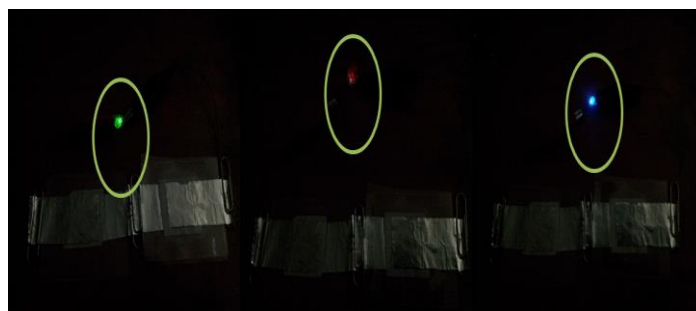


Figure 5.3.13 Green, red and blue LED driven by two solid state symmetric supercapacitors connected in series; inset shows the enlarged portion of LED glow.

5.3.4. Conclusion

The graphene–TiO₂ hybrid nanostructure as an electrode material for supercapacitors was successfully synthesized using a microwave-assisted method. The surface morphology, microstructure, composition, and capacitive behaviors of the as-prepared materials were well investigated. FE-SEM and TEM images confirmed the uniform distribution of TiO₂ nanoparticles on the surface of graphene sheets. Our results showed that the graphene–TiO₂ hybrid electrode exhibited a maximum specific capacitance (single electrode in cell) is 101 F g⁻¹ at a scan rate of 5 mV s⁻¹ in 1 M Na₂SO₄ electrolyte solution. The improved specific capacitance of the graphene–TiO₂ hybrid electrode was mainly attributed to the pseudocapacitance of the TiO₂ phase and was partially influenced by the intrinsic double-layer capacitance of the graphene sheets. Moreover, the material exhibited excellent electrochemical stability (long cycle stability), along with 80% retention for specific capacitance, even after a 2000 cycle test. These results suggest that graphene–TiO₂ hybrid electrodes are a highly suitable, promising electrode material for next-generation high-performance supercapacitors.

5.3.5. References

- [1] Z. Lei, N. Christov, and X. S. Zhao, Intercalation of mesoporous carbon spheres between reduced graphene oxide sheets for preparing high-rate supercapacitor electrodes. *Energy Environ. Sci.* 4 (2011) 1866-1873.
- [2] H. C. Schniepp, J. L. Li, M. J. McAllister, H. Sai, M. Herrera-Alonso, D. H. Adamson, R. K. Prud'homme, R. Car, D. A. Saville, and I. A. Aksay, Functionalized single graphene sheets derived from splitting graphite oxide. *J. Phys. Chem. B* 110 (2006) 8535-8539.
- [3] J. Yan, J. Liu, Z. Fan, T. Wei, and L. Zhang, High-performance supercapacitor electrodes based on highly corrugated graphene sheets. *Carbon* 50 (2012) 2179-2188.
- [4] W. Yang, Z. Gao, J. Wang, B. Wang, Q. Liu, Z. Li, T. Mann, P. Yang, M. Zhang, and L. Liu, Synthesis of reduced graphene nanosheet/urchin-like manganese dioxide composite and high performance as supercapacitor electrode. *Electrochim. Acta* 69 (2012) 112-119.
- [5] M. Jayalakshmi, and K. Balasubramanian, Simple capacitors to supercapacitors - an overview. *Int. J. Electrochem. Sci.* 3 (2008) 1196 – 1217.
- [6] C. Xiang, M. Li, M. Zhi, A. Manivannan, and N. Wu, Reduced graphene oxide/titanium dioxide composites for supercapacitor electrodes: shape and coupling effects. *J. Mater. Chem.* 22 (2012) 19161-19167.
- [7] X. Sun, M. Xie, G. Wang, H. Sun, A. S. Cavanagh, J. J. Travis, S. M. George and J. Lian, Atomic layer deposition of TiO₂ on graphene for supercapacitors. *J. Electrochem. Soc.* 159 (4) (2012) A364-A369.

- [8] X. Liu, L. Pan, T. Lv, G. Zhu, T. Lu, Z. Sun, and C. Sun, Microwave-assisted synthesis of TiO₂-reduced graphene oxide composites for the photocatalytic reduction of Cr(VI). *RSC Advances* 1 (2011) 1245-1249.
- [9] H. Hu, X. Wang, F. Liu, J. Wang, and C. Xu, Rapid microwave-assisted synthesis of graphene nanosheets–zinc sulfide nanocomposites: Optical and photocatalytic properties. *Synth. Met.* 161 (2011) 404–410.
- [10] J. Zhang, J. Jiang, H. Li, and X. S. Zhao, A high-performance asymmetric supercapacitor fabricated with graphene-based electrodes. *Energy Environ. Sci.* 4 (2011) 4009-4015.
- [11] H. M. A. Hassan, V. Abdelsayed, A. E. R. S. Khder, K. M. AbouZeid, J. Turner, M. S. El-Shall, S. I. Al-Resayes and A. A. El-Azhary, Microwave synthesis of graphene sheets supporting metal nanocrystals in aqueous and organic media. *J. Mater. Chem.* 19 (2009) 3832-3837.
- [12] Y. Zhang, N. Zhang, Z. Tang, and Y. Xu, Improving the photocatalytic performance of graphene–TiO₂ composites via a combined strategy of decreasing defects of graphene and increasing interfacial contact. *Phys. Chem. Chem. Phys.* 14 (2012) 9167-9175.
- [13] A. Ramadoss, K. Krishnamoorthy, and S. J. Kim, Facile synthesis of hafnium oxide nanoparticles via precipitation method. *Mater. Lett.* 75 (2012) 215-217.
- [14] J. Yan, Z. Fan, T. Wei, W. Qian, M. Zhang, and F. Wei, Fast and reversible surface redox reaction of graphene–MnO₂ composites as supercapacitor electrodes. *Carbon* 48 (2010) 3825-3833.

- [15] X. Y. Peng, X. X. Liu, D. Diamond, and K. T. Lau, Synthesis of electrochemically-reduced graphene oxide film with controllable size and thickness and its use in supercapacitor. *Carbon* 49 (2011) 3488-3496.
- [16] S. Liu, C. Liu, W. Wang, B. Cheng, and J. Yu, Unique photocatalytic oxidation reactivity and selectivity of TiO₂-graphene composites. *Nanoscale* 4 (2012) 3193-3200.
- [17] Q. Xiang, J. Yu, and M. Jaroniec, Enhanced photocatalytic H₂-production activity of graphene-modified titania nanosheets. *Nanoscale* 3 (2011) 3670-3678.
- [18] S. Stankovich, D. A. Dikin, R. D. Piner, K. A. Kohlhaas, A. Kleinhammes, Y. Jia, Y. Wu, S. B. T. Nguyen, and R. S. Ruoff, Synthesis of graphene-based nanosheets via chemical reduction of exfoliated graphite oxide. *Carbon* 45 (2007) 1558-1565.
- [19] H. Zhang, X. J. Lv, Y. M. Li, Y. Wang, and J. H. Li, P25-Graphene composite as a high performance photocatalyst. *ACS Nano* 4 (2010) 380-386.
- [20] K. Zhang, K. C. Kemp, and V. Chandra, Homogeneous anchoring of TiO₂ nanoparticles on graphene sheets for waste water treatment. *Mater. Lett.* 81 (2012) 127-130.
- [21] C. Zhu, S. Guo, P. Wang, L. Xing, Y. Fang, Y. Zhai, and S. Dang, One-pot, water-phase approach to high-quality graphene/TiO₂ composite nanosheets. *Chem. Commun.* 46 (2010) 7148-7150.
- [22] L. Sun, Z. Zhao, Y. Zhou, and L. Liu, Anatase TiO₂ nanocrystals with exposed {001} facets on graphene sheets via molecular grafting for enhanced photocatalytic activity. *Nanoscale* 4 (2012) 613-620.

- [23] F. Dong, S. Guo, H. Wang, X. Li, and Z. Wu, Enhancement of the visible light photocatalytic activity of C-doped TiO₂ nanomaterials prepared by a green synthetic approach. *J. Phys. Chem. C* 115 (2011) 13285-13292.
- [24] M. S. Sher Shah, A. R. Park, K. Zhang, J. H. Park, and P. J. Yoo, Green synthesis of biphasic TiO₂-reduced graphene oxide nanocomposites with highly enhanced photocatalytic activity. *ACS Appl. Mater. Interfaces* 4 (2012) 3893-3901.
- [25] D. Wang, X. Li, J. Chen, and X. Tao, Enhanced photoelectrocatalytic activity of reduced graphene oxide/TiO₂ composite films for dye degradation. *Chem. Eng. J.* 198-199 (2012) 547-554.
- [26] B. Jiang, C. Tian, Q. Pan, Z. Jiang, J. Q. Wang, W. Yan, and H. Fu, Enhanced photocatalytic activity and electron transfer mechanisms of graphene/TiO₂ with exposed {001} facets. *J. Phys. Chem. C* 115 (2011) 23718-23725.
- [27] W. W. Liu, X. Yan, J. Lang, C. Peng, and Q. Xue, Flexible and conductive composite electrode based on graphene sheets and cotton cloth for supercapacitor. *J. Mater. Chem.* 22 (2012) 17245-17253.
- [28] J. Wang, J. Polleux, J. Lim, and B. Dunn, Pseudocapacitive contributions to electrochemical energy storage in TiO₂ (Anatase) nanoparticles. *J. Phys. Chem. C* 111 (2007) 14925-14931.
- [29] B. E. Conway, V. Birss, and J. Wojtowicz, The role and utilization of pseudocapacitance for energy storage by supercapacitors. *J. Power Sources* 66 (1997) 1-14.

- [30] J. Yan, T. Wei, W. Qiao, B. Shao, Q. Zhao, L. Zhang and Z. Fan, Rapid microwave-assisted synthesis of graphene nanosheet/Co₃O₄ composite for supercapacitors. *Electrochim. Acta* 55 (2010) 6973-6978.
- [31] J. Yan, T. Wei, W. Qiao, B. Shao, Q. Zhao, L. Zhang, and Z. Fan, Rapid microwave-assisted synthesis of graphene nanosheet/Co₃O₄ composite for supercapacitors. *Electrochim. Acta* 55 (23) (2010) 6973-6978.
- [32] J. Wang, Z. Gao, Z. Li, B. Wang, Y. Yan, Q. Liu, T. Mann, M. Zhang, and Z. Jiang, Green synthesis of graphene nanosheets/ZnO composites and electrochemical properties. *J. Solid State Chem.* 184 (2011) 1421-1427.
- [33] D. Zhang, X. Zhang, Y. Chen, C. Wang, and Y. Ma, An environment-friendly route to synthesize reduced graphene oxide as a supercapacitor electrode material. *Electrochim. Acta* 69 (2012) 364-370.



5.4. Synthesis and Electrochemical Performance of Graphene-V₂O₅ Nanocomposites

5.4.1. Introduction

It is well-known that the charge storage and capacitance of supercapacitors greatly depend on the properties of electrode materials. Nanostructured materials are considered as one of the most promising materials for storage application over their bulk counterparts due to its high surface area, and short diffusion pathways for electrons and ions transport [1, 2]. Among the various electrode materials studied so far, vanadium pentoxide (V₂O₅) has been considered to be the most promising candidate in view of its layered structure, low cost, ease of synthesis, abundant in nature, higher capacity and an wide range of oxidation states varying from V²⁺ to V⁵⁺ [3-6]. However, a major setback is electrically poor conductive and structural instability, which hinders its ideal capacitance behavior and long-term cycling stability. A way to improve the capacitance and cyclic stability, several strategies have been proposed, for instance, incorporating some materials with good electrical conductivity and structural stability into V₂O₅, forming a V₂O₅-conductive matrix hybrid nanostructure to obtain better electrochemical performance [4, 6].

Recently, graphene has emerged as one of the most appealing material in various applications, including supercapacitor, batteries and optoelectronics due to its high surface area, high flexibility and better conductivity, high thermal and chemical stabilities [7-10]. However, the graphene exhibited a lower capacitance value than its predicted value, because of the agglomeration during the synthesis process which, limits its practical applications. Therefore, the development of hybrid nanostructure with V₂O₅ has been expected to improve the electrode performance for

supercapacitor applications. Only a few of investigations have been performed on graphene-V₂O₅ composite as an electrode material for supercapacitors in three electrode configuration. Xu et al [11] synthesized graphene/V₂O₅ xerogels nanocomposite by hydrothermal method and obtained a maximum specific capacitance of 195.4 F g⁻¹ at the current density of 1A g⁻¹ in a 0.5 M K₂SO₄ solution. Bonso et al [12] prepared exfoliated graphite nanoplatelet and V₂O₅ nanotube composite and exhibited a specific capacitance of 35 F g⁻¹ in the aqueous electrolyte (2 M KCl) and 226 F g⁻¹ in the organic electrolyte (1 M LiTFSI in acetonitrile) at a scan rate of 10 mV s⁻¹. However, the cycling stability of the electrode is still unsatisfactory. Therefore, it is important to exploit electrode materials with good electrochemical performance.

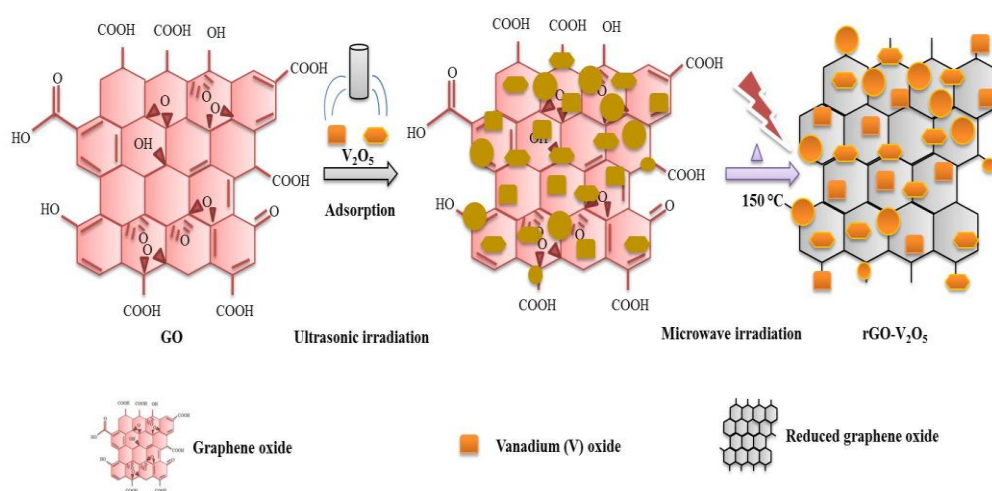
In this chapter, an economical and environmentally friendly microwave route was used to synthesize reduced graphene oxide/vanadium pentoxide (GV) composites electrode for high-performance supercapacitors. Compared with conventional methods, the microwave reduction method has the following advantages: quite faster, low cost, energy efficient, homogeneous heating, and, in general, heat generation within the material [13]. The structural, morphological, compositional and electrochemical characterization of the reduced graphene oxide/vanadium pentoxide composites was performed to evaluate their electrochemical utilizations in an aqueous electrolyte.

5.4.2. Experiment details

5.4.2.1. Synthesis of reduced graphene oxide/vanadium pentoxide composites

Graphene oxide (GO) was successfully prepared from expandable graphite powder using a modified Hummer's method as described elsewhere [14,15].

Reduced graphene oxide/vanadium pentoxide composites were synthesized by microwave irradiation technique, and it is schematically represented in **Scheme 5.4.1**. In a typical preparation of reduced graphene oxide/vanadium pentoxide composites (GO to V_2O_5 ratio is 1:1), as-prepared GO (75 mg) was first dispersed in 200 mL of distilled water and sonicated for 45 min. Then, 75 mg of V_2O_5 nanoparticles was added to the above solution with continuous sonication for 45 min to create a uniform dispersion. Then a small amount of hydrazine was added to that solution and stirred for 30 min further to uniform dispersion as well as reduction. After that, the mixture was transferred to an automated household microwave oven and irradiated for 15 min at 150 °C. After the reaction, the color of the suspension changed into grayish-black, which indicated the reduction of GO. The precipitate was collected with a centrifuge at 10,000 rpm for 10 min and washed thoroughly with distilled water. Afterwards, the obtained powders were dried at 60 °C for overnight in hot air oven and named as GV-2.



Scheme 5.4.1 Schematic representation of reduced graphene oxide/vanadium pentoxide composites growth process.

For comparison, the other weight ratio of reduced graphene oxide/vanadium pentoxide composites 2:1 (GV-1) and 1:2 (GV-3) are also prepared by the same experimental procedure. Pure reduced graphene oxide (rGO) was prepared according to a report by Ramadoss [14]. V_2O_5 purchased from Sigma Aldrich and used without any purifications.

5.4.2.2. Fabrication of working electrodes and their electrochemical characterization

The working electrodes were prepared by mixing 80 wt.% of active materials, 10 wt.% of carbon black and 10 wt.% of polyvinylidene difluoride (PVDF), in the presence of N-methyl pyrrolidinone (NMP), and this slurry was pasted on nickel foam (1 cm × 1 cm) and then heat treated at 80 °C under vacuum overnight. The mass of the electro-active material was 3.5 mg. All the electrochemical experiments were investigated using an AUTOLAB PGSTAT302N electrochemical work station. A typical three-electrode experimental cell, equipped with a working electrode, platinum foil as a counter electrode, and an Ag/AgCl reference electrode in 1 M Na_2SO_4 electrolyte solution. The cyclic voltammetry (CV) and galvanostatic charge-discharge test were performed over the potential range from 0 to 0.8 V at various scan rates (5 to 125 $mV s^{-1}$) and different current densities (0.1 to 0.75 $A g^{-1}$). Electrochemical impedance spectroscopy (EIS) measurements were carried out using a direct current (dc) bias of 0.1 V with a signal of 10 mV over the frequency range of 0.1 Hz to 100 kHz. For comparison, the electrochemical performance of V_2O_5 and rGO were also investigated under the same conditions.

5.4.2.3. Electrochemical measurements in two electrode system

The symmetric supercapacitor was assembled by a two piece of G-V₂O₅ (positive and negative) electrodes on Ni foam with filter paper separator in middle. The each electrode contained 3 mg of electroactive material and had a geometric surface area of about 1 cm². The electrochemical measurements of the symmetric supercapacitors were carried out in 1M Na₂SO₄ aqueous electrolyte using the electrochemical work station in a two electrode cell at room temperature.

5.4.2.4. Fabrication of solid-state supercapacitors

The solid-state supercapacitor devices were assembled by two pieces of G-V₂O₅ composites electrodes on aluminum foil with a separator sandwiched in between and LiCl/PVA gel as a solid electrolyte. The LiCl/PVA electrolyte was prepared by mixing 4 g PVA and 8.5 g LiCl in 40 mL deionized water. Then the mixture was heated at 85 °C under vigorous stirring until the solution became clear. Prior to the assembling, all the electrodes and the separator were immersed into the LiCl/PVA gel electrolyte solution for 5 min and then assembled one by one and kept at 45°C for 12 h to vaporize the excess water in the electrolyte.

5.4.3. Results and discussion

The synthesis of reduced graphene oxide/vanadium pentoxide composites is schematically represented in **Scheme 5.4.1**. First, GO sheets were uniformly dispersed in water under sonication. Then, V₂O₅ nanoparticles were also dispersed in above mixture. After continuous sonication, almost all of the V₂O₅ nanoparticles will be adsorbed onto GO surface to form V₂O₅-GO mixtures. Finally, the GO-V₂O₅ mixture was converted into rGO-V₂O₅ by microwave irradiation method. Afterwards,

the obtained reduced graphene oxide/vanadium pentoxide composites samples were centrifuged and dried at 60 °C for 2 hr.

5.4.3.1. Structural analysis of the as-prepared samples

The crystal structure, size and phase purity of the as-prepared samples was analyzed by XRD. **Figure 5.4.1** shows the XRD pattern of GO, rGO, GV-1, GV-2 and GV-3 samples. The XRD pattern of GO reveals a strong peak at $2\theta = 10.2^\circ$, which correspond to the (002) plane with interplanar spacing value of 8.1 Å, well agreed with the previous report [24]. For rGO sample, the broad peak shifted to $2\theta = 24.6^\circ$, which indexed as (002) characteristics diffraction of rGO sample [14], which suggests that the GO reduced to rGO under the present condition.

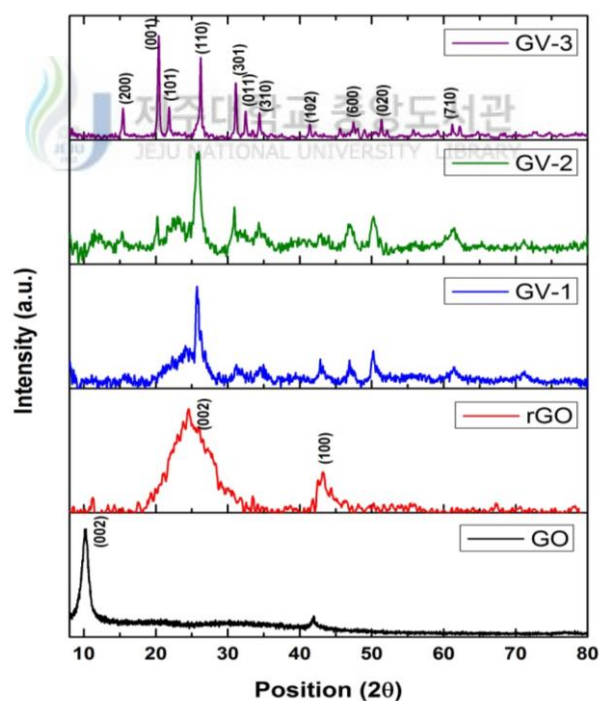


Figure 5.4.1 XRD spectra of GO, rGO, GV-1, GV-2, and GV-3.

The XRD pattern of reduced graphene oxide/vanadium pentoxide composites exhibited an orthorhombic structure with polycrystalline nature. The GV-1 and GV-2

samples confirmed the presence of rGO peak at 24.5° which corresponds to (002) plane. In case of GV-3 samples, no diffraction peaks of graphene were observed. This is due to the main characteristic peak of rGO at 24.6° has a low diffraction intensity, which can overlap with the (110) plane of V_2O_5 at 26.1° . Further, the prominent diffraction peaks at the diffraction angles (2θ) of about 15.4° , 20.4° , 21.8° , 26.2° , 31.1° , 32.4° , 34.4° , 41.4° , 47.4° , 51.3° and 61.2° corresponds to (200), (001), (101), (110), (301), (011), (310), (102), (600), (020) and (710) planes, respectively, which represent the orthorhombic structure of V_2O_5 [16]. In addition to that, no other crystalline phase was observed, which clearly indicating that the high purity of the as-prepared samples.

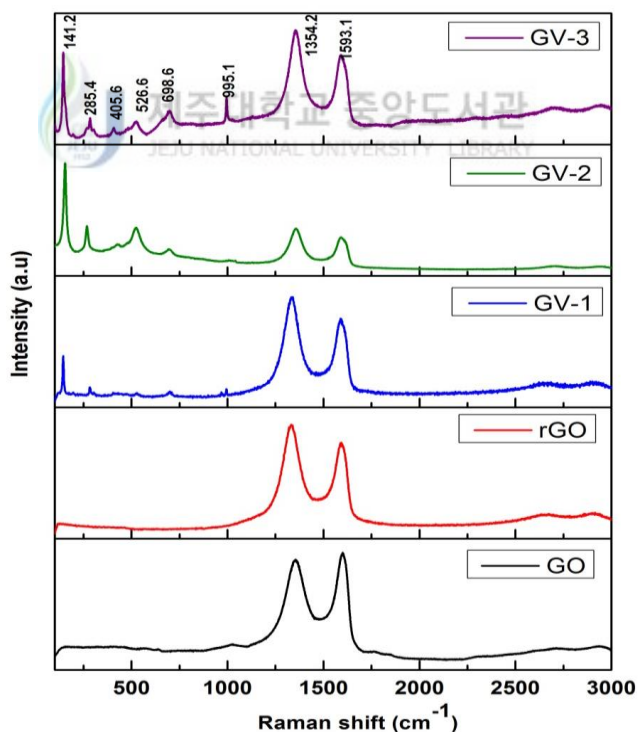


Figure 5.4.2 Raman spectra of GO, rGO, GV-1, GV-2, and GV-3.

In order to further confirm the structure of the as-prepared materials, the Raman spectroscopy measurements were done. **Figure 5.4.2** shows the typical

Raman spectra of GO, rGO, GV-1, GV-2 and GV-3 samples. The G and D bands are the main features of carbon-based materials, which are arising from the vibrations of sp^2 -hybridized carbon atoms, appeared at around 1593.1 and 1354.2 cm^{-1} , respectively [14,17,18]. Thus, the G-band is the result of vibration of sp^2 -hybridized carbon atoms, and the D-band arises from the disorder and defect intensity of the crystal structure. Almost all of the samples are exhibited the broad D and G bands. Compared with GO and rGO, the GV samples exhibited the new distinct peaks located at 141.2, 285.4, 405.6, 526.6, 698.6 and 995.1 cm^{-1} , which correspond to the orthorhombic structure of V_2O_5 [19,20]. The strong and high-intensity peak at 143 cm^{-1} could be assigned to the skeleton vibration of the V-O-V bond [19]. The low-intensity peaks located at 285.4 and 405.6 cm^{-1} are assigned to the bending vibration of the V=O bonds [20]. The two broad peaks at 526.6 and 698.6 cm^{-1} are attributed to the bending vibrations of the triply coordinated oxygen (V_3-O) and the doubly coordinated oxygen (V_2-O) bond in a disordered V-O-V framework, respectively [21]. The peak centered at 995.1 cm^{-1} correspond to the stretching vibration mode of V=O bond [19]. Moreover, the intensity ratio of D to G band (I_D/I_G) can be used to quantify the relative content of defects and the sp^2 domain. The I_D/I_G values of GO, rGO, GV-1, GV-2 and GV-3 samples are 0.96, 1.28, 1.28, 1.26, and 1.24 respectively. Compared with GO, the I_D/I_G asset value of other samples were increased, which indicates the decrease in the average size of the sp^2 domains upon reduction [14]. From these results, we have confirmed that the V_2O_5 nanoparticles are physically attached to the rGO nanosheets and introduce conductivity within the GV electrode providing pathways for charge transfer. The rGO from reduction of

graphene oxide was also confirmed by using Fourier transform infrared (FT-IR) spectroscopy and X-ray photoelectron spectroscopy measurements.

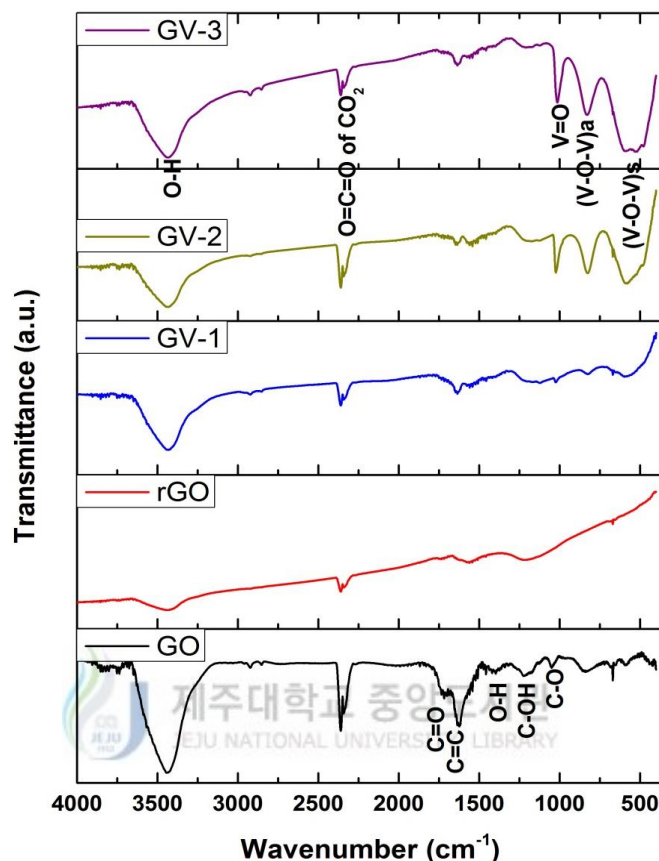


Figure 5.4.3 FT-IR spectra of GO, rGO, GV-1, GV-2, and GV-3.

The rGO from reduction of graphene oxide was also confirmed by using Fourier transform infrared (FT-IR) spectroscopy measurements. The typical FT-IR spectra of GO, rGO, GV-1, GV-2 and GV-3 samples are given in **Figure 5.4.3**. It can be seen that all the samples exhibited the absorption peaks at around 3440 and 2363 cm^{-1} , which corresponds to the O-H stretching vibrations of water molecules and CO_2 , respectively [14]. In the FT-IR spectrum of GO, the absorption peaks observed in 1721, 1622, 1390, 1215, and 1046 cm^{-1} can be assigned to the stretching vibrations of C=O (carboxyl or carbonyl), C=C (aromatic stretching), O-H (hydroxyl), C-OH, C-O

(carboxyl), and C-O (epoxy or alkoxy), respectively [22]. While in the spectrum of rGO and GV samples, the absorption peaks of oxygen functionalities are disappeared or weaken, after the microwave treatment, representing the high purity of graphene could be achieved. Furthermore, compared to rGO spectrum, the three new and strong absorption peaks are appeared in GV samples, which correspond to the vibrational modes of the V^{5+} species in the vanadyl group [23]. The absorption peaks around 1010 and 500-600 cm^{-1} are attributed to the stretching vibrational modes of V=O and V-O-V (symmetric stretch) bond, respectively, and the peak at 825 cm^{-1} can be assigned to the coupled vibration between V=O and V-O-V (asymmetric stretch) bond [16].

5.4.3.2. Compositional analysis of the as-prepared samples

The chemical composition, chemical state and binding energy information of the as-prepared materials were analyzed by XPS. The XPS spectra of the survey, V 2p, C1s and O1s region of GO, rGO, GV-1, GV-2 and GV-3 samples are shown in **Figure 5.4.4**. The survey spectrum (**Figure 5.4.4a**) of the samples shows the main peaks of carbon, oxygen and vanadium species with their corresponding binding energies, which confirming the formation of the products. The high-resolution spectrum of V 2p exhibited two main peaks at 518.5 and 525.9 eV, correspond to V^{5+} state of V 2p $_{3/2}$ and V 2p $_{1/2}$, respectively in V_2O_5 , with an energy separation of 7.4 eV, as shown in **Figure 5.4.4b** and the values are in good agreement with the previously reported data of V_2O_5 phase [16, 24].

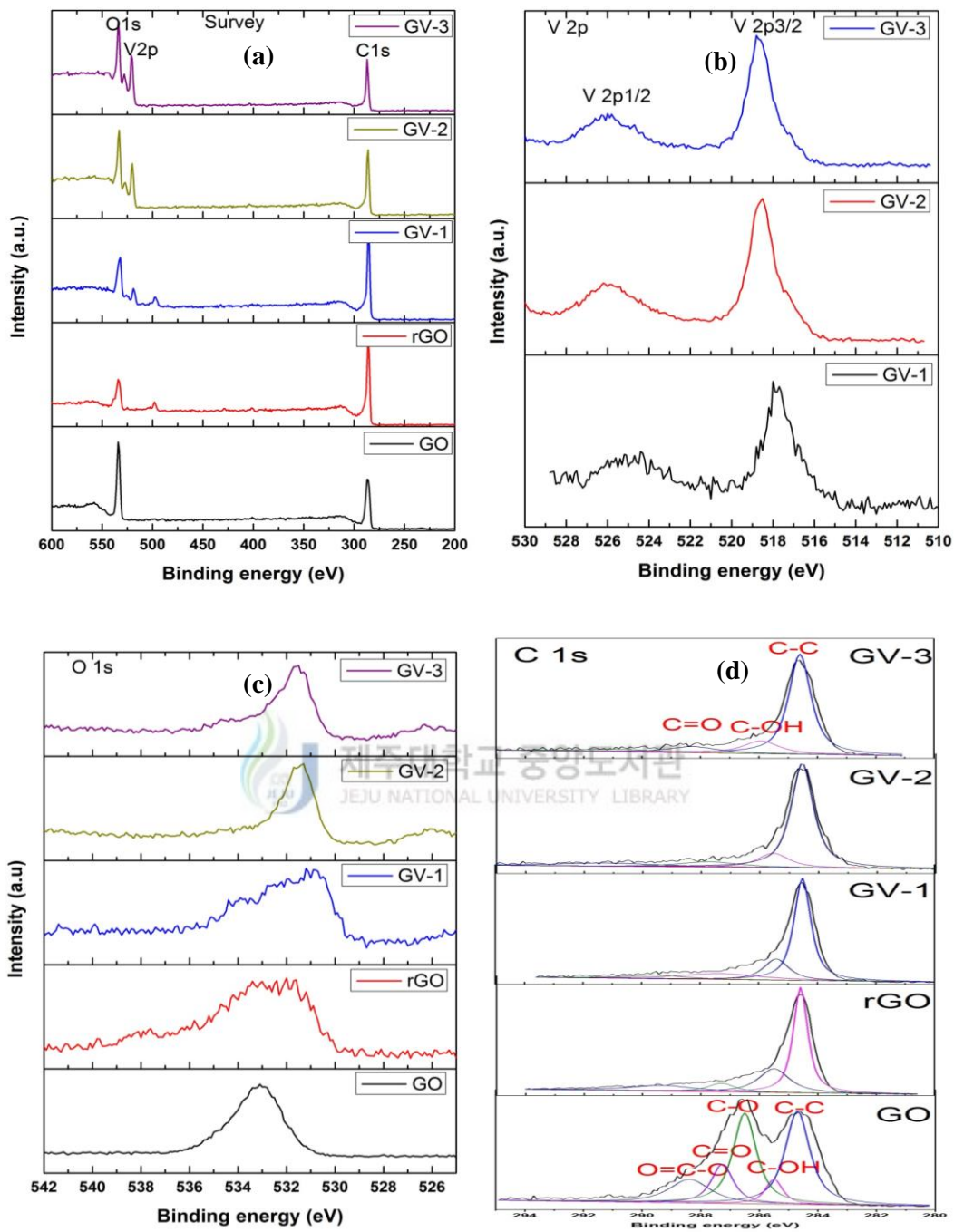


Figure 5.4.4 XPS spectra of GO, rGO, GV-1, GV-2 and GV-3 for (a) the survey scan, (b) V 2p, (c) O 1s, and (d) C 1s.

For the O 1s core-level spectrum (**Figure 5.4.4c**), the binding energy peak around 530.9 eV assigned to the oxygen species of (V-O bond) V_2O_5 , while the peak at 533.1 eV corresponds to the hydroxyl (OH) bond. **Figure 5.4.4d** shows the de-

convoluted C1s XPS spectrum. The C1s core-level spectrum of GO can be deconvoluted into five peaks centered at the binding energies of 284.6 eV (C-C, aromatic), 285.5 eV (C-OH, carbonyl), 286.5 eV (C-O, epoxy/alkoxy), 287.2 eV (C=O, carbonyl carbon), and 288.4 eV (O=C-O, carboxylate carbon), respectively, which clearly indicates the considerable degree of oxidation [14, 22]. Compared the C 1s spectrum of rGO and GV samples with GO, it can be seen that the oxygenated functional groups distinctly decreased, which suggest that considerable deoxygenation occur after microwave irradiation treatment. These results, further indicates that the reduction of the oxygen-containing functional groups in rGO and GV samples.

5.4.3.3. Morphology and microstructure analysis of the as-prepared samples

The morphology and microstructure of the as-prepared GV-3 composites was elucidated by FE-SEM and TEM analysis, and they are shown in **Figure 5.4.5**. The FE-SEM images (**Figure 5.4.5a-b**) clearly shows that the V₂O₅ nanoparticles are densely, distributed onto the rGO surface. The average sizes of the V₂O₅ nanoparticles are in the range of 150-200 nm. Further, TEM images (**Figure 5.4.5c-d**) also confirmed the presence of V₂O₅ nanoparticles on the rGO surface. The strong adhesions of V₂O₅ particles with rGO nanosheets are increases the electronic conductivity and also facilitate the fast ion/electron transport between the electrode and electrolyte to enhance the electrochemical performance The SAED pattern of GV-3 composites displays (**Figure 5.4.5e**) the clear ring patterns, revealing the polycrystalline nature of the as-prepared samples and the rings are indexed to be (001), (101), (201), (310), (401), and (302) planes of orthorhombic V₂O₅ phase (JCPDS card 41-1426). EDX spectrum of GV-3 sample is presented in **Figure 5.4.5f**.

The result confirmed the presence of C, V, and O elements. The C element is arising from the graphene layers and V and O is due to the V_2O_5 .

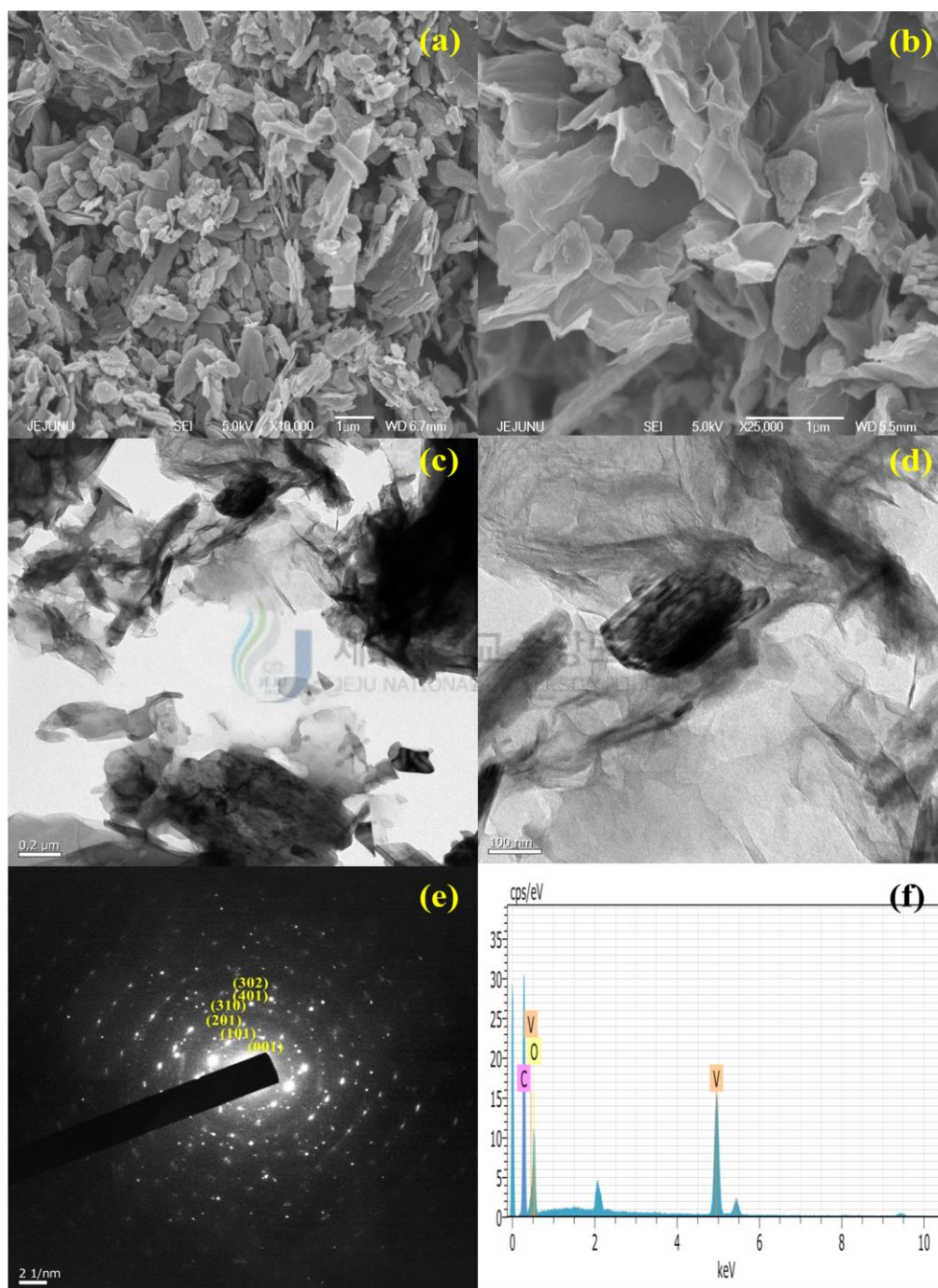


Figure 5.4.5 Morphological studies of GV-3 sample: FE-SEM (a-b), TEM images (c-d), SAED pattern (e), and EDS spectrum (f) of reduced graphene oxide/vanadium pentoxide composites. The morphological studies showed the V_2O_5 nanoparticles are uniformly distributed on the graphene nanosheets.

5.4.3.4. Electrochemical performance of the as-prepared samples

To fully explore the properties of as-prepared reduced graphene oxide/vanadium pentoxide composites, its electrochemical behavior was investigated in detail as follows. In order to evaluate the electrochemical performance of the as-prepared electrodes, electrochemical impedance spectroscopy (EIS), cyclic voltammetry (CV), and galvanostatic charge/discharge measurements were performed in 1 M Na₂SO₄ aqueous solution.

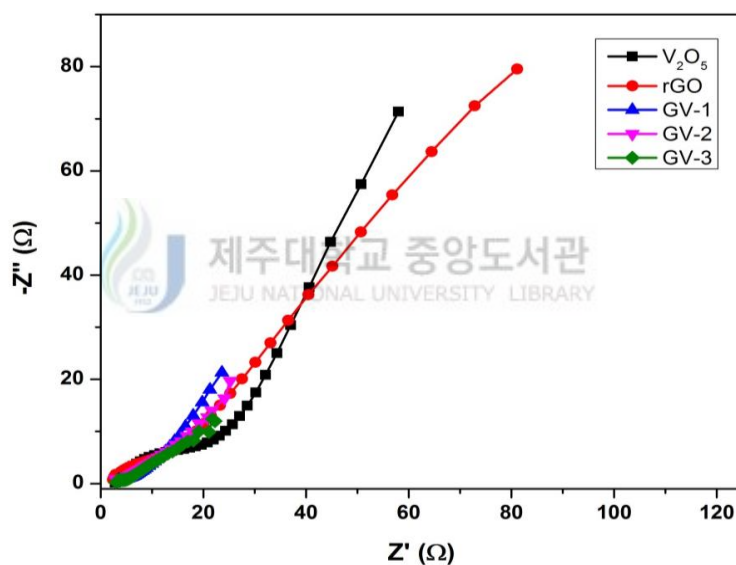


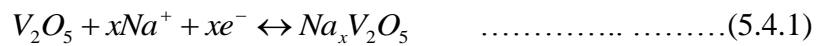
Figure 5.4.6 EIS curves of V₂O₅, rGO, GV-1, GV-2, and GV-3 electrodes.

EIS is a powerful tool to understand the capacitive behavior and resistance associated with the as-prepared electrode surface. **Figure 5.4.6** displays the Nyquist plots of V₂O₅, rGO, GV-1, GV-2 and GV-3 electrodes recorded in the frequency range of 0.1 Hz to 100 kHz with an AC excitation signal of 5 mV in 1M aqueous Na₂SO₄ solution. All of the Nyquist plots showed the semicircle arc at the high-frequency region, followed by a straight line in the low-frequency region. The semi-

circle arc in the high-frequency range is corresponds to the charge transfer limiting process and is attributed to the double-layer capacitance (C_{dl}) in parallel with the charge transfer resistance (R_{ct}) at the contact interface between electrode and electrolyte solution [25, 26]. The charge transferred resistance (R_{ct}) of the as-prepared V_2O_5 , rGO, GV-1, GV-2 and GV-3 electrodes are 18.7, 10.43, 3.18, 1.97, and 1.86Ω , respectively. It can be found that the reduced graphene oxide/vanadium pentoxide (GV) composites electrodes showed lower charge-transfer resistance compared to rGO and V_2O_5 electrodes, which indicates that the introduction of rGO provides more convenient conductive pathways for electron conduction. The straight line in the low-frequency range is attributed to the ion diffusion process in the electrolyte called the Warburg impedance [25,26]. From these result, we have concluded that the low resistance of GV electrode may facilitate the fast ion/electron transfer between electrode and electrolyte to enhance the supercapacitor performance.

To confirm the capacitive behavior and quantify the specific capacitance of the as-fabricated electrodes, CV and GCD test was performed. CV is generally considered to be an appropriate tool for estimating the difference between the non-Faradic and Faradic processes in an electrochemical reaction. **Figure 5.4.7a** represents the CV curves of V_2O_5 , rGO, GV-1, GV-2 and GV-3 electrodes measured in the potential window of 0 to 0.8 V in 1M aqueous Na_2SO_4 solution. It can be observed that all of the electrodes are exhibited closed to rectangular shape with small indicative of a faradic pseudocapacitive nature, which indicates an ideal capacitive behavior. Although there are no distinct redox peaks were observed. Compared with V_2O_5 and rGO, the GV electrodes revealed a high integrated area of

the CV curves, which confirmed that the amount of V_2O_5 loaded on the rGO nanosheets greatly, impacts the capacitive behavior of the final products. Therefore, the integrated area under CV curves increases in the order of $V_2O_5 < rGO < GV-1 < GV-2 < GV-3$ electrode. The electrochemical reaction of Na^+ insertion/extraction process occurring at the GV electrodes surface can be expressed as the following equation (1) [11,27],



Where x indicates the mole fraction of inserted sodium ions. The above equation suggests that the pseudocapacitance behavior of V_2O_5 arise from the reversible redox transition.

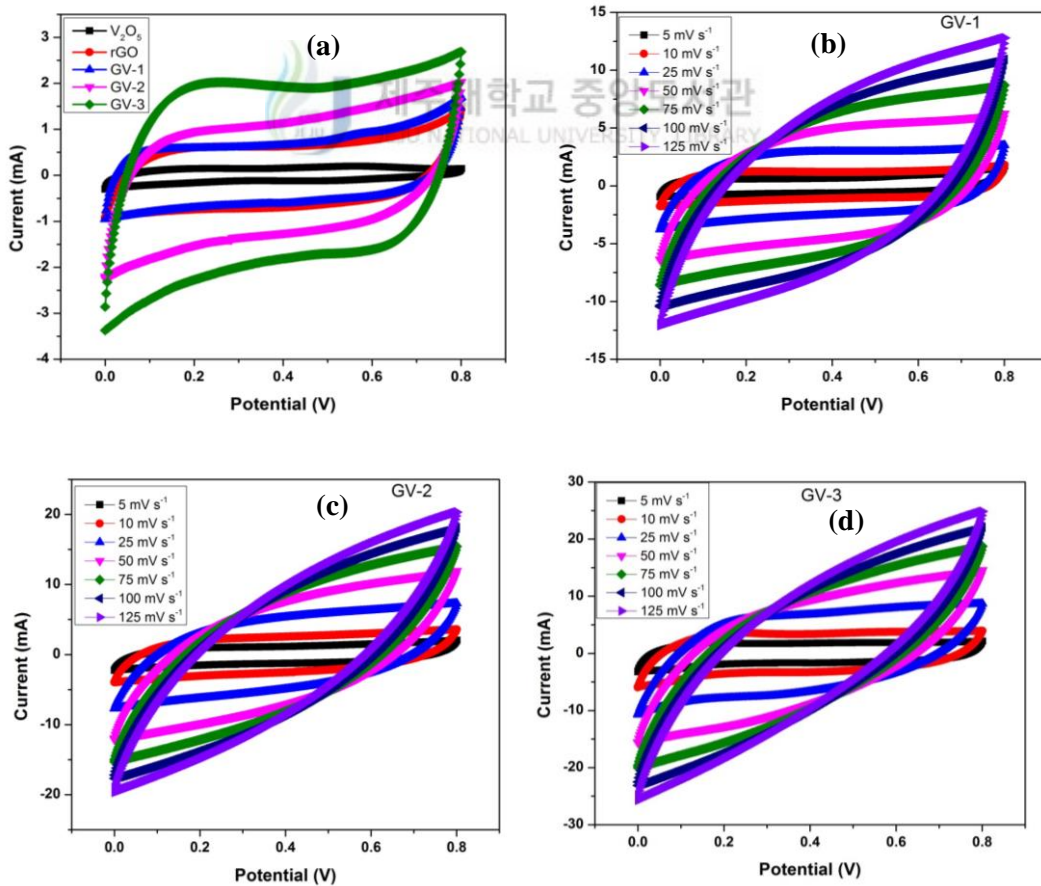


Figure 5.4.7 (a) CV curves of V_2O_5 , rGO, GV-1, GV-2, and GV-3 electrodes. CV curves of (b) GV-1, (c) GV-2, and (d) GV-3 electrodes at different scan rates in 1 M Na_2SO_4 solution.

Furthermore, the capacitive performance of GV-1, GV-2 and GV-3 electrodes was studied by CV analysis at various scan rates in 1M Na₂SO₄ solution is shown in **Figure 5.4.7b-d**. As the scan rate increases, the integrated areas under CV curves are also increased, which is a typical result of adsorption and desorption characteristics of the EDLCs. In addition, the shape of the CV curves maintained a relatively rectangular and symmetric shape with only a slight distortion by increasing the scan rates from 5 to 125 mV s⁻¹, implying that the excellent capacitance behavior and fast diffusion of electrolyte ions toward the GV electrodes.

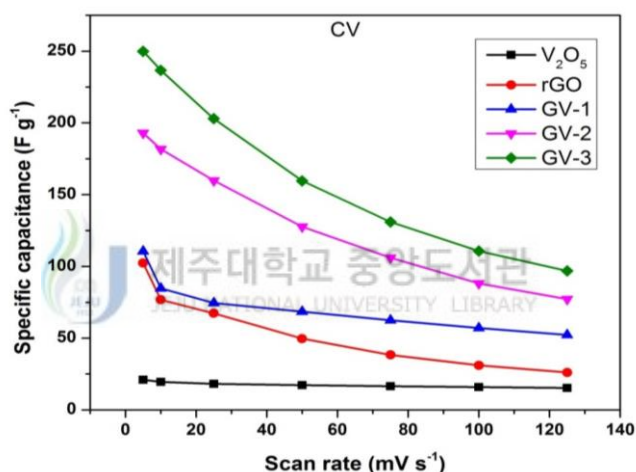


Figure 5.4.8 Specific capacitance of V₂O₅, rGO, GV-1, GV-2 and GV-3 electrodes at different scan rates calculated from CV curves.

The specific capacitances of V₂O₅, rGO, GV-1, GV-2 and GV-3 electrodes obtained from the CV loops are 22, 103, 110, 193 and 250 F g⁻¹, respectively at a scan rate of 5 mV s⁻¹. It is also observed that the specific capacitance of the reduced graphene oxide/vanadium pentoxide composites electrode is much higher than that of rGO and V₂O₅ electrodes at the same scan rate. Compared with GV-1 and GV-2, the GV-3 electrode exhibited higher specific capacitance, which is due to the higher mass loading of V₂O₅ on graphene nanosheets. **Figure 5.4.8** shows the variation in

the specific capacitance as a function of scan rates for all electrodes. It can be observed that the specific capacitance of each electrode decreases with an increase of scan rate from 5 to 125 mV s⁻¹. This is a common phenomenon and is caused by the insufficient time available for ion diffusion and adsorption inside the smallest pores within large particles due to the diffusion limit at a high scan rate [28].

The GV-3 electrode revealed an enhanced specific capacitance compared with the values of the earlier reported in the literature, such as exfoliated graphite nanoplatelets–V₂O₅ nanotube composite electrodes (35 / 226 F g⁻¹ at 10 mV s⁻¹ in 2M KCl / 1M LiTFSI), and vanadium oxide nanowire graphene binder free nanocomposite paper electrodes (80 F g⁻¹ at 0.5 A g⁻¹ in LiTFSI in acetonitrile solution). The significantly enhanced capacitance and electrochemical performance of the GV-3 electrode compared to other electrodes are considered to be the following points; (i) the capacitance of GV electrode strongly depends on the mass ratio of V₂O₅/rGO in reduced graphene oxide/vanadium pentoxide composites electrode, because V₂O₅ has high theoretical capacitance and fast redox kinetics, and rGO has high conductivity and large surface area. (ii) The combination of V₂O₅ and rGO could overcome the disadvantages of rGO (agglomeration) and V₂O₅ (low conductivity), and leads to the excellent electrochemical performance in supercapacitor. The high specific area and conductivity of rGO in GV electrodes provide a good supporting matrix to an decorate large number of V₂O₅ and an excellent interfacial contact between V₂O₅ and rGO, which results increased electro-active sites and reduced diffusion path length of Na⁺ ion in the electrode matrix, finally leads to the fast electron transport between the electrode and electrolyte [11,29]. In addition, the excellent mechanical strength of rGO in GV electrode might

provide a long cycle life during the charge/discharge process. Further, the microwave synthesis method was a simple, cost effective, efficient approach and required less preparation time, compared with the hydrothermal method.

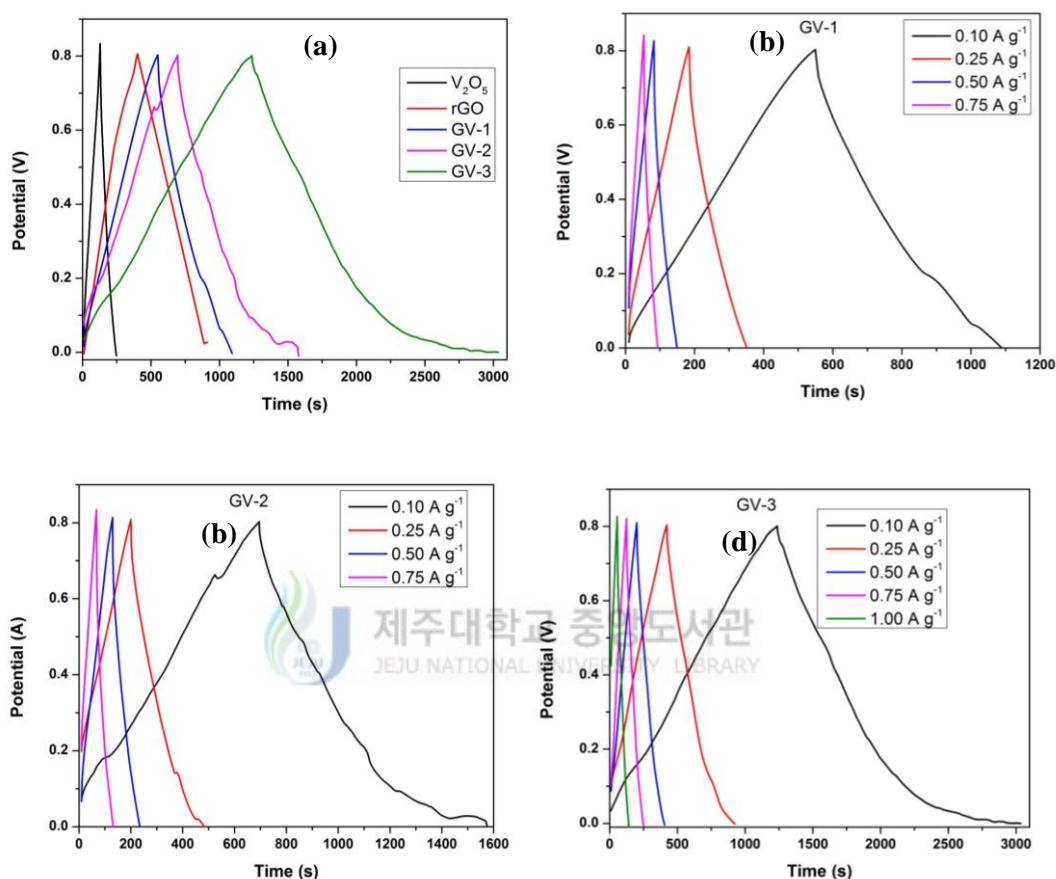


Figure 5.4.9 (a) GCD curve of the V_2O_5 , rGO, GV-1, GV-2, and GV-3 electrodes at a constant current density of 0.1 A g^{-1} in $1 \text{ M Na}_2\text{SO}_4$ electrolyte solution. GCD curves of (b) GV-1, (c) GV-2, and (d) GV-3 electrode at different current densities.

The galvanostatic charge/discharge (GCD) studies are the most important and direct approach to evaluate the applicability of supercapacitors. The GCD curves of V_2O_5 , rGO, GV-1, GV-2 and GV-3 electrodes obtained in the potential range of 0 to 0.8 V at current density of 0.1 A g^{-1} are shown in **Figure 5.4.9a**. From the figure, it can be seen that all of the curves are a linear, symmetric and almost triangles in shape with slight curvature, suggesting that the electrodes have good capacitive characteristics. Among all the electrodes, GV-3 electrode exhibited the longest

charge/discharge time, which confirming the higher specific capacitance. The calculated specific capacitance of V₂O₅, rGO, GV-1, GV-2 and GV-3 electrodes at current density of 0.1 A g⁻¹ are found to be 14.7, 62.3, 67.1, 109.2, and 226.6 F g⁻¹, respectively. Furthermore, the GCD measurement of GV electrodes were carried out at different current densities from 0.1 to 1 A g⁻¹.

Figure 5.4.9b-d represents the GCD curves of GV-1, GV-2 and GV-3 electrodes at various current densities. All of the GCD curves are exhibited a linear and symmetrical at various current densities demonstrating an ideal capacitive behavior and excellent electrochemical reversibility. The specific capacitance of the GV electrodes at various current densities can be calculated from the above equation (3). **Figure 5.4.10a** shows the calculated specific capacitance as a function of current densities. It can be found that the specific capacitance significantly decreases with the increases of discharge current densities for all samples. The decrease of the specific capacitance is likely caused by the relatively insufficient faradaic redox reaction of the active materials under higher discharge current densities. Compared to other electrodes, GV-3 electrode exhibited higher specific capacitance (226.6 F g⁻¹), as well as excellent rate capability. The enhanced specific capacitance of GV-3 electrode is mainly attributed to the uniformly loaded V₂O₅ on the rGO nanosheets, showing high efficient ion-accessible surface area and excellent electrical conductivity of the overall electrode. Moreover, during the charge and discharge processes, hybrid nanostructure can form an open structure to improve the connection between electro-active materials and electrolyte and take advantage of the electroactive GV. These results are consistent with CV studies and further confirm that the hybrid structure is helpful for ion diffusion and charge accumulation.

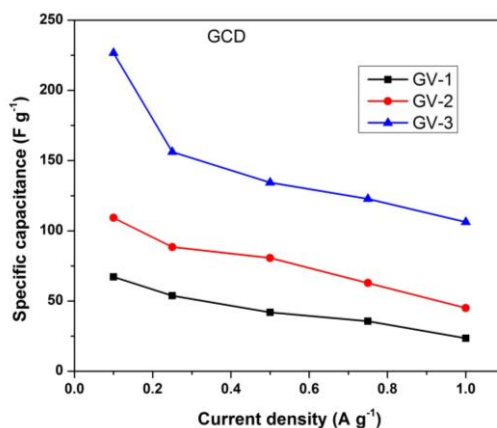


Figure 5.4.10 Specific capacitance of GV-1, GV-2 and GV-3 electrodes at different current densities calculated from GCD curves.

To further demonstrate the practical application of supercapacitors, the reversibility, electrochemical stability and long cycle life of the as-prepared electrodes at the high-current density or high scan rate are quite essential. Therefore, the as-prepared GV-1, GV-2, and GV-3 electrodes were measured by repeating the CV test at a constant scan rate of 150 mV s^{-1} for 5000 cycles in $1\text{M Na}_2\text{SO}_4$ solution, and the specific capacitance retention as a function of cycle numbers is presented in **Figure 5.4.11a**. It is could be observed that all of the GV electrodes exhibited satisfactory cycling stabilities over the entire cycle numbers and retaining 92% of the initial specific capacitance, even after 5000 cycles indicating a good cycling stability of the GV electrodes. Furthermore, the cyclic stability of GV-3 electrode is higher than that of GV-1 and GV-2 electrodes. The enhanced electrochemical stability and long cycle life of the GV-3 electrode is mainly attributed to the uniformly distributed V_2O_5 (higher mass loading) on the graphene nanosheets. The V_2O_5 nanoparticles could serve as a potential reservoir for ions, and therefore, the charge diffusion kinetics is enhanced within the electrode and also improves the adsorption/desorption

process of alkali cations on the surface of the materials. In addition, rGO sheets can provide more efficient contact between the electro-active material and the electrolyte and make full use of electrochemical active V_2O_5 during the electrochemical process. The high electrical conductivity of rGO improved the overall conductivity of the hybrid electrode, which shortening the ion transport/diffusion path between electrode and electrolyte. This result highlights the capability of the reduced graphene oxide/vanadium pentoxide composites electrode meet the requirements of both long cycle life and good rate capability, which are important advantages for the commercial energy storage devices.

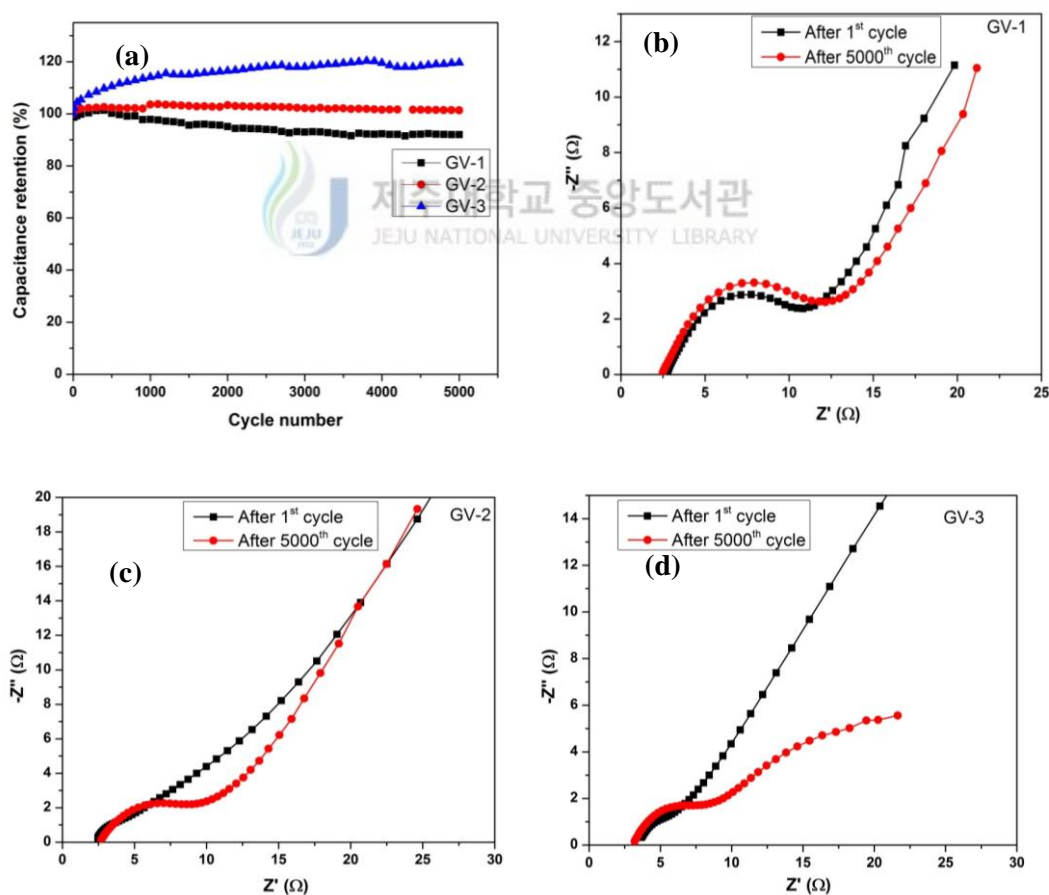


Figure 5.4.11 Stability measurement of G-V₂O₅ electrodes: (a) Variation of the specific capacitance of the GV-1, GV-2 and GV-3 electrodes as a function of a cycle number measured at 150 mV s⁻¹ in a 1 M Na₂SO₄ aqueous solution. Nyquist plots of the (b) GV-1, (c) GV-2 and (d) GV-3 electrodes, after the 1st and 5000th cycles.

For additional understating of the GV electrodes, EIS spectra of the GV-1 (**Figure 5.4.11b**), GV-2 (**Figure 5.4.11c**) and GV-3 (**Figure 5.4.11d**) electrodes before and after 5000 cycles were measured in the frequency range of 0.1Hz to 100 kHz in 1 M Na₂SO₄ solution. The result showed that the Nyquist plots were similar in shape in the form of semi-circle arc at the high-frequency range and straight line at low frequency range. Further, it can be observed that the after 1st cycle, the semi-circle loop at high frequency is too small, which indicates the small interfacial charge transfer resistance and good electrical conductivity. After 5,000 cycles, a small enlarged semi-circular arc could be found from the curve, which indicates the R_{ct} of the electrode is increased during the cycling process. As shown in **Figure 5.4.11b-d**, the arc increment from the 1st to the 5000th cycles is not obvious indicates that the GV electrodes are well maintained and preserved overall after 5000 cycles. The small enlargement is due to the loss of active materials on the current collector, and the corrosion of the current collector caused by electrolytes during the charge/discharge process [31, 32].

5.4.3.5. Electrochemical performance in two-electrode system

To completely investigate the electrochemical performance of the G-V₂O₅ electrode material, the G-V₂O₅/ G-V₂O₅ supercapacitor was studied in 1 M Na₂SO₄ aqueous solution. **Figure 5.4.12a** shows the CV curves of a symmetric supercapacitor at different potential windows up to 2V in 1M Na₂SO₄ solution at a 25 mV s⁻¹. The CV curves show mostly rectangular shapes for a low value of upper potential limit of 1.6 V, demonstrating the capacitive behavior. When the upper potential limit increases over 1.6 V, a current leap at the end of potential window was observed, which might be due to the gas evolution from the positive and/or the

negative electrode. **Figure 5.4.12b** shows the CVs of the symmetric supercapacitor between 0 and 1.6 V at different scan rates from 5 to 125 mV s^{-1} . It can be seen that all these curves, exhibit nearly rectangular shape even at a higher scan rates, indicating the ideal capacitive behavior and a fast charge/discharge behavior. The specific capacitance calculated from the CV curves using the equations 2.1 and 2.3. **Figure 5.4.12c** displays the calculated cell capacitance and single electrode capacitance in cell as a function of scan rate. The calculated cell capacitance and single electrode capacitance in the cell is around 49 and 199 F g^{-1} at a scan rate of 5 mV s^{-1} .

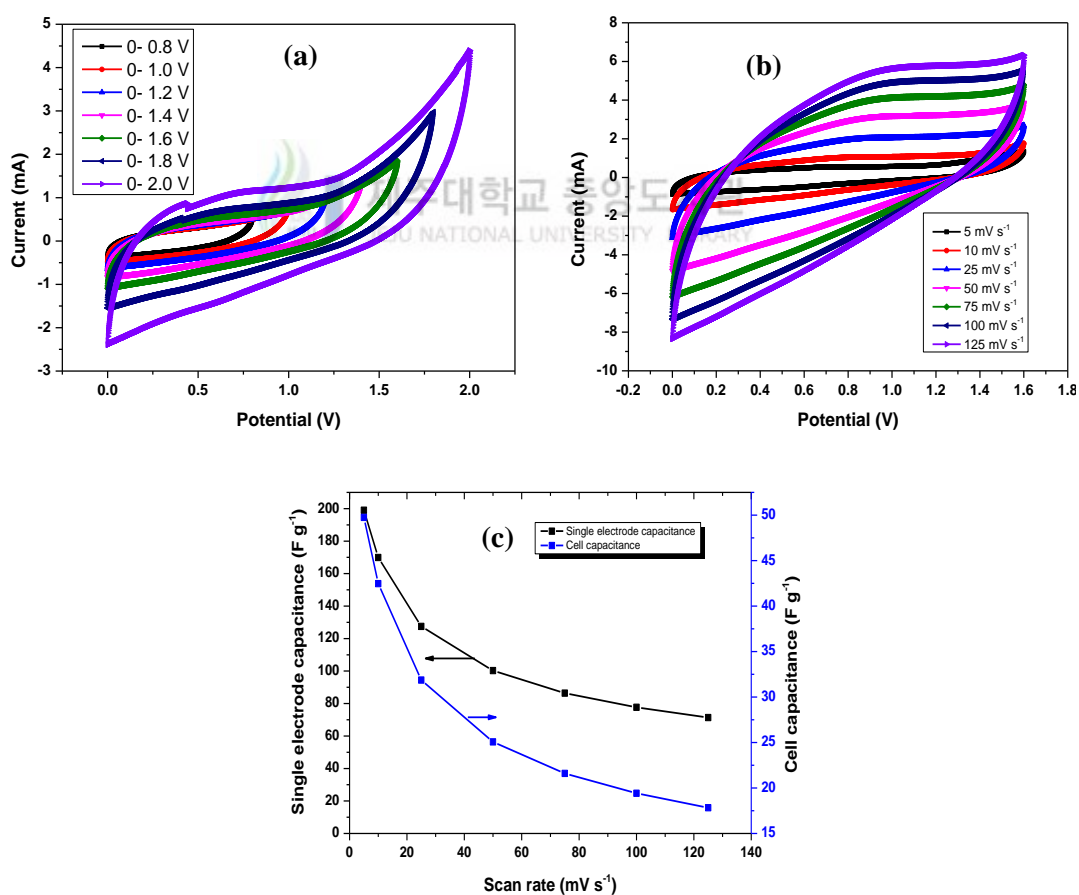


Figure 5.4.12 (a) CVs of symmetric G- V_2O_5 supercapacitor with different potential windows. (b) CVs of symmetric G- V_2O_5 supercapacitor between 0.0 to 1.6 V at various scan rates. (c) The cell and single electrode capacitance of symmetric supercapacitor as a function of scan rate.

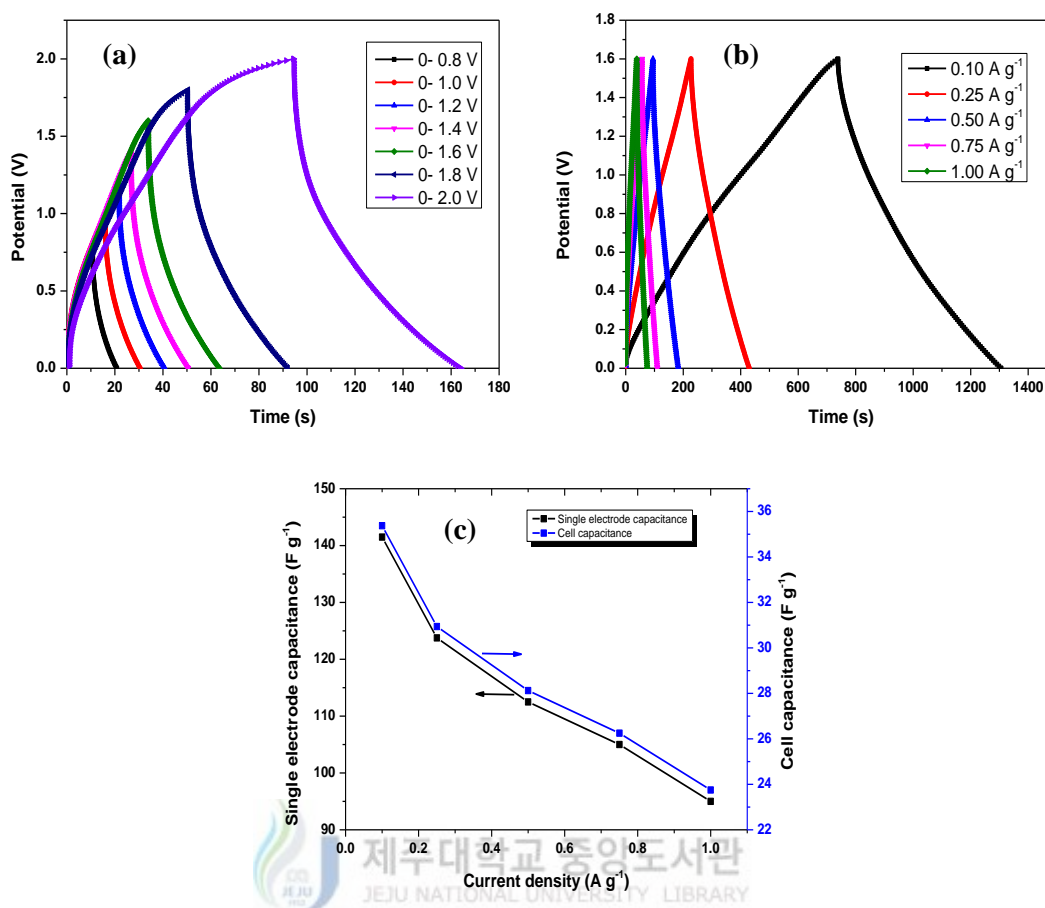


Figure 5.4.13 (a) Galvanostatic charge/discharge curves of symmetric G-V₂O₅ supercapacitor with different potential windows. (b) GCD curves of symmetric G-V₂O₅ supercapacitor between 0.0 to 1.6 V at various current densities. (c) The cell and single electrode capacitance of symmetric supercapacitor as a function of current density.

In order to further evaluate, the electrochemical performance of the symmetric supercapacitor, galvanostatic charge/discharge measurements were carried out. **Figure 5.4.13a** shows the GCD curves of a symmetric supercapacitor with various voltage windows at a current density of 0.5 A g⁻¹. Both the charge and the discharge curves remained in reasonably good symmetry at all voltages. The charge and discharge time were nearly proportional to the charge–discharge potential, indicating ideal capacitive characteristics. Further, the charge–discharge characteristics of symmetric supercapacitor in the potential window of 0 to 1.6 V were evaluated at different current densities. As shown in **Figure 5.4.13b**, the

discharge curves of this cell are relatively symmetrical with its corresponding charge counterparts, confirming the ideal capacitive characteristics and rapid charge/discharge property of the fabricated symmetric supercapacitor. Furthermore, the specific capacitance can be calculated from the discharge curves using the equation (2.2 and 2.3). **Figure 5.4.13c** shows the specific capacitance versus current densities. The calculated cell capacitance and single electrode capacitance in cell are 35 F g^{-1} and 142 F g^{-1} , at a current density of 0.1 A g^{-1} , respectively. Moreover, the symmetric supercapacitor retained 68% of cell capacitance, when the current density is increased from 0.1 to 1 A g^{-1} , demonstrating a good rate capability.

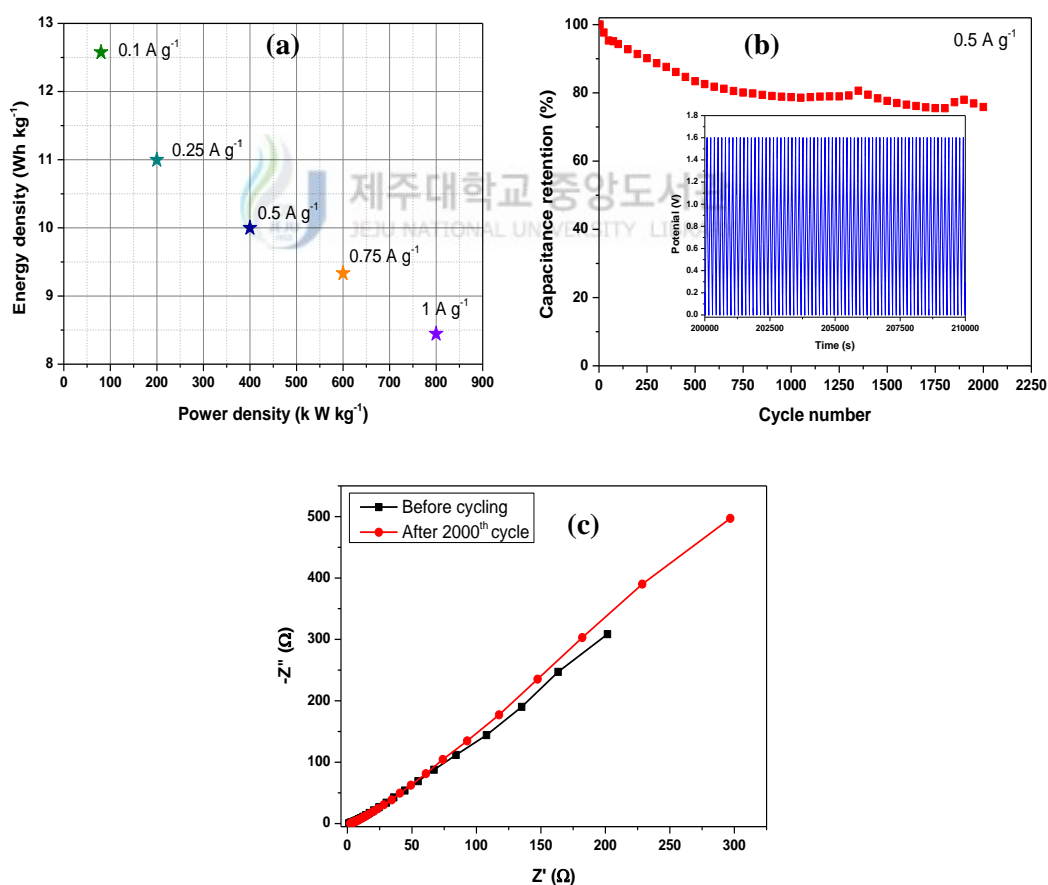


Figure 5.4.14 (a) Ragone plot of symmetric supercapacitor at various current densities. (b) The cycle performance of the symmetric supercapacitor in the potential window between 0.0 to 1.6 V at 0.5 A g^{-1} for 2000 cycles; the inset shows the GCD cycles. (c) Nyquist plots of symmetric supercapacitor before and after 2000 cycles.

The suitability of GV for supercapacitor applications was further evaluated by examining its energy and power density using the equations (2.5 and 2.6). **Figure 5.4.14a** shows the Ragone plots of the symmetric supercapacitor at various current densities. The energy density of the symmetric supercapacitor reached 12.5 W h kg^{-1} at a power density of 79.9 kW kg^{-1} and sustained 8.4 W h kg^{-1} at a power density of 799.9 kW kg^{-1} . The long-term cycling stability of our symmetric supercapacitor was also tested by repeating the galvanostatic charge/discharge technique with the potential window of 1.6 V, as demonstrated in **Figure 5.4.14b**. It is confirmed that the 75% of the initial capacitance can be retained after even 2000 cycles, indicating the better cycling performance of the fabricated symmetric supercapacitor. To further study the cyclic stability and fundamental behavior of symmetric supercapacitor, we have compared the EIS (**Figure 5.4.14c**) of the before and after cycle tests. The Nyquist plots composed of semi-circle arc at the high-frequency region followed by a straight line at the low-frequency region, which correspond to electron transfer-limited processes and diffusional-limited electron-transfer processes, respectively. It could be observed that the Nyquist plots almost have no changes, also indicating that the symmetric supercapacitor have good cyclic stability.

5.4.3.6. Performance of solid-state supercapacitor devices

In order to demonstrate the potential application of as-prepared electrode material, we have fabricated all-solid-state symmetric supercapacitor by sandwiching two pieces of GV-3 electrode with a polymer-gel electrolyte separator in a middle. We have assembled two supercapacitors in series, and found that the device could power a green (2.5 V) and red (1.5 V) light-emitting diode (LED) for about 5 min (**Figure 5.4.15a**), after being charged. Further, we demonstrated that the

device could be also drive a 4-digit seven segment display (**Figure 5.4.15b**) with character “NANO”.

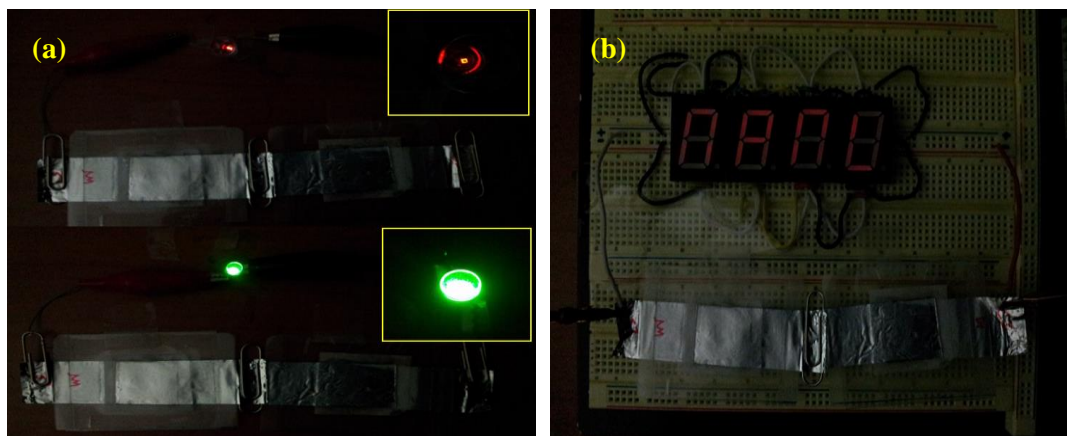


Figure 5.4.15 (a) Red and green LED driven by two solid state symmetric supercapacitors connected in series; inset shows the enlarged portion of LED glow. (b) Seven segment display with character “nano” powered by two tandem devices.

5.4.4. Conclusion

In summary, we have successfully synthesized the reduced graphene oxide/vanadium pentoxide composites electrode for electrochemical supercapacitors. The structural, compositional and morphological properties of the as-prepared electrodes are well characterized. The electrochemical studies clearly confirm the G-V₂O₅ symmetric supercapacitor exhibiting a maximum cell capacitance of 49 F g⁻¹ (scan rate of 5 mV s⁻¹) and excellent cycling stability, even after 2000 cycles. The symmetric supercapacitor exhibits an energy density of 12.57 Wh kg⁻¹ at a power density of 79.99 kW kg⁻¹. Further, we have demonstrated the performance of the solid-state supercapacitor by lighting-up of LED and also showed the 4-digit seven segmented display. These results encourage the utilization of the reduced graphene oxide/vanadium pentoxide composites electrode as a potential electrode in developing simple, low cost, and environmentally friendly energy storage devices.

5.4.5. References

- [1] A. L. M. Reddy, M. M. Shaijumon, S. R. Gowda, and P. M. Ajayan, Coaxial MnO₂/carbon nanotube array electrodes for high-performance lithium batteries. *Nano Lett.* 9 (2009) 1002-1006.
- [2] Y. Luo, D. Kong, J. Luo, S. Chen, D. Zhang, K. Qiu, X. Qi, H. Zhang, C. M. Li and T. Yu, Hierarchical TiO₂ nanobelts@MnO₂ ultrathin nanoflakes core-shell array electrode materials for supercapacitors. *RSC Advances* 3 (2013) 14413-14422.
- [3] S. Boukhalifa, K. Evanoff, and G. Yushin, Atomic layer deposition of vanadium oxide on carbon nanotubes for high-power supercapacitor electrodes. *Energy Environ. Sci.* 5 (2012) 6872-6879.
- [4] S. D. Perera, A. D. Liyanage, N. Nijem, J. P. Ferraris, Y. J. Chabal, and K. J. Balkus Jr, Vanadium oxide nanowire – Graphene binder free nanocomposite paper electrodes for supercapacitors: A facile green approach. *J. Power Sources* 230 (2013) 130-137.
- [5] B. H. Kim, C. H. Kim, K. S. Yang, A. Rahy, and D. J. Yang, Electrospun vanadium pentoxide/carbon nanofiber composites for supercapacitor electrodes. *Electrochim. Acta* 83 (2012) 335-340.
- [6] M. Jayalakshmi, M. Mohan Rao, N. Venugopal, and K. B. Kim, Hydrothermal synthesis of SnO₂-V₂O₅ mixed oxide and electrochemical screening of carbon nano-tubes (CNT), V₂O₅, V₂O₅-CNT, and SnO₂-V₂O₅-CNT electrodes for supercapacitor applications. *J. Power Sources* 166 (2007) 578-583.

- [7] Y. Sun, Q. Wu, and G. Shi, Graphene based new energy materials. *Energy Environ. Sci.* 4 (2011) 1113-1132.
- [8] J. Yoo, K. Balakrishnan, J. Huang, V. Meunier, B. Sumpter, A. Srivastava, M. Conway, A. L. Reddy, J. Yu, R. Vajtai, and P. M. Ajayan, Ultrathin planar graphene supercapacitors. *Nano Lett.* 11 (2011) 1423-1427.
- [9] S. J. Guo, and S. J. Dong, Graphene nanosheet: synthesis, molecular engineering, thin film, hybrids, and energy and analytical applications. *Chem. Soc. Rev.* 40 (2011) 2644-2672.
- [10] M. D. Stoller, S. J. Park, Y. W. Zhu, J. H. An, and R. S. Ruoff, Graphene-based ultracapacitors. *Nano Lett.* 8 (2008) 3498-3502.
- [11] J. Xu, H. Sun, Z. Li, S. Lu, X. Zhang, S. Jiang, Q. Y. Zhu, and G. S. Zakharova, Synthesis and electrochemical properties of graphene/V₂O₅ xerogels nanocomposites as supercapacitor electrodes. *Solid State Ionics* 262 (2014) 234-237.
- [12] J. S. Bonso, A. Rahy, S. D. Perera, N. Nour, O. Seitz, Y. J. Chabal, K. J. Balkus Jr. J. P. Ferraris, and D. J. Yang, Exfoliated graphite nanoplatelets–V₂O₅ nanotube composite electrodes for supercapacitors. *J. Power Sources* 203 (2012) 227-232.
- [13] H. Hu, X. Wang, F. Liu, J. Wang, and C. Xu, Rapid microwave-assisted synthesis of graphene nanosheets–zinc sulfide nanocomposites: Optical and photocatalytic properties. *Synth. Met.* 161 (2011) 404-410.
- [14] A. Ramadoss, and S. J. Kim, Improved activity of a graphene–TiO₂ hybrid electrode in an electrochemical supercapacitor. *Carbon* 63 (2013) 434-445.

- [15] A. Ramadoss, G. S. Kim, and S. J. Kim, Fabrication of reduced graphene oxide/TiO₂ nanorod/reduced graphene oxide hybrid nanostructures as electrode materials for supercapacitor applications. *Cryst. Eng. Comm.* 15 (2013) 10222-10229.
- [16] H. Zhao, L. Pan, S. Xing, J. Luo, and J. Xu, Vanadium oxides–reduced graphene oxide composite for lithium-ion batteries and supercapacitors with improved electrochemical performance. *J. Power Sources* 222 (2013) 21-31.
- [17] M. S. Dresselhaus, A. Jorio, M. Hofmann, G. Dresselhaus, and R. Saito, Perspectives on carbon nanotubes and graphene Raman spectroscopy. *Nano Lett.* 10 (2010) 751-758.
- [18] L. M. Malard, M. A. Pimenta, G. Dresselhaus, and M. S. Dresselhaus, Raman spectroscopy in graphene. *Phys. Rep.* 473 (2009) 51-87.
- [19] C. Sanchez, J. Livage, and G. Lucazeau, Infrared and Raman study of amorphous V₂O₅. *J. Raman Spectrosc.* 12 (1982) 68-72.
- [20] S. H. Lee, H. M. Cheong, M. J. Seong, P. Liu, C. E. Tracy, A. Mascarenhas, J. Roland Pitts, and S. K. De, Raman spectroscopic studies of amorphous vanadium oxide thin films. *Solid State Ionics* 165 (2003) 111-116.
- [21] B. Yan, L. Liao, Y. You, X. Xu, Z. Zheng, and Z. Shen, Single-crystalline V₂O₅ ultralong nanoribbon waveguides. *Adv. Mater.* 21 (2009) 2436-2440.
- [22] W. Yue, Z. Lin, S. Jiang, and X. Yang, Preparation of graphene-encapsulated mesoporous metal oxides and their application as anode materials for lithium-ion batteries. *J. Mater. Chem.* 22 (2012) 16318-16323.

- [23] J. Yang, T. Lan, J. Liu, Y. Song, and M. Wei, Supercapacitor electrode of hollow spherical V_2O_5 with a high pseudocapacitance in aqueous solution. *Electrochim. Acta*, 105 (2013) 489-495.
- [24] J. Mendialdua, R. Casanova, and Y. Barbaux, XPS studies of V_2O_5 , V_6O_{13} , VO_2 and V_2O_3 . *J. Electron Spectrosc. Relat. Phenom.* 71 (1995) 249-261.
- [25] J. Li, W. Zhao, F. Huang, A. Manivannan, and N. Q. Wu, Single-crystalline $Ni(OH)_2$ and NiO nanoplatelet arrays as supercapacitor electrodes. *Nanoscale* 3 (2011) 5103-5109.
- [26] J. Wang, Z. Gao, Z. Li, B. Wang, Y. Yan, and Q. Liu, Green synthesis of graphene nanosheets/ ZnO composites and electrochemical properties. *J. Solid State Chem.* 184 (2011) 1421-1427.
- [27] B. Saravanakumar, K. K. Purushothaman, and G. Muralidharan, Interconnected V_2O_5 nanoporous network for high-performance supercapacitors. *ACS Appl. Mater. Interfaces* 4 (2012) 4484-4490.
- [28] J. Yan, T. Wei, W. Qiao, B. Shao, Q. Zhao, L. Zhang, and Z. Fan, Rapid microwave-assisted synthesis of graphene nanosheet/ Co_3O_4 composite for supercapacitors. *Electrochim. Acta* 55(23) (2010) 6973-6978.
- [29] G. Zhou, D. W. Wang, L. C. Yin, N. Li, F. Li, and H. M. Cheng, Oxygen bridges between NiO nanosheets and graphene for improvement of lithium storage. *ACS Nano* 6 (2012) 3214-3223.
- [30] H. Sun, L. Cao, and L. Lu, Bacteria promoted hierarchical carbon materials for high-performance supercapacitor. *Energy Environ. Sci.* 5 (2012) 6206-6213.

- [31] J. Yan, Z. Fan, T. Wei, W. Qian, M. Zhang, and F. Wei, Fast and reversible surface redox reaction of graphene-MnO₂ composites as supercapacitor electrodes. *Carbon* 48 (2010) 3825-3833.
- [32] D. Zhang, X. Zhang, Y. Chen, C. Wang, and Y. Ma, An environment-friendly route to synthesize reduced graphene oxide as a supercapacitor electrode material. *Electrochim. Acta* 69 (2012) 364-370.



CHAPTER-VI

Self-Powered Systems

6.1. Introduction

Increasing demand for energy, limitations in fossil fuel availability, and environmental concerns have promoted the study and development of new eco-friendly technologies for energy harvesting and storage. Furthermore, the rapid growth of technology and the introduction of nanotechnology have enabled device miniaturisation and lowered their operating power requirements; this has encouraged the development of self-powered devices [1–6]. The electrochemical capacitor is one of the most promising alternative energy storage devices to the conventional battery because of its higher power capacity, longer cyclic stability, and fast charging/discharging capability.

On the other hand, energy harvesting from the ambient environment—such as by solar, wind, thermal, and vibrational energy-harvesting techniques—has attracted a great deal of interest [7–10]. Among the conversion methods, nanogenerator is an effective device tool to harvest the low frequency mechanical energy through piezoelectric and tribo-electrification processes [11-16]. Recently, researchers are trying to develop a new hybrid system by integrating the energy harvesting device along with a storage device to perform a self-powered operation. The integrated hybrid device converts mechanical energy into electrical energy and then electrical energy into an electrochemical energy. Renewable energy is probably the cleanest energy in the world, but it is always limited by time, location, and weather. Integrating energy harvesting device with energy storage devices such as SCs and

batteries may offer a promising solution to build stand-alone self-powered systems, which potentially break the limitations of time, location, and weather. Especially, if supercapacitors are integrated with a sustainable and renewable energy source, forming an energy module, they could make electronic devices work persistently [17-19].

Based on the above concept, in this chapter built an energy module to verify the proficiency and efficiency of the fabricated all solid state supercapacitors (SSC) was demonstrated in a self-powered system by integrating with nanogenerator, and photodetector.

6.2. Fabrication of a flexible solid-state SSC

The fabrication of all-solid state supercapacitor was discussed in earlier **Chapeter.4.2**. Briefly, SSC was assembled by separating two pieces of electroactive material coated electrodes with a filter paper separator and a solid gel electrolyte. Prior to the assembling, the electrodes and the separator were immersed in the gel electrolyte for 3 min and then allowed to solidify at room temperature over 6 h. Finally, they were assembled together and dried at room temperature for 12 h to remove the excess water in the electrolyte. The performance of the self-powered device was assessed with a picoammeter (Model 6485, Keithley Instruments Inc.). The charging performance of supercapacitor was measured with a nanovoltmeter (Model 6482, Keithley Instruments Inc.).

6.3. Piezoelectric output of the Lead zirconate titanate (PZT) film

The commercial thin film based nanogenerator was purchased from MULTICOMP (EPX3FHDW) with dimension of 20 x 0.22 mm (Diameter x Thickness). The purchased nanogenerator was used as an energy source to harvesting

mechanical energy and stored in the graphene based symmetric supercapacitor. The open circuit voltage and short circuit current of the nanogenerator under periodic pressing through finger was shown in **Figure 6.1.1 and 6.1.2**. The nanogenerator was generated an average voltage and current of 6 V and 20 μ A in forward connection and 8 V and 20 μ A in reverse connection.

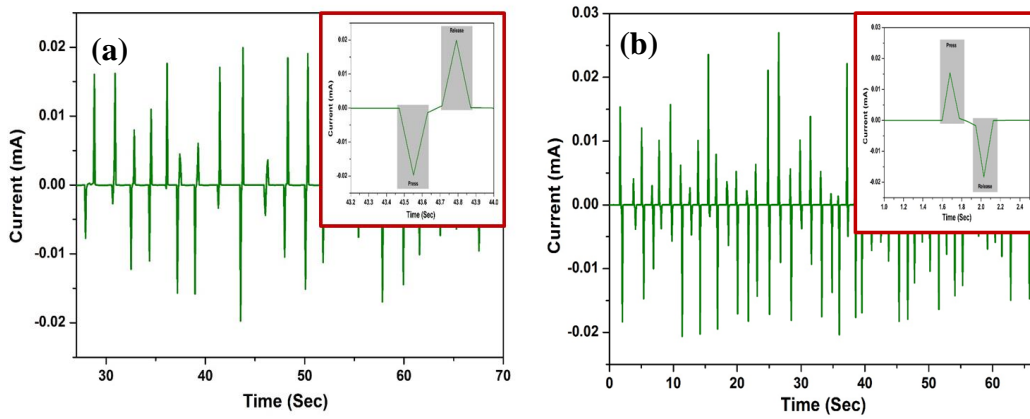


Figure 6.1.1 The measured electrical output performance of the commercial PZT film based nanogenerator under continuous pressing and releasing through finger. Short circuit current under (a) forward and (b) reverse connection with measuring system. The insets show the enlarged portion of the current profile in single press and release under forward and reverse connection.

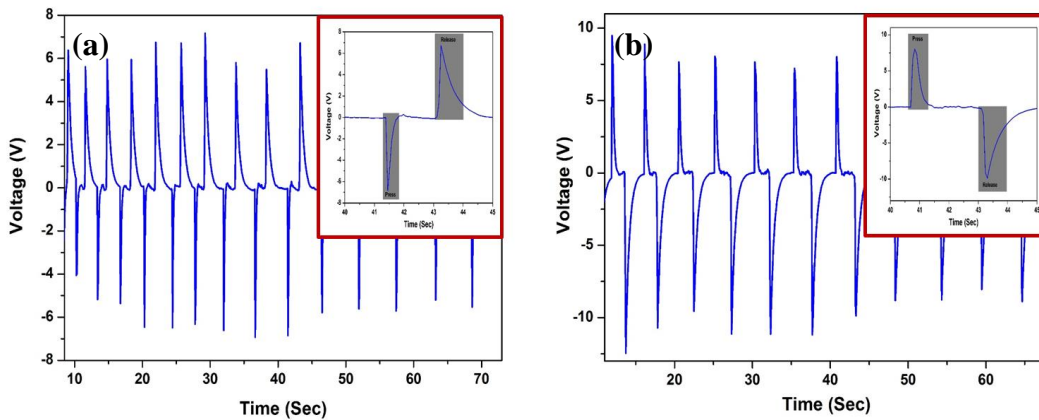
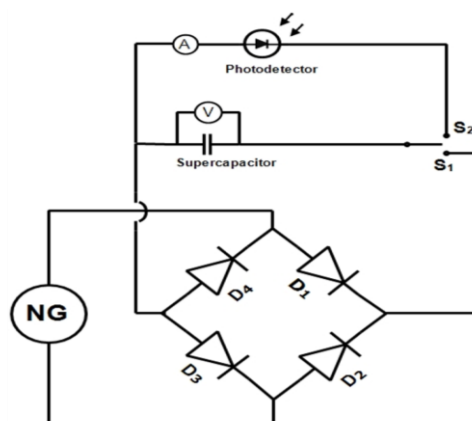


Figure 6.1.2 The measured electrical output performance of the commercial PZT film based nanogenerator under continuous pressing and releasing through finger. Open circuit voltage under (c) forward and (d) reverse connection with measuring system. The insets show the enlarged portion of the voltage profile in single press and release under forward and reverse connection.

6.4. Self-powered UV sensors



Scheme 6.1.1 Electric circuit diagram for the self-powered photosensor.

The proficiency and efficiency of the fabricated SSC (graphene, graphene-TiO₂ and graphene-V₂O₅ based supercapacitors) was demonstrated in a self-powered photosensor application where a nanogenerator and photodetector were integrated with the supercapacitor. The nanogenerator was used as a sustainable energy source to power-up the supercapacitor, which harvested the energy from vibrational and mechanical deformation. The stored energy was then used to drive the photosensor without interruption. The generated potential was rectified through a bridge rectifier and stored in the serially connected supercapacitor; the detailed schematic diagram is shown in **Scheme 6.1.1**.

6.4.1. Graphene-based all-solid state flexible supercapacitor for self-powered systems

Figure 6.1.3a shows the charging curve of the serially connected four supercapacitors. The serially connected supercapacitor was charged (0.3 V over 280 s) by the nanogenerator under continuous finger pressure. To demonstrate a self-powered application, the photodetector was connected to the supercapacitor to monitor UV light (**Figure 6.1.3b**) by closing switch S₂ and opening switch S₁.

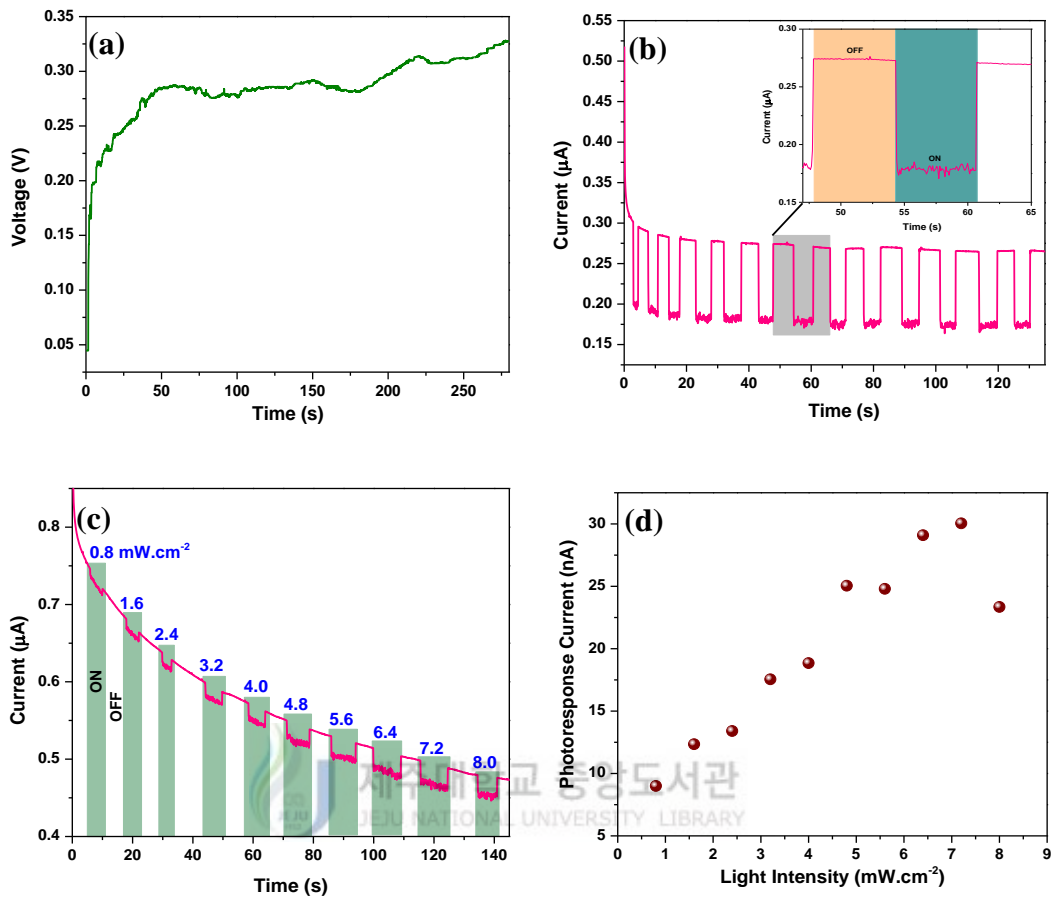


Figure 6.1.3 Demonstration of a self-powered photosensor using the supercapacitor as an energy storage device. (a) Charging of four serially connected graphene-coated fabric-based SSCs by the nanogenerator. (b) Time- dependent photoresponse for multiple ON/OFF cycles at a constant illumination intensity of 8 mW cm⁻² at λ = 365 nm. Inset shows the zoomed portion of one ON/OFF cycle. (c) Time-dependent photoresponse with different illumination intensities at λ = 365 nm. (d) Photoresponse current as a function of illumination intensity.

The supercapacitor was used as the power source to supply the appropriate current to the photodetector. The resistance of the photodetector varied linearly with the incident light intensity, which changed the discharge current. Multiple ON/OFF cycles under a constant illumination intensity of 8 mW cm⁻² at a wavelength of 365 nm were monitored to explore the stability of the photosensor with the supercapacitor. A uniform variation in current during the light illumination was observed over the entire ON/OFF cycle, providing the stable response shown in

Figure 6.1.3b. Additionally, the photoresponse was measured at 0.8 mW cm^{-2} steps for incident light intensity ranging from 0.8 to 8 mW cm^{-2} (**Figure 6.1.3c**). The photoresponse current increased linearly with increasing incident intensity (**Figure 6.1.3d**). This study suggested that the self-powered device has a huge potential in wearable and portable device applications.

6.4.2. Graphene-TiO₂ symmetric supercapacitor for self-powered systems

The charging curve of the serially connected two supercapacitors are shown in **Figure.6.1.4a**. The supercapacitor was charged to 0.27 V at 280 s by using nanogenerator under continuous finger pressure. After that, by closing switch S_2 and opening switch S_1 , the photodetector was connected to the supercapacitor to monitor UV light (demonstrating the self-powered operation). The charged supercapacitor was used as the power source to supply the appropriate current to the Photodetector to monitor the UV light. The resistance of the photodetector varied linearly with the incident light intensity, which changed the discharge current. Multiple ON/OFF cycles under a constant illumination intensity of 8 mW cm^{-2} at a wavelength of 365 nm were monitored to explore the stability of the photosensor with the supercapacitor. A uniform variation in current during the light illumination was observed over the entire ON/OFF cycle, providing the stable response shown in **Figure 6.1.4b**. Furthermore, the photoresponse was measured at various incident light intensity (**Figure 6.1.4c**). The photoresponse current increased linearly (**Figure 6.1.4d**) with increasing incident intensity, which confirming the better performance of self-powered operation.

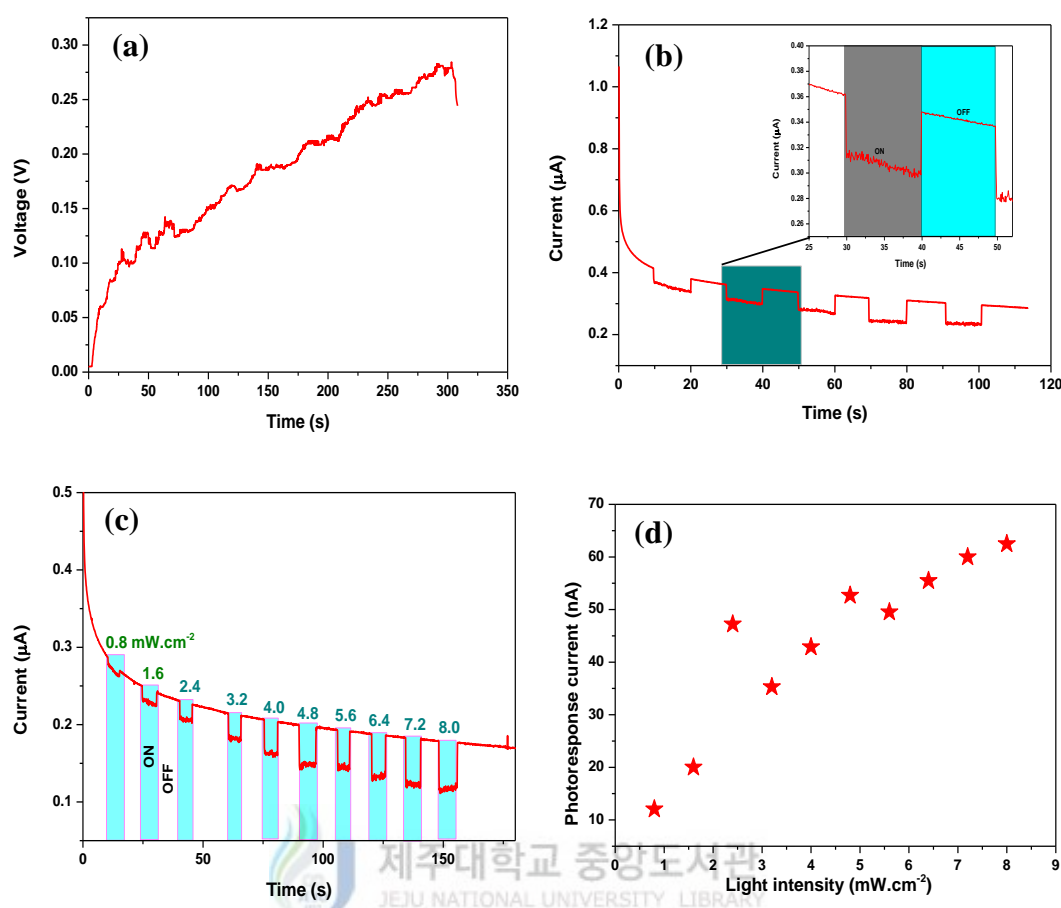


Figure 6.14 Demonstration of a self-powered photosensor using the supercapacitor as an energy storage device. (a) Charging of two serially connected graphene-TiO₂ SSCs by the nanogenerator. (b) Time- dependent photoresponse for multiple ON/OFF cycles at a constant illumination intensity of 8 mW cm⁻² at $\lambda = 365$ nm. Inset shows the zoomed portion of one ON/OFF cycle. (c) Time-dependent photoresponse with different illumination intensities at $\lambda = 365$ nm. (d) Photoresponse current as a function of illumination intensity.

6.4.3. Graphene-V₂O₅ symmetric supercapacitor for self-powered systems

By integrating with a nanogenerator, the supercapacitor could be charged and drive the commercial portable electronics. After 300 s charging under continuous pressing, the voltage of the supercapacitor increased approximately 120 mV (**Figure 6.1.5a**). The charging curve of the supercapacitor was shown in **Figure 6.1.5a**. When the compressive force was released, closing the switch S₂ and opening switch S₁ and the charged supercapacitor could drive the Photodetector to monitor UV light illumination.

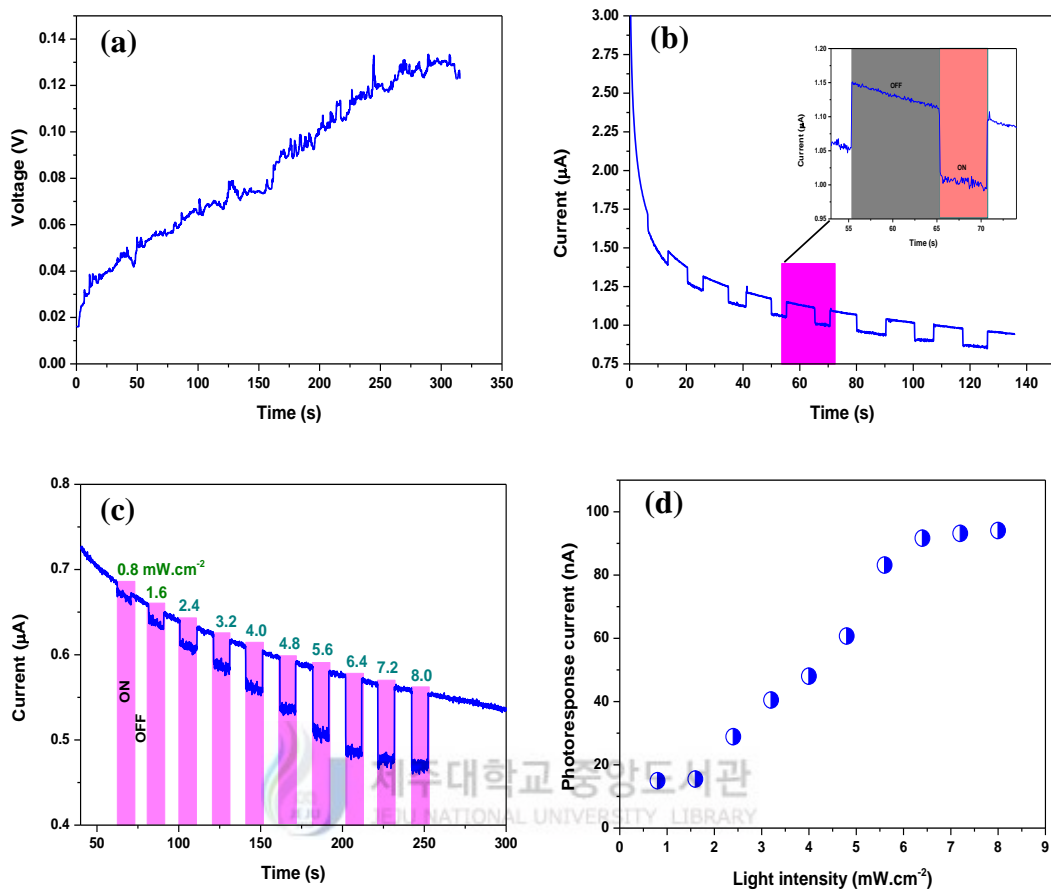


Figure 6.1.5 Demonstration of a self-powered photosensor using the supercapacitor as an energy storage device. (a) Charging of graphene- V_2O_5 SSCs by the nanogenerator. (b) Time-dependent photoresponse for multiple ON/OFF cycles at a constant illumination intensity of 8 mW cm^{-2} at $\lambda = 365 \text{ nm}$. Inset shows the zoomed portion of one ON/OFF cycle. (c) Time-dependent photoresponse with different illumination intensities at $\lambda = 365 \text{ nm}$. (d) Photoresponse current as a function of illumination intensity.

The supercapacitor was used as the power source to supply the appropriate current to the photodetector. The resistance of the Photodetector varied linearly with the incident light intensity, which changed the discharge current. The photoresponse was measured under the illumination of 8 mW cm^{-2} at wavelength of 365 nm by recording multiple ON/OFF cycles to explore the stability of the photosensor with the supercapacitor. A uniform variation in current during the light illumination was observed over the entire ON/OFF cycle, providing the stable response presented in

Figure 6.1.5b. Also, the photoresponse was measured at various incident light intensity ranging from 0.8 to 8 mW cm⁻² (**Figure 6.1.5c**). With increasing incident light intensity, the photoresponse current was increased linearly (**Figure 6.1.5d**). This results suggested that the fabricated supercapacitor device as efficient storage components and have potential applications for self-powered nanotechnology.

6.5. Conclusion

In summary, a self-powered system was demonstrated by charging the fabricated supercapacitor using a nanogenerator to power a photosensor. The various results demonstrated the feasibility of using fabricated solid state supercapacitor as efficient energy storage components and their application in self-powered devices.



6.6. References

- [1] J. F. Ihlefeld, P. G. Clem, B. L. Doyle, P. G. Kotula, K. R. Fenton, and C. A. Appleton, Fast lithium-ion conducting thin-film electrolytes integrated directly on flexible substrates for high-power solid-state batteries. *Adv. Mater.* 23 (2011) 5663–5667.
- [2] D. J. Lipomi, M. Vosgueritchian, B. C. Tee, S. L. Hellstrom, J. A. Lee, C. H. Fox, and Z. Bao, Skin-like pressure and strain sensors based on transparent elastic films of carbon nanotubes. *Nat. Nanotechnol.* 6 (2011) 788–792.
- [3] X. Zhang, L. Gong, K. Liu, Y. Cao, X. Xiao, W. Sun, X. Hu, Y. Gao, J. Chen, J. Zhou, and Z. L. Wang, Tungsten oxide nanowires grown on carbon cloth as a flexible cold cathode. *Adv. Mater.* 22 (2010) 5292–5296.
- [4] L. Yuan, X. Xiao, T. Ding, J. Zhong, X. Zhang, Y. Shen, B. Hu, Y. Huang, J. Zhou, and Z. L. Wang, Paper-based supercapacitors for self-powered nanosystems. *Angew. Chem. Int. Edit.* 5 (2012) 4934–4938.
- [5] C. Xu, C. Pan, Y. Liu, and Z. L. Wang, Hybrid cells for simultaneously harvesting multi-type energies for self-powered micro/nanosystems. *Nano Energy*, 1(2) (2012) 259–272.
- [6] L. G. H. Staaf, P. Lundgren, and P. Enoksson, Present and future supercapacitor carbon electrode materials for improved energy storage used in intelligent wireless sensor systems. *Nano Energy*, 9 (2014) 128–141.
- [7] B. Tian, X. Zheng, T. J. Kempa, Y. Fang, N. Yu, G. Yu, J. Huang, and C. M. Lieber, Coaxial silicon nanowires as solar cells and nanoelectronic power sources. *Nature* 449 (2007) 885–888.

- [8] B. Poudel, Q. Hao, Y. Ma, Y. Lan, A. Minnich, B. Yu, X. Yan, D. Wang, A. Muto, D. Vashaee, X. Chen, J. Liu, M. S. Dresselhaus, G. Chen, and Z. Ren, High-thermoelectric performance of nanostructured bismuth antimony telluride bulk alloys. *Science* 320 (2008) 634–638.
- [9] Z. Shao, S. M. Haile, J. Ahn, P. D. Ronney, Z. Zhan, and S. A. Barnett, A thermally self-sustained micro solid-oxide fuel-cell stack with high power density. *Nature* 435 (2005) 795–798.
- [10] Z. L. Wang, and J. H. Song, Piezoelectric nanogenerators based on zinc oxide nanowire arrays. *Science* 312 (2006) 242–246.
- [11] R. S. Yang, Y. Qin, L. M. Dai and Z. L. Wang, Power generation with laterally packaged piezoelectric fine wires. *Nat. Nanotechnol.* 4 (2009) 34-39.
- [12] B. Saravanakumar, R. Mohan, K. Thiyagarajan and S. J. Kim, Fabrication of a ZnO nanogenerator for eco-friendly biomechanical energy harvesting. *RSC Advances*, 3 (2013) 16646-16656.
- [13] Z. L. Wang, Self-powered nanotech, *Scientific American*, 298 (2008) 82-87.
- [14] Z. L. Wang and W. Wu, Nanotechnology-enabled energy harvesting for self-powered micro-/nanosystems. *Angew. Chem. Int. Ed.*, 51 (2012) 11700-11721.
- [15] F. R. Fan, Z. Q. Tian and Z. L. Wang, Flexible triboelectric generator. *Nano Energy*, 1 (2012) 328-334.
- [16] Z. L. Wang, Triboelectric nanogenerators as new energy technology for self-powered systems and as active mechanical and chemical sensors. *ACS Nano*, 2013, 7, 9533-9577.

- [17] G. Wee, T. Salim, Y. M. Lam, S. G. Mhaisalkar, M. Srinivasan, Printable photo-supercapacitor using single-walled carbon nanotubes. *Energy Environ. Sci.* 4 (2011) 413–416.
- [18] C. Pan, W. Guo, L. Dong, G. Zhu, Z. L. Wang, Optical fiber- based core-shell coaxially structured hybrid cells for self-powered nanosystems. *Adv. Mater.* 24 (2012) 3356– 3361.
- [19] W. Guo, X. Xue, S. Wang, C. Lin, Z. L. Wang, An integrated power pack of dye-sensitized solar cell and Li battery based on double-sided TiO₂ nanotube arrays. *Nano Lett.* 12 (2012) 2520–2523.



CHAPTER-VII

Self-Charging Supercapacitor Power Cell: Energy Conversion and Storage

A rapidly developing worldwide economy has triggered serious global warming and the lack of fossil fuels, which possess significant threats to the survival and development of mankind [1-4]. To address these issues, scientists and engineers have been conducting intense research efforts into the design and fabrication of efficient energy conversion and storage devices to exploit sustainable and clean energy [1]. Usually, energy harvesting and storage are two different processes, which performed through two different techniques and separated physical units [5-8].

Among the conversion methods, nanogenerator is an effective device tool to harvest the low frequency mechanical energy through piezoelectric and tribo-electrification processes [9-15]. On the other hand, the electrochemical capacitors (ECs) or supercapacitors are considered to be one of the most important next-generation energy storage devices, mainly due to their high power density, fast charge-discharge rates and long life times than rechargeable batteries and conventional dielectric capacitors [16-18]. Such a device can be used as a primary power storage source or auxiliary power storage source with rechargeable batteries in electric vehicles and other electronic devices for the purpose of power enhancement. Different types of energy conversion and storage devices are available in the market. Researchers are trying to develop a new hybrid system by integrating the energy harvesting device along with a storage device to perform a self-powered operation. The integrated hybrid device converts mechanical energy into electrical energy and then electrical energy into an electrochemical energy. Recently, a new concept of

self-charging power cell was introduced [19-23], in which the mechanical energy is directly converted into the electrochemical energy via piezoelectric effect, that are directly stored in Li-ion battery.

7.1. Symmetric Supercapacitor Based on MnO₂ with PVDF-ZnO Separator

7.1.1. Introduction

This section describes the fabrication and self-charging performance of Self-Charging Supercapacitor Power Cell (SCSPC) device using PVDF-ZnO as a piezoelectric as well as a separator and electrochemically active manganese oxide (MnO₂) nanowires as positive and negative electrodes, respectively. Among the various metal oxides, MnO₂ exhibits intriguing properties such as high theoretical specific capacitance (~1400 F g⁻¹), low cost and environmental friendliness, suggesting it as promising electrode materials for supercapacitors [24-28]. Here for the first time, fabricated and demonstrated the self-charging behavior of supercapacitor. The fabrication and working mechanism of a SCSPC was discussed in detail.

7.1.2. Experiment details

7.1.2.1. Synthesis of MnO₂ nanowires

In a typical synthesis, 4 g of potassium permanganate (KMnO₄) was dissolved in 80 ml of deionized water under constant stirring for 30 min. While stirring, 2 g of Ammonium persulfate ((NH₄)₂S₂O₈) and 1 ml of nitric acid (HNO₃) were added to above solution and stirred for another 30 min. The resultant solution was then transferred to a 100 ml sealed Teflon-line stainless steel autoclave and maintained at 180 °C for 15 h. After that, the autoclave was naturally cooled to room

temperature and the obtained product was centrifuged sequentially with deionized water and ethanol several times at 7000 rpm for 5 min and then the resulting products was dried in an oven at 80 °C for 10 h.

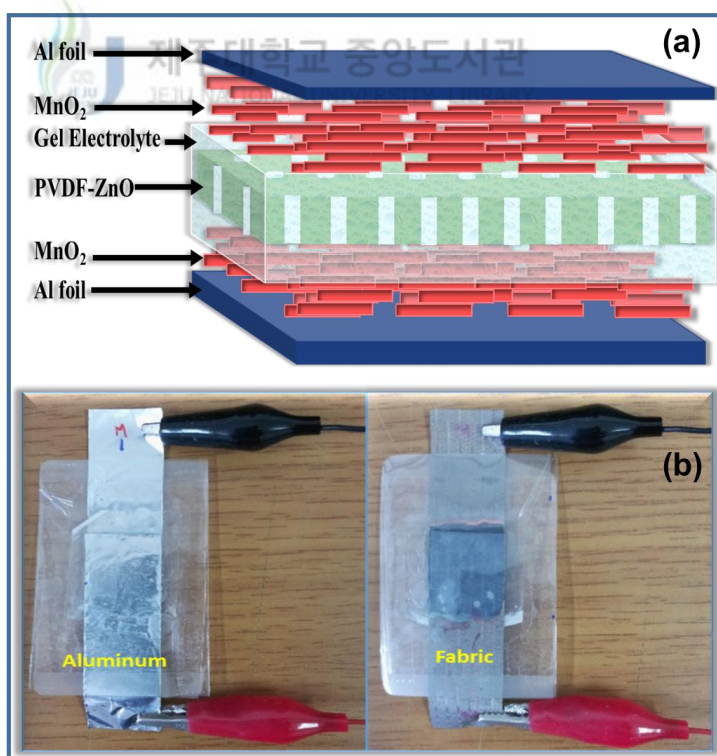
7.1.2.2. Fabrication of a self-charging supercapacitor power cell (SCSPC)

The working electrodes (MnO_2) were prepared by mixing 80 wt.% of active materials, 10 wt.% of carbon black and 10 wt.% of polyvinylidene difluoride (PVDF), in N-methyl pyrrolidinone (NMP), and this slurry was pasted on aluminium foil as well as conductive fabric and then heat treated at 100 °C under vacuum overnight. Then the SCSPC was assembled by a two piece of MnO_2 (positive and negative) electrodes on aluminium foil with PVA/ H_3PO_4 gel electrolyte separator (PVDF-ZnO) in a middle. The assembled power cell was further dried at room temperature for 12 h. Here, PVDF-ZnO acts as a separator as well as a power source (piezoelectric effect). The PVDF-ZnO film separator was prepared by a solution-casting method in a ratio of 1:0.1 (PVDF:ZnO) in Dimethylformamide (DMF). The PVA/ H_3PO_4 gel electrolyte was prepared by mixing 3 g of polyvinyl alcohol (PVA) in 30 mL deionized water at 95 °C with stirring. After, the PVA was completely dissolved, 3 g of phosphoric acid (H_3PO_4) was added into the PVA solution under vigorous stirring until it formed a homogeneous sticky solution. Then the solution was cooled at room temperature and the solution became a clear and transparent gel. Prior to assembling, the electrodes and the separator were immersed in PVA/ H_3PO_4 gel electrolyte for 5 min and then assembled one by one and kept at room temperature for 12 h to vaporize the excess water present in the electrolyte. The structure of the samples was characterized by a XRD, FT-IR and Raman analysis. The morphology of the samples was investigated using FE-SEM. The

electrochemical and self-charging performance of the as-prepared electrodes was investigated using an AUTOLAB PGSTAT302N electrochemical work station.

7.1.3. Results and discussion

The fabricated SCSPC was schematically represented in **Scheme 7.1.1a**. The device consists of three components: a positive electrode, a separator and a negative electrode. The MnO_2 nanowires/conductive carbon/binder mixtures on aluminum foil used as the positive and negative electrodes. The PVDF-ZnO film used as a separator (as well as a piezoelectric) instead of a conventional separator. Further, **Scheme 7.1.1b** shows the digital images of fabricated SCSPC (Aluminum foil and fabric). The basic characteristics of the separator and electrode materials are discussed below.



Scheme 7.1.1 (a) Schematic diagram of the fabricated SCSPC. (b) The digital images of SCSPC based on aluminum foil and conductive fabric.

7.1.3.1. Characterization of piezoelectric materials (separator as well as power source)

The FT-IR spectrum (**Figure 7.1.1a**) confirmed the presence of the β -phase of PVDF at 512, 606, 838, and 1282 cm^{-2} , and ZnO stretching vibration mode peaks at 518 and 420 cm^{-1} ; the remaining peaks were related to other phases of PVDF [29]. **Figure 7.1.1b** displays the FE-SEM image of the PVDF-ZnO separator, which confirms the homogeneous distribution of ZnO nanowires in crystalline superulites of the PVDF matrix.

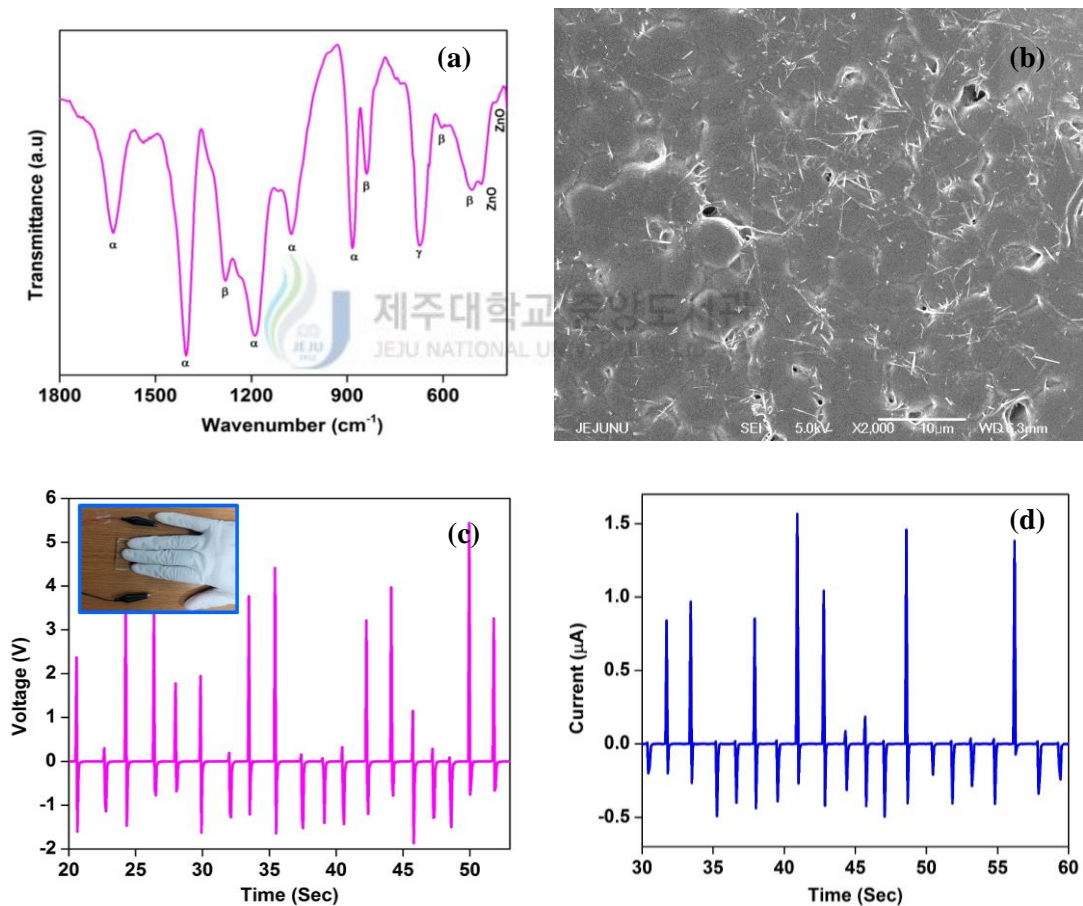


Figure 7.1.1 (a) FT-IR spectrum and (b) FE-SEM image of PVDF-ZnO separator. The β phase of PVDF and ZnO stretching vibrations are indexed. Open circuit voltage (b), and short-circuit current (c) generated in PVDF-ZnO separator. The inset shows the digital image of fabricated PVDF-ZnO nanogenerator device.

Further, the nanogenerator (Energy harvesting) device was fabricated using PVDF-ZnO film with Au as top and bottom electrodes. Under the mechanical deformation, the piezoelectric potential was generated on the surface of PVDF-ZnO film due to the polarization of PVDF as well as ZnO. The generated output voltage was represented in **Figure 7.1.1c**. To compensate the piezopotential, a transient flow of free electron in an external circuit [30] as shown in **Figure 7.1.1d**. The inset of **Figure 7.1.1c** shows the fabricated PVDF-ZnO nanogenerator device. The presence of ZnO nanowires in the PVDF matrix induces the polarization of ions in the composite film without electrical poling [31]. From these results, we concluded that our separator can generate piezopotential in the fabricated SCSPC.

7.1.3.2. Characterization of electrode materials

The morphology and structure of as-synthesized MnO₂ nanowires were characterized by FE-SEM, XRD, and Raman observations. The high magnification FE-SEM images of MnO₂ nanowires are shown in **Figure 7.1.2a**. FE-SEM image revealed that the as-synthesized MnO₂ products are composed of uniform and smooth nanowires with diameters of 40 - 60 nm and lengths up to several micrometers. The crystal phase and crystallinity of the as-prepared MnO₂ nanowires were analyzed by X-ray diffraction and is shown in **Figure 7.1.2b**. All of the diffraction peaks are in consistent with the tetragonal phase of MnO₂; it was confirmed by comparing with the standard data file JCPDS no. 44-0141. No impurity peaks are observed, indicating the high-purity of the as-prepared products. Moreover, the strong diffraction peaks indicate that the MnO₂ nanowires are well-crystallized.

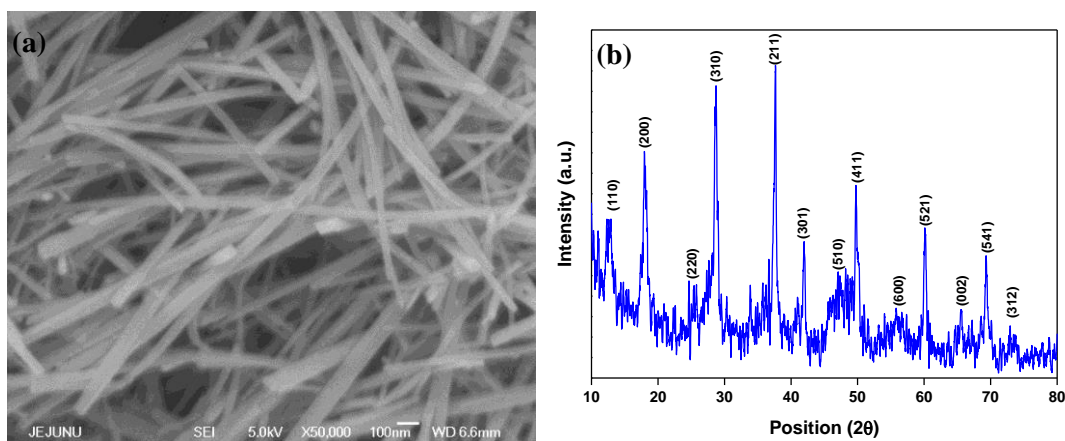


Figure 7.1.2 (a) FE-SEM image of MnO₂ nanostructure. (b) XRD spectrum of MnO₂ nanowires.

The electrochemical behavior of the MnO₂ electrode in three electrode system was evaluated by cyclic voltammetry (CV), galvanostatic charge-discharge (GCD) and electrochemical impedance spectroscopy (EIS) tests. The capacitive performance of MnO₂ electrode was studied by CV analysis at various scan rates is shown in **Figure 7.1.3a**. No peaks are observed, indicating that the as-prepared electrode is charged and discharged at a pseudo-constant rate over the complete voltammetric cycle. In addition, the shape of the CV curves maintained a relatively rectangular and symmetric shape with only a slight distortion by increasing the scan rates from 5 to 125 mV s⁻¹, implying that the excellent capacitance behavior and fast diffusion of electrolyte ions toward the MnO₂ electrode. The calculated specific capacitance value of the MnO₂ electrode is 146 F g⁻¹ at a scan rate of 5 mV s⁻¹, respectively. It can be observed that the specific capacitance of the electrode decreases (**Figure 7.1.3b**) with an increase of scan rate from 5 to 125 mV s⁻¹. This is a common phenomenon which is caused by the insufficient time for ion diffusion and adsorption inside the smallest pores within large particles due to the diffusion limit at a high scan rate.

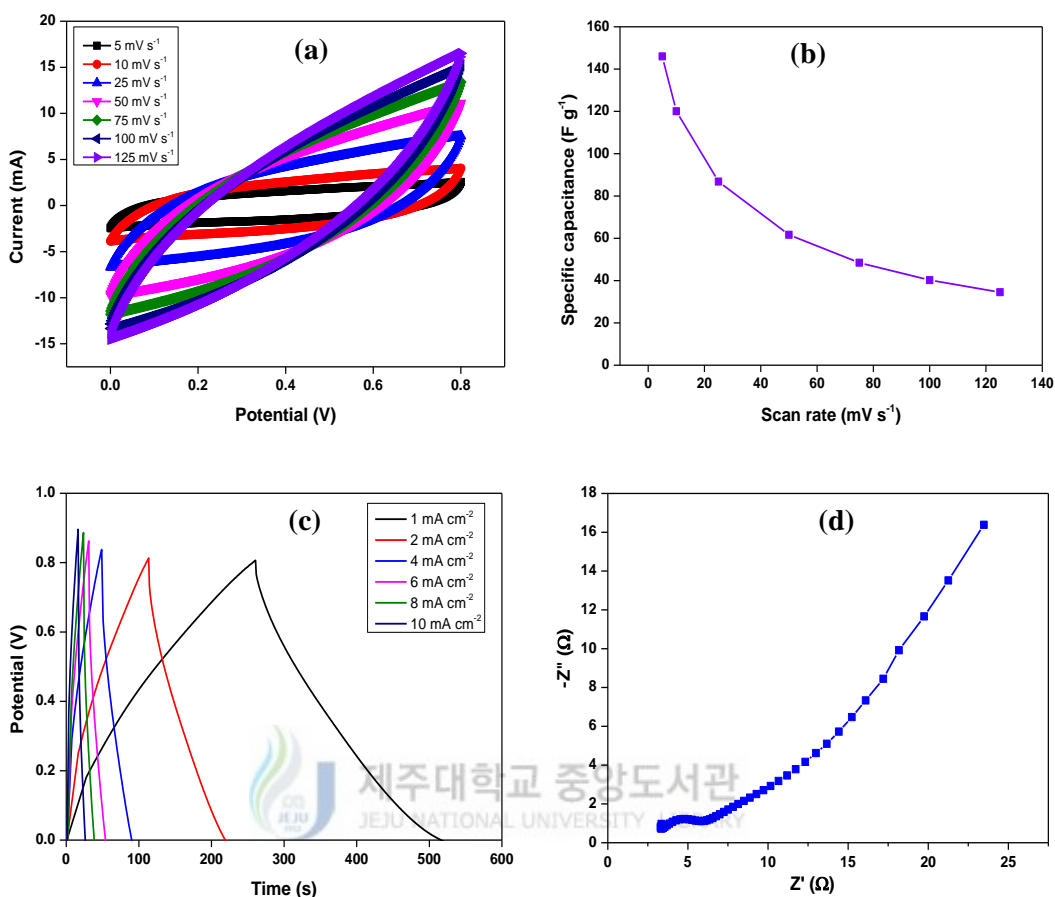


Figure 7.1.3 Electrochemical performance of MnO₂ electrode in three electrode system: (a) Cyclic voltammograms of MnO₂ electrode at different scan rates. (b) Relationship between the specific capacitance and scan rates of cyclic voltammograms tests. (c) Galvanostatic charge/discharge curves of MnO₂ electrode at different current densities in 1 M Na₂SO₄ aqueous electrolyte solution. (d) Nyquist plot of MnO₂ electrode.

The galvanostatic charge/discharge curves of MnO₂ electrode obtained in the potential window of 0 to 0.8 V at different current densities are shown in **Figure 7.1.3c**. From the figure, it can be seen that all of the curves are a linear, symmetric and almost triangles in shape with slight curvature, suggesting that the electrodes have good capacitive characteristics. The calculated specific capacitance of MnO₂ electrode is found to be 72, 59, 46, 41, 34 and 29 F g⁻¹, at a current density of 1, 2, 4, 6, 8 and 10 mA cm⁻², respectively. EIS measurement was performed for MnO₂

electrode (**Figure 7.1.3d**) to further understand the electrochemical behavior. A smaller semicircle arc in the high-frequency region was observed, demonstrating its lower interfacial charge-transfer resistance between electrode and electrolyte. Further, the linear line (Warburg line) at the low-frequency region indicating a decreased diffusion resistance of the electrolyte ions in the electrode, as expected for supercapacitor.

7.1.3.3. Electrochemical behavior of the self-charging supercapacitor power cell

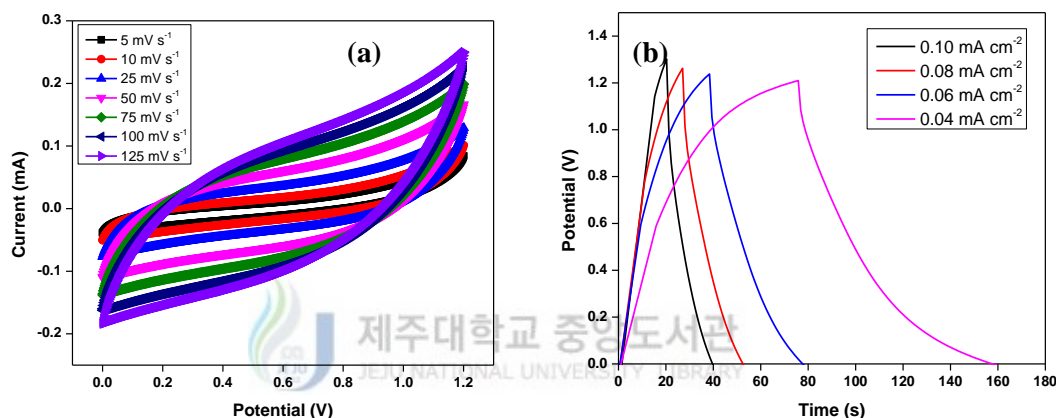


Figure 7.1.4 Electrochemical performance of SCSPC device in PVA/H₃PO₄ gel electrolytes: (a) Cyclic voltammetry scans of SCSPC at different scan rates. (b) Galvanostatic charge/discharge curves of SCSPC at different current densities.

The supercapacitor behavior of the as-prepared SCSPC (PVDF-ZnO film separator) was investigated by the CV and GCD measurements. The CV scans of the fabricated SCSPC (PVDF-ZnO film separator) at a potential window of 0 to 1.2 V are shown in **Figure 7.1.4a**. These CV curves exhibit rectangular like shapes indicating the ideal capacitive behavior. The GCD curves of the SCSPC at different current densities exhibit the linear and symmetric behavior indicating the capacitive and fast charge/discharge property (**Figure 7.1.4b**). The specific capacitance of the SCSPC device was 455 mF g⁻¹ at 0.04 mA cm⁻². The suitability of this SCSPC device for supercapacitor applications was further estimated by examining its power

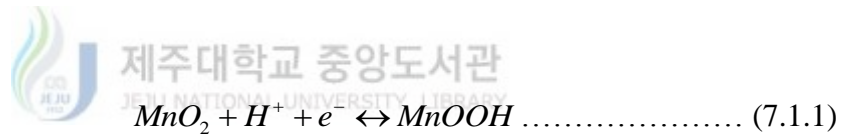
and energy densities. The power and energy densities were calculated using Equations 4 and 5 and the charge/discharge curves at different current densities. The energy density of the SCSPC reached 91 mW h kg^{-1} at a power density of 3.9 kW kg^{-1} and sustained 58 mW h kg^{-1} at a power density of 9.9 kW kg^{-1} . This result confirmed that the as-fabricated devices had a good charge storage behavior.

7.1.3.4. Mechanism of self-charging supercapacitor power cell

The working mechanism of the self-charging supercapacitor power cell (SCSPC) is based on piezoelectric-potential driven electrochemical oxidation and reduction reaction (faradaic reaction) [19,20]. The fabricated SCSPC (**Figure 7.1.5**) consists of piezoelectric material (PVDF-ZnO film) as a separator as well as a potential generator, MnO_2 nanowire as positive and negative electrodes for the electrochemical reaction and PVA/ H_3PO_4 as the electrolyte, which is uniformly distributed through the entire surface of the separator and the surface of the electro-active materials. At the beginning, the device is at the discharge state (**Figure 7.1.5a**), in which, there is no electrochemical reaction due to the electrochemical equilibrium between the electrolyte and electrodes (active material). At this stage, there is no external deformation applied to the device. When a compressive stress was applied to the device by means of palm impact from the top side of the device (**Figure 7.1.5b**), which causes the polarization of PVDF film by the piezoelectric effect [19]. The polarization of ions generates a potential difference across the thickness of the separator (PVDF-ZnO). Suppose a positive and negative piezoelectric potential was generated at the top and the bottom side of the film, driving the electrolytic ions (PVA/ H_3PO_4) towards the positive and negative electrodes. The piezoelectric field induced cationic (H^+) movement in the electrolyte

to screen the generated piezo-potential across the separator (ionic conduction path represents in **Figure 7.1.5b**). This ionic movement induces an electrochemical imbalance in the electrolyte and the positive and negative electrode sides. To obtain chemical equilibrium, the oxidation and reduction reaction (faradaic) occur at the surfaces of the positive and negative electrodes (**Figure 7.1.5c**), respectively.

The migration of H⁺ ions from the electrolyte towards negative electrode, leads to the reduction reaction in (MnO₂)_{surface} through H⁺ ions insertion (without disruption of the oxide lattice) and builds the positive charges at the negative electrode (Al foil). Meanwhile, the oxidation reaction occurs at the positive electrode through the H⁺ ion desertion, which leaves free electrons to the current collector at the positive electrode side (Al foil). The electrochemical reaction can be expressed as follows [25];



The liberated electrons are transported to the negative electrode to maintain the charge neutrality as well as the continuity of charging process. There are two possibilities for the electron transfer; one is inside the SCSPC and another is through the external circuit via monitoring system (Electrochemical workstation) [19,20]. In order to verify the electron flow in the SCSPC, we have directly measured the stored voltage through multimeter before and after compression without any external circuit/monitoring system. The open circuit voltage was found to increase under repeated compression, clearly indicating the self-charging process of SCSPC. From this study, we concluded that the electron may flow through inside the device. The detailed mechanisms of electron flow inside the SCSPC are still under debate. In

such SCSPC, the charging process involves cations insertion into the negative electrode surface and desorption onto the positive electrode surface.

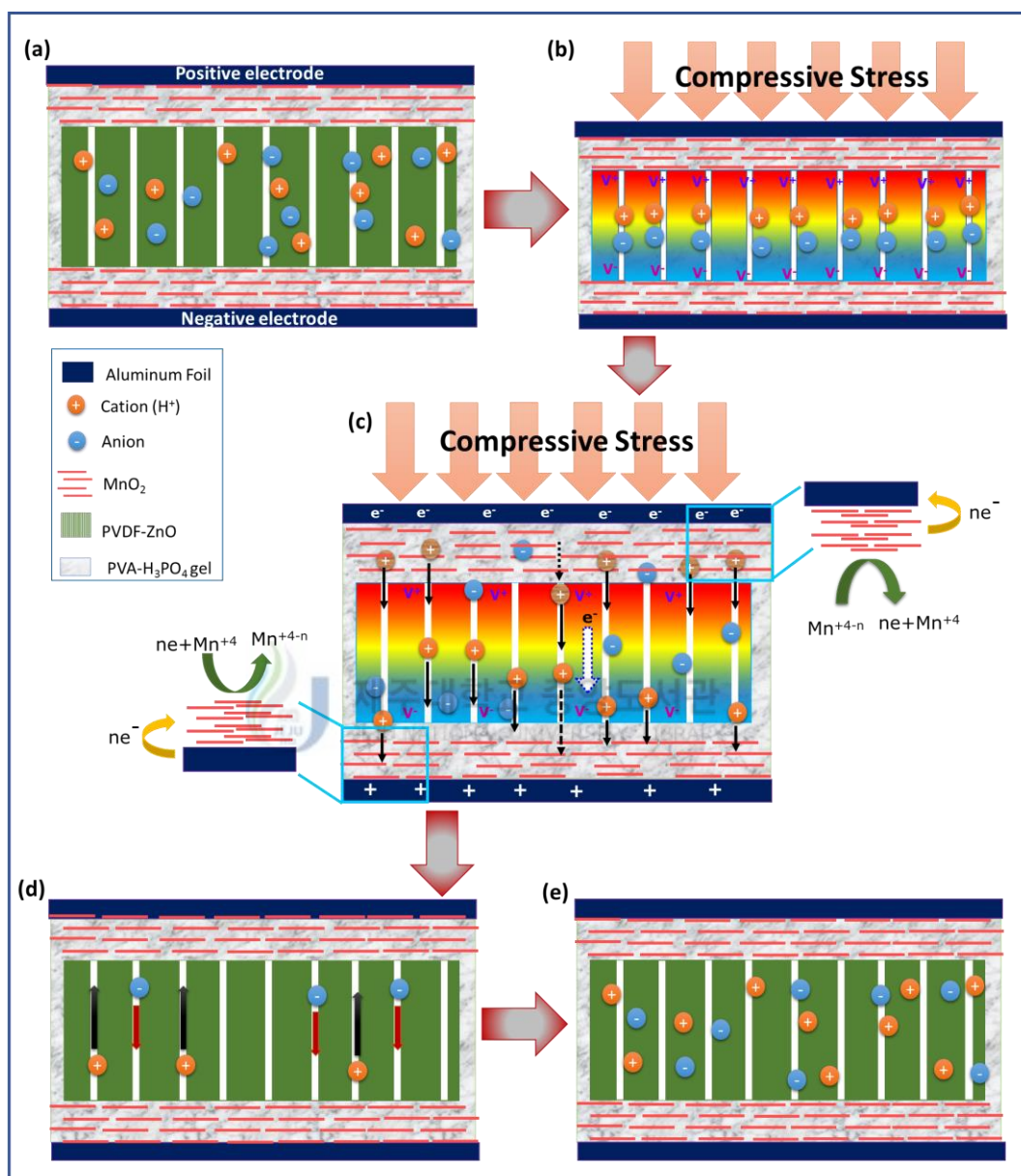


Figure 7.1.5 Working mechanism of the Self-Charging Supercapacitor Power Cell (SCSPC) driven by mechanical deformation. (a) Schematic diagram of the fabricated SCSPC at discharge condition. The MnO_2 on aluminum foil are used as the positive and negative electrodes; PVDF-ZnO film as a separator. (b) The mechanical deformation is applied on the top of the device; it creates a piezoelectric field (potential) in the PVDF-ZnO separator film. (c) Under the piezoelectric field, the H^+ ions will migrate through PVDF-ZnO separator in the electrolyte to the negative electrode, leading to the corresponding charging reactions at the two electrodes. (d) When external deformation is released, there is no piezoelectric field at the separator which breaks the attained chemical equilibrium; it causes a reverse reaction on both sides of the electrode, and ions are relocated into original position. (e) Completed self-charging cycle

Under continuous compression force, the charging process was repeated until to attain chemical equilibrium of two electrodes with piezoelectric potential; at this point, there is no further ionic polarization in the device. This is the process of converting mechanical energy directly into electrochemical energy. When removing the compression force, piezoelectric potential disappeared in the PVDF film (**Figure 7.1.5d**); it breaks the electrochemical equilibrium of the device. To compensate, a small amount of ions will move back, indicating the completion of charging cycle (**Figure 7.1.5e**). When a charging cycle is completed through the electrochemical reaction, a small of oxidation and reduction occurred at the positive and negative electrode surfaces. The continuing applied force to the device, the charging cycle is repeated as such which results conversion of mechanical energy directly into electrochemical energy. From the above discussion, it could be argued that there are three main processes occur in self-charging process; the generation of piezoelectric potential on PVDF-ZnO film by palm impact, the migration of ions towards electrodes through ionic conduction path, and the reduction (negative electrode) and oxidation (positive electrode) reactions occurred at MnO_2 via insertion/desertion of H^+ ions.

The self-charging mechanism can be also explained by using Nernst equation which shows the relationship between electrode potentials and H^+ concentration [19, 22]. When the piezoelectric field is formed by external compression, H^+ ions migrate from the positive (i.e., MnO_2 in oxidation process) to the negative (i.e., MnO_2 in the reduction process) electrode. As a consequence, the concentration of H^+ on the oxidative electrode decreases and the increase in H^+ concentration on the reductive electrode is simultaneously constructed. As this change of H^+ concentration

electrochemically creates the potential of the negative electrode to be larger than that of the positive electrode, the device is finally self-charged by the change of redox potential through the concentration gradient of H^+ ions.

7.1.3.5. Self-charging performance of as-fabricated SCSPC

To show the self-charging capability of the SCSPC (Aluminum foil), we have performed the self-charging process under continuous palm impact for 300 s, which is shown in **Figure 7.1.6a**. When a compressive force applied to SCSPC, the voltage of the device increased from 35 to 145 mV (110 mV charged) in 300 s. After removing the compression force, the stored energy was sustained around 150 s, and then again giving deformation to device, the voltage starts to increases (see Fig.5a.). This concludes that our SCSPC has the ability to self-charge under mechanical deformation/vibration. The device showed slight decrease in voltage at the initial ~25 s and then started to increase in voltage under continuous force. This may be attributed to the random movement of ions in the electrolyte solution under external force. At the initial stage, the device becomes un-equilibrium state (voltage decreases; discharging) due to the sudden force applied to the device. After continuous palm impact the device attain chemical equilibrium at the both electrode sides (faradaic reaction was take place at the electrode material surface) and starts to increase the device voltage (charging) after ~25 s.

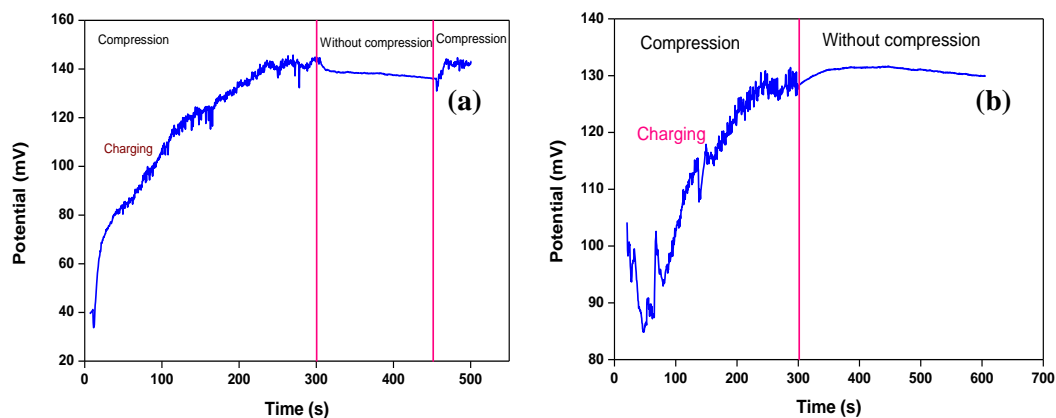


Figure 7.1.6 Self-charging performance of SCSPC monitored using electrochemical work station under periodic compressive straining: (a) The self-charging process of the SCSPC by human palm impact. During vibration the voltage keeps raising, indicating that the charging process is occurred due to the migration of the ions. (b) The self-charging process of the fabric based SCSPC.

To demonstrate the flexible, light-weight and wearable based self-powered device applications, we have fabricated and tested the self-charging process of the fabric based SCSPC under continuous palm impact for 300 s. **Figure 7.1.6b** represents the self-charging process of the fabric based SCSPC using PVDF-ZnO separator films. Under continuous vibration, fabric based SCSPC showed the increase in voltage (charging) from 85 to 130 mV (45 mV charged) in 300 s. After removing deformation, the device showed the increase in voltage for 50 s and then sustained the stored voltage for 250 s, which confirm the self-charging capability of the as-fabricated fabric based SCSPC. The increase in voltage was observed after deformation, which may be due to the vibration continued for few seconds after deformation, and the light-weight of the fabricated fabric based SCSPC. Both the devices showed the increased in voltage (charging) under the continuous force, confirming the self-charging performance of the SCSPC.

The self-charging performance of the device mainly depends on applied compressive force. To verify that, we have studied the self-charging performance of

SCSPC under various compressive force condition. Varied compressive force of approximately 9.8, 12.2, 14.9 and 18.8 N was applied through human hand (using metal cylinder). **Figure 7.1.7a** shows the self-charging and discharging cycles under different compressive stress. When increasing the applying force to SCSPC, the self-charging result would be enhanced. The enhancement in self-charging process is due to the increase in piezopotential with the higher applied strain (compressive force). After the self-charging process, the device was discharged back to its original voltage under a constant discharge current of 1 μ A. These results confirmed that the self-charging process is due to the piezoelectric effect. Besides, we have checked the self-charging process of SCSPC connected to opposite sign (polarity change), which is displayed in **Figure 7.1.7b**. Under vibration, the voltage of the device increased from 105 to 140 mV at negative direction in 300 s. After deformation, the device sustained the stored energy for 100 s. This also confirms the self-charging performance of the SCSPC.

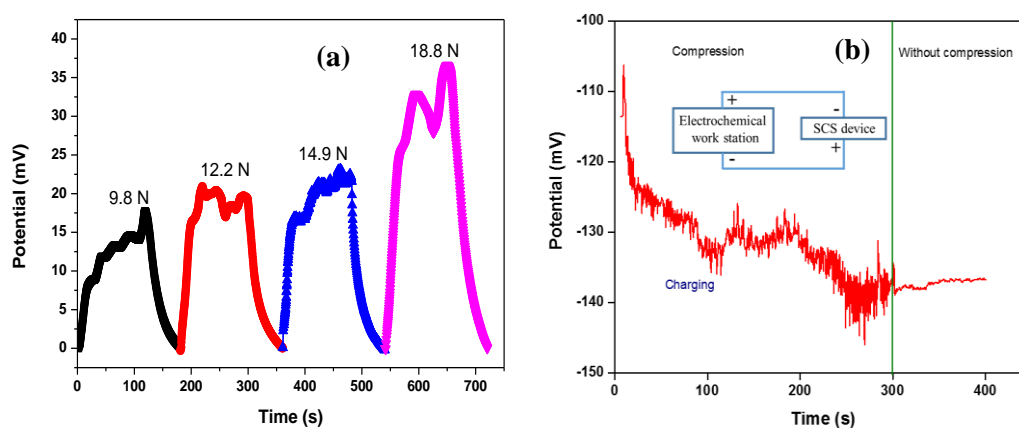


Figure 7.1.7 Self-charging and discharge cycles of SCSPC under different forces (9.8, 12.2, 14.9, and 18.8 N). (b) At force applied to the bottom side of the SCSPC. When the compressive force applied to the opposite side (bottom side) of SCSPC, the stored voltage was decreased (discharge) due to generation of opposite potential in separator.

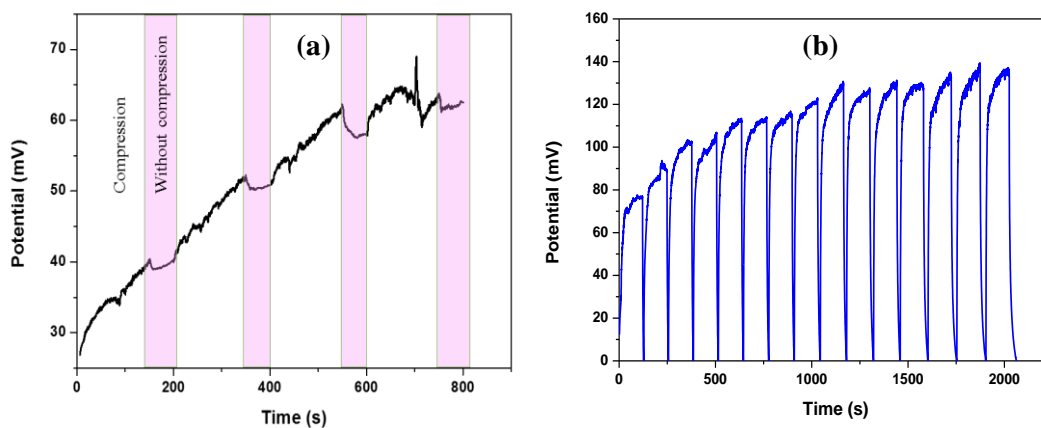


Figure 7.1.8 (a) Cycling performance of the SCSPC under compressive force. (b) Self-charging and discharging cycles of the SCSPC via periodic deformation. The discharge current is $10 \mu\text{A}$.

The cycling performance of the fabricated SCSPC was performed under a compressive force. As shown in **Figure 7.1.8a**, the voltage of the device increased (self-charging) under the compressive force ($\sim 9.8 \text{ N}$) applied to the device for 150s. After the self-charging process, the device sustained the charged voltage (highlighted in magenta color) for 50s. Approximately, the SCSPC stored 15 mV in 150s under compressive force. When repeating the compressive force, the device starts to self-charging, confirm the repeatability (cycling performance) of the fabricated device. Further, **Figure 7.1.8b** shows the self-charging process and the discharging at a constant current of $10 \mu\text{A}$ for 15 cycles. The voltage of the device was increased under the compressive strain ($\sim 18.8 \text{ N}$ for 120s) and then the device was back to its original voltage under a constant discharge current. The average self-charge voltage of the device was 110 mV in 120s under compressive force. In addition, the specific capacitance of the SCSPC can be calculated using the discharge current, discharge time and self-charged voltage (voltage window). The calculated device capacitance was 0.2575 F g^{-1} (257 mF g^{-1}). The increasing voltage trend was observed due the variation of applying compressive force (through human hand difficult to control the

input force) and then after few cycles, the device attained stabilized state. This result confirms that the better cycling performance (repeatability) of the fabricated SCSPC.

Furthermore, the self-charging capability of the five SCSPC are connected in serially was tested under the continuous human palm impact to all devices and it is shown in **Figure 7.1.9a**. Under a continuous impact, the open circuit voltage increases from 160 to 280 mV (120 mV charged) in 350 s and then sustained the stored voltage for 250 s, even after removing the deformation. The inset of **Figure 7.1.9a** shows the photograph of the serially connected SCSPC. In addition, the compression force was applied to each to individually one by one and measured the self-charging capability, which is shown in **Figure 7.1.9b**. The inset **Figure 7.1.9b** displays the circuit diagram for the serial connections. All the devices are showing the self-charging capability, when the force was applied to the individual devices. The voltage was increased from 230 to 350 mV (120 mV) in 360 s. The self-charging process mainly depended on the piezoelectric potential generation in the separator, which is directly related to mechanical deformation.

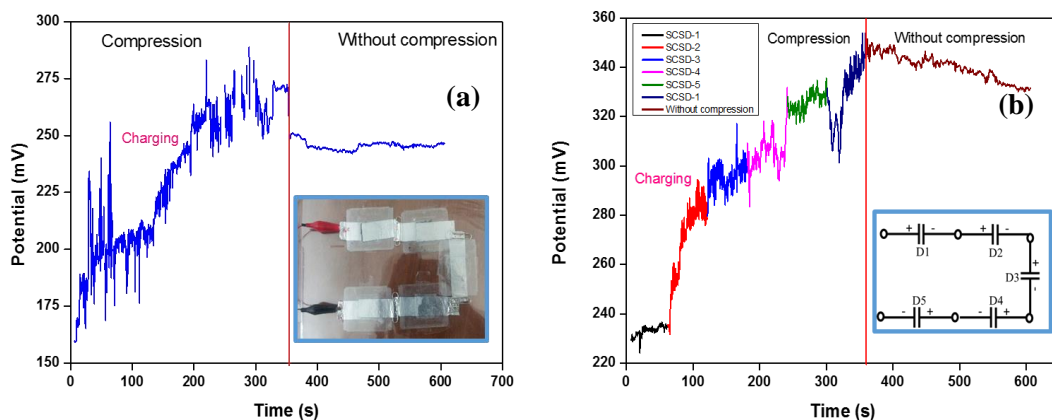


Figure 7.1.9 Self-charging performance of serially connected five SCSPC: (a) The self-charging process of the serially connected five SCSPC under periodic compressive straining given by human palm impact to the whole devices. Inset shows photograph of the serially connected SCSPC. (b) The self-charging process of the serially connected five SCSPC under periodic compressive straining given by human palm impact to the each device for 60s interval. Inset shows the circuit diagram of serial connection.

To demonstrate the potential application (self-powered devices) of these SCSPC, we have assembled eleven SCSPC in serially to drive LED. Required amount of potential was charged using SCSPC as power sources. Finally, we showed that the SCSPC can drive a green light-emitting diode (LED), as displayed in **Figure 7.1.10**. The inset of **Figure 7.1.10**. (red color border) showed the zoomed portion of the powered green LED. From the above results and discussion, we have concluded that the as-fabricated SCSPC is an initiation of new smart power electronics with self-power sources. In future, the described method can be extended for the synthesis of other carbons, oxide based electrode materials and various piezoelectric separator for self-charging supercapacitor power cell, which are currently under investigation.

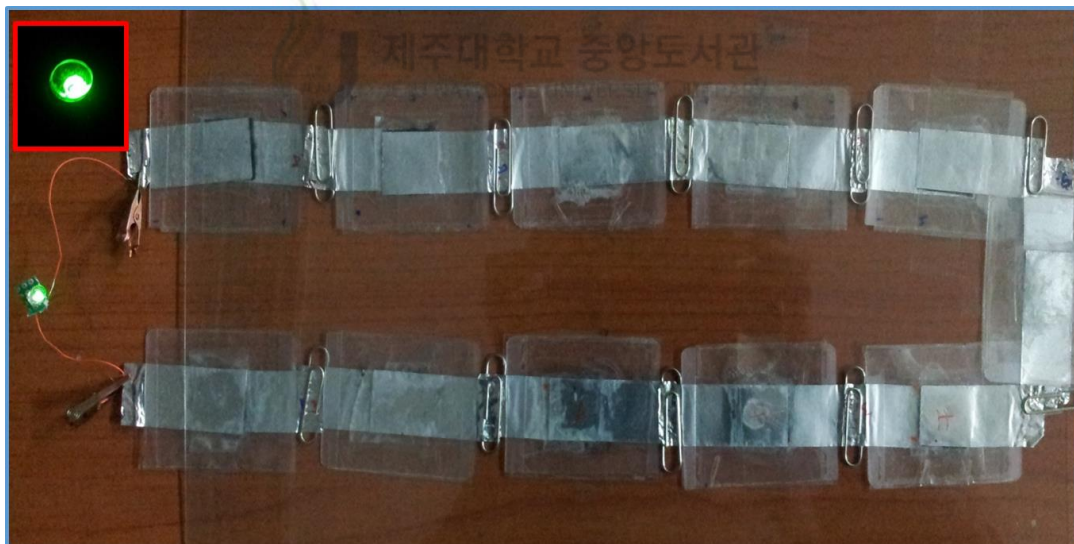


Figure 7.1.10 The operation of green LED using serially connected SCSPC as the power source.

7.1.4. Conclusion

In summary, we have successfully fabricated the first self-charging supercapacitor power cell that consists of PVDF-ZnO separator (piezoelectric nanogenerator) and MnO₂ nanowires used as the positive and negative electrodes

(supercapacitor), which can be used to simultaneously harvest and store the mechanical energy to electrochemical energy. The SCSPC exhibited the self-charging capability under palm impact (Aluminum foil based SCSPC = 110 mV for 300 s; Fabric based SCSPC = 45 mV for 300 s). Further, the green LED was operated using serially connected SCSPC as the power source. The SCSPC provide a new promising direction in the supercapacitor research for the development of next generation self-powered sustainable power source for wearable and flexible electronic devices.



7.1.5. References

- [1] X. Yu, B. Lu and Z. Xu, Super long-life supercapacitors based on the construction of nano honey comb-like strongly coupled CoMoO_4 -3D graphene hybrid electrodes. *Adv. Mater.* 26(7) (2014) 1044-1051.
- [2] H. Wang and H. Dai, Strongly coupled inorganic–nano-carbon hybrid materials for energy storage. *Chem. Soc. Rev.* 42 (2013) 3088-3113.
- [3] E. A. Rosa and T. Dietz, Human drivers of national greenhouse-gas emissions. *Nature Clim. Change* 2 (2012) 581-586.
- [4] S. Chu and A. Majumdar, Opportunities and challenges for a sustainable energy future. *Nature* 488 (2012) 294-303.
- [5] A. S. Arico, P. Bruce, B. Scrosati, J. M. Tarascon and W. Van Schalkwijk, Nanostructured materials for advanced energy conversion and storage devices. *Nat. Mater.* 4 (2005) 366-377.
- [6] J. M. Tarascon and M. Armand, Issues and challenges facing rechargeable lithium batteries. *Nature* 414 (2001) 359-367.
- [7] Z. L. Wang, Towards Self-powered nanosystems: From nanogenerators to nanopiezotronics. *Adv. Funct. Mater.* 18 (2008) 3553-3567.
- [8] Y. F. Hu, Y. Zhang, C. Xu, L. Lin, R. L. Snyder and Z. L. Wang, Self-powered system with wireless data transmission. *Nano Lett.* 11 (2011) 2572-2577.
- [9] R. S. Yang, Y. Qin, L. M. Dai and Z. L. Wang, Power generation with laterally packaged piezoelectric fine wires. *Nat. Nanotechnol.* 4 (2009) 34-39.

- [10] B. Saravanakumar, R. Mohan, K. Thiyagarajan and S. J. Kim, Fabrication of a ZnO nanogenerator for eco-friendly biomechanical energy harvesting. *RSC Advances* 3 (2013) 16646-16656.
- [11] Z. L. Wang and J. H. Song, Piezoelectric nanogenerators based on zinc oxide nanowire arrays. *Science* 312 (2006) 242-246.
- [12] Z. L. Wang, Self-powered nanotech. *Scientific American* 298 (2008) 82-87.
- [13] Z. L. Wang and W. Wu, Nanotechnology-enabled energy harvesting for self-powered micro-/nanosystems. *Angew. Chem. Int. Ed.* 51 (2012) 11700-11721.
- [14] F. R. Fan, Z. Q. Tian and Z. L. Wang, Flexible triboelectric generator. *Nano Energy* 1 (2012) 328-334.
- [15] Z. L. Wang, Triboelectric nanogenerators as new energy technology for self-powered systems and as active mechanical and chemical sensors. *ACS Nano* 7 (2013) 9533-9557.
- [16] Y. Zhu, S. Murali, M. D. Stoller, K. J. Ganesh, W. Cai, P. J. Ferreira, A. Pirkle, R. M. Wallace, K. A. Cychoz, M. Thommes, D. Su, E. A. Stach and R. S. Ruoff, Carbon-based supercapacitors produced by activation of graphene. *Science* 332 (2011) 1537-1541.
- [17] C. Liu, Z. Yu, D. Neff, A. Zhamu and B. Z. Jang, Graphene-based supercapacitor with an ultrahigh energy density. *Nano Lett.* 10 (2010) 4863-4868.
- [18] J. C. Chou, Y. L. Chen, M. H. Yang, Y. Z. Chen, C. C. Lai, H. T. Chiu, C. Y. Lee, Y. L. Chueh and J. Y. Gan, RuO₂/MnO₂ core-shell nanorods for supercapacitors. *J. Mater. Chem. A* 1 (2013) 8753-8758.

- [19] X. Xue, P. Deng, B. He, Y. Nie, L. Xing, Y. Zhang and Z. L. Wang, Flexible self-charging power cell for one-step energy conversion and storage. *Adv. Energy Mater.* 4(5) (2014) 1301329.
- [20] X. Xue, S. Wang, W. Guo, Y. Zhang and Z. L. Wang, Hybridizing energy conversion and storage in a mechanical-to-electrochemical process for self-charging power cell. *Nano Lett.* 12 (9) (2012) 5048-5054.
- [21] L. Xing, Y. Nie, X. Xue, and Y. Zhang, PVDF mesoporous nanostructures as the piezo-separator for a self-charging power cell. *Nano Energy* 10 (2014) 44-52.
- [22] X. Xue, P. Deng, S. Yuan, Y. Nie, B. He, L. Xing and Y. Zhang, CuO/PVDF nanocomposite anode for a piezo-driven self-charging lithium battery. *Energy Environ. Sci.* 6 (2013) 2615-2620.
- [23] Y. Zhang, Y. Zhang, X. Xue, C. Cui, B. He, Y. Nie, P. Deng and Z. L. Wang, PVDF–PZT nanocomposite film based self-charging power cell. *Nanotechnology* 25 (2014) 105401-105407.
- [24] C. Yuan, L. Hou, L. Yang, D. Li, L. Shen, F. Zhang and X. Zhang, Facile interfacial synthesis of flower-like hierarchical α - MnO_2 sub-microspherical superstructures constructed by two-dimension mesoporous nanosheets and their application in electrochemical capacitors. *J. Mater. Chem.* 21 (2011) 16035-16041.
- [25] P. Yu, X. Zhang, D.L. Wang, L. Wang and Y.W. Ma, Shape-controlled synthesis of 3D hierarchical MnO_2 nanostructures for electrochemical supercapacitors. *Cryst. Growth Des.* 9 (2009) 528-533.

- [26] D.Y. Sung, I.Y. Kim, T.W. Kim, M.S. Song and S.J. Hwang, Room temperature synthesis routes to the 2D nanoplates and 1D nanowires/nanorods of manganese oxides with highly stable pseudocapacitance behaviors. *J. Phys. Chem. C* 115 (2011) 13171-13179.
- [27] A. Ramadoss and S. J. Kim, Hierarchically structured TiO₂@MnO₂ nanowall arrays as potential electrode material for high-performance supercapacitors. *Int. J. Hydro. Energy* 39(23) (2014) 12201-12212.
- [28] W. Wei, X. Cui, W. Chen and D.G. Ivey, Manganese oxide-based materials as electrochemical supercapacitor electrodes. *Chem. Soc. Rev.* 40 (2011) 1697-1721.
- [29] H. Yu, T. Huang, M. Lu, M. Mao, Q. Zhang and H. Wang, Enhanced power output of an electrospun PVDF/MWCNTs-based nanogenerator by tuning its conductivity. *Nanotechnology* 24 (2013) 405401-405409.
- [30] M. Lee, C.Y. Chen, S. Wang, S. N. Cha, Y. J. Park, J. M. Kim, L.J. Chou and Z. L. Wang, A hybrid piezoelectric structure for wearable nanogenerators. *Adv. Mater.* 24(13) (2012) 1759-1764.
- [31] B. Saravanakumar, S. Soyoon and S. J. Kim, Self-powered pH sensor based on a flexible organic-inorganic hybrid composite nanogenerator. *ACS Appl. Mater. Interfaces* 6 (16) (2014) 13716-13723.

7.2. Asymmetric Supercapacitor Based on Graphene and Graphene-V₂O₅ with PVDF-ZnO Separator

7.2.1. Introduction

This chapter presents the self-charging performance of self-charging supercapacitor power cell (SCSPC) using PVDF-ZnO as a piezoelectric as well as separator and electrochemically active reduced graphene oxide (rGO) and V₂O₅ anchored graphene (G-V₂O₅) as positive and negative electrodes, respectively. Vanadium pentoxide (V₂O₅) has layered structure, low cost, ease of synthesis, higher capacity and a wide range of oxidation states varying from V²⁺ to V⁵⁺ [1-4]. Next, graphene has emerged as one of the most appealing material in various applications, including supercapacitor, batteries and optoelectronics due to its high surface area, high flexibility and better conductivity, high thermal and chemical stabilities [5-8]. The fabrication, working mechanism self-charging performance of self-charging supercapacitor power cell were discussed in detail.

7.2.2. Experiment details

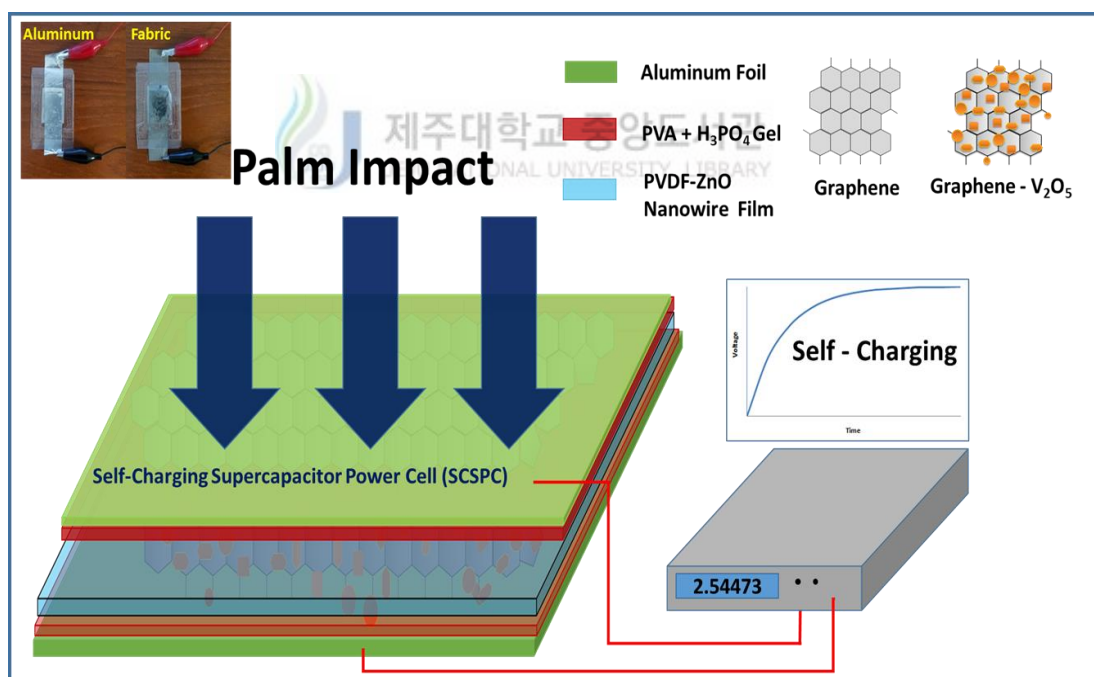
7.2.2.1. Fabrication of a self-charging supercapacitor power cell (SCSPC)

The synthesis and electrode preparation of reduced graphene oxide (rGO) and V₂O₅ anchored graphene nanosheets (G-V₂O₅) were discussed in previous **Chapter.5**. The SCSPC was assembled by a piece of G-V₂O₅ and rGO electrode on aluminium foil with PVA-H₃PO₄ electrolyte separator (PVDF-ZnO) in a middle. Here, PVDF-ZnO act as a separator as well as a power source (piezoelectric effect). The PVDF-ZnO film separator was prepared by a solution-casting method in a of ratio 1:0.1 (PVDF:ZnO) in Dimethylformamide (DMF). The electrochemical performance was investigated using an AUTOLAB PGSTAT302N electrochemical

work station. Self-charging performance of the as-fabricated SCSPC was characterized by using electrochemical workstation and Keithly Nanovoltmeter (2182A).

7.2.3. Results and discussion

The fabricated SCSPC was schematically represented in **Scheme 7.2.1**. The device consists of three components: positive electrode, separator and negative electrode. The rGO on aluminum foil used as the positive electrode and G-V₂O₅/conductive carbon/binder mixtures on aluminium foil used as the negative electrode. The PVDF-ZnO film used as a separator (as well as piezoelectric) instead of a conventional separator.



Scheme 7.2.1 Schematic representation of the self-charging supercapacitor power cell (SCSPC) structure. The rGO on aluminum foil are used as the positive electrode and G-V₂O₅ composite on aluminum foil are used as the negative electrode; PVDF-ZnO as a separator. Inset shows the photograph of the SCSPC devices based on aluminum foil and conductive fabric.

The inset in **Scheme 7.2.1** shows the photographs of the fabricated SCSPC (Aluminum foil and fabric) devices. The basic characterization and the confirmation of piezoelectric potential of the as-prepared separator was discussed in **previous section**. Also the electrode materials basic characterization and electrochemical performance was discussed in **Chapter.5.4**.

7.2.3.1. Electrochemical behavior of the self-charging supercapacitor power cell

The supercapacitor behavior of the as-prepared SCSPC devices (PVDF-ZnO film separator) were investigated by the cyclic voltammetry (CV) and galvanostatic charge-discharge measurements. The cyclic voltammetry scans of the fabricated SCSPC (PVDF-ZnO film separator) device at a potential window of 0 to 2 V are shown in **Figure 7.2.1a**. It can be observed that the SCSPC device exhibit the rectangular-like shapes even at higher scan rates indicates the ideal capacitive behavior.

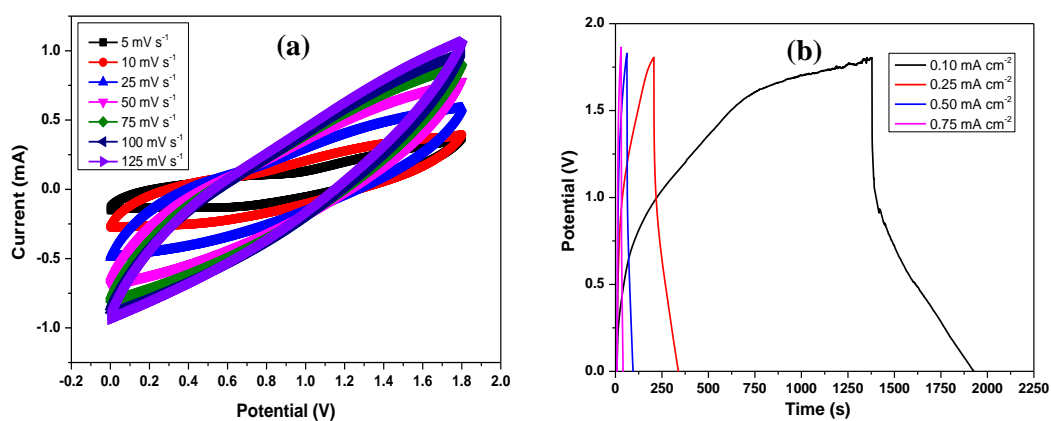


Figure 7.2.1 Electrochemical performance of SCSPC device in $\text{H}_3\text{PO}_4/\text{PVA}$ gel electrolytes: (a) Cyclic voltammetry scans of SCSPC device at different scan rates. (b) Galvanostatic charge/discharge curves of SCSPC device at different current densities.

Figure 7.2.1b show the galvanostatic charge/discharge curves of the SCSPC device at different current densities exhibit the linear and symmetric behavior

indicating the capacitive and fast charge/discharge property. In addition, a small potential plateau was observed in the galvanostatic charge/discharge curves, which is arisen from the Faradaic reaction. This result confirmed that the as-fabricated devices had a good charge storage behavior.

7.2.3.2. Mechanism of self-charging supercapacitor power cell

The working mechanism of the self-charging supercapacitor power cell (SCSPC) is based on piezoelectric-potential driven electrochemical reaction [9, 10]. The fabricated SCSPC device (**Figure 7.2.2**) consists of piezoelectric material (PVDF-ZnO) as a separator as well as potential generator, graphene act as a positive electrode and G-V₂O₅ act as a negative electrode for electrochemical reaction and the PVA-H₃PO₄ used as a electrolyte, which is uniformly distributed through the entire surface of the separator. At the beginning, the device is at the discharge state (**Figure 7.2.2a**), in which, there is no electrochemical reaction occurs due to the electrochemical equilibrium between the electrolyte and electrodes. In this state, there is no external deformation applied to the device.

When a compressive stress was applied to the device by means of palm impact (**Figure 7.2.2b**), which causes the polarization of ions in the PVDF film as well as in ZnO nanowires by piezoelectric effect [9]. The polarization of ions generates a potential difference across the thickness of PVDF. Suppose a positive and negative piezoelectric potential was generated at the top and the downside of the film, which drives the electrolytic ions (PVA-H₃PO₄) towards the positive (PO_4^{3-} ions) and negative (H^+ ions) electrodes. The piezoelectric field induced PO_4^{3-} and H^+ ions movement through ionic conduction paths represents in the PVDF-ZnO film separator for ion conductions in order to screening the piezo-potential, and

finally which produces an electrochemical imbalance in the electrolyte at the positive and negative electrode sides. To obtain the chemical equilibrium at the both electrode sides, the non-faradaic and faradaic reaction was take place at the electrode material surface present at the positive and negative electrode (**Figure 7.2.2c**), respectively.

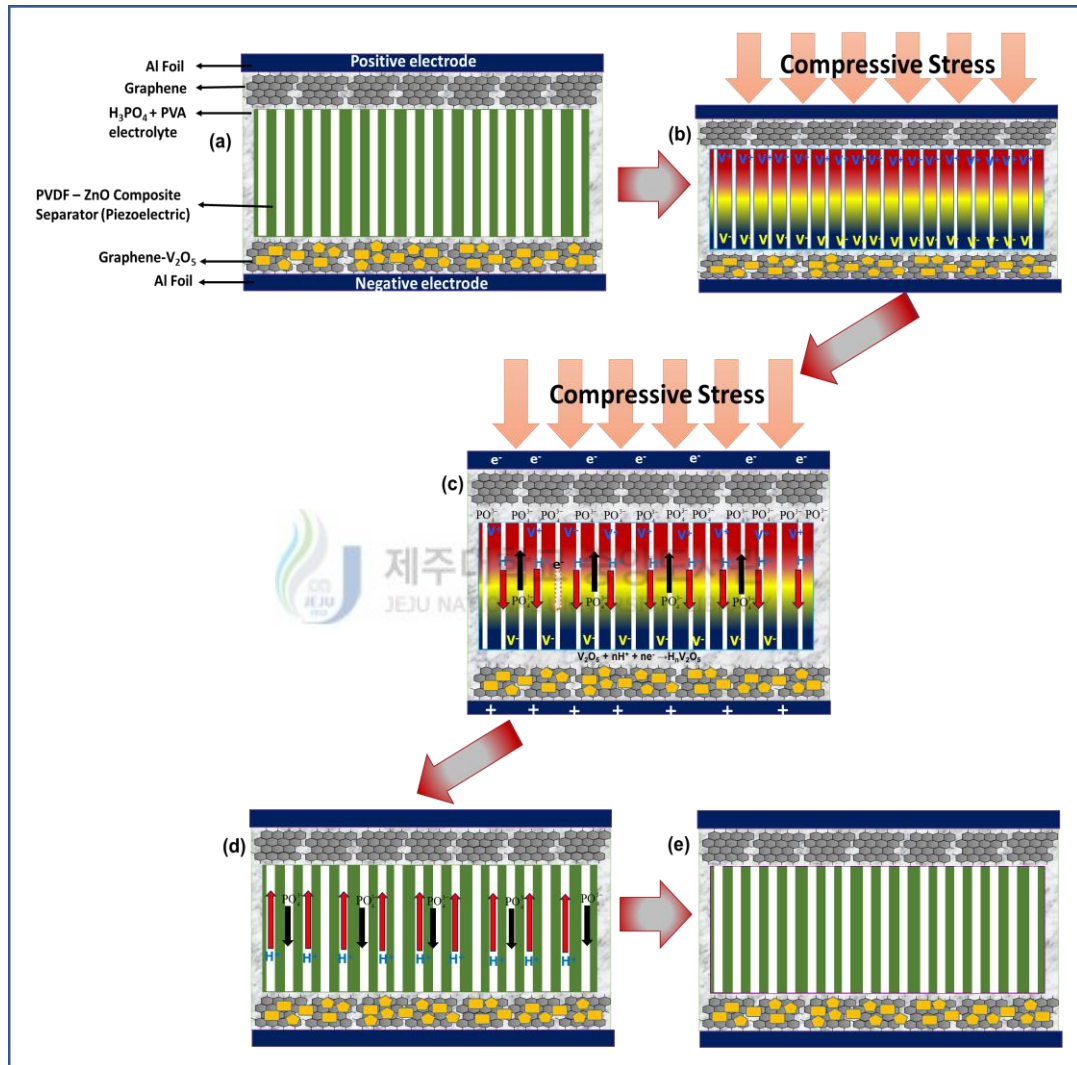
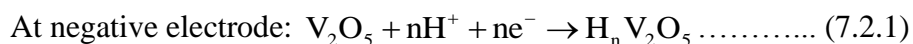


Figure 7.2.2 Working mechanism of the Self-Charging Supercapacitor Power Cell (SCSPC) driven by mechanical deformation. (a) Schematic diagram of the fabricated SCSPC device at discharge condition. (b) The mechanical deformation is applied on the top of the device; it creates a piezoelectric field (potential) in the PVDF-ZnO separator film. (c) Under the piezoelectric field, the H⁺ ions will migrate towards negative electrode and PO₄³⁻ ions migrate towards positive electrode, leading to the corresponding charging reactions at the two electrodes. (d) When external deformation is released, there is no piezoelectric field at the separator which breaks the attained chemical equilibrium; it causes a reverse reaction on both sides of the electrode, and ions are relocated into original position. (e) Completed self-charging cycle.

Due to the migration of H^+ ions towards negative electrode, leads to the reduction reaction at the electrode material surface (G- V_2O_5) through H^+ ions insertion and build the positive charges at the Al foil (current collector of the negative electrode). The reaction can be expressed as follows;



At the same time, the PO_4^{3-} ions migrates towards to the positive electrode and forms the double layer on the graphene surface through the absorption process. Due to the formation of double layer at positive electrode leaves the free electrons to the current collector (Al foil). The liberated electrons are transported to the negative electrode to maintain the charge neutrality as well as continuity of charging the reaction.

There are two possibility for the electron transfer; one is inside the SCSPC device system and the other is through the external circuit via monitoring system (Electrochemical workstation) [9, 10]. Although the exact mechanism is under investigation. Herein, the V_2O_5 generates pseudocapacitance and the reduced graphene sheet makes the conducting paths for the electrons as well as generates an electrochemical double layer capacitance, likewise the overall charge storage capacity of the composite electrode was improved. In such SCSPC devices, the charging process involves cations insertion into the negative electrode surface and anions adsorption onto the positive electrode surface.

Under continuous mechanical deformation, the charging process was repeated as like until to attain chemical equilibrium of two electrodes with piezoelectric potential; at this point, there is no further ionic polarization in the device. This is the process of converting mechanical energy directly into electrochemical energy. When removing the mechanical deformation, piezoelectric potential was disappearing in

the PVDF film (**Figure 7.2.2d**); it breaks the electrochemical equilibrium of the device. To compensate, a small amount of H^+ and PO_4^{3-} ions moving back to its original position, which indicating the completion of charging cycle (**Figure 7.2.2e**). When a charging cycle is completed through electrochemical reaction, a small of absorption and reduction occurred at positive and negative electrode surface. Again applying the mechanical deformation the charging cycle repeated as such, which results the conversion of mechanical energy into electrochemical energy. Finally, it could be argued that there are three main process occurs, first the generation of piezoelectric potential on PVDF-ZnO film by palm impact, second migration of H^+ and PO_4^{3-} ions towards negative and positive electrodes through ionic conduction path, and third, faradaic and non-faradaic reaction occurred at V_2O_5 layers and graphene via insertion/absorption of H^+ / PO_4^{3-} ions, which leads to store the lesser amount of generated energy.

7.2.3.3. Self-charging performance of as-fabricated SCSPC

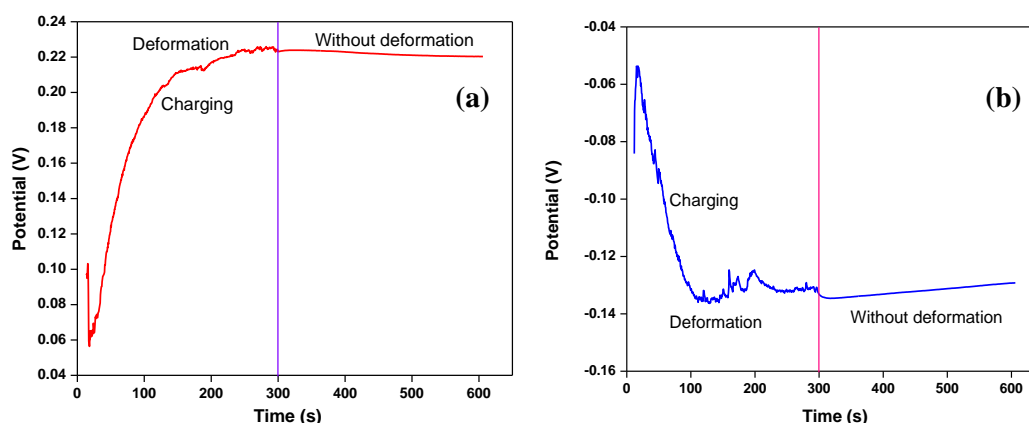


Figure 7.2.3 Self-charging performance of SCSPC device measured using electrochemical work station under periodic compressive straining: (a) The self-charging process of the SCSPC device by human palm impact. During vibration the voltage keeps raising, indicating that the charging process is occurred due to the migration of the ions. (b) The self-charging process of the polarity changed SCSPC device.

To show the self-charging capability of the SCSPC device (Aluminum foil); we have performed the self-charging process under continuous palm impact for 300 s, which is shown in **Figure 7.2.3a**. When a compressive force applied to SCSPC, the voltage of the device increased from 60 to 220 mV in 300 s. After removing the deformation, the stored energy was sustained around 300 s, which concludes that the device has the ability to self-charge under mechanical deformation/ vibration. The device showed slight decrease in voltage at the initial ~15 s and then starts to increase in voltage under continuous force. This may be due to un-equilibrium state occurred at the electrode materials surface. At the initial stage, the device becomes un-equilibrium state (voltage decreases; discharging) due to the sudden force applied to the device, after continuous palm impact the device attain chemical equilibrium at the both electrode sides (faradaic and non-faradaic reaction was take place at the electrode material surface) and starts to increase the device voltage (charging) after ~15 s. Further, we have checked the self-charging process of SCSPC device connected to opposite sign (polarity change), which is displayed in **Figure 7.2.3b**. Under vibration, the voltage of the device increased from -60 to -135 mV in 300 s. After deformation, the device sustained the stored energy for 300 s. At both condition, the SCSPC device showed a good response.

To demonstrate the flexible, light-weight and wearable based self-powered device applications; we have fabricated and tested the self-charging process of the fabric based SCSPC devices under continuous palm impact for 150 s. **Figure 7.2.4a** represents the self-charging process of the fabric based SCSPC devices using PVDF-ZnO separator films. Under continuous vibration, the device showed the increase in voltage (charging); the voltage of the SCSPC increased from 24 to 36 mV in 150 s.

After removing deformation, the device showed the increase in voltage for 50 s and then sustained the stored voltage for 100 s, which confirm the self-charging capability of the as-fabricated fabric based SCSPC. The increase in voltage was observed after deformation, which may be due to the vibration continued for few seconds after deformation also, because of light-weight of the fabricated fabric based SCSPC. In order to cross check the self-charging process of the SCSPC device, we have tested the self-charging process using Keithley instrument under continuous straining and it is shown in **Figure 7.2.4b**. In this case also, the voltage of the device increased from 26 to 52 mV (charging) in 300 s; after that the stored voltage sustained for 300 s, which confirms the self-charging capability of the as-fabricated SCSPC device.

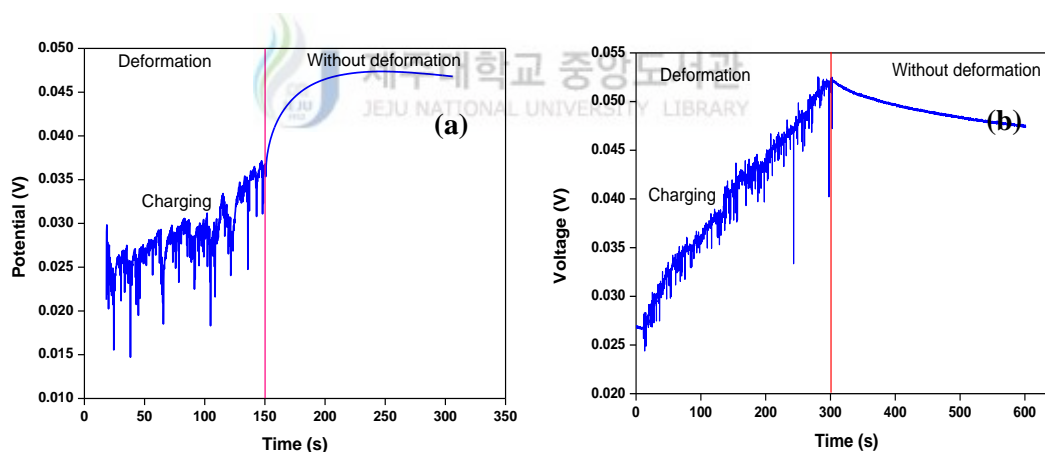


Figure 7.2.4 (a) The self-charging process of the fabric based SCSPC device. (b) The self-charging process of the SCSPC device measured using Keithley instruments.

Second to check, the self-charging capability of the six SCSPC devices are connected in series was tested under the continuous human palm impact to whole devices and it is shown in **Figure 7.2.5a**. Under a continuous impact; the voltage of the device increases from 0.96 to 1.07 V in 300 s and the sustained the stored voltage for 300 s, even after removing the deformation. The inset of **Figure 7.2.5a** shows the

photograph of the serially connected SCSPC devices. Further, the compression force was applied to each to individually one by one and measured the self-charging capability, which is shown in **Figure 7.2.5b**. All the devices are showing the self-charging capability, when applying force to device individually. The voltage was increased from 1.435 to 1.50 V in 300 s.

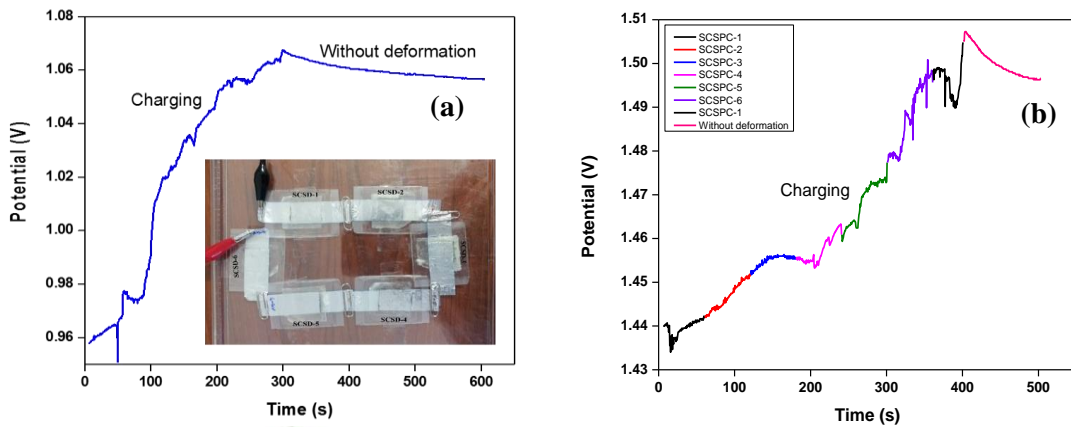


Figure 7.2.5 Self-charging performance of series connected six SCSPC devices: (a) The self-charging process of the series connected six SCSPC devices under periodic compressive straining given by human palm impact to the whole devices. Inset shows photograph of the series connected SCSPC devices. (b) The self-charging process of the series connected six SCSPC devices under periodic compressive straining given by human palm impact to the each device for 60 s interval. Inset shows the circuit diagram of series connection.

Further, to demonstrate the potential application (self-powered devices) of these SCSPC device; we have assembled six SCSPC devices in series to drive LED. Required amount of potential was charged using SCSPC as power sources for several hours. Finally, we showed that the SCSPC device can drive a green light-emitting diode (LED), as displayed in **Figure 7.2.6**. The inset of **Figure 7.2.6** red color border showed the zoomed portion of the powered green LED.

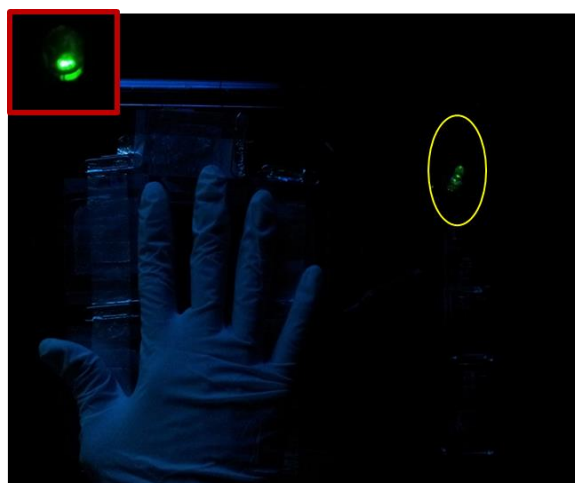


Figure 7.2.6 The operation of green LED using series connected six SCSPC devices as the power source.

From the above results and discussion, we have concluded that the as-fabricated SCSPC device is an initiation of new smart power electronics with self-power sources. In future, the described method can be extended for the synthesis of other carbons, oxide based electrode materials and various piezoelectric separator for self-charging supercapacitor power cell, which is currently under investigation.

7.2.4. Conclusion

In summary, we have successfully fabricated the first self-charging supercapacitor power cell that consists of PVDF-ZnO separator (piezoelectric nanogenerator) and V_2O_5 anchored graphene hybrid electrode used as the negative electrode and rGO used as the positive electrode (supercapacitor), which can be used to simultaneously harvest and store the mechanical energy to electrochemical energy. The SCSPC exhibited the self-charging capability under palm impact (Aluminum foil based SCSPC device = 160 mV for 300 s; Fabric based SCSPC device = 24 mV for 150 s). Further, the green LED was operated using series connected six SCSPC devices as the power source. In addition to that, the fabrication of SCSPC can be

extended to other carbons, and oxide based electrode materials as well other piezoelectric separator for self-charging application and can further be used in self-powered flexible and wearable hybrid electronic devices like LCD, LEDs and sensors.



7.2.5. References

- [1] S. Boukhalifa, K. Evanoff, and G. Yushin, Atomic layer deposition of vanadium oxide on carbon nanotubes for high-power supercapacitor electrodes. *Energy Environ. Sci.* 5 (2012) 6872-6879.
- [2] S. D. Perera, A. D. Liyanage, N. Nijem, J. P. Ferraris, Y. J. Chabal, and K. J. Balkus Jr, Vanadium oxide nanowire – Graphene binder free nanocomposite paper electrodes for supercapacitors: A facile green approach. *J. Power Sources* 230 (2013) 130-137.
- [3] B. H. Kim, C. H. Kim, K. S. Yang, A. Rahy, and D. J. Yang, Electrospun vanadium pentoxide/carbon nanofiber composites for supercapacitor electrodes. *Electrochim. Acta* 83 (2012) 335-340.
- [4] M. Jayalakshmi, M. Mohan Rao, N. Venugopal, and K. B. Kim, Hydrothermal synthesis of $\text{SnO}_2\text{-V}_2\text{O}_5$ mixed oxide and electrochemical screening of carbon nano-tubes (CNT), V_2O_5 , $\text{V}_2\text{O}_5\text{-CNT}$, and $\text{SnO}_2\text{-V}_2\text{O}_5\text{-CNT}$ electrodes for supercapacitor applications. *J. Power Sources* 166 (2007) 578-583.
- [5] Y. Sun, Q. Wu, and G. Shi, Graphene based new energy materials. *Energy Environ. Sci.* 4 (2011) 1113-1132.
- [6] J. Yoo, K. Balakrishnan, J. Huang, V. Meunier, B. Sumpter, A. Srivastava, M. Conway, A. Reddy, J. Yu, R. Vajtai, and P. Ajayan, Ultrathin planar graphene supercapacitors. *Nano Lett.* 11 (2011) 1423-1427.
- [7] S. J. Guo, and S. J. Dong, Graphene nanosheet: synthesis, molecular engineering, thin film, hybrids, and energy and analytical applications. *Chem. Soc. Rev.* 40 (2011) 2644-2672.

- [8] M. D. Stoller, S. J. Park, Y. W. Zhu, J. H. An, and R. S. Ruoff, Graphene-based ultracapacitors. *Nano Lett.* 8 (2008) 3498-3502.
- [9] X. Xue, P. Deng, B. He, Y. Nie, L. Xing, Y. Zhang and Z. L. Wang, Flexible self-charging power cell for one-step energy conversion and storage. *Adv. Energy Mater.* 4(5) (2014) 1301329.
- [10] X. Xue, S. Wang, W. Guo, Y. Zhang and Z. L. Wang, Hybridizing energy conversion and storage in a mechanical-to-electrochemical process for self-charging power cell. *Nano Lett.* 12 (9) (2012) 5048-5054.



CHAPTER-VIII

Conclusions and Future Work

8.1. Conclusions

This chapter describes the general conclusions of overall thesis and future directions of this work. In this thesis, typical one dimensional, two dimensional and graphene-metal oxide nanocomposite materials have been intensively studied for energy storage applications: TiO₂ NRs, TiO₂@MnO₂, TiO₂@Co₃O₄, TiO₂@Co(OH)₂, MnO₂, MoS₂, Graphene, Graphene-ZnO, Graphene-TiO₂, and Graphene-V₂O₅. The nanostructured materials were prepared via novel routes, well characterized and evaluated individually as supercapacitor electrodes (**Chapter 3 to 5**). The proficiency and efficiency of the fabricated SSC (graphene, graphene-TiO₂ and graphene-V₂O₅ based supercapacitors) have been demonstrated in a self-powered photosensor application. For the first time, the self-charging performance of symmetric SCSPC (MnO₂ electrodes) and asymmetric SCSPC (graphene, and G-V₂O₅ electrodes) have been evaluated individually as detailed in **Chapter 7**.

From this thesis, the following conclusions could be drawn:

In the first section of this thesis (**Chapter-3**), a simple and cost-effective approach was developed for the fabrication of binder free electrodes such as vertically aligned TiO₂ nanorods, TiO₂@MnO₂ core-shell, TiO₂@Co₃O₄ core-shell and TiO₂/Co(OH)₂ hybrid nanostructure on FTO substrate. The as-prepared binder free electrodes exhibited an areal capacitance of 0.085, 22, 44, and 274 mF cm⁻² at a scan rate of 5 mV s⁻¹. The overall electrochemical performance of TiO₂/Co(OH)₂ hierarchical nanostructure showed best performance (including capacitance, and cyclic stability), when compared to that of TiO₂ nanorods, TiO₂@MnO₂ core-shell,

and $\text{TiO}_2@\text{Co}_3\text{O}_4$ core-shell electrodes. The enhanced electrochemical performance of the hierarchical nanostructures is mainly due to the porous structure, which delivers fast ion and electron transfer, a large surface area, short ion diffusion paths, and a favourable volume change during the cycling process.

In order to still improve the mechanical performance and surface area of the electrode materials, a flexible supercapacitor was effectively fabricated using two dimensional materials and investigated their electrochemical performance in the second section of this thesis (**Chapter-4**). The electrochemical tests showed that the as-prepared MoS_2 and graphene nanosheets electrode exhibited an ideal capacitive behavior with a maximum specific capacitance of 403 and 414 F g^{-1} at a scan rate of 5 mV s^{-1} , respectively in three electrode configuration. Further, a flexible solid-state graphene-coated fabric supercapacitor exhibited excellent electrochemical performance with an energy density of 5.8 W h kg^{-1} at a power density of 27.7 kW kg^{-1} . In addition, the flexible supercapacitor demonstrated excellent flexibility and could be bent without destroying the structural integrity of the device. The results suggested that present method is simple and scalable to fabricate the graphene nanosheets on conductive cotton fabrics, which have considerable advantages as freestanding and binder-free electrodes for flexible and wearable supercapacitors.

To mitigate the shortcomings of both graphene and transition metal oxides, the graphene-transition metal oxide composites (G-ZnO , G-TiO_2 and $\text{G-V}_2\text{O}_5$) were synthesized and evaluated their electrochemical performance as a supercapacitor electrodes in the third section (**Chapter-5**). The electrochemical tests showed that the as-fabricated G-ZnO , G-TiO_2 and $\text{G-V}_2\text{O}_5$ composite electrodes exhibited a capacitive behavior with a specific capacitance of 109, 165, and 250 F g^{-1} at 5 mV s^{-1}

in three electrode system. The electrochemical studies clearly confirm that the G-V₂O₅ electrode exhibited a better performance such as specific capacitance and cycling stability when compare to G-ZnO, G-TiO₂, graphene, TiO₂ and ZnO electrodes. Further the G-V₂O₅/G-V₂O₅ symmetric supercapacitor (based on full cell), delivered a high energy density of 12.5 W h kg⁻¹ at a power density of 79.9 kW kg⁻¹ and sustained 8.4 W h kg⁻¹ at a power density of 799.9 kW kg⁻¹ compared to G-TiO₂ (3.2 W h kg⁻¹ at a power density of 79.9 kW kg⁻¹). The enhanced electrochemical performance could be owing to the following aspects: (i) Graphene in the hybrid structure can act as a conducting agent, which greatly improves the electrical conductivity of the hybrid structure and benefit the charge transfer through electrolyte to electrode, consequently leading to much enhanced electrochemical behavior. (2) the anchoring of well dispersed nanoparticles can effectively prevent the agglomeration and restacking of the graphene nanosheets, thus facilitating ion transport in the electrode material, and ultimately improving the electric double-layer capacitance. (3) Moreover, graphene nanosheets with a large surface area in the hybrid structure not only provided double-layer capacitance to the overall energy storage, but also effectively inhibited the aggregation of nanoparticles and keep them well distributed during materials synthesis and also during the electrochemical activity, resulting to the fast electron transfer throughout the entire electrode matrix as well as an overall improvement in the electrochemical performance. This study provides fundamental insights into the role of a graphene support in transition metal oxide-graphene electrode materials for supercapacitors.

In the fourth section (**Chapter-6**), a self-powered system was demonstrated by charging the fabricated supercapacitor using a nanogenerator to power a photo-

sensor. The obtained results demonstrated the feasibility of using fabricated solid state supercapacitors as efficient energy storage device and their application in self-powered devices. Further, the performance of the solid-state supercapacitor was demonstrated by lighting-up of LED and 4-digit seven segmented display.

The self-charging supercapacitor power cell (SCSPC) was developed for the first time which has been described in the last section (**Chapter-7**) of the thesis. PVDF-ZnO was used as a separator (piezoelectric nanogenerator) and various electroactive materials were used as the positive and negative electrodes (for supercapacitors), the fabricated device could simultaneously harvest and store the mechanical energy into electrochemical energy. The fabricated SCSPC exhibited the self-charging capability under palm impact. The clear piezo-electrochemical process (mechanism) of SCSPC was discussed in detail. Further, in order to demonstrate the practical application, we powered the green LED using serially connected SCSPC as the power source. This finding provides a new promising direction in the supercapacitor research for the development of next generation self-powered sustainable power source for wearable and flexible electronic devices.

8.2. Suggestions for the Future Work

Ever increasing R&D efforts are going on in the study of energy harvesting and energy storage devices. In the present study, enhancement on energy storage capacity was achieved by designing novel architecture electrode materials with the combination of both EDLC and pseudo-capacitance. Further, for the first time, we have fabricated and demonstrated the self-charging supercapacitor power cell using piezoelectric film as a separator and electro-active materials as a positive and negative electrodes. However, the preserve of both EDLC and pseudo-capacitance in the final product is the key for the ultimate performance of a supercapacitor.

- Therefore, it is suggested that the design of a suitable hybrid electrode configuration with optimized EDLC and pseudo-capacitance of the active materials in a two-electrode cell perhaps a good research direction towards commercialization of advanced materials in supercapacitors.
- To improve the self-charging performance of the SCSPC for sustainable self-powered device operation, finding new nanostructured materials with higher redox reactions with better pseudocapacitive behavior as well as better piezoelectric separator would provide a significant improvement to the future SCSPC devices.

Appendix A: List of publications

1. [Ananthakumar Ramadoss](#), Sang Jae Kim, Fabrication of hybrid TiO₂@MnO₂ core-shell nanostructure as potential electrode material for high-performance supercapacitor applications. *International Journal of Hydrogen Energy*, 39(23) (2014) 12201-12212.
2. [Ananthakumar Ramadoss](#), Sang Jae Kim, Enhanced supercapacitor performance using hierarchical TiO₂ nanorod/Co(OH)₂ nanowall array electrodes. *Electrochimica Acta*, 136 (2014)-105-111.
3. [Ananthakumar Ramadoss](#), Taehyun Kim, Gui-Shik Kim, Sang Jae Kim, Enhanced activity of hydrothermally synthesized mesoporous MoS₂ nanostructure for high performance supercapacitor applications. *New Journal of Chemistry*, 38 (2014) 2379-2385.
4. [Ananthakumar Ramadoss](#), Sang Jae Kim, Improved activity of a graphene–TiO₂ hybrid electrode in an electrochemical supercapacitor. *Carbon*, 63 (2013) 434-445.
5. [Ananthakumar Ramadoss](#), Gui-Shik Kim, Sang Jae Kim, Fabrication of reduced graphene oxide/TiO₂ nanorod/reduced graphene oxide hybrid nanostructures as electrode materials for supercapacitor applications. *CrystEngComm*, 15 (2013) 10222-10229.
6. [Ananthakumar Ramadoss](#), Sang Jae Kim Vertically aligned TiO₂ nanorod arrays for electrochemical supercapacitor. *Journal of Alloys and Compounds*, 561 (2013) 262-267.
7. [Ananthakumar Ramadoss](#), Sang Jae Kim Facile preparation and electrochemical characterization of graphene-ZnO nanocomposite for

- supercapacitor applications. *Materials Chemistry and Physics*, 140 (2013) 405-411.
8. Shin SoYoon, [Ananthakumar Ramadoss](#), Balasubramaniam Saravanakumar, Sang Jae Kim, Novel Cu/CuO/ZnO hybrid hierarchical nanostructures for non-enzymatic glucose sensor application, *Journal of Electroanalytical chemistry*, 717-718 (2014) 90-95.
 9. [Ananthakumar Ramadoss](#), Sang Jae Kim, Nanostructured TiO₂/TiN multilayer coatings on AISI 316L stainless steel for biomedical applications. *Science of Advanced Materials*, 5 (9) (2013) 1168-1178.
 10. [Ananthakumar Ramadoss](#), Sang Jae Kim, Synthesis and characterization of HfO₂ nanoparticles by sonochemical approach. *Journal of Alloys and Compounds*, 544 (2012) 115-119.
 11. [Ananthakumar Ramadoss](#), Karthikeyan Krishnamoorthy, Sang Jae Kim, Resistive switching behaviors of HfO₂ thin films by sol-Gel spin coating for nonvolatile memory applications. *Applied Physics Express*, 5(8) (2012) art. no. 085803-085805.
 12. [Ananthakumar Ramadoss](#), Karthikeyan Krishnamoorthy, Sang Jae Kim, Novel synthesis of hafnium oxide nanoparticles by precipitation method and its characterization. *Materials Research Bulletin*, 47(9) (2012) 2680-2684.
 13. [Ananthakumar Ramadoss](#), Karthikeyan Krishnamoorthy, Sang Jae Kim, Facile synthesis of hafnium oxide nanoparticles via precipitation method. *Materials Letter*, 75 (2012) 215-217.

List of submitted papers:

1. [Ananthakumar Ramadoss](#), Balasubramaniam Saravanakumar, Sang Jae Kim, Vanadium pentoxide/reduced graphene oxide composites as an efficient electrode materials for high-performance supercapacitors.
2. [Ananthakumar Ramadoss](#), Balasubramaniam Saravanakumar, Seung Woo Lee, Young-Soo Kim, Sang Jae Kim, Zhong Lin Wang, Self-charging supercapacitor power cell
3. [Ananthakumar Ramadoss](#), Balasubramaniam Saravanakumar, Sang-Jae Kim, Graphene-coated fabrics for flexible supercapacitors and self-powered systems
4. So-Yoon Shin, Balasubramaniam Saravanakumar, [Ananthakumar Ramadoss](#), Taehyun Kim, Sang Jae Kim, Fabrication of PDMS-based triboelectric nanogenerator for self-sustained power source application

Appendix B: List of Conferences

1. [Ananthakumar Ramadoss](#), Balasubramaniam Saravanakumar, Gui-Shik Kim, and Sang Jae Kim, Graphene coated flexible fabrics for high-performance supercapacitors. *Asian Conference on Nanoscience & Nanotechnology -2014*, October 26-29, 2014, Ramada Plaza, Jeju, Republic of Korea.
2. Taehyun Kim, [Ananthakumar Ramadoss](#), Balasubramaniam Saravanakumar and Sang Jae Kim, Facile hydrothermal synthesis of NiCo₂O₄ nanoplatelet as efficient electrode for high-performance supercapacitors. *The Korean Society of Mechanical Engineers (KSME)*, February 27-28, 2014, ICC Jeju National University, Jeju, Republic of Korea.
3. [Ananthakumar Ramadoss](#), Gui-Shik Kim, and Sang Jae Kim, Fabrication of TiO₂ nanorods/ Co₃O₄ nanowall hybrid structure for electrochemical supercapacitor application. *The 2nd International Conference on Advanced Electromaterials*, November 12-15, 2013, ICC Jeju, Jeju, Republic of Korea.
4. [Ananthakumar Ramadoss](#), and Sang Jae Kim, Enhanced supercapacitor performance of Graphene/V₂O₅ nanocomposites. *224th ECS Meeting*, October 27 – November 1, 2013, The Hilton San Francisco Hotel, San Francisco, CA, USA.
5. [Ananthakumar Ramadoss](#), and Sang Jae Kim, Hydrothermal synthesis of TiO₂@MnO₂ core-shell nanowires for electrochemical supercapacitors. *Nano Korea 2013, The 11th International Nanotech Symposium & Nano convergence Expo in Korea*, July 10-12, 2013, Coex, Seoul, Republic of Korea.
6. [Ananthakumar Ramadoss](#), Gui-Shik Kim, and Sang Jae Kim, Fabrication of TiO₂@Co₃O₄ core-shell nanostructure for high-performance supercapacitor applications. *The 16th International Symposium on the Physics of*

- Semiconductors and Applications (ISPSA)*, July 02-05, 2013, Ramada Plaza Jeju Hotel, Jeju, Republic of Korea.
7. [Ananthakumar Ramadoss](#), and Sang Jae Kim, Rapid microwave-assisted synthesis of graphene/TiO₂ composite for high performance supercapacitor. *Korean Sensors Society 2012*, Jeju National University International Center, Jeju, November 16-17 2012, Republic of Korea.
 8. Soyeon Shin, [Ananthakumar Ramadoss](#), Balasubramaniam Saravanakumar, Rajneesh Mohan, and Sang Jae Kim, Electrochemical properties of non-enzymatic glucose sensor using ZnO/CuO heterostructure. *KMEMS*, KAL Hotel, Jeju, April 4 - 6, 2013, Republic of Korea.
 9. Soyeon Shin, [Ananthakumar Ramadoss](#), Balasubramaniam Saravanakumar, Rajneesh Mohan, and Sang Jae Kim, Fabrication of CuO/ZnO heterostructure for nonenzymatic glucose sensor application. *Korean Sensors Society 2012*, Jeju National University International Center, Jeju, November 16-17 2012, Republic of Korea.
 10. [Ananthakumar Ramadoss](#), Karthikeyan Krishnamoorthy, and Sang Jae Kim, Corrosion behavior of TiN/TiO₂ multilayer coatings in phosphate buffered saline solutions for biomedical applications. *Nano Korea 2012, The 10th International Nanotech Symposium & Nano-Convergence Expo in Korea*, August 16-18 2012, COEX, Republic of Korea.
 11. T. Sakthivel, K. Karthikeyan, [R. Ananthakumar](#), Sang-Jae KIM and V. Gunasekaran, An investigation of optical and thermal properties of tin-oxide/graphene nanocomposites. *Nano Korea 2012, The 10th International*

Nanotech Symposium & Nano-Convergence Expo in Korea, August 16-18
2012, COEX, Republic of Korea.

12. [Ananthakumar Ramadoss](#), Karthikeyan Krishnamoorthy, and Sang Jae Kim,
Resistive switching characteristics of HfO₂ thin films grown by sol-gel spin
coating method. *Korean Physical Society, 2012 Spring Meeting*, April 24-26
2012, Daejeon Convention Centre, Daejeon, Republic of Korea

